



**NASA/ OHIO SPACE GRANT
CONSORTIUM**

**2016-2017 ANNUAL
STUDENT RESEARCH SYMPOSIUM
PROCEEDINGS XXV**



**During the solar eclipse (August 21, 2017),
scientists will take ground measurements
in Casper, Wyoming, and Columbia, Missouri**

Photo Credit: NASA/Katy Mersmann

**March 31, 2017
Held at the Ohio Aerospace Institute
Cleveland, Ohio**



Follow OSGC on:



TABLE OF CONTENTS

	<u>Page(s)</u>
Table of Contents	2-7
Foreword	8
Member Institutions	9
Acknowledgments	10
Agenda	10-16
Symposium Photographs	17-28

Click on any Student Name to be immediately linked to the first page of his/her report!

<u>Student Name</u>	<u>College/University</u>	<u>Page(s)</u>
Andersen, Kayla B.	Case Western Reserve University	29-33
Mini Worm: A Small SMA Actuated Worm-like Robot		
Arnott, Matthew M.	The Ohio State University.....	34-38
Investigation of an Excited Mach 0.9 Jet in Forward Flight Simulation		
Athie, Salif A.	Cincinnati State Technical & Community College	39-40
The Toxicity of Blue Dyes in M&M's® Candies		
Avouris, Dulcinea M.	Kent State University	41-44
Hyperspectral Imagery of the 2016 Harmful Algal Bloom in Lake Erie		
Ballard, Molly C.	Ohio Northern University.....	45-50
CFD Analysis of ONU SAE Aero Competition Airplane		
Bartholomew, Marisa D.	Cuyahoga Community College	51-53
The Road to Interoperability in Health Care		
Bennett, Jeffrey E.	University of Cincinnati	54-57
Water Testing Utilizing Unmanned Aerial Systems		
Boyd, Jonathan W.	Kent State University	58-61
Reduction of Graphene Oxide via Electron Beam Irradiation		
Brinkerhoff, Edward S.	University of Dayton.....	62-66
Energy Analysis of a Two Degree of Freedom Robot		
Burrage, Miles A.	Wright State University	67-68
Small-Scale Autonomous Hexapod Stair-Climbing Robot		
Burrow, Joshua A.	University of Dayton.....	69-74
Bio-Sensing with Ultra-flexible Planar Terahertz Metamaterials		

<i>Student Name</i>	<i>College/University</i>	<i>Page(s)</i>
Cancian, Anthony J.	Cuyahoga Community College	75-76
Insulated Concrete Forms: An Energy Efficient Building Solution		
Casey, Julian L.	Sinclair Community College	77-80
Electromagnetic Interference		
Ceraolo, Rosario J.	Lakeland Community College	81-82
City of Cleveland Analysis of Crime to Income Relative to Police Stations		
Conrath, Ellie N.	Ohio University	83-84
Wondrous Weather		
Coolidge, Chad A.	Lorain County Community College	85-87
Carbon Nanotubes Improvement of Granulated Activated Carbon as a Filter Media Abstract		
Crider, Hayley R.	Wright State University	88-89
Can You Go the Distance?		
Curtice, Michael C.	Central State University	90-91
Development of a Haptic Joystick System for Human Interaction		
Drennen, Charles E., Jr.	Marietta College	92-93
Development of Formation Evaluation Program to Test Lithology Crossplot Hypothesis		
Ellison, Solomon, III	Cincinnati State Technical & Community College	94-95
Design of Clothing Integrated with Circuitry to Regulate Body Temperature		
Enders, Brett K.	Lakeland Community College	96
LCC Parcel Ortho Mosaic Pixel Analysis to Identify Phragmites Plants		
Fadel, Joanna A.	Wright State University	97-100
Modeling of a Bioinspired Water Filtration System: A Sustainable Approach		
Fairley, Steven A.	Cuyahoga Community College	101-104
Tri-C's Extreme Green Experience		
Felicelli, Andrea L.	The University of Akron	105-106
Low Cost 3D Printing Using Vat-Free Photopolymerization		
Gardner, Jeanette A.	Sinclair Community College	107-108
The Beginning of an Autonomous Robotic Hand		
Gerges, Daniel G.	Cleveland State University	109-116
Altitude Combustion Stand Low Power Thrust Stand Design, Fabrication and Integration		
Gibson, Amanda E.	Cincinnati State Technical & Community College	117-118
Graphene and Energy Storage		

<i>Student Name</i>	<i>College/University</i>	<i>Page(s)</i>
Goetze, Paul A.	Miami University	119-120
Computational Analysis of Pulsatile Flow in Abdominal Arterial Bifurcation Models		
Gore, AlRitia J.	The University of Akron	121-124
Determining the Minimum Distance Needed Between a Hip Implant and Knee Implant Using Finite Element Analysis (FEA)		
Graf, Eric S.	Ohio University	125-130
ARGOS 8-Cable Suspended Robot Analysis		
Griffin, Katie S.	Cincinnati State Technical & Community College	131-132
Heart Disease Awareness on a College Campus		
Harding, James D.	Youngstown State University	133-134
Development of a Shape Memory Smart Structure via 3D Printing		
Herting, Elizabeth L.	Cedarville University	135-136
The Great Space Race: Thrust and Efficiency Rates of Burning Fuel		
Horn, Nicholas R.	The Ohio State University	137-140
Review and Design of Non-Axisymmetric Nozzles with Active Flow Control Capability		
Hummell, Kayla M.	Ohio Northern University	141-145
Spacesuits of the Future: Adapting Technology for Further Exploration		
Jarvis, Kenton C. D.	Ohio Northern University	146-149
Projectile Motion: A Manned Mission to the Moon and Mars		
Johnson, Josephine	Central State University	150-154
Engineering Feasibility Study for the Evaluation of Source Water Alternatives for Central State University's Water Distribution System		
Kordeleski, Zachary D.	Cleveland State University	155-156
You Can't Handle the "Physically Correct" Truth		
Kornblum, Kayle L.	Cuyahoga Community College	157-158
Eradicating Bacteria Using Ultraviolet Light		
Kuchta, Heidi E.	The University of Toledo	159-160
Searching for Brown Dwarfs and Ultra Cool Dwarfs in the Orion Molecular Clouds		
Kudrna, Jeffrey M.	Cuyahoga Community College	161-162
Aging of Photovoltaic Solar Panels		
Kyles-Stewart, Maiya A.	Sinclair Community College	163-167
Arugula Plants and Their Various Responses to H₂O₂		

<i>Student Name</i>	<i>College/University</i>	<i>Page(s)</i>
Lange, Eric M.	Cleveland State University	168-174
Catalytic Gasification: A Sustainable Waste Management Alternative		
Layden, Brittany A.	The University of Toledo	175-176
Investigating Our Climate System: Clouds and the Earth's Radiant Energy System		
Lonardo, Joseph V.	Youngstown State University	177-178
Low-Cost Metal Printing		
Maisonnet, Maxime	Wilberforce University	179-182
An Intelligent Fuzzy Sensor Based Motion Control System for Autonomous Mobile Robot		
Maniglia, Joanna C.	Lakeland Community College	183-184
Analysis of Red-Tailed Hawk Breeding and Land Cover Change in Ohio		
Marquardt, Ryan M.	Cedarville University	185-188
MiR-146a Upregulates Phagocytosis of Jurkats in a Human Macrophage Sjögren's Syndrome Model		
Mazursky, Alex J.	Miami University	189-190
Design and Performance Evaluation of a Miniature Haptic Actuator based on Electrorheological Fluid		
McIntosh, Joshua D.	Cincinnati State Technical & Community College	191-193
Diabetes: The Community College Student's Perspective		
McNair, Cameron R.	Columbus State Community College	194-198
Analyzing Silicon Carbide as an Engineering Material		
Miller, Amanda M.	University of Cincinnati	199-201
Active Exoskeleton for the Sit-to-Stand Transition		
Morin, Joseph R.	Cedarville University	202-205
An Electrochemical Analysis of Fretting Corrosion in Metal-on-Metal Hip Implants Subjected to High Impaction Loads		
Mullet, Sheldon P.	Marietta College	206-210
Waterless Fracturing Potential in the Appalachian Basin		
Musci, Daniel D.	Ohio Northern University	211-216
Feasibility of Creating a Home Drone System Controlled by a Raspberry Pi		
Nelson, McKenzie L.	Ohio University	217-220
Predictions of Human Arm Bone Strength from Measurements of Stiffness of Radii		
Oliver, Alexandra C.	Wright State University	221-223
Testing Game Design Choices in a New Genre of Educational Games		

<i>Student Name</i>	<i>College/University</i>	<i>Page(s)</i>
Omari, Dennis	The Ohio State University	224-225
Plasma Controlled Cavity in a Transient Unstart Environment		
Petrey, Olivia L.	The University of Akron	226-230
Effects of Anti-Gravity on Bone Formation in Coculture		
Pinder, Lauren B.	Central State University	90-91
Development of a Haptic Joystick System for Human Interaction		
Recker, Abigail E.	Kent State University	231-233
Lake Erie Water Quality Investigation		
Reece, Adam L.	Miami University	234-239
Dynamic Responses of Bending Actuators Based on Magneto-Rheological Elastomers		
Reynolds, John A.	Columbus State Community College	240-241
Augmented Reality and Virtual Reality in the Construction Industry		
Richards, Nathaniel L.	University of Cincinnati	242-245
Applying Genetic Fuzzy Systems to Time-Optimal Control Problems		
Rouse, Sarah C.	Cedarville University	246-247
Characterization of Ultrafine Textured Sandstone (Permian), Arizona, From the Study of Thin Sections		
Schlaerth, Hannah L.	Kent State University	248-250
Detection and Analysis of Biogeophysical Factors Influencing Local Water Quality and Coral Reef Health in the US Virgin Islands		
Singhal, Achal S.	The Ohio State University	251-258
Control of Dynamic Stall over a NACA 0015 Airfoil using NS-DBD Plasma Actuators		
Smoktonowicz, Anthony O.	The University of Toledo	259
Wide Area Sampling Prototype		
Starkey, Jennifer A.	Marietta College	260-263
Locating Abandoned Wells; Using Historical Documents and Records with Practical Physical and Technical Methods		
States, Lindsey A.	Miami University	264-266
The Earth, Sun, Stars, and Math?		
Tamburro, Lydia E.	Lakeland Community College	267-268
Inundated Destinations: An Analysis on Sea Level Rise in Puerto Rico and the US Virgin Islands		

<i>Student Name</i>	<i>College/University</i>	<i>Page(s)</i>
Tolbert, Nicholas Z.	Cuyahoga Community College	269-272
A Comparison of the Efficiency of Two Types of Experimental Photovoltaic Cells		
Tornes, Emily D.	Marietta College	273-275
Self-Sustaining Ecosystems		
Weaver, Valerie A.	Case Western Reserve University	276-279
Hybrid Neuroprostheses for Individuals with Paraplegia		
Wilber, Ryan S.	The Ohio State University	280-283
Parametric Reduced Order Model Applications in Gas Turbines		
Wilson, Kweisi F.	Wilberforce University	284-286
Capsule Endoscopy Lens Design		
Wolfe, Courtney N.	Kent State University	287-290
Investigation of Thermodynamic Cooperativity Pseudourylation Enzyme RsuA and rProteins During Bacterial 30S Ribosomal Assembly		
Wolfe, Marlo R.	Lakeland Community College	291-292
Prophylactic Braces and Athletic Performance		
Wright, Christopher B.	Cleveland State University	293-294
GC-MS Analysis of Chinese Baijiu Spirit Flavored as American Whiskey		
Zhu, Yonry R.	Ohio University	295-297
Plasma-Assisted Combustion in a Rotating Detonation Combustor		
Zwagerman, Bryce J.	Lakeland Community College	298-299
Adjustable 3D Printed Prosthetics		



MEMBER INSTITUTIONS

Affiliate Members

- Air Force Institute of Technology Eric D. Swenson. Ph.D.
- Case Western Reserve University Roger D. Quinn, Ph. D.
- Cedarville University Robert Chasnov, Ph.D., P.E.
- Central State University Augustus Morris, Jr., Ph.D., P.E.
- Cleveland State University Ms. Rose Begalla, M.A.
- Kent State University..... Joseph D. Ortiz, Ph.D.
- Miami University James Moller, Ph.D., P.E.
- Ohio Northern University..... Jed E. Marquart, Ph.D., P.E. *
- Ohio University..... Dr. Shawn Ostermann
- The Ohio State University Dr. Mo Samimy
- The University of Akron.....Dr. Craig C. Menzemer
- University of Cincinnati Dr. Kelly Cohen
- University of Dayton..... Dr. John G. Weber
- The University of ToledoDr. Lesley M. Berhan
- Wilberforce University Jennifer N. Williams, Ph.D.
- Wright State University Mitch Wolff, Ph.D.

Campus Representative

Participating Institutions

- Marietta College..... Prof. Craig Rabatin, P.E.
- Youngstown State University Hazel Marie, Ph.D., P.E.

Campus Representative

Community Colleges

- Cincinnati State Technical and Community College Professor Abigail Yee
- Columbus State Community College..... Professor Jeffery M. Woodson, M.S., I.E.
- Cuyahoga Community College Dr. Lam F. Wong
- Lakeland Community College.....Dr. Steven Oluic, USA (ret.)
- Lorain County Community College..... Rosa E. Rivera-Hainaj, Ph.D.
- Owens Community College Dean Glenn Rettig
- Sinclair Community College Lorraine A. Kapka, P.E.
- Terra Community College..... Mr. Andrew Carroll

Campus Representative

NASA Glenn Research Center - Representatives

- Dr. M. David Kankam
- Ms. Susan M. Kohler
- Mr. Robert F. LaSalvia

Lead Institution

- Ohio Aerospace Institute Ms. Ann O. Heyward

Representative

*Dr. Marquart also serves as Director of the Ohio Space Grant Consortium

ACKNOWLEDGMENTS

Thank you to all who helped with the OSGC's 25th Annual Research Symposium!

Ohio Aerospace Institute

- Mark Cline
- Matt Grove
- Valerie Hale
- Ann O. Heyward
- Gary R. Leidy
- Jeff Rolf
- Demetrious Towns
- Joshua Allen
- Emilio J. Borges
- Robert Charvat
- Derick Endicott
- James Gilland
- Andrew Gyekenyesi
- Christopher Hocevar
- Frederic A. Holland

Evaluators

- Paul Penko
- Raquel Redhouse
- Robert Setlock
- Mrityunjay Singh
- Kim Tanger
- Jen-Ching Tsao
- Jacqueline Vance
- Andrew H. Work

STEM Panel:

- Joshua Allen (NASA Glenn Research Center)
- Emilio Borges (NASA Glenn Research Center)
- Ashlie Flegel (NASA Glenn Research Center)
- Derick Endicott (Space X)
- Rob Charvat (GE Aviation)
- Chad Yoshikawa (Google) participated via Skype

Campus Representatives – 4-Year Universities

- Dr. Eric D. Swenson, Air Force Institute of Technology
- Dr. Roger Quinn, Case Western Reserve University
- Robert Chasnov, Ph.D., P.E., Cedarville University
- Augustus Morris, Jr., Ph.D., P.E., Central State University
- Ms. Rose Begalla, M.A., Cleveland State University
- Dr. Joseph D. Ortiz, Kent State University
- Professor Craig Rabatin, Marietta College
- James Moller, Ph.D., P.E., Miami University
- Jed E. Marquart, Ph.D., P.E., Ohio Northern University*
- Dr. Shawn Ostermann, Ohio University
- Dr. Mo Samimy, The Ohio State University
- Dr. Craig C. Menzemer, The University of Akron
- Dr. Kelly Cohen, University of Cincinnati
- Dr. John G. Weber, University of Dayton
- Dr. Lesley M. Berhan, The University of Toledo
- Jennifer N. Williams, Ph.D., Wilberforce University
- Mitch Wolff, Ph.D., Wright State University
- Hazel Marie, Ph.D., P.E., Youngstown State University

Campus Representatives - Community Colleges

- Professor Abigail Yee, Cincinnati State Technical and Community College
- Professor Jeffery M. Woodson, M.S., I.E., Columbus State Community College
- Dr. Lam F. Wong, Cuyahoga Community College
- Dr. Steven Oluic, USA (ret.), Lakeland Community College
- Rosa E. Rivera-Hainaj, Ph.D., Lorain County Community College
- Dean Glenn Rettig, Owens Community College
- Lorraine A. Kapka, P.E., Sinclair Community College
- Mr. Andrew Carroll, Terra Community College

Special thanks go out to the following:

- Jeff Rolf and OAI for hosting the event.
- Jay N. Reynolds, Cleveland State University, for coordinating the Poster Session.
- Industry Attendees
- NASA Glenn Research Center – Human Resources – Christina Koleno
- Ohio Aerospace Institute staff whose assistance made the event a huge success!
- Silver Service Catering (Scot and Mary Lynne)
- Sharon Mitchell Photography

*Dr. Marquart also serves as Director of the Ohio Space Grant Consortium



2017 OSGC Student Research Symposium
Hosted By: Ohio Aerospace Institute (OAI)
22800 Cedar Point Road • Cleveland, OH 44142
• (440) 962-3000
Friday, March 31, 2017



AGENDA

8:00 AM – 8:30 AM	Sign-In / Continental Breakfast / Student Portraits (30 minutes).....Lobby
8:35 AM – 8:40 AM	Welcome to OAI (5 minutes) Forum (Lobby Level) <i>Jeff Rolf</i> President and Chief Executive Officer, Ohio Aerospace Institute
8:40 AM – 8:45 AM	Welcome and Introductions (5 minutes) <i>Jed E. Marquart</i> Director, Ohio Space Grant Consortium
8:45 AM – 8:50 AM	Symposium Logistics (5 minutes) <i>Laura A. Stacko</i> Program Manager, Ohio Space Grant Consortium
8:50 AM – 9:00 AM	Group Photograph (10 minutes).....Lobby / Atrium Stairwell
9:00 AM – 11:00 AM	Student Oral Presentations – Senior Scholars and Fellows (120 minutes) •Group 1 Forum (Lobby Level) •Group 2 Presidents’ Room (Lower Level) •Group 3 Industry Room (2nd Floor) •Group 4 Board Room (2nd Floor)
11:00 AM – 12:15 PM	Various Displays (75 minutes) •Student Poster Presentations.....Lobby Junior, Community College, and Pre-Service Teacher (Education) Scholars •NASA and Industry Displays Lobby •Student Team Displays.....Atrium (Lower Level)
12:15 PM – 1:15 PM	Luncheon Buffet (60 minutes).....Atrium / Sunroom (Lower Level)
1:15 PM – 2:15 PM	Panel Discussion and Q&A (60 minutes)..... Forum (Lobby Level) <i>“Launching a STEM Career”</i>
<i>Panel Members:</i>	
*Joshua E. Allen, NASA Glenn Research Center	*Derick S. Endicott, Space X
*Emilio J. Borges, NASA Glenn Research Center	*Ashlie B. Flegel, NASA Glenn Research Center
*Robert C. Charvat, GE Aviation	*Chad O. Yoshikawa, Google
2:15 PM – 2:30 PM	Presentation of Best Poster Awards (15 minutes).....Forum
2:30 PM	Symposium Adjourns



STUDENT ORAL PRESENTATIONS
9:00 AM to 11:00 AM (120 minutes)

Group 1 – Mechanical Engineering FORUM (AUDITORIUM – LOBBY LEVEL)	
Evaluators: Emilio J. Borges, Robert Setlock, Andrew H. Work	
9:00	Kayla B. Andersen, Senior, Mechanical Engineering, Case Western Reserve University <i>Mini-Worm: A Small Worm-Like Robot Actuated Via Nitinol</i>
9:15	Molly C. Ballard, Senior, Mechanical Engineering, Ohio Northern University <i>CFD Analysis of SAE Aero Competition Plane</i>
9:30	Kayla M. Hummell, Senior, Mechanical Engineering, Ohio Northern University <i>Spacesuits of the Future: Adapting Technology for Further Exploration</i>
9:45	Joseph R. Morin, Senior, Mechanical Engineering, Cedarville University <i>An Electrochemical Analysis of Fretting Corrosion in Metal-on-Metal Hip Implants</i>
10:00	Adam L. Reece, Senior, Mechanical Engineering, Miami University <i>Characterization of Dynamic Responses of Bending Actuators Based on Magneto-Rheological Elastomers</i>
10:15	Valerie A. Weaver, Senior, Mechanical Engineering, Case Western Reserve University <i>Hybrid Neuroprostheses for Individuals with Paraplegia</i>
10:30	Daniel G. Gerges, Master’s 2, Mechanical Engineering, Cleveland State University <i>Design, Fabrication and Integration of a Low Thrust Measurement Stand for the Altitude Combustion Chamber at Glenn Research Center</i>
10:45	Achal S. Singhal, Master’s 2, Mechanical Engineering, The Ohio State University <i>Control of Dynamic Stall Over a NACA 0015 Airfoil Using NS-DBD Plasma Actuators</i>

Group 2 – Aeronautical & Astronautical Engineering / Aerospace Engineering / Mechanical Engineering PRESIDENTS’ ROOM (LOWER LEVEL)	
Evaluators: Derick Endicott, Paul Penko, Jen-Ching Tsao	
9:00	Matthew M. Arnott, Senior, Aeronautical & Astronautical Engineering, The Ohio State University <i>Comparison of an Excited Flow with an Unheated Subsonic Jet in Forward Flight</i>
9:15	Nicholas R. Horn, Senior, Aeronautical & Astronautical Engineering, The Ohio State University <i>Review and Design of Non-Axisymmetric Nozzles with Active Flow Control Capability</i>
9:30	Jeffrey E. Bennett, Senior, Aerospace Engineering, University of Cincinnati <i>Water Testing Utilizing Unmanned Aerial Systems</i>
9:45	Nathaniel L. Richards, Senior, Aerospace Engineering, University of Cincinnati <i>Closed-Loop, Near Time-Optimal Control of a Double Cart Oscillator Under Uncertainty by Genetic Fuzzy Machine Learning</i>
10:00	Eric S. Graf, Jr., Senior, Mechanical Engineering, Ohio University <i>ARGOS 8-Cable Suspended Robot</i>
10:15	Ryan S. Wilber, Senior, Mechanical Engineering, The Ohio State University <i>Parametric Reduced Order Model Applications in Gas Turbines</i>
10:30	Dennis Omari, Master’s 1, Aeronautical & Astronautical Engineering, The Ohio State University <i>Plasma Controlled Cavity as a Shock Trap in a Transient Environment</i>



STUDENT ORAL PRESENTATIONS (Continued)

9:00 AM to 11:00 AM (120 minutes)

Group 3 – Biology / Biological Sciences / Biomedical Engineering / Chemistry / Chemical Engineering	
INDUSTRY ROOM (SECOND FLOOR)	
Evaluators: Robert Charvat, Mrityunjay Singh	
9:00	Ryan M. Marquardt, Senior, Biology, Cedarville University <i>MiR-146a Upregulation of Phagocytosis in Human Macrophage</i>
9:15	McKenzie L. Nelson, Senior, Biological Sciences, Ohio University <i>Predictions of Human Arm Bone Strength from Measurements of Stiffness of Radii</i>
9:30	Joanna A. Fadel, Senior, Biomedical Engineering, Wright State University <i>Modeling of a Bioinspired Water Filtration System: A Sustainable Approach</i>
9:45	AlRitia J. Gore, Senior, Biomedical Engineering, The University of Akron <i>Determining the Minimum Distance Needed Between a Hip Implant and Knee Implant Using Finite Element Analysis (FEA)</i>
10:00	Olivia L. Petrey, Senior, Biomedical Engineering, The University of Akron <i>The Effects of Anti-Gravity on Bone Formation in Coculture</i>
10:15	Aaron K. Smith, Senior, Chemical Engineering, Cleveland State University <i>Implementing a Micromixer on a 3-D Printer</i>
10:30	Courtney N. Wolfe, Senior, Chemistry, Kent State University <i>Investigation of Thermodynamic Cooperativity Pseudourylation Enzyme RsuA and rProteins During Bacterial 30S Ribosomal Assembly</i>
10:45	Eric M. Lange, Master's 1, Chemical Engineering, Cleveland State University <i>Catalytic Gasification: A Sustainable Waste Management Alternative</i>

Group 4 – Petroleum Engineering / Water Resources Management / Physics /	
Manufacturing Engineering / ElectroOptics / Applied Geology	
BOARD ROOM (SECOND FLOOR)	
Evaluators: Joshua Allen, Raquel Redhouse	
9:00	Sheldon P. Mullet, Senior, Petroleum Engineering, Marietta College <i>Exploring Alternatives to Hydraulic Fracturing</i>
9:15	Jennifer A. Starkey, Senior, Petroleum Engineering, Marietta College <i>Locating Abandoned Wells: Using Historical Documents and Records with Practical Physical and Technical Methods</i>
9:30	Josephine Johnson, Senior, Water Resources Management, Central State University <i>Central State's Pipe System</i>
9:45	Jonathan W. Boyd, Senior, Physics, Kent State University <i>Reduction of Graphene Oxide via Electron Beam Acceleration</i>
10:00	Lauren B. Pinder, Senior, Manufacturing Engineering, Central State University <i>3D Hapkit Modeling</i>
10:15	Joshua A. Burrow, Master's 1, Electro Optics, University of Dayton <i>Bio-sensing with Ultra-flexible Planar Terahertz Metamaterials</i>
10:30	Dulcinea M. Avouris, PhD 3, Applied Geology, Kent State University <i>Hyperspectral Imagery of the 2016 Harmful Algal Bloom in Lake Erie</i>

**STUDENT POSTER PRESENTATIONS
LOBBY (MAIN FLOOR)**

11:00 AM to 12:15 PM (75 minutes)

Dr. Jay N. Reynolds, Coordinator of Poster Session

Evaluators: James Gilland, Andrew Gyekenyesi, Frederic A. Holland, Christopher Hocevar, Robert Setlock, Mrityunjay Singh, Kim Tanger, Jacqueline Vance, Andrew H. Work

Junior Science, Technology, Engineering, and Mathematics (STEM) Scholarship Recipients
Edward S. Brinkerhoff, Mechanical Engineering, University of Dayton <i>Energy Analysis of a Two Degree of Freedom Mechanical System</i>
Miles A. Burrage, Electrical Engineering, Wright State University <i>Small-Scale Autonomous Hexapod Robot</i>
Michael C. Curtice, Manufacturing Engineering, Central State University <i>Development of a Haptic Joystick System for Human Interaction</i>
Charles E. Drennen, Jr., Petroleum Engineering, Marietta College <i>Development of Formation Evaluation Program to Test Lithology Crossplot Hypothesis</i>
Andrea L. Felicelli, Mechanical Engineering, The University of Akron <i>Low Cost 3D Printing Using Vat-Free Photopolymerization</i>
Paul A. Goetze, Mechanical Engineering, Miami University <i>Computational Analysis of Pulsatile Flow in Abdominal Arterial Bifurcation Models</i>
James D. Harding, Chemical Engineering, Youngstown State University <i>Development of a Shape Memory Smart Structure Via 3D Printing</i>
Heidi E. Kuchta, Astrophysics, The University of Toledo <i>Searching for Brown Dwarfs and Ultra Cool Dwarfs in the Orion Molecular Clouds</i>
Joseph V. Lonardo, Mechanical Engineering, Youngstown State University <i>Low-Cost Metal Printing</i>
Maxime Maisonnet, Computer Science, Wilberforce University <i>An Intelligent Fuzzy Sensor Based Motion Control System for Autonomous Mobile Robots</i>
Alex J. Mazursky, Mechanical Engineering, Miami University <i>Design and Performance Evaluation of a Miniature Haptic Actuator Based on Electrorheological Fluid</i>
Amanda M. Miller, Mechanical Engineering, University of Cincinnati <i>Design of an Active Exoskeleton for the Sit-to-Stand Transition</i>
Daniel D. Musci, Electrical Engineering, Ohio Northern University <i>Feasibility of Drone Networks Controlled by Raspberry Pis</i>
Alexandrea C. Oliver, Computer Science, Wright State University <i>The Impact of Game Design Choices in Interactive Education Games</i>
Sarah C. Rouse, Geology, Cedarville University <i>Characterization of Massive vs. Laminated Texture of the Coconino Sandstone (Permian), Arizona from the Study of Thin Sections</i>
Hannah L. Schlaerth, Environmental Geology, Kent State University <i>Detection and Analysis of Biogeophysical Factors Influencing Local Water Quality and Coral Reef Health in the US Virgin Islands</i>
Anthony O. Smoktonowicz, Electronics Engineering Technology, The University of Toledo <i>Wide Area Air Sampling Prototype</i>
Alexis R. Staniel, Computer Science, Wilberforce University <i>Cybersecurity Strategies in Law Enforcement</i>
Kweisi F. Wilson, Electrical Engineering, Wilberforce University <i>Design of a Sensitive Probe for Endoscopic Imaging</i>
Yonry R. Zhu, Engineering Physics/ Mechanical Engineering, Ohio University <i>Plasma-Assisted Rotating Detonation Combustor</i>

STUDENT POSTER PRESENTATIONS (Continued)
LOBBY (MAIN FLOOR)
11:00 AM to 12:15 PM (75 minutes)

Community College STEM Scholarship Recipients
Amanda M. Baluch, Electrical Engineering Technology, Cuyahoga Community College <i>Automatization and Enhancement of Hydroponically Grown Crops</i>
Marisa D. Bartholomew, Health Information Management Technology, Cuyahoga Community College <i>Interoperability & Health Care</i>
Anthony J. Cancian, Construction Engineering Technology, Cuyahoga Community College <i>Insulated Concrete Forms: An Energy Efficient Building Solution</i>
Rosario J. Ceraolo Jr., Geographic Information Systems, Lakeland Community College <i>Analysis of Crime to Income Relative to Police Stations</i>
Chad A. Coolidge, Automation Engineering, Lorain County Community College <i>Activated Carbon and Carbon Nanotubes</i>
Griffin M. Derr, Computer Engineering, Sinclair Community College
Solomon Ellison, III, Pre-Engineering, Cincinnati State Technical and Community College <i>Wearable Technology for Regulating Body Temperature</i>
Brett K. Enders, Geospatial Technology, Lakeland Community College <i>LCC Parcel Ortho Mosaic Pixel Analysis to Identify Phragmites Plants</i>
Steven A. Fairley, Engineering, Cuyahoga Community College <i>Tri-C's Extreme Green Ecosystems Experience</i>
Jeanette A. Gardner, Electrical Engineering, Sinclair Community College <i>The Beginning of an Autonomous Robotic Hand</i>
Amanda E. Gibson, Pre-Engineering, Cincinnati State Technical and Community College <i>Graphene and Energy Storage</i>
Katie S. Griffin, Dietetics & Pre-Nutrition Science, Cincinnati State Technical and Community College <i>Heart Disease Awareness on a College Campus</i>
Kayle L. Kornblum, Electrical/Electronic Engineering Technology, Cuyahoga Community College <i>Eradicating Bacteria Using Ultraviolet Light</i>
Jeffrey M. Kudrna, Electronic Engineering Technology, Cuyahoga Community College <i>The Aging of Solar Panels</i>
Maiya A. Kyles-Stewart, Biology, Sinclair Community College <i>Arugula Plants and Their Various Responses to H₂O₂</i>
Joanna C. Maniglia, Geospatial Technology, Lakeland Community College <i>Analysis of Red-tailed Hawk Breeding and Land Cover Change in Ohio</i>
Joshua D. McIntosh, Dietetic Technology, Cincinnati State Technical and Community College <i>Diabetes: The Community College Student's Perspective</i>

STUDENT POSTER PRESENTATIONS (Continued)
LOBBY (MAIN FLOOR)
11:00 AM to 12:15 PM (75 minutes)

Community College STEM Scholarship Recipients
John A. Reynolds, Construction Management, Columbus State Community College <i>Virtual Reality in Construction</i>
Lydia E. Tamburro, Biology, Lakeland Community College <i>Inundated Destinations: An Analysis on Sea Level Rise in Puerto Rico and the US Virgin Islands</i>
James I. Timotiwiu, Pre-Engineering, Cuyahoga Community College <i>Multisensory-based Autonomous Navigation in Constrained Indoor Environments</i>
Nicholas Z. Tolbert, Electrical Engineering, Cuyahoga Community College <i>A Comparison in the Cost Effectiveness of Experimental Photovoltaic Cells</i>
Marlo R. Wolfe, Biology, Lakeland Community College <i>Prophylactic Braces and Athletic Performance</i>
Tyland J. Worrell, Mechanical Engineering Design, Cincinnati State Technical and Community College <i>Robotics</i>
Christopher B. Wright, Applied Science, Lorain County Community College/Cleveland State University <i>GC-MS Analysis of Chinese Baijiu Spirit Flavored as American Whiskey</i>
Bryce J. Zwagerman, Pre-Engineering, Lakeland Community College <i>3D Printed Prosthetics</i>

Pre-Service Teacher (Education) Scholarship Recipients
Ellie N. Conrath, Early Childhood Education, Ohio University <i>Wondrous Weather</i>
Hayley R. Crider, Early Childhood Education, Wright State University <i>Can You Go the Distance?</i>
Elizabeth L. Herting, Adolescent to Young Adult (AYA) Education, Mathematics, Cedarville University <i>The Great Space Race: Thrust and Efficiency Rates of Burning Fuel</i>
Kenton C. D. Jarvis, Adolescent to Young Adult (AYA) Education, Mathematics, Ohio Northern University <i>Project Blast Off</i>
Zachary D. Kordeleski, Middle Childhood Education, Physics and Mathematics, Cleveland State University <i>Why Physicists Can't Enjoy Movies</i>
Brittany A. Layden, Adolescent to Young Adult (AYA) Education, Science, The University of Toledo <i>Climate Change Investigation: Clouds and Weather</i>
Abigail E. Recker, Early Childhood Education, Kent State University <i>Lake Erie Water Quality Investigation</i>
Lindsey A. States, Adolescent to Young Adult (AYA) Education, Mathematics, Miami University <i>The Earth, Sun, Stars, and ... Math?</i>
Emily D. Tornes, Early Childhood Education, Marietta College <i>Self Sustaining Ecosystems</i>

STUDENT TEAMS
ATRIUM (OUTSIDE PRESIDENT'S ROOM/LOWER LEVEL)
11:00 AM to 12:15 (75 minutes)

Lorain County Community College Unmanned Aircraft Systems (UAS) Team
Professor Marlin Linger

The Ohio State University Buckeye Space Launch Initiative Team
<i>Team Members:</i> Bryce Huber Joe Yanoska <i>Advisor:</i> Dr. Jen-Ping Chen

The University of Akron (UA) NASA Robotics Mining Competition Team
<i>Team Members:</i> Dana Cressman Cody Gruber Reed Jacobsen Zachary Kilburn Jack Wolfe, III <i>Advisor:</i> Dr. Seungdeog Choi

Ohio Space Grant Consortium



25th Annual OSGC Student Research Symposium

**Friday, March 31, 2017
Ohio Aerospace Institute
Cleveland, Ohio**

Welcome Session



Jeff Rolf, new President and CEO of the Ohio Aerospace Institute, bids everyone good morning and expresses his excitement about participating in his first Symposium.

OSGC Director Dr. Jed Marquart follows up by congratulating the students on another year of impressive research projects.



Symposium attendees were surprised with a visit from District 14 Representative Martin Sweeney. He encouraged them to blaze trails with STEM and to be active in their civic duties.

Senior and Fellow Presentations



Joshua Burrow's research on "Bio-Sensing with Ultra-flexible Planar Terahertz Metamaterials" kicks off the morning.



Kayla Andersen's presents her work on "Mini Worm: A Small SMA Actuated Worm-like Robot."



Joanna Fadel explains "Modeling of a Bioinspired Water Filtration System: A Sustainable Approach."



Dennis Omari sheds light on "Plasma Controlled Cavity in a Transient Unstart Environment."



Ryan Marquardt presenting his research: "MiR-146a Upregulates Phagocytosis of Jurkats in a Human Macrophage Sjögren's Syndrome Model."



Dulcinea Avouris and her observations on "Hyperspectral Imagery of the 2016 Harmful Algal Bloom in Lake Erie."

Senior and Fellow Presentations



Jeffrey Bennett and the drone he utilized in his project on “Water Testing Utilizing Unmanned Aerial Systems.”



Kayla Hummell presenting her research on “Spacesuits of the Future: Adapting Technology for Further Exploration.”



Josephine Johnson explains “Pipe Reconstruction and Water Flow on Central State University’s Campus.”



Eric Graf’s passionate talk on “ARGOS 8-Cable Suspended Robot Analysis.”

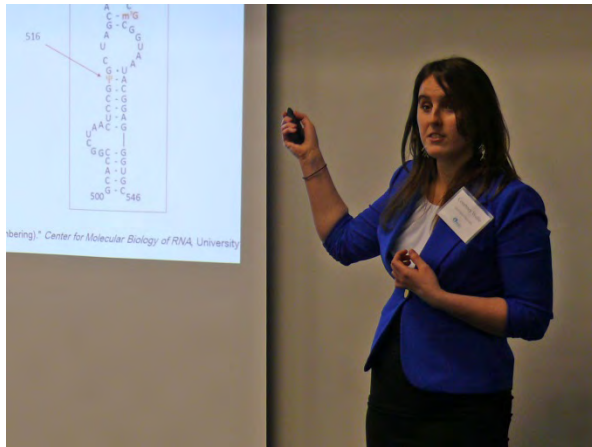


Nicholas Horn on “Review and Design of Non-Axisymmetric Nozzles with Active Flow Control Capability.”



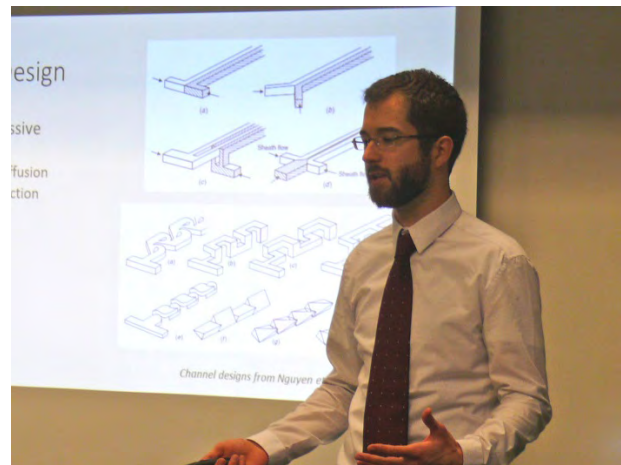
Jennifer Starkey presents “Locating Abandoned Wells; Using Historical Documents and Records with Practical Physical and Technical Methods.”

Senior and Fellow Presentations



Courtney Wolfe's "Investigation of Thermodynamic Cooperativity Pseudourylation Enzyme RsuA and rProteins During Bacterial 30S Ribosomal Assembly."

Aaron Smith explains the process of "Implementing a Micromixer on a 3-D Printer."



Olivia Petrey presents the findings of her research on "Effects of Anti-Gravity on Bone Formation in Coculture."

Lauren Pinder presents her ideas on the "Development of a Haptic Joystick System for Human Interaction."



Student Teams



Professor Marlin Linger representing his UAS (Unmanned Aerial Systems) Program at Lorain County Community College sponsored by the Ohio Space Grant Consortium's CC-STARS! Program.

The University of Akron Lunabotics Team (from left to right):

- Reed Jacobsen,
- Jack Wolfe, III,
- Zac Kilburn,
- C.H.R.I.S.T.E.E. The Robot,
- Dana Cressman,
- and
- Cody Gruber



Joe Yanoska and Bryce Huber of the Buckeye Space Launch Initiative based at The Ohio State University.

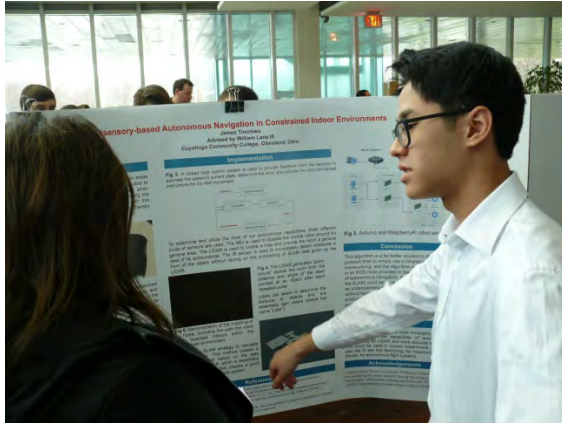


NASA Glenn HR



Christina Koleno
NASA Glenn Research Center Human Resources

Poster Session



James Timotiwu showing Raquel Redhouse his project on "Disensory-based Autonomous Navigation in Constrained Indoor Environments."



Hannah Schlaerth shares "Detection and Analysis of Biogeophysical Factors Influencing Local Water Quality and Coral Reef Health in the US Virgin Islands" with Kweisi Wilson.



John Reynolds explains the application of "Augmented Reality and Virtual Reality in the Construction Industry" to Alex Mazursky.



Anthony Smoktonowicz and his "Wide Area Sampling Prototype."



University of Dayton students Edward Brinkerhoff and Miles Burrage enjoying the day.



Hayley Crider and Ellie Conrath share their excitement about presenting their Education posters.



Amanda Baluch and her poster on “Automatization and Enhancement of Hydroponically Grown Crops.”



Solomon Ellison, Steven Fairley, and Joseph Morin discuss Solomon’s research on “Design of Clothing Integrated with Circuitry to Regulate Body Temperature.”



Representing Cuyahoga Community College (left to right): Amanda Baluch, Nicholas Tolbert, Joseph Arendt, Anthony Cancian, Jeffrey Kudrna, Steven Fairley, Dr. Lam Wong, Kayle Kornblum, and James Timotiwu.



Jacqueline Vance (HyQ Academy) evaluating Elizabeth Herting’s lesson plan on “The Great Space Race: Thrust and Efficiency Rates of Burning Fuel.”



Education Scholars Abigail Recker, Emily Tornes, and Lindsay States



Tyland Worrell, Marlo Wolfe, and Bryce Zwagerman

Launching A STEM Career

This year's Symposium was special not only because it was the 25th anniversary, but also because a panel of OSGC alumni came together to share their experiences how they came to be established in their careers and also to give advice to the up and comers who are paving their own way.



Upper Screen: Chad Yoshikawa (Google) who participated via Skype.

Below Screen (from left to right): Joshua Allen (NASA Glenn Research Center), Emilio Borges (NASA Glenn Research Center), Ashlie Flegel (NASA Glenn Research Center), Derick Endicott (Space X), and Rob Charvat (GE Aviation)





Poster Competition Winners

The evaluators of the Poster Session selected their winners who were presented with a certificate and NASA briefcase by OSGC Director, Dr. Jed Marquart.



From left to right:

Zachary Kordeleski (Cleveland State University), "Best Education Poster"; Alexandra Oliver (Wright State University), "Best STEM Poster"; OSGC Director, Dr. Jed Marquart; and Chad Coolidge (Lorain County Community College), "Best Community College Poster".

Not pictured, Christopher Wright (Cleveland State University), "Best Bridge Poster"

Mini Worm: A Small SMA Actuated Worm-like Robot

Student Researcher: Kayla B. Andersen

Advisor: Dr. Roger Quinn

Case Western Reserve University
Department of Mechanical and Aerospace Engineering

Abstract

The mini-worm robot is intended to be one of the next iteration of worm robots striving towards potential inside-the-body applications. To this end, the robot is compliant, has a diameter of less than 1 in., and is actuated via Nitinol coil actuators- a technology that has been proven in the body. Additionally, Mini-worm will employ a suite of pressure sensors that enable the robot to determine if it has contacted an external surface. Prototypes were constructed to determine the feasibility of using in-lab materials, and two versions of the robot (actuators only) were created and tested. The current version of this robot is capable of forward motion (6mm in 3 cycles) and lifting segments off the ground in a searching type behavior. Further testing is needed to improve the robot's forward motion and to determine if the robot can turn. Once the desired motions have been achieved, force sensitive resistors will be added that enable the robot to sense external contact.

Background

The driving desire behind the creation of worm robots is two-fold: firstly, creating a worm robot that mimics a biological worm enables insight into how biological worms may control their movements, and secondly, a worm-like robot would function uniquely well in scenarios such as inside a pipe, search and rescue and inside the body [1,2,3,4]. Worms move via a unique form of motion called peristalsis (sequential contraction waves down the body), and are known to have a variety of sensors, such as stretch receptors and pressure receptors in their skin [3,6].

Objective

The objective of the Mini-worm research project is to design, build, and test a worm-inspired robot with a diameter less than 1 in. Mini-worm, aims to incorporate several features found in similarly scaled worm robots, such as Nitinol (NiTi) coils for actuation [1] and return force provided by the structure of the robot itself [4], thus eliminating the need for external springs. Functionally, Mini-Worm should be able to move forward via peristaltic motion, turn while moving forward, lift its front segments upwards, perform a "searching" motion, and detect the walls of a pipe.

Design and Construction Methodology

To realize the various objectives of this project, a construction method, an actuation method, and a sensor type/component had to be determined. Based on the work on similar small scale robots, the decision was made to use a braided mesh tube as the structure [1], and to use NiTi coil springs as the actuation method [1,5]. To sense external contacts, force sensitive resistors (FSRs) were selected because of their availability and small size. For control, an Arduino Mega was selected, with an intermediate circuit board of MOSFETs to handle the current necessary to power the NiTi coils (~0.7A per coil).

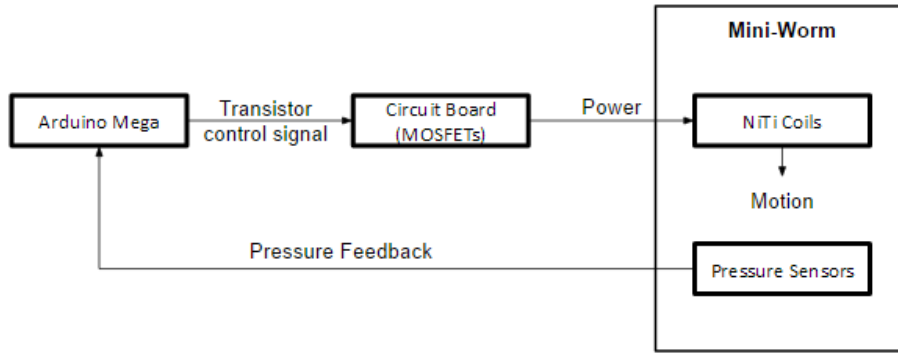


Figure 1. Planned architecture for Mini-worm

Prototypes and Version 1

After determining the architecture, the exact materials for construction were determined. Both braided mesh tube cable holders and NiTi spring coil actuators (Dynalloy 90°C Flexinol® Actuator Spring, 0.008" Wire dia) of the appropriate size for the desired scale were already in the lab. Several sequential prototypes were created to determine the feasibility of these materials. Because NiTi springs require a return force to stretch back to their pre-actuated length, it was particularly important to determine if the mesh was able to provide this return force.

These prototypes use three longitudinal actuators per segment to enable out of plane motion, forward motion, and turning, without the need for overlapping actuators (which lead to heat contamination and unwanted motion).

To construct the prototype, a mandrel was inserted into the mesh and the assembly placed in an 80°C oven for 10min to “set” the mesh to a circular shape. Concurrently, a circuit board was soldered to power the NiTi coils, and a test Arduino sketch written to control the coils. The prototype began as a single segment, and as tests were conducted additional segments were added, culminating in the five segment robot (figure 2). For the 1, 2, and 3 segment prototypes, the coils were “screwed” into the mesh and the wires routed on the outside. For the 5 segment robot, the coils were tied in place by nylon string threaded into the mesh, and the wires routed on the inside. A double mesh version, with a second mesh placed over the five segment worm, was also created to test if greater return force would yield better performance.



Figure 2. Mini-worm Version 1. Single mesh (left), double mesh (center), circuit board (right)

Version 2

A number of improvements and changes were made to the design based on version 1’s performance. Thinner wires were used because those in version 1 added too much stiffness. The

segments were spaced out more to enable segments adjacent to contracted (increased diameter) segments to remain small in diameter. The NiTi spring's attachment points were placed further apart to allow for greater diameter change per contraction. The first and last inch of the version 2 robot have no actuators to make sure there is enough return force to stretch out the springs in segments 1 and 5. The two side actuators were attached across from one another at the half-way point. Finally, version 2 used a double mesh to provide enough return force to the NiTi coils.



Figure 3. Version 2: front view at minimum diameter 1.8cm (left), and total length 23cm (right)

To construct version 2, one mesh was inserted into the other mesh prior to attaching the coils. The NiTi coils were then tied into both meshes and attached to wires fed through the body of the robot. These wires were then soldered to a PCB board containing the MOSFET circuits, and the PCB was connected to the Arduino Mega.

Tests Conducted

Test and experiments were conducted at each stage of the design and construction process to determine how the system behaves. The primary tests for each stage are list below.

Prototypes

Before construction the actuators were tested independently to determine the required voltage and time for full contraction.

A variety of tests were conducted with the 1, 2 and 3 segment prototypes to determine the viability of the materials. The segments were contracted to determine if the actuators were able to contract the segment, and the mesh able to return to its original shape. The top actuators were contracted to determine if actuating the top coil allowed the segment to lift off the ground. In another test, the side actuators were contracted to see if the segments could bend to the left and to the right, as would be required by turning.

Version 1

Tests were conducted to determine if the segments could return to their original positions to determine if forward motion was feasible and to document the out of plane motion. After determining greater return force was necessary, a variety of actuation sequences were tried to determine how to best achieve forward progress for the double mesh robot.

Version 2

Before version 2 was constructed, the stiffness of the mesh was measured by compressing the mesh on top of a scale and plotting displacement versus force, to determine if the mesh needed to be doubled. On version 2, tests were conducted to determine if segments could return to their original positions, if segments could be lifted off the ground by contracting the two neighboring segments, document out of plane searching motion, and to determine how to effectively achieve forward motion.

Results

Prototypes

The prototypes demonstrated their ability to successfully return to an equilibrium length after actuation, their ability to produce the out of plane motion, and their ability to “turn” to both the left and right. The various tests showed that it took approximately 20s for the segments to return to their original shape.

Version 1

With the wires inside the robot and one mesh, the robot would not return to the original diameter (especially segments 1 and 5), and was unable to make forward progress. In the double mesh configuration, the robot was able to move forward 4mm in 3 waves of contraction. In both cases the robot was barely able to lift segments off of the ground (segments in the air are necessary for effective locomotion). Also, barely any difference in diameter was observed for the double mesh.

Version 2

The robot’s segments could be lifted off the ground by contracting the two neighboring segments, as is needed for effective forward motion. However, when actuating just the first segment the front of the robot lifts off of the ground. Despite this, in 3 waves of contraction down the body Mini-worm moved 6mm. When actuating just the top coils, the robot lifts its front vertically over 75mm.

Conclusion

The first version robot had the ability to move forward, but the mesh provided too much resistance to actuation in the double mesh configuration and inadequate return force in the single mesh configuration to effectively create forward motion. The likely reason for the underperformance of version 1 is the increase in stiffness of the robot from the wires inside the mesh.

The second version has the potential to meet all the objectives of the project, but the lightweight nature of the mesh has caused the mesh to curl upwards when the first segments are actuated because the side actuators are slightly above the horizontal. Overall, the results indicate there is a very fine balance between correct return forces, required actuation force (due to the mesh/wires), the placement of actuators on the mesh, and robot performance.

Future Work

Version 2 testing is ongoing. Once the first segment lifting issue is solved, experiments will be conducted to determine the segment actuation pattern that yields the most effective forward progress. Then, the speed of forward motion on various substrates will be measured. Following successful forward motion, experiments will be conducted to determine how to best actuate the robot to turn while moving forward. Once effective forward, turning, and searching motions are achieved, the next step will incorporate the force sensitive resistors and determine how to effectively sense the wall of a pipe. These steps are expected to be complete by the beginning of June.

Acknowledgments

I would like to thank my advisor Dr. Quinn for providing me with a project and resources, Akhil Kandhari for helping me troubleshoot problems and being the worm robot expert, and Anna for helping me take measurements and making sure I did not overcomplicate things. I would also like to thank Anno van den Akker for designing the PCB based on my circuit, to allow me to save time soldering protoboards.

References

1. S. Sangok, C.D. Onal, K. Cho, R. J. Wood, D. Rus, S. Kim. "Meshworm: A Peristaltic Soft Robot With Antagonistic Nickel Titanium Coil Actuators" *IEEE/ASME Transactions on Mechantronics*, Vol. 18, No. 5, October 2013, pp. 1485-1496.
2. Yanagida, T., Adachi, K., Yokojima, M., Nakamura, T. "Development of a peristaltic crawling robot attached to a large intestine endoscope using bellows - type artificial rubber muscles". *Intelligent Robots and Systems, 2012 IEEE/RSJ International Conference on*, Vilamoura, Algarve, Portugal, pp. 2935-2940 (goal of "inside the body").
3. Horchler, Andrew D., Kandhari Akhil, Daltorio Kathryn A., Moses Kenneth C., Ryan James C., Stultz Kristen A., Kanu Elishama N., Andersen Kayla B., Kershaw Joseph A., Bachmann Richard J., Chiel Hillel J., and Quinn Roger D. " Peristaltic Locomotion of a Modular Mesh-Based Worm Robot: Precision, Compliance, and Friction". *Soft Robotics*. December 2015, 2(4): pp. 135-145. doi:10.1089/soro.2015.0010.
4. T. Manwell, T. Vitek, T. Ranzani, A. Menciassi, K. Althoefer and H. Liu, "Elastic mesh braided worm robot for locomotive endoscopy", *Conf Proc IEEE Eng Med Biol Soc*. 2014, 2014, pp. 848-51. (goal of "inside the body").
5. D. Mândru, I. Lungu, S. Noveanu and O. Tătar, "Shape memory alloy wires as actuators for a minirobot," *Automation Quality and Testing Robotics (AQTR)*, 2010 IEEE International Conference on, Cluj-Napoca, 2010, pp. 1-4. doi: 10.1109/AQTR.2010.5520861 (for "SMA's used for stuff")
6. Kenji Mizutani, Toshinobu Shimoi, Hiroto Ogawa, Yoshiichiro Kitamura, Kotaro Okaa, "Modulation of motor patterns by sensory feedback during earthworm locomotion", *Neuroscience Research* Vol. 48 (2004) 457–462 (the fact earthworms have pressure sensors).

Investigation of an Excited Mach 0.9 Jet in Forward Flight Simulation

Student Researcher: Matthew M. Arnott

Advisor: Dr. Mo Samimy

The Ohio State University

Aerospace Engineering, Aerospace Research Center

Abstract

Developed at the Ohio State University Gas Dynamics and Turbulence Laboratory, localized arc filament plasma actuators (LAFPAs) have been used to perturb the flow and acoustic fields of subsonic and supersonic jets. LAFPAs are capable of producing various excitation azimuthal modes ($m = 0, 1, 3,$ and ± 4) at different excitation frequencies. The purpose of this study is to compare baseline far-field acoustic conditions of an unheated subsonic jet ($M_j=0.9$) in forward flight (up to $M_f = 0.3$) to those of a LAFPA equipped excited flow under the same conditions.

Project Objective

Jet engine noise during takeoff and landing poses an issue for both civilian and military aircraft, resulting in complications anywhere from an annoyance to major hearing damage. To mitigate the problem of jet engine noise, passive and active flow control technologies have been investigated and implemented for real world use. Of particular interest are active flow control technologies, as they can be utilized during takeoff and landing while powering down during cruise. The Gas Dynamics and Turbulence Laboratory (GDTL) at The Ohio State University has developed localized arc filament plasma actuators which can provide excitation signals of high amplitude and high frequency for high-speed and high Reynolds number flows [1]. While this technology has been extensively tested in the lab, its effectiveness in forward flight conditions has not yet been investigated. The focus of this study is to determine if LAFPAs are capable of reducing jet noise in forward flight conditions.

Methodology Used

This study was conducted in the anechoic chamber, shown in Figure 1, at the GDTL within the Aerospace Research Center at The Ohio State University. Air is compressed by three five-stage reciprocating compressors, filtered, dried, and stored in two 43 m³ tanks at pressures up to 16 MPa. This compressed air is passed to the stagnation chamber of the jet facility and subsequently released horizontally through a contoured converging nozzle of 1 in. exit diameter into the anechoic chamber. The air then exits the chamber to the outdoors through an exhaust system on the wall opposite the nozzle. For this study, the jet was run at $M_j = 0.9$ for all tests. Stationed around the nozzle is a co-flow section, allowing for a flow to pass alongside the jet to simulate forward flight conditions. The co-flow section is operated at $M_f = 0.09$ to 0.3.

At the end of the nozzle is a boron nitride ring for holding 8 LAFPAs spaced uniformly around the nozzle exit. Each individual LAFPA is comprised of two electrodes exposed to the passing flow. These electrodes are energized, creating an arc between them and allowing for excitation of the natural instability modes of the flow. The modes considered in this study are modes 0 and 3 ($m = 0$ and $m = 3$). To run the wiring across the co-flow section, the electrodes were uniformly laid against the outer diameter of the jet nozzle and held in place with Kapton tape to prevent arcing outside of the desired zone. The bundle of wires was then run directly down from the jet nozzle and anchored to the floor of the anechoic chamber to minimize flutter, which could affect the flow of air from the co-flow. A visualization of the LAFPA

setup with the jet and co-flow can be seen in Figure 2. More information on LAFPAs can be obtained from Samimy et al [1].

Far-field acoustic measurements were taken in the chamber with 11 ¼ in. B&K 4939 microphones located at polar angles of 30-105 degrees with respect to the jet axis. The far field acoustic results were scaled to a distance of 80 jet diameters. Acoustic signals from each microphone were bandpass filtered from 20 to 100 kHz, amplified by B&K Nexus 2690 amplifiers, and acquired using National Instruments A/D boards and LabVIEW software.

Of note in the following sections is the use of terminology in the displayed figures. Sound Pressure Level (SPL) is the resulting amplitude of the spectrum recorded in the anechoic chamber as measured in decibel (dB). Strouhal number (St) denotes the dimensionless frequency measurement. St_{DF} refers to the Strouhal number at which the LAFPA was run during the test being discussed. The term “baseline” refers to the case of just the jet running with no excitation.

Results Obtained

To use the co-flow in the GDTL effectively, the setup was first validated to ensure the LAFPA wiring would not interfere with the forward flight condition. This was accomplished by taking data with just the jet running, then with the jet and the co-flow running and comparing the trends to previous research Veltin [2]. Figure 3 shows the results of this test. In the forward flight condition, it is evident that there is some form of noise contamination at low frequencies. In Figure 4, Viswanathan [3] has demonstrated that this phenomenon is caused by the excess tunnel noise. The open circles equate to the jet only condition, the closed circles are in forward flight $M_f = 0.20$, the squares are $M_f = 0.24$, and the x markers are $M_f = 0.28$. The open and closed circles are most similar to the conditions run for this test, and show that with forward flight the low-level noise contamination is expected. It is also evident that as forward flight speed increases, low level noise contamination increases. Figure 5 shows results of running the GDTL co-flow at varying speeds, demonstrating the same trend as shown by Viswanathan [3]. With the knowledge of this low-level contamination, the data that was considered in determining noise reduction ranges from $St = 0.05$ to 2. While this highlights some of the contamination present in a jet in forward flight, there is still an issue of physical microphone location versus the perceived microphone location due to the forward flight stream [2]. To compensate, the data was processed through a correction code to account for the difference in actual versus perceived microphone position. A detailed explanation of this phenomenon and the correction used can be found in Veltin and Amiet [2,4]. The results of the jet data in static and forward flight corrected position can be seen in Figure 6. The trends shown by Figure 1 (pre-correction) and Figure 6 (post correction) align as expected with the results presented by Veltin [2]; in forward flight conditions, the overall noise produced by the jet is reduced. Figure 6 also agrees with the results from Viswanathan [3] as the noise reduction from forward flight alone is more present at jet downstream angles.

Previous work done by Kearney-Fischer [5] demonstrates that the use of LAFPAs can reduce far-field noise by 2-3 dB, outlined in Figure 7 at $St_{DF} = 1.24$. Figure 8 shows the comparison of a baseline jet to a jet excited at both $m = 0$ and $m = 3$ modes at $St_{DF} = 1.35$. The results are similar to those of Kearney-Fischer [5], and demonstrate the repeatability of the LAFPA system. While the excitation Strouhal numbers from 0.05 to 1.75 were evaluated and all exhibited some amount of reduction, $St_{DF} = 1.35$ was selected to represent the overall trend as the reduction was easily visible for all polar angles. Figure 9 details the baseline, $m = 0$ and $m = 3$ excitation modes in forward flight conditions. Once again, $St_{DF} = 1.35$ was used for the sake of comparison. It is clear there is a reduction in forward flight conditions as well. Additionally, in the forward flight condition, mode 3 excitation is less significant than mode 0.

Significance and Interpretation of Results

The trends shown in Figure 9 shed some light on the performance of LAFPAs on a subsonic unheated jet in forward flight conditions, where LAFPAs are shown to be effective in reducing far-field jet noise. Additionally, with the co-flow system at the GDTL tested and validated, it is possible for experimentation with the system to continue as necessary.

It is important to note that there is much more information that can be readily obtained from the data taken in this study. There appear to be trends regarding the St_{DF} used for the excitation modes of the jet in forward flight conditions, as were observed by Kearney-Fischer [5] with static jets. This will be further investigated as a future work.

Figures/Charts

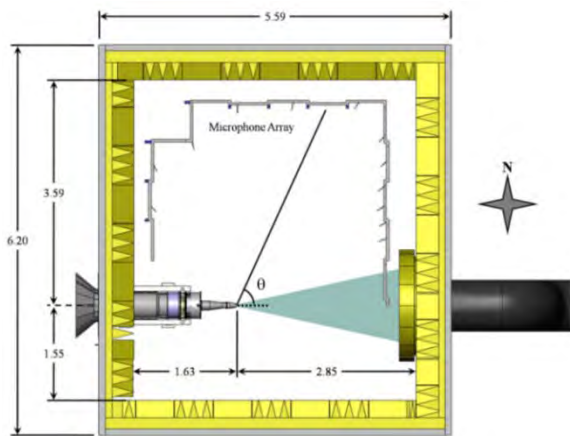


Figure 1. Anechoic chamber at the GDTL



Figure 2. LAFPA setup on nozzle with co-flow

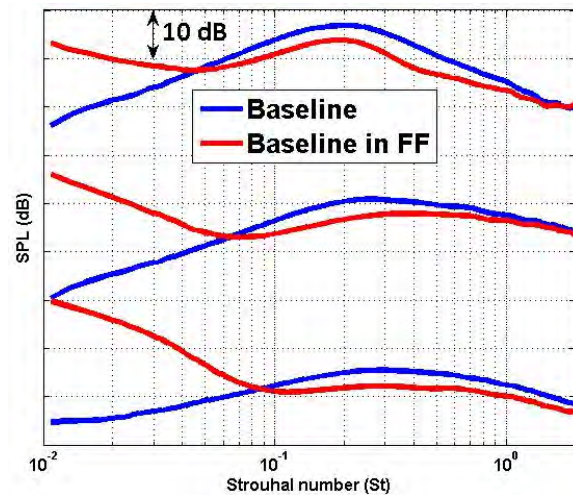


Figure 3. Comparison of baseline static jet to baseline jet in forward flight at 30°, 50°, and 90° (top to bottom)

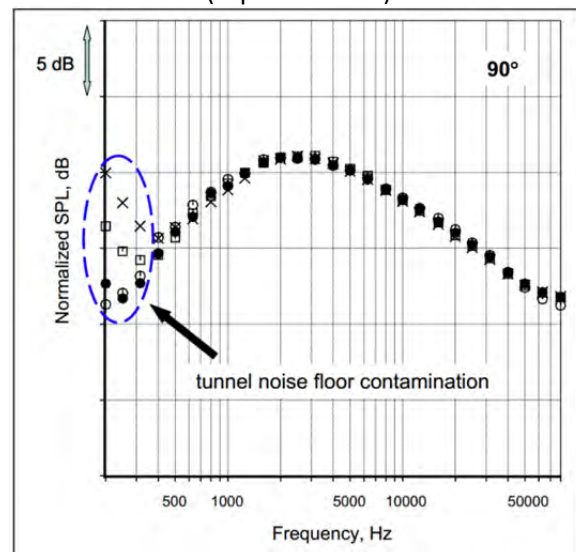


Figure 4. Example of low frequency noise contamination in forward flight simulation [3]

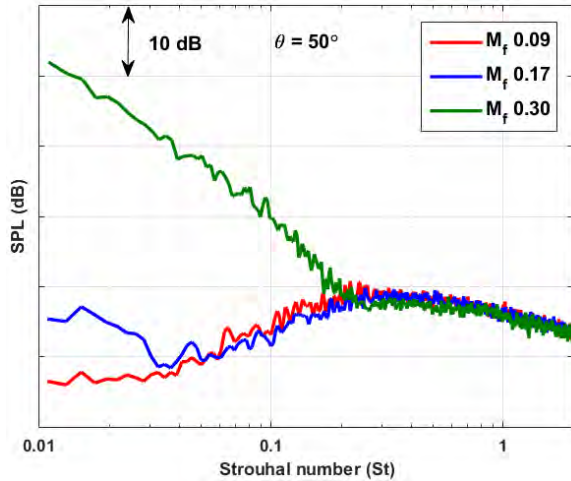


Figure 5. Comparison of SPL at varying co-flow speeds at GDTL measured at 50°

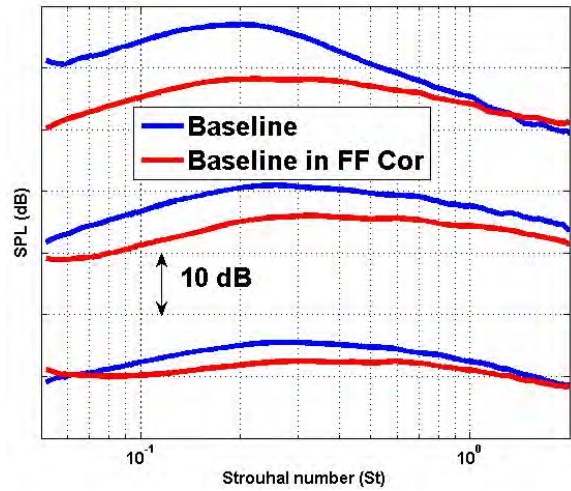


Figure 6. Comparison of baseline static jet to baseline jet in forward flight with correction at 30°, 50°, and 90° (top to bottom)

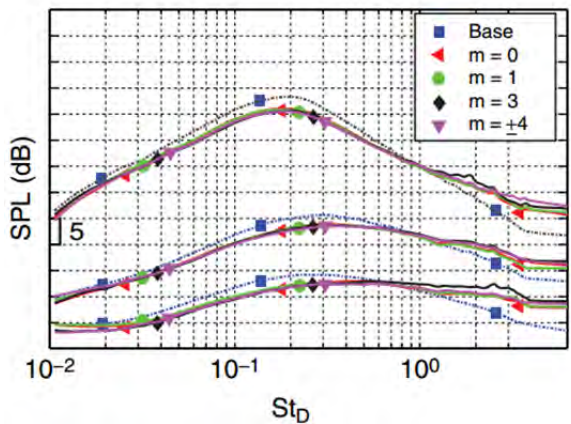


Figure 7. LAFPA use on a static jet at $St_{DF} = 1.24$ at 30°, 60°, and 90° (top to bottom) [5]

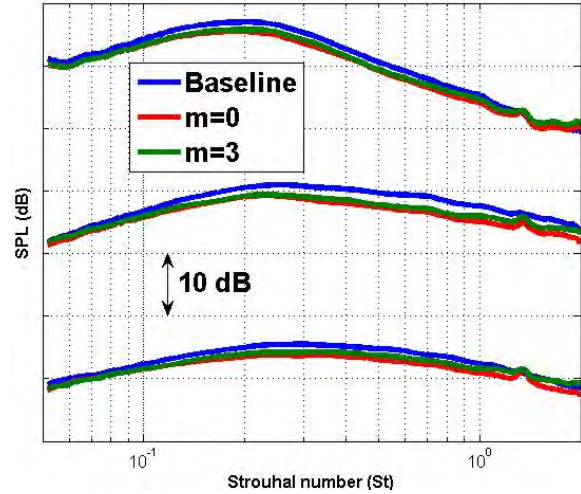


Figure 8. Comparison of baseline jet to $St_{DF} = 1.35$ excitation at 30°, 50°, and 90° (top to bottom), all static

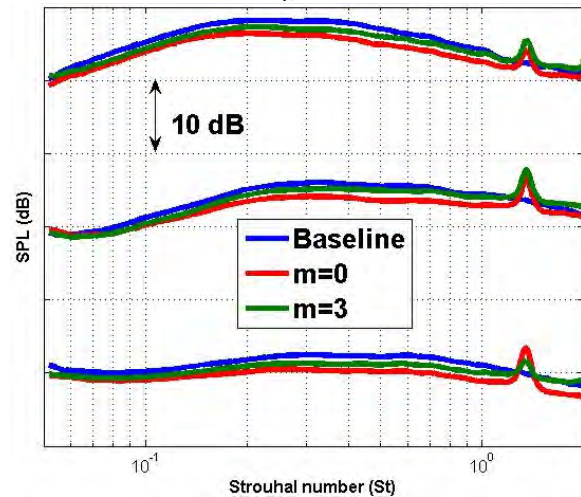


Figure 9. Comparison of baseline jet to $St_{DF} = 1.35$ excitation at 30°, 50°, and 90° (top to bottom), all in forward flight

References

1. Samimy, M., Kim, J.-H., Kastner, J., Adamovich, I., and Utkin, Y., "Active control of high-speed and high-Reynolds-number jets using plasma actuators," *Journal of Fluid Mechanics*, vol. 578, 2007, p. 305.
2. Veltin, J., Day, B., and Mclaughlin, D., "Forward Flight Effect on Small Scale Supersonic Jet Acoustics," 16th AIAA/CEAS Aeroacoustics Conference, Jul. 2010.
3. Viswanathan, K., and Lee, I., "Shear Layer Corrections for Non-Axisymmetric Wind Tunnel and Applications," 18th AIAA/CEAS Aeroacoustics Conference (33rd AIAA Aeroacoustics Conference), Jun. 2012.
4. Amiet, R. K., "Refraction of sound by a shear layer," *Journal of Sound and Vibration*, vol. 58, 1978, pp. 467–482.
5. Kearney-Fischer, M., Kim, J.-H., and Samimy, M., "Noise Control of a High Reynolds Number High Speed Heated Jet Using Plasma Actuators," *International Journal of Aeroacoustics*, vol. 10, Jan. 2011, pp. 635–658.

The Toxicity of Blue Dyes in M&M's® Candies

Student Researcher: Salif A. Athie

Advisor: Ed Burton

Cincinnati State Technical and Community College
Chemical Technology Program

Abstract

Much research has been conducted regarding the health issues triggered by eating M&M's®. Children are more vulnerable because they like to eat M&M's® candies. Therefore, the food industry needs to be more regulated to bring down the level of toxicity of dyes used in food coloring and food coating in M&M's®. The government should prescribe strict rules destined to the food industry using dyes during the food processing. The concern is far reaching since there are claims regarding diseases being caused or traced back to dyes in M&M's®.

Unfortunately, children are the most exposed to the health issues related to the M&M's® dyes. Children consume significant amount of candies such as M&M's®. For the welfare of our children, the behavior of the food industry needs to stop the damage they already inflicted in children's health, due to regular ingesting of food dyes. The concern is more serious with children due to their immature immune system.

Project Objective

My project objective is to find the daily allowed intake of M&M® without harming the consumers, to prevent any health issues that those may contain. Diseases such cancer, are lethal, carcinogenic food should not be allowed to be produced.

Material used	Mobile Phase	Stationary Phase	Wavelength
28% Acetic acid 50 ml beakers (4)	Disposable pipette (2) Funnel	20% Methanol 80% K ₂ HPO ₄	C-18Phase 580nm

Methodology Used

Blue #1: Weight 0.121 of crystals using an analytical balance. Deliver the crystals in a 100ml volumetric flask by adding DI water to the volume, to make a stock solution with a concentration of [121µg/ml]. Make five dilutions solutions from the stock solution with the dilution factor being 1:10. Here are the dilutions solutions concentration, respectively: 4.84µg/ml; 12.1µg/ml; 24.2µg/ml; 48µg/ml; 121µg/ml.

Blue #2: Weigh 0.1000g of crystals using an analytical balance. Deliver the weighing in a 100ml volumetric flask by adding DI water to the volume, to make a stock solution with the concentration of [100µg/ml]. Make four dilutions solutions from the stock solution with the dilution factor being 1:10. The following are the dilutions solutions concentration: 10µg/ml; 25µg/ml; 50µg/ml; 100µg/ml. M&M's® is the matrix of the unknown sample used to separate the Blue #1 and the Blue #2 from the coating of the M&M's®. To run the calibration curve, I used known samples of Blue #1 and Blue #2. I used High Performance Liquid Chromatography (HPLC), to run the quantitative analysis for both the known and the unknown samples. Before loading the samples in the HPLC machine, it was necessary to set it up with the right conditioning. 580nm was the chosen wavelength. Method Run control: Flow rate (1ml/min); Stop time (14mins). Fill out vials with each sample of known and unknown to run them through the HPLC. The detection of peaks, were a success for both known samples of Blue#1, and Blue#2 with the respective retention time (7.384 mins, 3.351 mins). However, Blue #1 was the only unknown sample that was detected with a peak (7.357mins retention time).

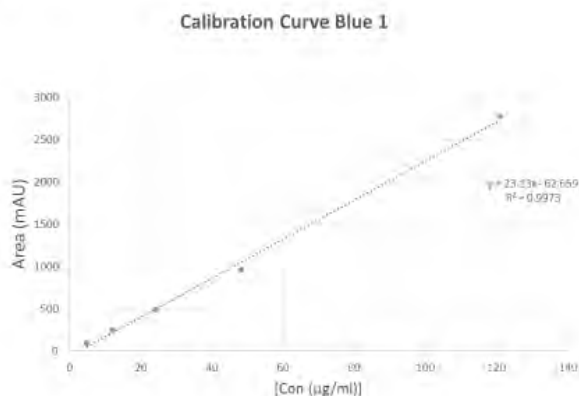
Result Obtained

Calibration Curve

- Blue Dye #1

Blue 1 Calibration Curve

[Conc] µg/ml	Area mAU
4.84	91.90872
12.1	244.49
24.2	486.81711
48.4	961.39655
121	2771.8332
slope	23.129771
intercept	-62.659298

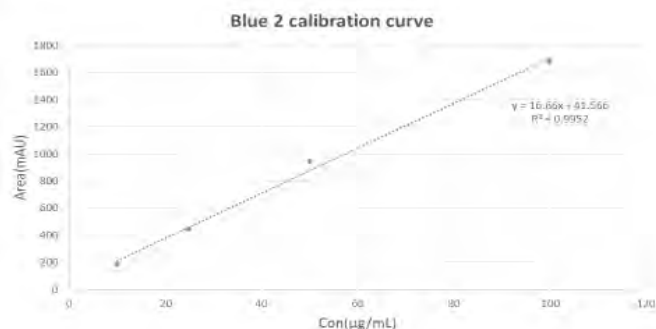


Calibration Curve

- Blue Dye #2

Blue #2 Calibration curve

Con µg/mL	Area mAU
10	183.86368
25	441.70428
50	942.8975
100	1679.9764



Concentration of Blue #1 Normalized by Mass

Sample	Area	[Blue 1]	mL Acetic Acid	g of M&M	[Blue 1]/g of M&M
1	316	16	22	3	134
2	207	12	25	3	110

Conclusion

The project was a success; I was able to get a peak for the Blue #1 from the analyte sample (M&M®). I assume that the analyte contained only Blue #1, and I was able to calculate the concentrations of the two samples I worked on respectively: [134µg/ml]; [110µg/ml]. Probably further analytical tests are needed with a suitable wavelength perhaps to detect a peak for Blue #2 which indicates the presence of the dye.

Reference

1. Yoshioka, N. and K. Ichihashi. "Determination of 40 Synthetic Food Colors in Drinks and Candies by High-Performance Liquid Chromatography Using a Short Column with Photodiode Array Detection." *Talanta*, vol. 74, no. 5, 15 Feb. 2008, pp. 1408-1413. EBSCOhost, doi:10.1016/j.talanta.2017.04.21.

Hyperspectral Imagery of the 2016 Harmful Algal Bloom in Lake Erie

Student Researcher: Dulcinea M. Avouris

Advisor: Dr. Joseph Ortiz

Kent State University
Department of Applied Geology

Abstract

Airborne hyperspectral imagers are a powerful tool for frequent and rapid assessment of the Harmful Algal Blooms (HABs) in Lake Erie. Hyperspectral instruments are designed to acquire data at 2-5nm intervals across the ultraviolet to near infrared spectrum, and provide very detailed reflectance spectra, comparable to lab-based instruments, for the surface of Lake Erie. However, hyperspectral instruments tend to be both spectrally and spatially noisy, requiring pre-processing steps to remove the noise [Othman, 2006]. Here we describe the method development for increasing the signal to noise ratio (SNR) of an airborne Hyperspectral Imager 2 (HSI2). During the 2016 field season, a team from NASA Glenn deployed a HSI2 on an S2 aircraft bi-weekly to acquire imagery data from the Western Basin of Lake Erie, specifically focusing on the HABs that develop over the summer months. These images contributed to a large data set collected by members of the HAB collaboration research group, and were used to test pre-processing methods in order to establish a noise removal protocol that can be implemented before further analysis using the derivative spectroscopy method [Ortiz, 2013]. We established that stripe removal and smoothing were necessary to improve the SNR in the spatial dimension. In the spectral dimension, the wavelength axis was interpolated from a ~3nm spacing to a standard 10nm axis from 400-700nm. When these steps were taken, a significant portion of the environmental signal was identified by the derivative spectroscopy analysis using Varimax-rotated principal component analysis (VPCA) to decompose the image. Prior to noise reduction steps, only a small amount of environmental signal was identified by the VPCA decomposition.

Project Objectives

This project encompasses two objectives. The first is to assess, test, and implement the steps needed to remove noise from the NASA HSI2 images, which increases the signal to noise ratio. These pre-processing steps are necessary for further analysis of environmental signal in the remote sensing data. The second objective is to decompose the images using derivative spectroscopy, and to identify the in-water constituents. The derivative spectroscopy analysis is also the final test of the effectiveness of the pre-processing steps.

Methodology Used

The 2016 field season for the HAB research group collaboration began in early June, and continued through October. The NASA group flew the HSI2 mounted on an S2 aircraft bi-weekly to collect imagery over the Western Basin of Lake Erie. These images are acquired in data swaths. Each image swath was calibrated by the NASA team, and made available through the Ohio Supercomputer Consortium file server to members of the research group. On June 21, 2016, the NASA plane flew over Maumee Bay State Park (MBSP) numerous times while research group teams were on site at the MBSP parking lot using field spectrophotometers to collect measurements of the parking lot surface and downwelling solar radiance. The data from this concurrent data collection were also used to improve and test the calibrations of the airborne HSI2 as well as the ground-based instruments used by both our group and other collaborators during the 2016 field season. Because the images acquired by the HSI2 on this day

were proximal in time, and of the same area of Lake Erie, we chose to test our noise removal techniques, as well as the reproducibility of our results from the derivative spectroscopy decomposition.

Each image showed significant noise that can be identified visually, including along-track striping due to detector offsets, and small scale spatial features. We process images using the ENVI/IDL software package because the image analysis tools in ENVI, paired with the coding platform in IDL allow us to use both built-in tools and to create our own data manipulation algorithms. ENVI has a suite of tools in the Spectral Processing Exploitation and Analysis Resource (SPEAR) toolbox, so we chose to use the Vertical Stripe Removal tool. The tool was tested using a mask feature that removes the highest and lowest 5% of pixel values within a chosen band of the image. When those pixels are masked, their values are not included in the stripe removal algorithm, and remain the original value when the stripe removal is completed. The tool was also tested with no pixels excluded (0% mask).

After the stripes were removed from the images, the image was smoothed spatially, with a 9x9 kernel. Each pixel in the image was assigned the median value of the pixels in a 9x9 square, centered on the pixel being evaluated. This process removes small scale spatial irregularities, while maintaining the larger scale features. After stripe removal and spatial smoothing, the image was spectrally smoothed by interpolating across the wavelength axis from ~3nm resolution to 10nm resolution. A correction factor developed by collaborators at the Michigan Tech Research Institute (MTRI) is applied to the image to convert from radiance measurements to surface reflectance measurements. This correction factor is based on in situ measurements taken of the Maumee Bay State Park parking lot blacktop & also corrects for atmospheric effects between the plane and the lake surface. The final processing step is applying the derivative spectroscopy method to the image. This involves calculating the centered first derivative of the reflectance spectra for each pixel in the image, and then applying a VPCA to the image. VPCA provides component loadings that describe the spectral shape of each component, and component scores, which describe the spatial distribution of each component. The component loadings are then compared to a spectral library for identification.

Results Obtained

Due to space considerations, for this report we focus on a single image, swath 15_MBSP. We found that the SPEAR vertical stripe removal tool was most effective when no pixels were masked. Using all the pixels to calculate the correction factor for removing striping allowed us to create a stripe-free image with one application of the tool. In contrast, when 5% of the highest and lowest value pixels were masked, three passes of the image through the SPEAR tool algorithm were needed to produce a stripe-free image. Figure 1 shows each pass of the SPEAR tool. The 9x9 kernel smoothing was effective at removing the small, wind driven, waves that can be seen in the original image (Figure 2), without modifying the larger scale environmental signal. Figure 3 shows the results of the VPCA. Figure 3a shows the VPCA scores, and figure 3b shows the component loadings.

Significance and Interpretation of Results

The result of the pre-processing testing shows that the noise intrinsic to hyperspectral imagers can be corrected. Offsets between detectors which lead to along-track stripes in the image are effectively corrected by available tools, once the tool is adjusted for the specific image. In this case, no pixels are excluded from the algorithm determining the offset correction. This is significant because the processing stream for each image is more efficient when tools are readily available. VPCA decomposition is a powerful tool because it evaluates the signal present in the image, and separates features that are spectrally distinct. However, the vertical striping is a coherent signal in these images, and so it overwhelms the true environmental signal, decreasing the signal to noise ratio within the image. It is a

strong enough signal that the VPCA algorithm pulls it out as a feature within the image. Figure 4 shows the difference between the VPCA with and without destriping. When the stripe removal step is omitted from pre-processing, the environmental signal is contained in VPCA components 3 & 4. The VPCA results when the stripes are left in the image show that the stripes convolve with the environmental signal, but once those stripes are removed, as shown in figure 3a, the environmental signal is isolated. In addition, the percentage of variance explained by the first 5 VPCA components is significantly higher (94.7%) than in the striped image (87.4%).

The VPCA for this image, after the processing steps that remove noise, results in 5 components, four of which contain signal, while the 5th is representative of atmospheric noise. Component 1 represents illite + haptophytes; component 2 represents diatoms + neoxanthin; component 3 represents goethite; component 4 represents hematite + phycocyanin; and component 5 represents aerosol residual errors. This is a significant step because we can show that the preprocessing steps vastly improve the signal to noise ratio of the image, which in turn allows us to effectively apply the derivative spectroscopy method to hyperspectral image files.

Figures

NASA HSI2 062116 Swath 15_MBSP: bad pixel edge removed

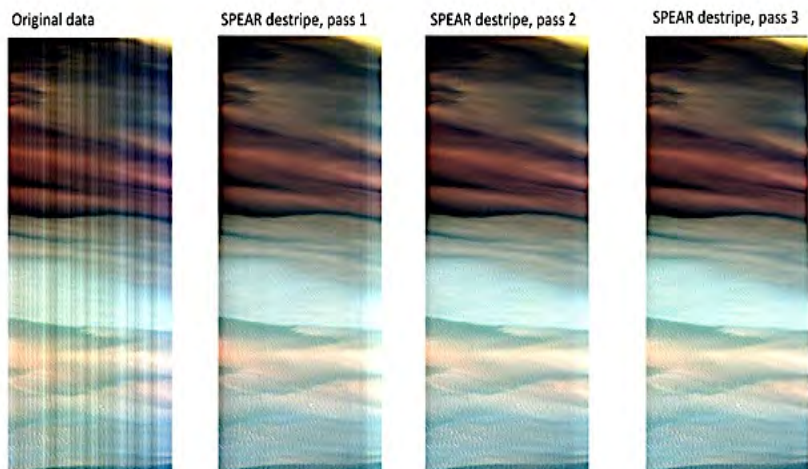


Figure 1. Example of vertical striping due to detector offsets in the HSI2 imagery. The ENVI SPEAR vertical stripe removal tool was used to correct the offsets, which increases the SNR. This swath is not georectified.

NASA HSI2 062116 Swath 15_MBSP

SPEAR destripe, 0% mask SPEAR destripe, 0% mask, smooth9

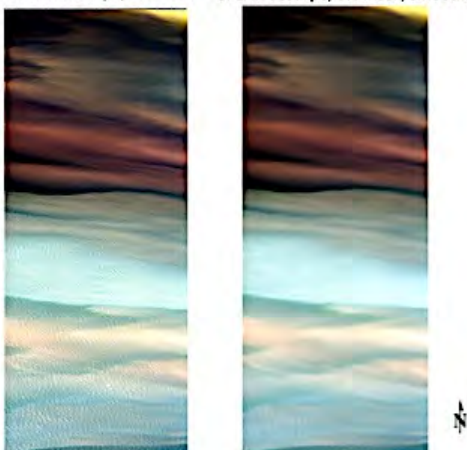


Figure 2. Effect of 9x9 pixel kernel smoothing on swath 15_MBSP. This swath is not georectified.

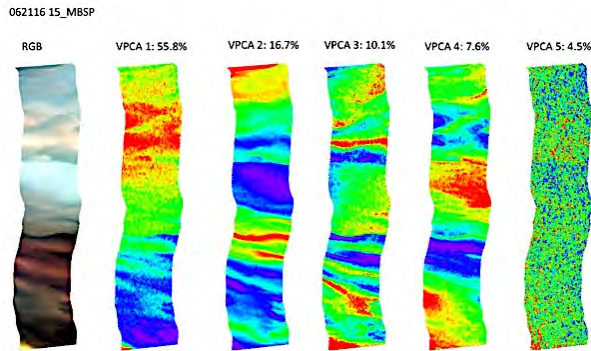


Figure 3a: Swath 15_MBSP VPCA scores

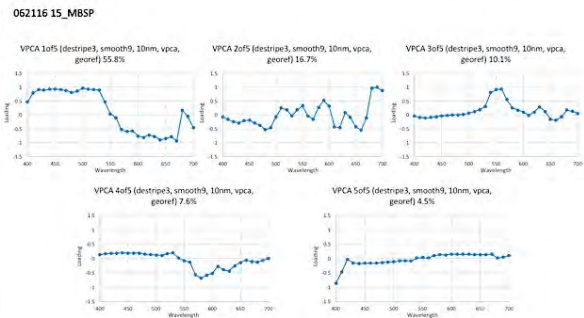


Figure 3b. Swath 15_MBSP VPCA loadings

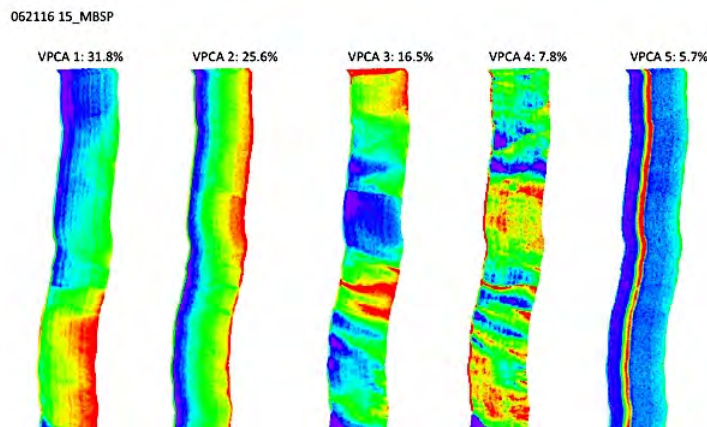


Figure 4. VPCA scores of swath 15_MBSP prior to stripe removal. Note the environmental signal is confined to components 3 & 4.

Acknowledgments

Many thanks to Dr. Ortiz for his continued guidance and support. Also to the invaluable assistance from our collaborators at NASA Glenn: John Lekki and Robert Anderson; and at the Michigan Tech Research Institute (MTRI): Robert Shuchman, Mike Sayers, & Reid Sawell. Thank you to the Ohio Space Grant Consortium for funding this project.

References

1. Ortiz, J. D. (2013), Evaluating multiple colour-producing agents in Case II waters from Lake Erie, *Int. J. Remote Sens.*, 34(24), 8854; 8854-8880; 8880.
2. Othman, H. (2006), Noise reduction of hyperspectral imagery using hybrid spatial-spectral derivative-domain wavelet shrinkage, *IEEE Trans. Geosci. Remote Sens.*, 44(2), 397-408, doi:10.1109/TGRS.2005.860982.

CFD Analysis of ONU SAE Aero Competition Airplane

Student Researcher: Molly C. Ballard

Ohio Northern University
Department of Mechanical Engineering

Abstract

This dissertation examines a Computational Fluid Dynamic (CFD) analysis of the airflow over the Ohio Northern University SAE Aero competition airplane. Analysis of the model was performed to determine coefficients of lift and drag of the airplane at angles of attack of 0 and 10 degrees. These results were then compared to the calculations performed by the team. Pressure distributions and velocity profiles were also of interest in this observation. It was concluded that the CFD results confirmed the team's calculations.

Nomenclature

C_l	=	coefficient of lift
C_d	=	coefficient of drag
F_x	=	X component of the resultant pressure force acting on the airplane (lb)
F_y	=	Y component of the resultant pressure force acting on the airplane (lb)
F_z	=	Z component of the resultant pressure force acting on the airplane (lb)

Introduction

For the Ohio Space Grant Consortium project, an analysis of the airflow over the ONU SAE Aero competition airplane was performed. The flight characteristics of the airplane, such as the coefficient of lift and drag, were analyzed. The geometry of the airplane was created by the ONU SAE Aero team in Solidworks⁽¹⁾ and was then imported into PointWise⁽²⁾ to create the viscous grid. The geometry of the airplane can be seen in Figure 1.

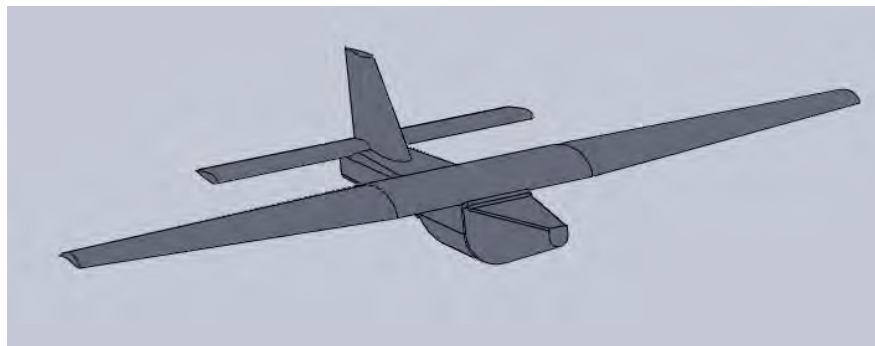


Figure 1. Geometry in SolidWorks

The flow conditions for the airplane represented those of the airplane in flight during the competition. The Mach number for the airplane traveling at 25 mph was used in the simulation. In order to simplify the grid, and reduce the size of the problem, only half of the airplane was modeled in the CFD analysis, and symmetry was utilized. Figure 2 shows the half of the airplane that was modeled, as well as the symmetry boundary plane.

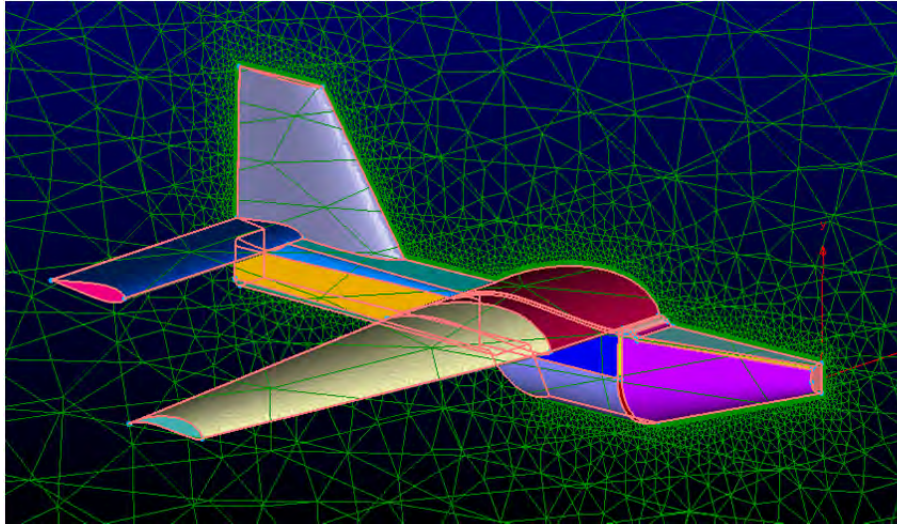


Figure 2. Domains of Airplane and Symmetry Wall in PointWise

Since the symmetry boundary wall was attached to the airplane, the boundary condition for the wall was set to be a slip wall. The remaining boundary conditions for the flow box that surrounded the airplane were set as farfield conditions. The airplane itself had a boundary condition of adiabatic no slip wall. Once the boundary conditions were set, the job file was modified to simulate the airplane traveling at 25 mph. The flow solver, Cobalt⁽³⁾, was used to compute the flow solution. Once the CFD runs were converged, post-processing was accomplished using Fieldview⁽⁴⁾. The coefficients of lift and drag were obtained directly from the Cobalt output files.

Problem Description

The analysis was of the ONU SAE Aero competition airplane during flight. The length of the airplane from nose to tail is 62.375 inches⁽⁵⁾. For one case, the air flowed from the nose to the tail as the airplane flew at a 0° angle of attack. For the other job file, the air flowed from the nose to the tail as the airplane flew at a 10° angle of attack. The goal of this analysis was to determine the performance characteristics of the airplane by calculating components such as lift and drag as the airplane flew with those angles of attack at a speed of 25 mph and then compare the results to the calculations performed by the team.

Results and Discussion

After running Cobalt for 16,000 iterations for the case of a 0° angle of attack, F_x , F_y , and F_z all converged. The data from the flow visualization file was imported into Fieldview so that post processing could be performed. First, the pressure distribution of the airplane was analyzed. The bottom of the airplane shows areas of yellow and some light green which indicates medium to high pressures. The pressure distribution of the bottom of the airplane can be seen in Figure 3.

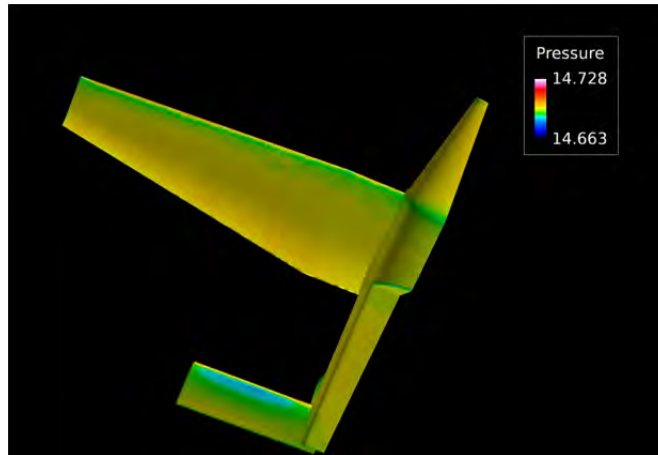


Figure 3. Pressure Distribution on Bottom of Plane

The pressure distribution on the top of the airplane was observed next. Figure 4 shows blue and dark green areas on the top of the wing which indicates medium to low pressure. Both of these results from the pressure distribution make sense because of the general knowledge of how pressure relates to flight. The air that flows under the wing produces high pressure which causes lift. The air that flows over the top of the wing produces low pressure.

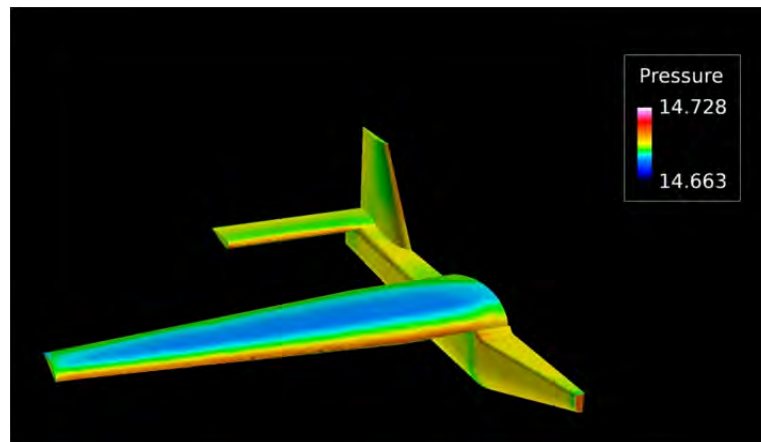


Figure 4. Pressure Distribution on Top of Airplane

Figure 5 shows the stagnation points that occur on the airplane. The leading edge of the wing and the nose of the airplane are where those points are expected and can be observed.

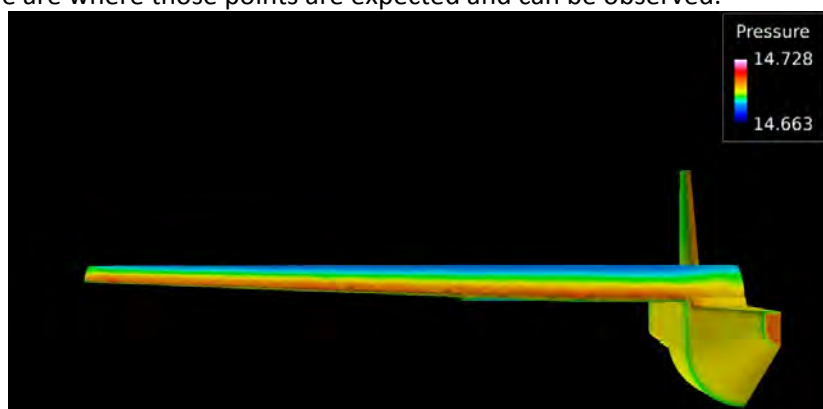


Figure 5. Pressure Distribution on Front of Airplane

After running Cobalt for 24,000 iterations for the case of a 10° angle of attack, F_x , F_y , and F_z all converged. The data from the flow visualization file was imported into Fieldview to begin post processing. The pressure distribution for the case of the airplane flying at a 10° angle of attack is very similar to the 0° angle of attack. Figure 6 shows the pressure distribution for the bottom of the plane. The dark oranges and light reds indicate medium to high pressures which again create lift.

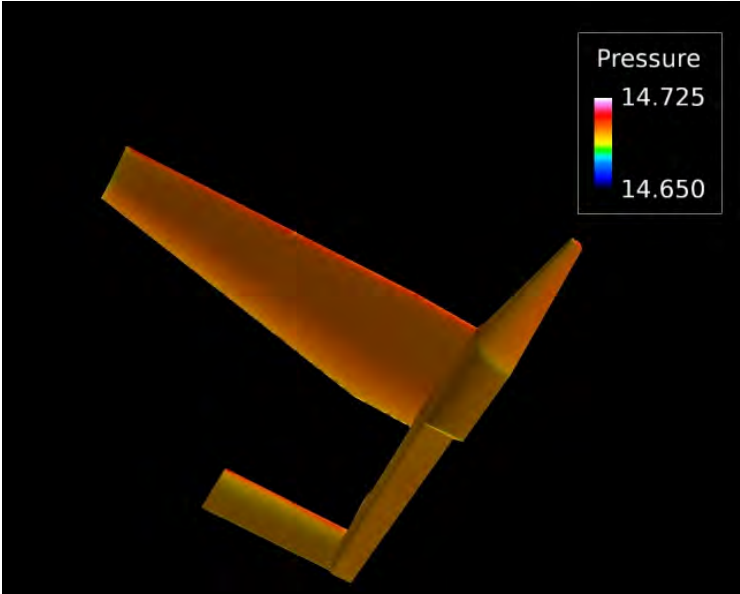


Figure 6. Pressure Distribution on Bottom of Airplane

The pressure distribution of the top of the airplane flying at 10° is again similar to the 0° case. Figure 7 shows the blues and greens on the top of the wing, indicating medium to low pressures.

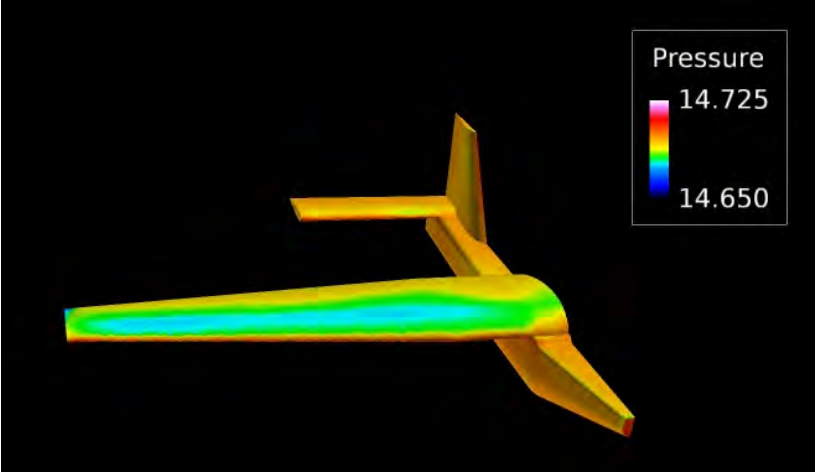


Figure 7. Pressure Distribution on Top of Airplane

The stagnation points on the airplane can be seen in Figure 8. Just like in the 0° case, the points are on the nose and leading edge of the wing as expected.

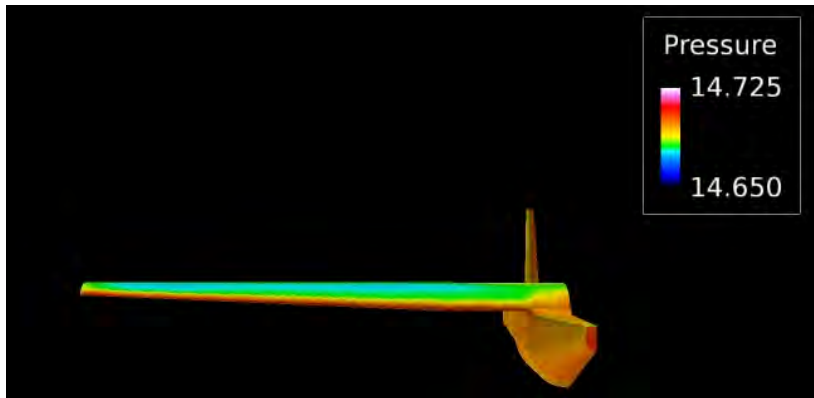


Figure 8. Pressure Distribution on Front of Airplane

After analyzing the pressure distribution for both cases, the analysis of the airflow around the airplane was done. A coordinate surface plane was created in Fieldview, and then seeds were added to the coordinate plane to generate streamlines. The results of the streamlines for the 0° angle of attack case can be seen in Figure 9.

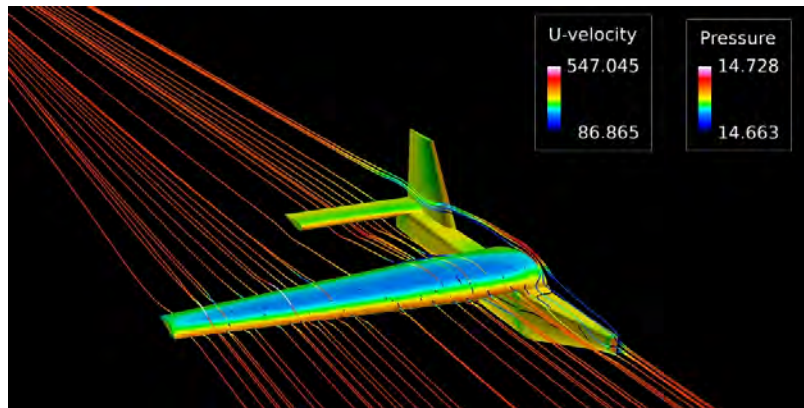


Figure 9. Streamlines of Airflow Around Airplane

It can be seen for some of the streamlines that they approach with a red and orange color indicating high velocities and then switch to blue and green signifying that they have significantly slowed as they pass over the wing. Once they are over the wing, they go back to the red and orange color for high velocities.

Figure 10 shows the streamlines for the 10° angle of attack case.

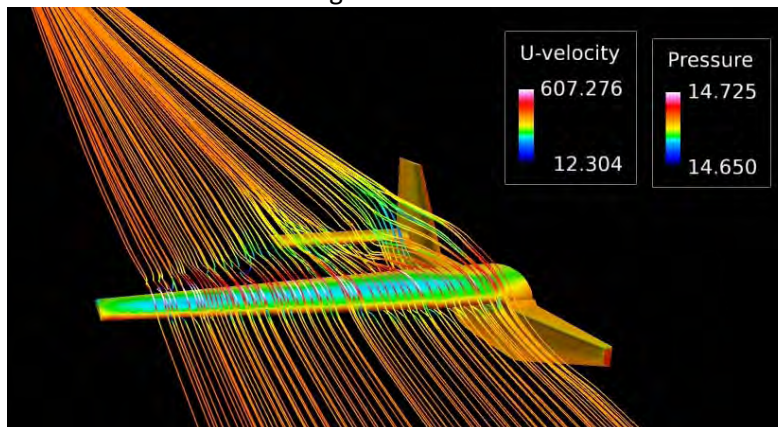


Figure 10. Streamlines of Airflow Around Airplane

It is much easier to see the transition of velocities the streamlines make as they flow over the wing in this case in comparison to the 0° angle of attack case.

In order to find the coefficients of lift and drag the reference area had to be calculated and changed from the default in the job file. The planform area of the wing was 900 in² but since the analysis was for only half of the airplane, the reference area was set as 450 in². Each job file was ran an additional iteration with the new reference area to get the coefficients of drag and lift. Table 1 shows the comparison between the ONU SAE Aero team’s calculations and what the results were from the CFD analysis ⁽⁵⁾.

Table 1. Lift and Drag Coefficients

Angle of Attack	Coefficients	Team	CFD Results
0°	C _l	1.006	1.15
	C _d	0.11	0.19
10°	C _l	1.862	2.12
	C _d	0.22	0.399

Conclusions and Recommendations

Referring to Table 1, it was concluded that the CFD results compared well to the calculations that were made by the team. The CFD results for the coefficients of lift were on average 14% higher than the team’s calculations. The CFD results for the coefficients of drag were on average 77% higher than the team’s calculations. One source of error in the coefficient of lift came from the team’s program to calculate the lift. It only accounted for the lift caused by the wing. The CFD results accounted for the entire airplane, including the fuselage and all control surfaces. Over all, this analysis helps the team by giving them another set of data to help them predict the performance of their aircraft.

Acknowledgments

I need to especially thank Dr. Marquart for helping me with this project. There were several problems that came up during the project that I was not sure of how to fix. His patience with me was much appreciated and I would not have been successful without his help. I would also like to thank the ONU SAE Aero team for giving me the information for this project. Their cooperation was very helpful.

References

1. SolidWorks, <http://www.solidworks.com>
2. Pointwise, <http://www.pointwise.com>
3. Cobalt, <http://www.cobaltcf.com>
4. Fieldview, <http://www.ilight.com/en/>
5. Reeves, J., Johnson, A., Douglass, R., Huff, A., Glauner, L., Paganelli, O., Edwards, J., Strahm, K., Turich, J., and Smith, D., “SAE Aero Design Report”, March 2017, pg 15.

The Road to Interoperability in Health Care

Student Researcher: Marisa D. Bartholomew

Advisor: Joslyn Dalton

Cuyahoga Community College

Health Information Management Technology Program

Abstract

An Ohio resident vacationing in Florida requires emergency care. The Florida physician accesses the patient's medical record and reviews the patient's medical history saving time, money and getting to a treatment faster. That's the model of interoperability. The Office of the National Coordinator (ONC) for Health IT defines interoperability in healthcare as "the ability of systems to exchange and use electronic health information from other systems without special effort on the part of the user"¹ For the patient, this means seamless care wherever he/she goes.

The Electronic Medical Record (EHR), a digital version of a patient's medical chart adopted due to a provision of the American Recovery and Reimbursement ACT (ARRA) in 2009 encouraged health care providers (via incentive money) to switch to the electronic medical record. There was not a focus toward interoperability at that time by the government or the health care provider. The result: "only 40% of hospitals can use the information they receive...only about a quarter of all hospitals can find, send, receive and use electronic information due to substantial barriers."²

An interoperable healthcare system would enable faster, more efficient care by not duplicating tests previously administered by a different provider. Patients would be able to access their full healthcare records no matter where they are. Healthcare providers could seamlessly receive patient information from different hospitals, and different providers enabling better decision making and avoiding the complications that arise when trying to access and interpret patient information from other providers. These benefits save money, time, enable better decision making, and information sharing. The faster a patient who has had a stroke has a procedure to remove the blood clot, the better. A study conducted by the University of Calgary on 1,300 patients showed the optimal time frame for surgery was within two hours. Benefits vanished when surgery occurred after 7 hours from symptom onset. When blood flow is blocked for an extended period, patients can become disabled. Time is essential to a stroke victim. If a patient suffers a stroke out of state, for example, an interoperable medical system will provide a healthcare giver immediate access to a patient's medical record. The immediacy of the information can keep a patient from potentially suffering some type of disability.

Objective

The biggest challenge interoperability faces is standardization of all the vendor supplied information systems. Many of these systems cannot "talk" to each other. And, each vendor wants the standards to be the way they are doing it. "In healthcare, standards provide a common language and set of expectations that enable interoperability between systems and/or devices."⁴ Standards allow data to be shared between clinician, lab, hospital, pharmacy, and patient regardless of application or application vendor.

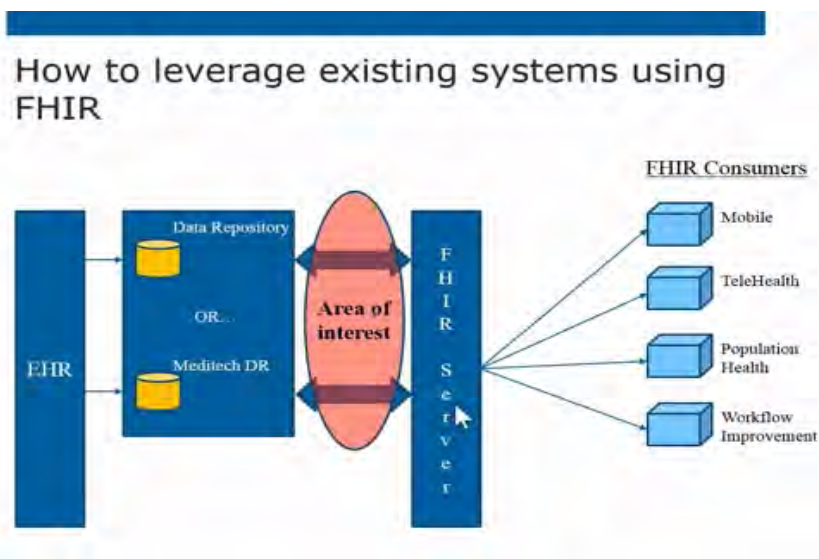
The other challenge is the use of incompatible terminology (semantics). Computers must have the ability to automatically interpret the information exchanged accurately to produce useful information for the

end user. The information sent from one system must be transferred, kept structurally sound, *and* coded so that the receiving system can interpret and use the data. Many IT products and software are not semantically interoperable with each other. One system might call a heart attack a myocardial infarction in its EHR, and another might call it a heart attack, unless the system is digitized with that standard, it may not recognize the two classifications as one and the same.

Method

Fast Healthcare Interoperability Resources (FHIR) is a standard being developed by Health Level Seven (HL7) a standards organization, which has quickly become one of the most popular protocols for joining disparate systems together, and holds great promise for the development of an application-based approach to interoperability and health information exchange. Users can access health care data regardless of underlying infrastructure or operating system. It enables faster access to data while keeping the basics of interoperability workflows intact. The resources can be accessed over HTTP and served in XML or JSON format. Only the specific data needed can be accessed. And, it has potential to facilitate data access for key HIT systems: EHR's, medical imaging, lab and payer systems, and health information exchanges.

The image below, provided by Iatric Systems, is a graphic of how FHIR will work. The source of the data is the EHR/data repository. The FHIR server is what talks to the FHIR consumers. To get the data from the repository to the FHIR server, many health care vendors may have a FHIR API server or they may use a third-party integrator to service the need.



Results

Work is continuing to advance FHIR, and it's being used by some large vendors in an increasing number of situations, but it has not yet reached a stable version for the healthcare industry.

Technology is a part of our everyday lives. An individual can swipe his bank card in a foreign country and his financial information is automatically updated. This is not yet the case with health care. This limits patient engagement. An individual should have full access to the health record in order to share in decision-making. He should also be able to manage the full record in one system. Imagine the Ohio resident vacationing in Florida providing the physician with his full medical record from an app on his phone.

References

- "What is Interoperability" Health IT.gov, N.p., 22 Dec. 2015. Web 18 Mar. 2017. <<https://www.healthit.gov/policy-researchers-implementers/interoperability>>
- N.p.: n.p., n.d. *Why Interoperability Matters*. American Hospital Association, 2015. Web. 18 Mar. 2017. <<http://www.aha.org/content/15/151007-interopmatters.pdf>>.
- "Report Highlights." *Commission on Systemic Interoperability: Ending the Document Game*. Commission on Semantic Interoperability, 2005. Web. 18 Mar. 2017. <<http://www.endingthedocumentgame.gov/>>.
- "Why Do We Need Standards?" HIMSS. N.p., 29 Dec. 2016. Web. 18 Mar. 2017. <<http://www.himss.org/library/interoperability-standards/why-do-we-need-standards>>.
- Butler, Mary. "Solving the Health IT Interoperability Quagmire" *Journal of AHIMA* 87, no.8 (August 2016): 14-18.
- Tressler, Kelsey. "Interoperability and Why It Matters." *Ultimate Medical Academy*. N.p., 06 June 2016. Web. 18 Mar. 2017.
- Fenton, Susan, Giannangelo, Kathy, Kallem, Crystal, Scichilone, Rita. "Data Standards, Data Quality, and Interoperability." *Journal of AHIMA* 78, no.2 (February 2007): extended online edition.
- "Interoperability in Healthcare: The Benefits, Challenges and Solutions" Iron Mountain N.p. N.d. Web 18 Mar. 2017. <<http://www.ironmountain.com/Knowledge-Center/Reference-Library/View-by-Document-Type/General-Articles/I/Interoperability-in-Healthcare-The-Benefits-Challenges-and-Solutions.aspx>>.
- "Connecting Health and Care for the Nation: A 10-Year Vision to Achieve an Interoperable Health IT Infrastructure" The Office of the National Coordinator N.p., 2014. Web 18 Mar. 2017. <<https://www.healthit.gov/sites/default/files/ONC10yearInteroperabilityConceptPaper.pdf>>
- Shah, Dhaval, and Manisha Bafna. "Web Exclusive." *FHIR: The Springboard to True Interoperability*. N.p., 2017. Web. 18 Mar. 2017. <http://www.fortherecordmag.com/news/111516_exclusive.shtml>.
- latic Systems. "Using FHIR for Interoperability." <https://www.youtube.com/watch?v=irTVgUGXg2s> YouTube, YouTube, 12 Aug. 2015. Web. 18 Mar. 2017.
- "After Stroke, Time Matters." RxWiki. Web 27 Mar. 2017. <http://www.rxwiki.com/news-article/disability-after-stroke-decreased-when-patients-had-surgery-remove-blood-clot-faster>.

Water Testing Utilizing Unmanned Aerial Systems

Student Researcher: Jeffrey E. Bennett

Advisor: Dr. Kelly Cohen

University of Cincinnati

Department of Aerospace Engineering

Abstract

Harmful algae blooms (HABs) are colonies of algae that grow rapidly out of control. The algae are toxic causing harmful effects to humans, marine life, and birds. HABs have been reported in every U.S. coastal state and many other inland states. The consensus is that HABs are on the rise, but the lack of scientific data has made it difficult to understand why HABs occur. More data is needed to build an accurate forecast model. The current method to collect data is by boat, buoys, and satellite imaging. These methods are costly, take time to setup, and can provide inaccurate data. Utilizing an unmanned aircraft system (UAS) is a better method to collect the data. The UAS accurately travels to a predetermined GPS coordinate (waypoint) lands on the water, take a sample, and then fly to the next waypoint. The autonomous flight plan can easily be saved to ensure that samples are being taken from the same spot every time. This method is relatively cheap, quick, and can easily be done by one person. The UAS built for water sampling is a heavy lifting octo-copter that is equipped with a multiparameter sonde (EXO²), floatation tubes, and a zero-latency high definition camera. With this configuration, a water sample can be taken every three minutes with a GPS coordinate label for every acquired sample. The same flight path is used throughout the year to watch the trends and possible sources of the HABs. The data collected has the potential to save human and marine lives.

Project Objectives

Collecting water samples has been a difficult task for scientists because its expensive and hard to replicate. Obtaining water samples by boat involves two people navigating to a predetermined GPS point by boat. The crew then must wait for ten minutes to let the bloom settle and then a sample can be taken. This method is not repeatable because of the distance the boat floats away from the intended GPS point in a ten-minute period. Buoy sampling utilizes stationary buoys at a known hot spot for HABs to gather accurate a repeatable data. This process takes a long time to set up but provides reliable data. Satellite imaging is most accurate, and the best at repeatability. Satellite imaging is very expensive and not available to majority.

This project utilizes UAS technology to rapidly take water samples that are accurate and repeatable at a relative inexpensive cost. This provides scientists a mobile platform to accurately sample many different bodies of water in a fraction of the time. This new repeatable data is what is needed for scientist to understand the source of the deadly HABs.

Methodology

UAS have been utilized in several other fields including agriculture, search and rescue, firefighting applications, and situational awareness for emergency responders. In all these applications, the UAS has been reliable and maintained an accurate GPS coordinate. Utilizing this technology will allow for accurate sampling that one person can do alone.

The requirements for the UAS (Figure 1) were met by an Octo-copter UAS that can carry ten pounds and float on water. The UAS is equipped with a Pixhawk flight controller and commutates it telemetry to ground station software (Mission Planner). A predetermined flight plan allows the UAS to fly completely autonomous which allows for repeatable data samples and easy flight. For safety, the UAS is equipped with a DJI Lightbridge II that allows the UAS to transmit high definition video in real time to the user. The floatation device is made from six 2.5 liter bottles that are inflated to 1 psi by a bicycle pump. The U-shaped configuration of the bottles allows the sensor float at the perfect height.

The sensor is a multiparameter sonde (EXO² from YSI) that has seven sensor ports and weighs 3.5 pounds. This sensor takes two minutes to take a sample and can clean itself after each use. The sensor needs 12-volt power to operate and stores all the data internally on a SD card. The UAS can easily power and carry the sensor making it an ideal companion.

An experiment is now created to test the accuracy and repeatability of the UAS. A flight plan was created for East Fork Lake in Batavia, Ohio (Figure 2). The flight plan consists of three way points that the UAS would land at and allow the sensor to take its measurement. The GPS coordinates are recorded for each flight and compared to determine the repeatability of each flight. Two test flight were done at two separate occasions, once in the fall and once in the spring. The GPS is then compared to the original flight plan to determine the level of repeatability a UAS can provide in this situation.

The standard deviation of the actual flight path was compared to the programmed flight path using the following formula. The results were then plotted for easy comparison (Figure 3).

$$\sigma = \sqrt{\frac{1}{N} \sum_{i=1}^N (x_i - \mu)^2}$$

Results Obtained

Overall the UAS proved to be accurate and repeatable with only a small deviation in GPS. As seen in figure 3, the UAS was able to accurately arrive at the intended GPS location and had minimal drift while waiting the two minuets for the sensor to take its measurement. Compared to the boat sampling method, the UAS saves times and consistently provides better data. Since the system is aerial based HABs remain undisturbed and eliminates the need for a boat. The increased mobility of the UAS allows users to easily sample many locations.

This UAS has proven to be an effective and reliable way to sample water. The increase in accurate reliable data will give scientist the opportunity to discover why and how these HABs are created. HABs are dangerous for the life that surrounds it, knowing the cause of the problem will help ensure we control the problem. Providing accurate and reliable data is essential to the answer. The water sampling UAS is the solution for the data collection.

Figures

UAS Requirements
Abel to lift 3.5-pound sensor
Float on water
Abel to log GPS location
Easy to fly
Reliable
Accurate
Safe

Figure 1. Shows the requirements that the UAS needs to fulfill.

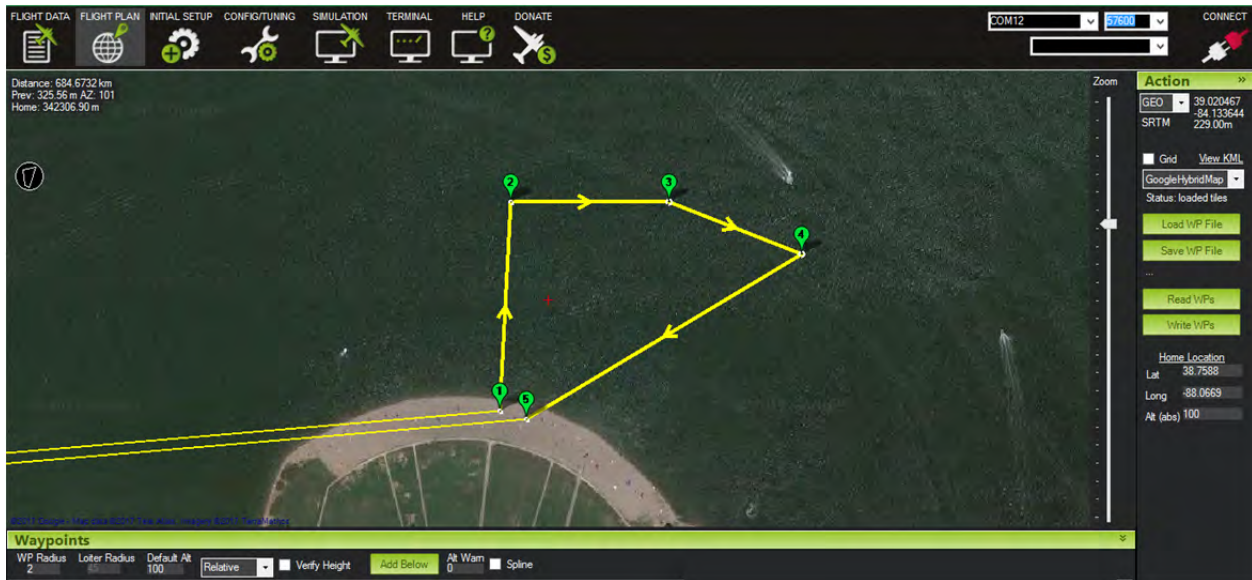


Figure 2. Shows the flight predetermined flight path at East Fork Lake in Batavia, Ohio.

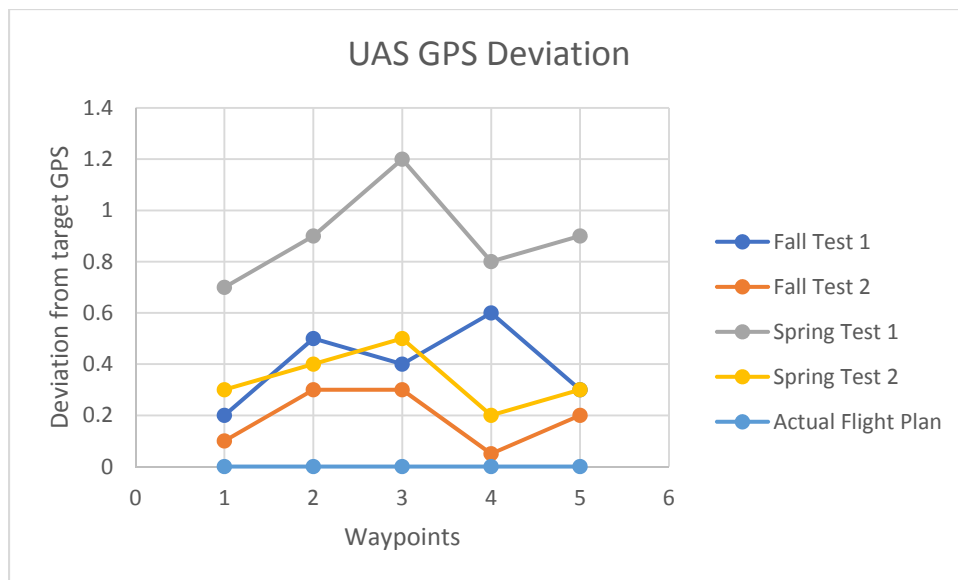


Figure 3. Shows the how much the UAS deviates from the actual flight plan.

References

1. YSI, Dayton, Ohio: Multiparameter Sonde (EXO²)
2. Mission Planner, <http://ardupilot.org>
3. Lightbridge II, <http://www.dji.com/lightbridge-2>
4. Pixhawk, <https://pixhawk.org/>
5. Response Strategy for HABs, http://epa.ohio.gov/Portals/28/documents/habs/PWS_HAB_Response_Strategy.pdf

Reduction of Graphene Oxide via Electron Beam Irradiation

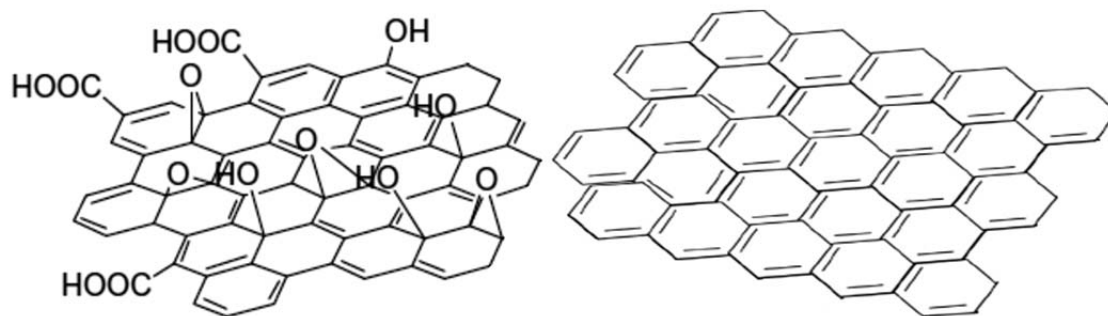
Student Researcher: Jonathan Wesley Boyd

Advisor: Dr. R.M. Uribe

Kent State University
Department of Physics

Abstract

Graphene is a fascinating material with exceptional properties and promises much technologic advancement. It is a single atom thick hexagonal lattice of sp^2 hybridized carbon atoms and its properties include high electron mobility even at room temperature and the highest thermal conductivity of any known material. Possible applications include more efficient solar cells, higher capacity batteries, and synthesis of strong lightweight composite materials. Currently the use of graphene in commercial products is limited due to the difficulty of obtaining large pure sheets. Another material, graphene oxide, is similar to graphene except oxygen-containing functional groups are attached to the carbon lattice. The structural differences are shown below with graphene oxide on the left and graphene on the right.



Graphene oxide can be created in a lab by using a mix of acids to dissolve pieces of graphite. The functional groups attached to the carbon lattice of graphene oxide diminish the electrical conductivity, one of the most desired properties of graphene. If these groups could be partially or fully removed from the material would possess properties closer to those of pure graphene. This process of removing oxygen groups is known as reduction and the final product is aptly called reduced graphene oxide. Several methods have successfully created reduced graphene oxide, one of the most notable being reduction with hydrazine vapors. Although successful, it takes up to 60 hours for maximum effectiveness, can let behind nitrogen impurities, and the byproducts from such a reduction are harmful. Other methods currently possess their own drawbacks, leaving many to look for better alternatives.

Objective

Our aim is investigating if radiation from an electron beam accelerator could reduce graphene oxide in a fast, safe, and controlled manner. This is a tried and tested technology that has been around for many years and already has industrial applications from crosslinking plastics to food sterilization. We aim to see if the electron beam has the effect of removing oxygen-containing functional groups from graphene oxide and if the removal of the groups impacts the electrical properties of the material.

Methodology

Samples of pre-prepared graphene oxide solution (from Graphene Supermarket Inc. USA) were deposited on glass slides, some of which were partially coated in indium tin oxide (ITO). The ITO coated slides started with a coating only on one side of the slide and then this conductive coating was masked

with a silicone-based tape and dipped in a mixture of nitric and hydrochloric acid to remove the coating everywhere there was not tape. The masks left two strips of conductive ITO separated by a non-conductive gap where the graphene oxide solution was placed. Other samples were deposited on non-coated microscope slides.

After placing some solution on the slides they were then put in an oven at 65°C for around an hour to drive off the water from the solution. This temperature was well below the temperature range of possible thermal reduction (Seung Hun Huh) and was only intended to leave a thin coating of graphene oxide on the slides to prepare them for irradiation. After being dried, the samples were irradiated in the dose interval from 100 kGy to 1700 kGy, using an electron beam accelerator at energies of 80 keV through 200 keV. These energies were chosen to sample both above and below the calculated 86 keV threshold for planar sp^2 hybridized carbon-carbon bond breaking by electron scattering (B. Smith & D. Luzzi). This energy is for a lattice plane perpendicular to the incident electrons, the energy to displace atoms increases as a function of the angle between the electrons and the lattice plane to a maximum of 139 keV for a lattice plane parallel to the beam.

The samples were tested using Fourier transform infrared spectroscopy to determine any structural changes induced by the radiation, paying special attention to the absorbance peaks corresponding to carboxyl (-COOH) and alcohol (-OH) functional groups as well as the carbon-carbon double bond. The samples were etched off of the glass slides and then placed into the spectroscope. This removed any interference caused by the glass, which is active in absorbing portions of the IR spectrum. The samples were scanned 32 times each to produce the absorption graphs that recorded normalized transmittance vs. wavenumber for wavenumbers between 4000 cm^{-1} and 700 cm^{-1} .

Four-probe resistivity measurements were later performed to determine the sheet resistance of the samples and characterize the conductivity changes caused by the radiation. A Keithley 2400LV unit was used in the electrical characterization. The probes were connected to the Indium tin oxide coating of the glass, allowing for good electrical contact while preserving the graphene oxide layer from damage that the probes could cause.

Results

Samples that had been irradiated showed two major differences from the control samples in the IR graphs, the decrease in a peak around 1700 cm^{-1} and a new peak around 2400 cm^{-1} . Graph 1 is an example of these changes for a sample that was irradiated at 120 keV at a dose of 700 kGy. The peak that decreased corresponds to the carbon-oxygen double bond in the carboxyl functional groups and the peak that appeared in the irradiated samples is the one that indicated CO_2 present in the sample.

The resistance between the ITO bands was measured and then this measured resistance was used to calculate the sheet resistance. The sheet resistance is the resistivity of the material divided by the thickness of the material and is routinely used for thin film measurements. It was calculated by taking the resistance value measured and multiplying by length of the gap (perpendicular to current flow) over the width of the gap (parallel to the current flow), which varied from sample to sample. The sheet resistance for several samples was calculated and the values are reported in chart 1.

Significance and Interpretation of Results

The structural changes seem to indicate that the beam was able to manipulate the structure of graphene oxide. Our theory is that the carboxyl groups are separating from the graphene lattice and forming carbon dioxide that is being trapped in the sample. This explains both structural changes that

were observed in the infrared spectrum. When the carboxyl groups are cleaved from the lattice the ratio of carbon to oxygen on the remaining sample increases, chemically reducing the sample. This is a promising step in showing that some reduction was achieved through irradiation.

The first thing to note on the sheet resistance measurements is that the resistance increased after the irradiation. This goes against the expected behavior of decreasing resistance as the oxygen-containing functional groups are removed. Further, we note that the percent change is a function of the energy of the electrons. This could indicate that the electrons are displacing carbon atoms from the charge-carrying lattice. This would match the theory mentioned earlier of electrons with energies greater than 86 keV having the energy to knock carbon atoms from the lattice when the lattice plane is perpendicular to the beam and 139 keV for a plane parallel to the beam. This would indicate that the orientation of carbon lattices is fairly random in our samples. This result also indicates that attempts at reduction with higher energy electrons damage the lattice and should be avoided if highly pure graphene is the desired result.

Graphene and graphene-like materials are going to shape the future of technology. Small quantities are already being used in high performance racecars, cell phones, and professional sporting equipment. Once the method of production becomes reliable and inexpensive graphene containing products could become widely available for consumers. In the future we plan on creating and irradiating thinner samples, eventually reaching the thickness of a single layer. This would increase dose uniformity throughout the sample and could help decrease the randomness in orientations of the carbon plane. We also plan on focusing on smaller dosages at the lowest energy range available to us and further reducing the total energy by introducing a gap between the beam and the sample. We hope these changes minimize damaging effects to the carbon lattice. We also plan to irradiate samples while in solution, which could allow experimentation at higher energies without causing damage to the carbon lattice and aid in the removal of the oxygen-containing functional groups.

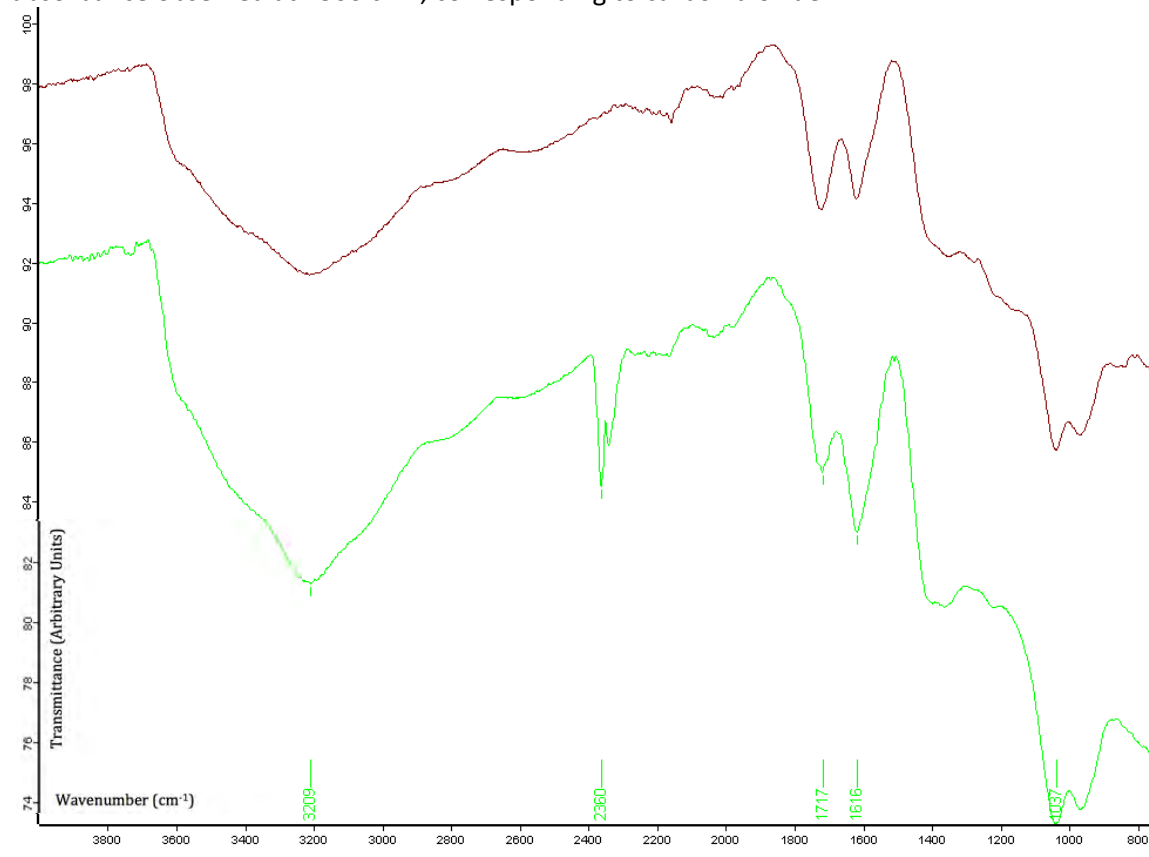
Figures/Charts

The calculated sheet resistances are reported in chart 1 below. All resistances increased after irradiation, indicating damage to the charge carrying carbon lattice. Further, the higher energy electrons had a larger effect of increasing the resistance, consistent with theory.

Sheet Resistance of Graphene Oxide Samples Irradiated at 400kGy			
Energy (keV)	Initial Sheet Resistance ($M\Omega\Box$)	Final Sheet Resistance ($M\Omega\Box$)	% Change
80	50.3	52.2	3.8%
100	53.2	57.9	11.1%
120	53.6	61.7	15.1%
200	52.4	62.8	19.9%

Graph 1, on the next page, is an infrared graph for both a control sample (red) and for a sample that was irradiated at 120 keV at a dose of 700 kGy. The transmittance is in arbitrary units and depended on how the sample rested on the detector. Peaks, which appear as valleys in the transmittance graph, are

related to other peaks in the same sample that are constant. The changes noted are the increased transmittance at 1717 cm^{-1} , corresponding to the carbon-oxygen double bond, and the increased absorbance observed at 2360 cm^{-1} , corresponding to carbon dioxide.



Acknowledgments

The author would like to thank The Ohio Space Grant Consortium, Kent State University, and Choose Ohio First for supporting this research.

References

1. Seung Hun Huh (2011). Thermal Reduction of Graphene Oxide, Physics and Applications of Graphene – Experiments, Dr. Sergey Mikhailov (Ed.), ISBN: 978-953-307-217-3, InTech, Available from: <http://www.intechopen.com/books/physics-and-applications-of-graphene-experiments/thermal-reduction-of-graphene-oxide>
2. Smith, Brian W., and David E. Luzzi. "Electron Irradiation Effects in Single Wall Carbon Nanotubes." *J. Appl. Phys. Journal of Applied Physics* 90.7 (2001): n. pag. Web.
3. Teweldebrhan, D., and A. A. Balandin. "Modification of Graphene Properties Due to Electron-beam Irradiation." *Appl. Phys. Lett. Applied Physics Letters* 94.1 (2009): n. pag. Web.
4. Tyagi, Chetna, G.B.V.S. Lakshmi, Sunil Kumar, Ambuj Tripathi, and D.K. Avasthi. "Structural Changes in Graphene Oxide Thin Film by Electron-beam Irradiation." *Nuclear Instruments and Methods in Physics Research Section B: Beam Interactions with Materials and Atoms* 379 (2016): 171-75. Web.

Energy Analysis of a Two Degree of Freedom Robot

Student Researcher: Edward Brinkerhoff

Advisors: Prof David Myszka and Prof. Andrew Murray

University of Dayton

Mechanical Engineering Department

Abstract

Energy usage is increasing in manufacturing operations. One reason for the increase is the shift to automation and robotics. Robots use an array of motors to manipulate objects, and each motor uses energy to operate and move the robot. In most cases, the motors use energy even when holding an object still or while the robot sits idle between tasks. This project focuses on the design and efficiency of a robot that requires fewer motors than a typical industrial robot yet is capable of performing many of the same industrial tasks. A CAD model of the robot is developed to perform an energy analysis during a typical operation cycle and then to optimize this cycle. Additionally, experimentation will augment the analysis through the use of a microprocessor controlled motor to measure current requirements while performing specified motions.

Project Objectives

The purpose of this project was to optimize the energy usage of a two degree of freedom robot through the mechanical design and actuation of a programmed task. Little to no consideration is given to the energy consumption of robotics. Low degree of freedom robotics, like the one being analyzed are There is a potential cost savings benefit and productivity increase to manufactures to analysis these types of robotic systems. Less energy consumption is also beneficial to reducing the overall Energy consumption of industrial manufacturing.

Methodolgy

For this project a two degree of freedom robot was developed from an unscaled kinematic diagram (Figure 1). In order to analyze a two degree of freedom system, two boundary conditions were established. The two boundary conditions are that the robot needs to pick up a mass at an arbitrary length away from the base with at an angle that is not simply 90° or 180° from the horizontal. The second boundary condition is that the robot will be able to place the mass at an arbitrary length that is less than the first condition. From these assumptions a series of equations was developed in order to solve for unknown lengths and angles from ones that were pick and based on the two boundary conditions. Matlab was used to solve for unknown lengths. Once all the lengths were determined, a CAD model was developed (figure 2). The CAD model will be used for future analysis of energy consumption through a motion study of the robot.

A motor was mounted to a vice and a mass was attached to a standard servo motor. The motor had three different masses applied to it and was run at three different speeds. Each sample was also run clockwise and counterclockwise. Power data was collected and from this data the energy was determined by multiplying the average power output by the time interval the motor was in motion. The energy data collected was run through a statistical data analysis program. Four factors, rotation, speed, action and mass, were considered as contributing factors in energy usage. Rotation was either clockwise or counter clockwise. The speed factor was when the motor rotated at three different speeds

considered to be slow, medium, and fast. The action factor was considered as the motor lifting the mass, holding the mass still, and then lowering the mass one quarter rotation. The mass factor was considered as three different masses, an empty bottle, a half full bottle and a full bottle of water attached by a string to the shaft of the motor.

Results

The CAD model of a two degree of freedom mechanism represents a device that can pick up a mass at a variety of angles. By having the ability to perform a task not simply vertical or horizontally, gravity can be used to reduce the energy consumption in a manufacturing task. This could reduce the power required of the motors to perform the task.

The statistical data showed that the highest contributing factor was the action of the motor. The highest energy used was lifting any of the masses, followed by holding an object still. Lowering an object had the least amount of energy used, but used twice as much when lowered at a slow controlled rate.

Future Needs

ore data is needed to accurately describe the energy used in a system. Data from industrial manufacturing servo motors is also needed to accurately determine what is actually going on in a manufacturing setting. Further motion studies on the CAD model is also needed in order to test what directions and angular velocities would optimize a motors energy usage.

Figures and Tables

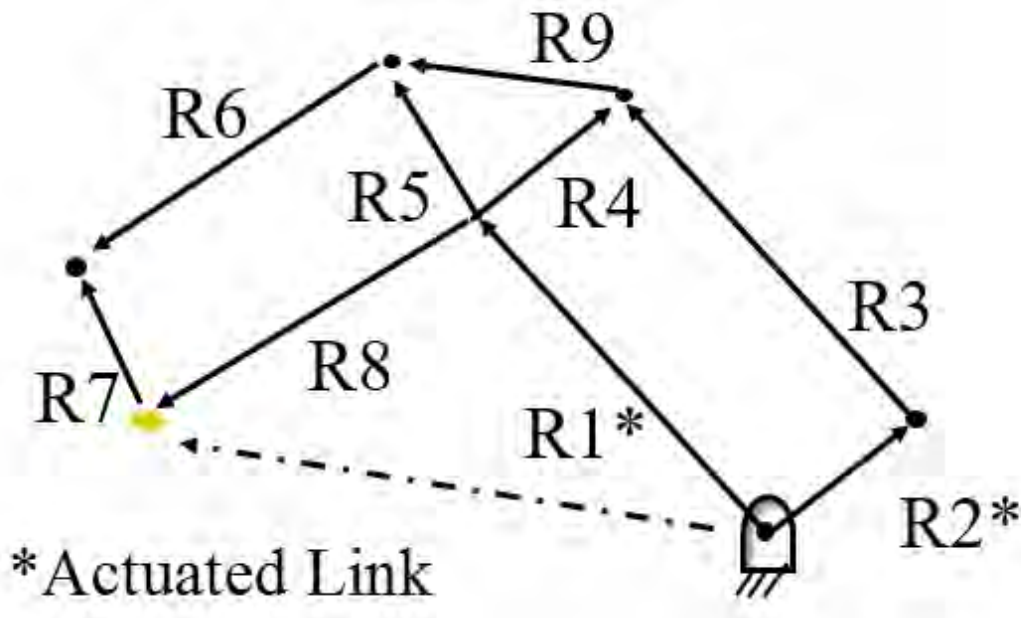


Figure 1. Two Degree of Freedom Unscaled Kinematic Sketch



Figure 2. CAD Model of a Two Degree of Freedom Robot

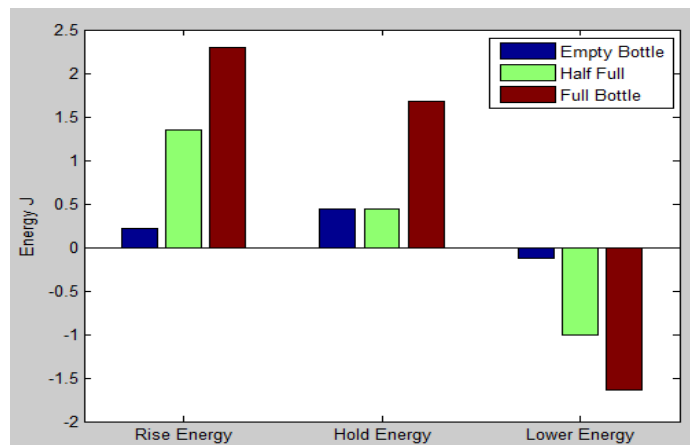


Figure 3. Slow Speed Counter Clockwise Trial

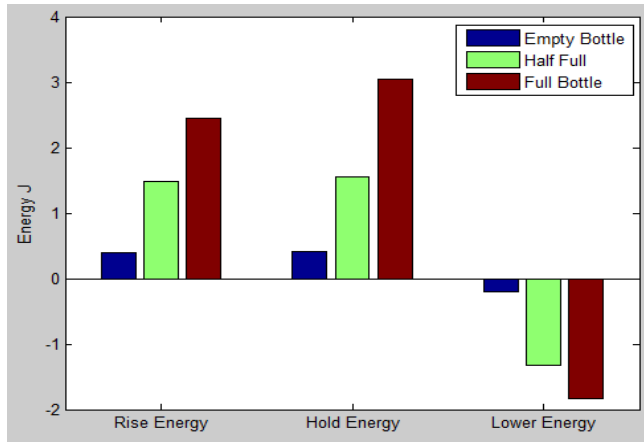


Figure 4. Slow Speed Clockwise

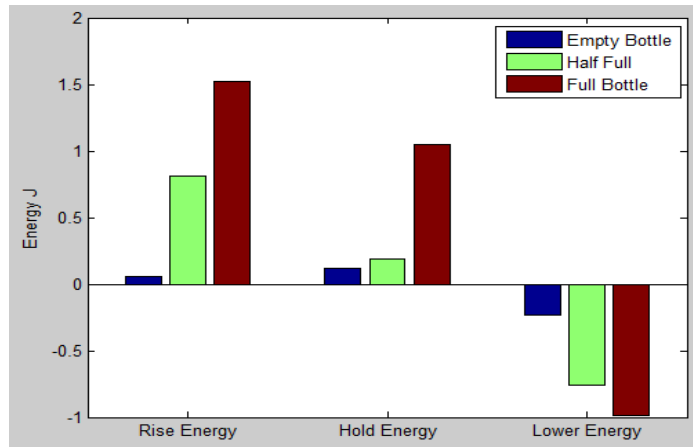


Figure 5. Medium Speed Counter Clockwise Trial

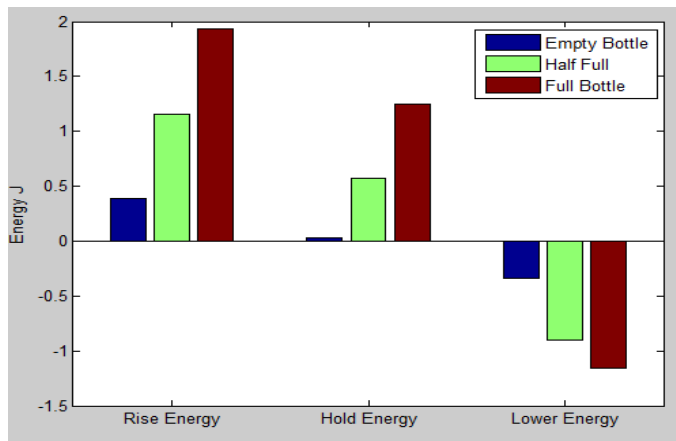


Figure 6. Medium Speed Clockwise Trial

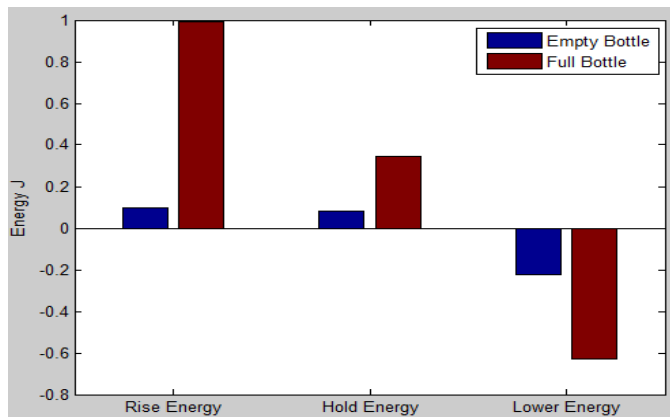


Figure 7. High Speed Counter Clockwise Trial

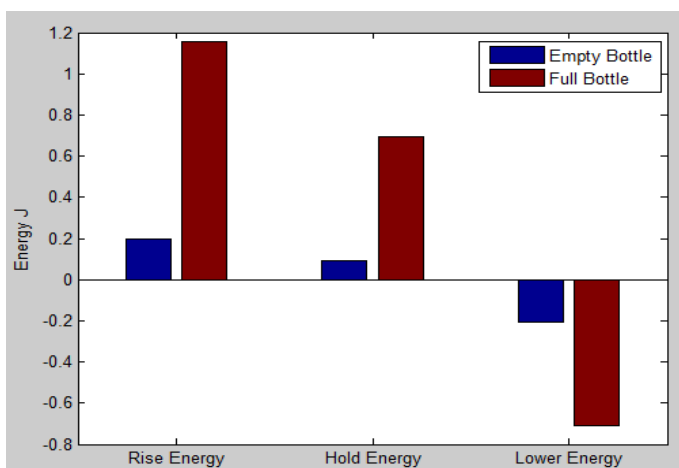


Figure 8. High Speed Counter Clockwise Trial

Small-Scale Autonomous Hexapod Stair-Climbing Robot

Student Researcher: Miles A. Burrage

Advisor: Dr. Luther Palmer

Wright State University

Electrical Engineering

Abstract

Section 4.2 of the 2015 NASA Technology Roadmap calls for autonomous systems that can achieve “mobility across terrains with challenging topologies and challenging regolith properties for bodies with substantial gravity.” This project seeks to address this need, as well as solutions for robot navigation. Stairs represent a similar challenge to robotic systems as uneven terrain such as rubble and rocks that could be found on other planets and/or moons.

Project Objectives

The scope of this project is to build a small-scale, autonomous, hexapod, stair-climbing robot. This robot is a six-legged machine that will perform tasks or behaviors with minor supervisory input from an operator. Although this project seeks only to walk up stairs, the platform, algorithm and tools developed in this work can be extended in the future to more complex gaits and modes of locomotion.

Methodology Used

The robot uses six legs because it offers redundancy if one leg has malfunctioned. If four legs were in use, and one leg fails, the robot would lose its ability to walk. Other popular solutions to this problem utilize tank treads, with rotational flippers. Tank treads with differential steering do not exhibit the mobility observed in legged animals. As a result, treaded systems cannot execute maneuvers such as turning around or moving horizontally on stairs. Other more simple wheeled systems are designed for sets of stairs with specific height and also cannot execute complex maneuvers on the steps.

Results

The pictures below in Figure 1, reveal the robot and its components. This robot is able to maneuver across flat and grass-like terrain.



Figure 1. The robot and hardware

Reference

1. NASA. 2015 NASA Technology Roadmaps TA 4: Robotics and Autonomous Systems. NASA, https://www.nasa.gov/sites/default/files/atoms/files/2015_nasa_technology_roadmaps_ta_4_robotics_and_autonomous_systems_final.pdf. Accessed 26 March 2017.

Bio-Sensing with Ultra-flexible Planar Terahertz Metamaterials

Student Researcher: Joshua A. Burrow

Advisors: Drs. Jay Mathews and Imad Agha

University of Dayton

Department of Electro-Optics and Photonics

Abstract

Terahertz (THz) spectroscopy has been labelled as an effective method for identifying bio-molecules in crystalline form due to their spectral fingerprints falling in the THz regime of the electromagnetic spectrum. Carefully engineering metamaterials to have spectral responses in the THz range can extend spectroscopy techniques to the quantification of bio-materials in aqueous form. We report experimental observations of multiple distinct resonances in an asymmetric metallic 4-gap square ring resonator (SRR) compared to a polarization insensitive 4-gap SRR. The asymmetry is introduced by shifting two of four adjacent metallic L brackets. These otherwise inaccessible resonances are exploited for bio-sensing applications in the terahertz regime of the electromagnetic spectrum. The proposed structures are simulated with finite element method software and show great agreement with the experimental results. The LC resonance is experimentally exploited as a sensing mechanism to quantify Bovine Serum Albumin (BSA). The results reveal a maximum sensitivity of 34.2 GHz/(mmol/L) and a minimal detection limit of 0.031 mmol/L (2 mg/mL) at the LC resonance exceeding the current THz bio-sensing limitations.

Introduction

The terahertz regime of the electromagnetic spectrum is often defined as light having frequencies between 100 GHz and 10 THz. Occupying the most recently explored region between microwaves and infrared radiation, molecular vibrations and rotations resonate at THz frequencies providing a spectral fingerprint of certain materials. Over the course of the last 20 years, terahertz (THz) spectroscopy systems have made great advancements in available sources and detectors. Thus, opening up the scientific community to many applications for characterizing a range of materials, including semiconductors and biomolecules.

Unfortunately, THz radiation suffers a great amount of attenuation due in the presence of water. Consequently, it's much more difficult to characterize or quantify a biomolecule in aqueous form. With the rising need for on-site, fast, highly sensitive, non-destructive techniques for the quantification of microorganisms, an alternative technique has been explored using metamaterials. Recent developments in metamaterials have proven them to be promising candidates for bio-sensing due to their distinctive spectral fingerprints. These exotic spectral features, governed by the topological metal features and the index of refraction of the substrate, serve as the sensing platform for the detection of analytes. The biomolecule thin films induce a frequency shift proportional to the concentration of the present biomolecule.

Objectives

The primary objectives of this project are to 1) design and model a low cost, ultra-flexible metamaterial biosensor 2) fabricate prototype sensors and characterize their spectral response by identifying each resonant mode of the devices 3) determine the bio-sensing limitations associated with the devices using a terahertz continuous wave spectrometer operating in a transmission optical setup and 4) compare the performances of multiple material and topological combinations. The first phase of the project was to

design and simulate the spectral response of the metamaterial biosensor using COMSOL, a comprehensive simulation software environment. The second phase of the project was to use standard photolithography techniques to fabricate the biosensors. The final phase was to analyze the performance of each sensor to determine the best THz metamaterial biological sensor. The responsiveness, resolution and minimal detectable concentration were the measures used to rate the performance of the devices.

Methodology Used

The periodic pattern of metallic square ring resonators (SRRs) were designed for qualitative analysis of biochemical concentrations with a continuous-wave THz spectrometer. The SRRs have square slits centered on all four sides of the square with a gap size of $35 \mu\text{m} \times 35 \mu\text{m}$ and periodicities, $P_x = P_y = 300 \mu\text{m}$. Asymmetry is induced into the structure by vertically separating the left and right L brackets to a $\sigma = 40 \mu\text{m}$ separation distance. The unit cells of the proposed THz metamaterial biosensor periodic structures are depicted in Figure 1.

Simulations are carried out of each device using COMSOL Multiphysics which is a finite element analysis solver and simulation software under a horizontal linearly polarized THz incident beam. The electric and magnetic field distributions, surface current distribution and transmission spectrum are determined once each region is assigned material properties and a sufficient tetrahedral mesh has been chosen. The electrical conductivity and refractive index of the substrate was assumed to be $3.77 \times 10^7 \text{ S/m}$ and $1.88 + 0.02i$, respectively. Simulations show an enhanced E-field in the top and bottom gaps at 0.564 THz that results in a significant transmission dip. This resonant frequency ω_{LC} is known as the inductance capacitance resonance and can be easily understood using an LC circuit model given by the equation

$$\omega_{LC} = \sqrt{\frac{1}{L_{eq}C_{eq}}}, \quad (1)$$

where L_{eq} is the equivalent inductance resulting from the current path of the SRR, and C_{eq} is the equivalent capacitance determined by the gaps and refractive index properties of the substrate. The field distribution plots located at the top of Figure 2 show the oscillating surface current J as arrows changing directions at 0.300 THz, 0.418 THz, 0.560 THz and 0.750 THz confirming the LC circuit model.

The planar metamaterial devices were fabricated by depositing 100 nm thick aluminum on the Kapton substrate. First, the Kapton dielectric substrate was mounted on a silicon wafer. Then, conventional photolithography processes was used to pattern the surface of the Kapton. Thermal evaporation was used to deposit 100 nm aluminum with a thickness of 100nm. Finally, lift-off was performed to remove aluminum from the areas that were not patterned during the lithography stage of the fabrication process. The samples were cut into 2cm x 2cm squares and a continuous wave THz spectrometer was employed to characterize the electromagnetic responses.

CW THz spectroscopy of the symmetric and asymmetric planar metamaterial devices was carried out on the commercially available Teraview Model CW Spectra 400 spectrometer, which can achieve extremely low spectral resolutions ($\leq 100 \text{ MHz}$) by incrementally varying the difference frequency by detuning two near infrared lasers. The measurements were performed in ambient air conditions. The transmission $T(\omega)$ of the devices were determined by

$$T(\omega) = \frac{|E_{sample}(\omega)|}{|E_{ref}(\omega)|}, \quad (2)$$

where $|E_{sample}(\omega)|$ and $|E_{ref}(\omega)|$ are the transmitted electric field amplitudes of the metamaterial device and the Kapton substrate, respectively. The influence of rotation is experimentally studied under 95% linearly polarized THz beam by performing measurements on multiple rotated orientations of the metamaterial device.

Demonstrations of the symmetric and asymmetric SRR devices were explored as label-free biosensors. BSA is a protein standard in lab experiments derived from cow blood. The solutions were prepared by mixing the BSA crystals with distilled water into concentrations ranging from 2 mg/mL (0.030 mmol/L) to 200 mg/mL (3 mmol/L). BSA solutions with a volume of ≈ 20 mL was drop casted and spread across the 2 cm x 2 cm surface area of the periodic SRRs. To combat the non-uniform analyte the devices were placed on a heating plate to decrease the evaporation time of water.

The sensitivity, S , of the devices are

$$S = \frac{\Delta f}{\Delta C}, \quad (3)$$

where $\Delta f = f_0 - f_i$ is the frequency shift from 0 concentration and ΔC is the change in concentration in mmol/L. The minimal detectable concentration is merely the smallest amount of BSA solution where we observe a shift in resonant frequency. Although not complete, these two characteristics will be sufficient to compare to similar terahertz bio-sensors.

Results and Discussion

The devices were successfully fabricated in the NanoFab Lab at the University of Dayton. Before we explored the bio-sensing capabilities of the devices, we first characterized the metamaterials through rotational measurements. The angular dependence of the LC resonance reveals through experimental measurements that the symmetric sensor has a small variance in resonant frequency. The maximal difference of the value is 2.15 GHz, which is much lower than the spectral resolution of most commonly used THz time-domain spectrometers. The LC mode of the asymmetric sensor varies in a sinusoidal behavior with an amplitude of 17.6 GHz. Further investigations of the asymmetric sensor reveal that modes at 714 GHz and 778 GHz are excited are selected rotations and does not fluctuate in frequency. Hence, these modes show great promise for the quantification of biomaterials.

The final step was to exploit the unique spectral features as platforms for biosensing utilizing the drop casting method to apply different concentrations of BSA. Figure 3(a) and 3(b) shows the results of the test of the symmetric sensor via the LC resonance and other two modes, respectively. The blue curve represents the symmetric sensor with no BSA concentration present, the green curve is for 25 mg/mL, gold curve for 100 mg/mL and red curve for 200 mg/mL. It is worth noting that the transmission spectra with just DI water and the bare biosensor were the exact same. The corresponding resonant frequencies for the LC resonance are $f_0 = 562.0$ GHz, $f_1 = 553.4$ GHz, $f_2 = 542.8$ GHz, and $f_3 = 534.5$ GHz. This shows that as the increase in BSA concentration of the bio-analyte yields a redshift, which means the effective index of refraction has increased. Figure 3(c) reveals of all three modes, the LC resonance exhibits the largest sensitivity of 8.6 GHz/(mmol/L).

The asymmetric results depicted in Figure 3(d), (e), and (f) was oriented 45 degrees with respect to the incident vertically polarized THz waves. Using the concentrations as the symmetric case, the results reveal two modes (LC and 3rd modes) exhibit larger sensitivities. The largest sensitivity obtained for the symmetric and asymmetric devices fabricated on 50.8 μm thick KaptonMT is 10.2 GHz/(mmol/L).

Dupont™ manufactures multiple variations of polyimide films, each possessing unique thermal, electrical, and optical properties. One of which is KaptonB which is a black, homogeneous opaque film. These characteristics make it ideal for uses that require low reflectivity. A symmetric sensor was fabricated under the same conditions and design properties and the concentration measurements are shown in Figure 4(a). The sensitivity for this device, $S = 34.2 \text{ GHz}/(\text{mmol/L})$ has tripled and has achieved the smallest measurable concentration of 2 mg/mL. Other groups such as S. Wang *et al.* have measured as low as 25 mg/mL [2]. Their group was limited to a THz time domain spectrometer with a spectral resolution of 13.5 GHz.

Overall, the project shows great promise for using an ultra-flexible metamaterial based biosensor together with a CW THz spectrometer to obtain a label-free highly sensitive bio-sensing scheme. We successfully designed and simulated two devices that show good agreement with the experimental results. In addition, multiple sensors were fabricated on different substrates and characterized to identify the LC modes of the each device. Finally, we used a robust approach to exceed the minimal detectable concentration reported by current groups in the THz metamaterial bio-sensing field.

Figures and Charts

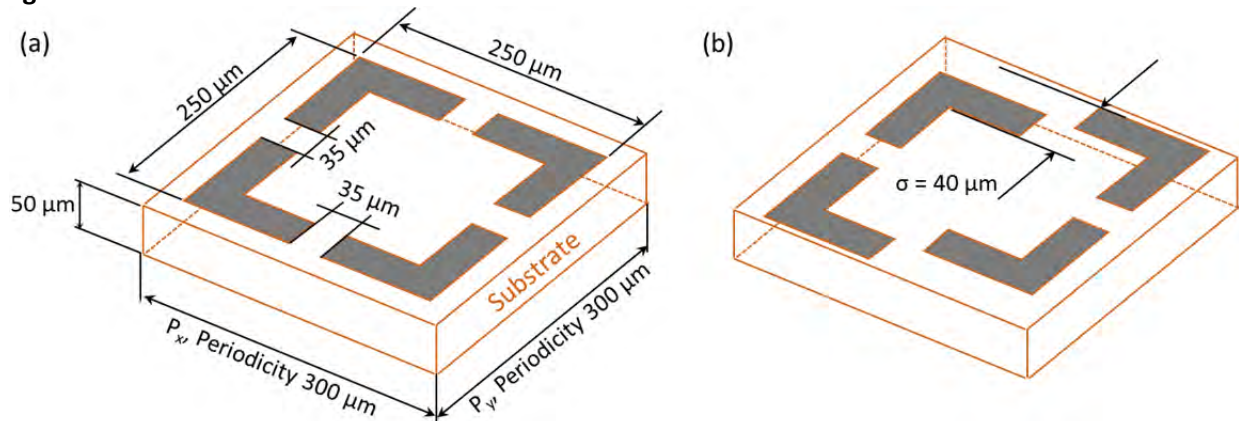


Figure 1. Schematic unit cell diagrams of (a) symmetric and (b) asymmetric metamaterial devices.

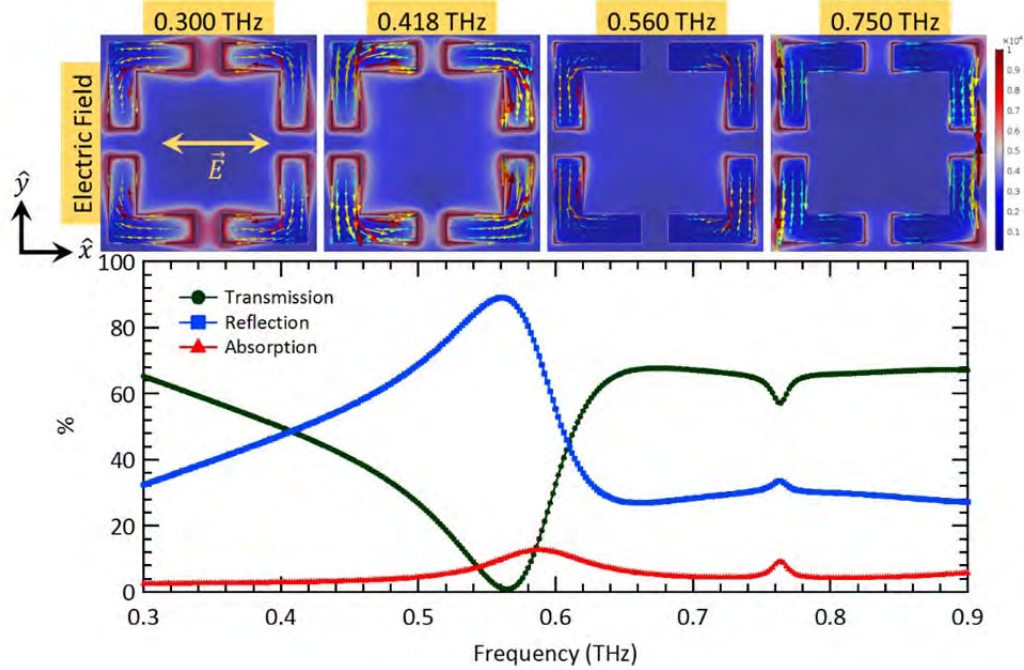


Figure 2. Finite element based simulation results of the symmetric metamaterial performed using COMSOL. Top plots are the e-field and surface current distribution plots at various frequencies. Bottom plot shows the transmission, reflection and absorption spectra of the device.

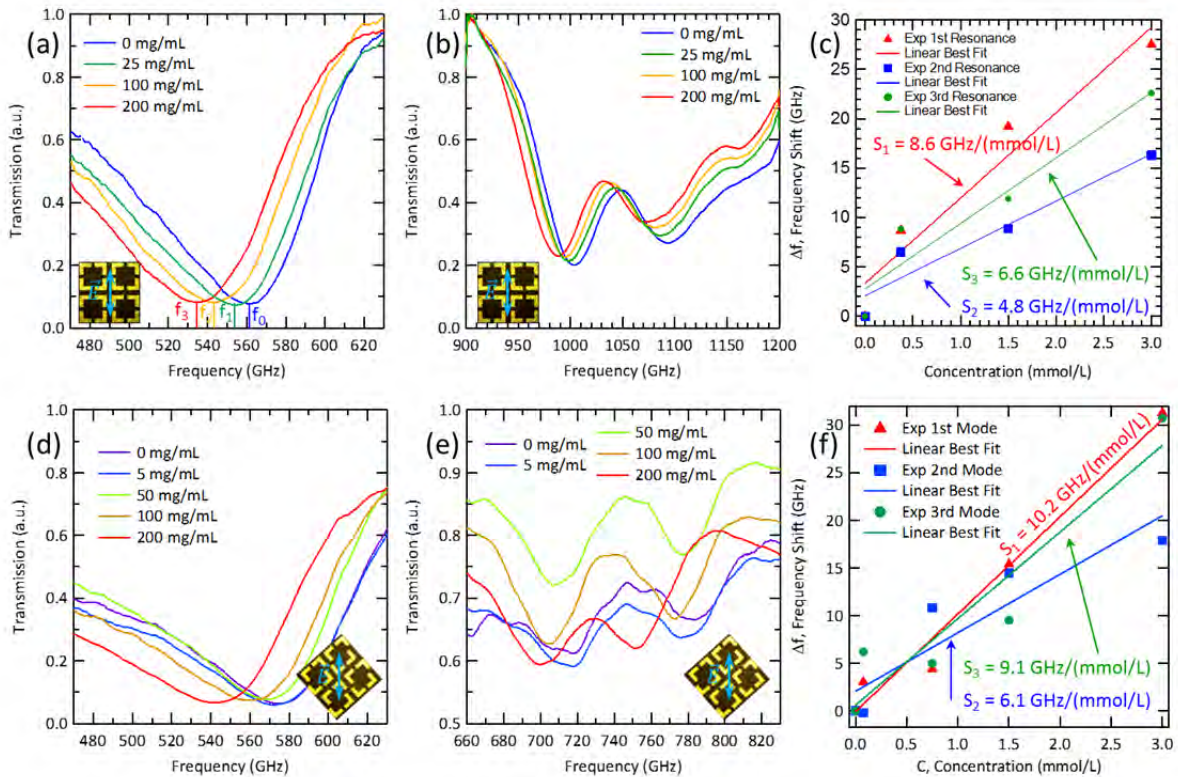


Figure 3. Experimental results for the symmetric (top) and the asymmetric oriented at 45 degrees (bottom). Devices were fabricated on KaptonMT (gold).

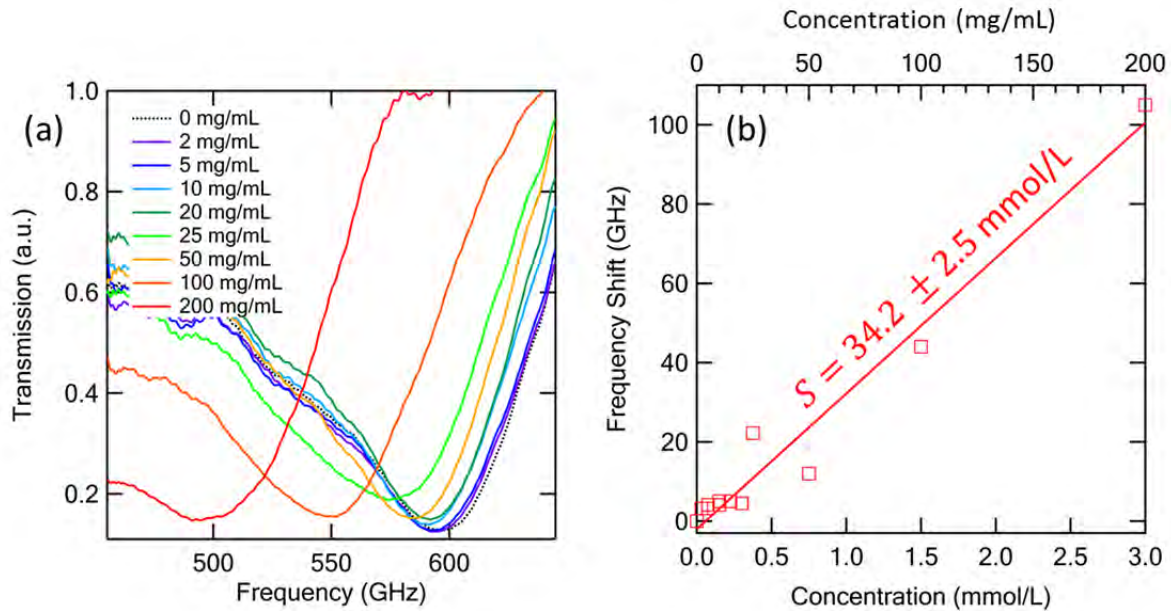


Figure 4. Experimental results for the symmetric device fabricated on KaptonB.

Acknowledgments

This research project was made possible by funding from the Department of Physics, the Department of Electro-Optics and Photonics at the University of Dayton, the Ohio Space Grant Consortium, and the Air Force Research Laboratory. The author would like to acknowledge assistance and support of his project advisors, Drs. Jay Mathews and Imad Agha. Additional thanks would like to be extended to Drs. Thomas A. Searles, Andrew Sarangan, Joseph Haus, and Karolyn Hansen for support and stimulated discussions. Last but not least, the author would like to thank his colleagues Gary Sevison, Thomas Iverson, John Hennen, and David Lombardo for daily fruitful scientific discussions.

References

1. R. Singh, I. A. I. Al-Niab, M. Koch, and W. Zhang, "Asymmetric planar terahertz metamaterials," *Opt. Express* **18**, 13044 – 13050 (2010).
2. S. Wang, L. Xia, H. Mao, X. Jiang, S. Yan, H. Wan, D. Wei, H.-L. Cui, and C. Du, "Terahertz Biosensing Based on a Polarization-Insensitive Metamaterial," *IEEE Photonics Technology Letters* **28**, 986-989 (2016).
3. R. S. Penciu, K. Aydin, M. Kafesaki, Th. Koschny, E. Ozbay, E. N. Economou, C. M. Soukoulis, "Multigap individual and coupled split-ring resonator structures," *Opt. Express* **16**, 18131 (2008).
4. R. Yahiaoui, S. Tan, L. Cong, R. Singh, F. Yan, and W. Zhang, "Multispectral terahertz sensing with highly flexible ultrathin metamaterial absorber," *Journal of Applied Physics* **118**, 083103 (2015).
5. J.F. O'Hara, R. Singh, I. Brener, E. Smirnova, J. Han, A. J. Taylor, and W. Zhang, "Thin-Film sensing with planar terahertz metamaterials: sensitivity and limitations," *Optics Express* **16**, 1786-1795 (2008).

Insulated Concrete Forms: An Energy Efficient Building Solution

Student Researcher: Anthony J. Cancian

Advisor: Dr. Trent Gages

Cuyahoga Community College
Construction Engineering Technology

Abstract

One of the lesser known building materials used in the construction of walls and/or floors is called Insulated Concrete Forms. In the building world, this procedure is known by contractors and designers for costing more money and providing future cost benefits, but the typical home buyer or business owner may not be aware of exactly how they can benefit. Insulated Concrete Forms (ICF) are a type of building material used in construction of residential homes and low-rise commercial buildings. ICFs are stay in place concrete forms that replace traditional plywood formwork. They are constructed of 2 pieces of EPS foam joined together by a system of plastic webbing. The foam pieces provide an R-value of 20 or more, based on 2.5" of foam, and act as a thermal break which prevents thermal transfer through the conductive concrete. This translates to a more efficient building envelope, saving the owner money on monthly heating and cooling expenses. In addition to the energy benefits, ICF also reduces construction time and enables construction during the cold season.

Project Objective

My objective is to find a measure of just how much a person can benefit by building their home out of ICF rather than traditional formed walls, or even wood framing. What are the up-front savings and what are the cost savings over time? What makes ICF a better choice?

Methodology Used

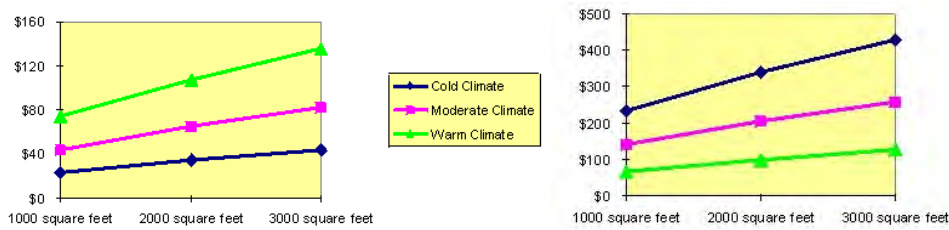
I sourced a couple internet sites that specialize in this material, but my most valuable source came from a personal communication with Paul Kaczanowski from Logix Insulated Concrete Forms Ltd. He is a professional in the field and offered his input into my studies.

Results Obtained

Since the R-value of a wall varies depending on the thickness of the wall and what it is made of, it is difficult to compare ICF with others. When discussing traditional frame walls, the problem area is the thermal bridging of the wooden studs as well as gaps in the insulation. Any concrete format has essentially no R-value at all. Concrete walls are considered mass walls because they are a heat sink (they will absorb heat and release it slowly). When concrete is sandwiched between EPS it acts as a collector and the thermal mass now serves to enhance the insulating properties of the composite wall. Wood framed walls are only as efficient as the insulation that is installed in the cavity or on the exterior of the wood studs.

Initial up-front costs can vary. Some influences could be the cost per yard of concrete, prevailing wages for all applicable trades and type of ICF that is being used are the largest. But ultimately the ICF does cost more up front, the pay back comes when heating and/or cooling season begin and the energy bills are reduced. A good average percentage would be that the ICF cost 10 to 20% more.

Savings over time is difficult to quantify because of several factors. A couple examples would be the number and type of windows and doors used in the structure, or the R-value of the insulation in the roof. ICF has delivered measurable results as follows:



Significance and Interpretation of Results

Building “Green” has become extremely important as people and organizations have insisted that we take better care of our natural resources (as they should), and this has created measuring systems (LEED for example) that provide industry guidelines and award those who build by their requirements. While building scenarios may differ, ultimately everyone realizes a long-term benefit. ICF construction reduces energy consumption and saves the owner money over time; two very important aspect of building in our modern era.

References

1. Project. (n.d.). Retrieved December 20, 2016, from <http://forms.org/content.cfm?act=energysaving>
2. Installer Advantages. (n.d.). Retrieved December 20, 2016, from <http://logixicf.com/advantages/logix-icf-advantages-installer>
3. Kaczanowski, Paul. (2017, January 17). Logix Insulated Concrete Forms [E-mail from].

Finding the Source of the 60 Hz Interference in an Electromagnetic Guitar Pick Up.

Student Researcher: Julian L. Casey

Advisors: Professor Doug Bradley-Hutchison and Professor Jessica Hendricks

Sinclair Community College
Electrical Engineering

Abstract

A common complaint amongst guitar players is a 60 Hz “hum” that comes through the guitar amplifier. By locating the causes of the 60 Hz sound a process can begin to find a way to reduce or eliminate the sound from being picked up. From the information gathered during this project, it can then be applied to other forms of electromagnetic pickups. In turn allowing the discovery of ways to more efficiently use pick-ups.

Materials

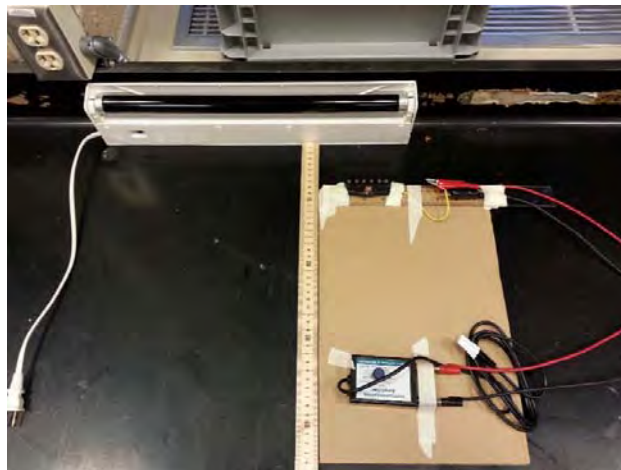
Generic passive guitar pickup, several straight edge measuring gauges, fluorescent lamp, Guitar amplifier, instrument cables, laptop with logger pro, microphone sensor and an mV sensor as seen below.



Methodology

In order to make the test run smoothly and consistent a platform was constructed that mounted the passive pickup in a fixed position. The platform was large enough to allow the pick up to be moved near a source without the operator interfering with the result. It turns out that if your hand is within 4 inches of the pickup, the voltage output became a sine wave.

The platform was constructed from a 0.125-inch-thick piece of cardboard mounting the pickup as well as the mV sensor. In order to insure straight movement and accurate distance measuring a large wood measuring gauge was securely mounted to the test bench. An additional plastic gauge was mounted on top of the rule to mark an accurate 0.00 mm reference point. The fluorescent light was mounted to the test bench and used to generate an interference that the passive pickup could receive. With the fluorescent light on and a starting position of the platform where the pickup had an output reading 0mV, the platform was slowly moved towards the light showing the effect of interference that the light generated. Voltage measurements were taken at 5mm intervals and plotted into logger pro to generate a distance vs voltage graph.



Voltage measurements were taken at 5mm intervals and plotted into logger pro to generate a distance vs voltage graph.

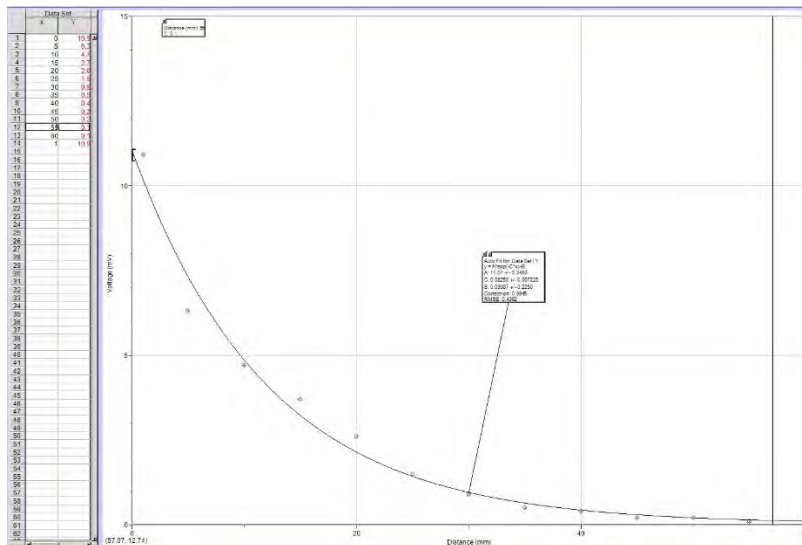
After finding data that suggests that a passive pickup can receive a signal from an outside source distorting the function of it, the focus of the project switched to finding the frequency that it is occurring on. With this in mind, an additional test was constructed using the above platform along with a guitar amplifier and microphone sensor. The passive pickup was wired to an instrument cable and ran through the amplifier simulating how it would be when a guitar is played.



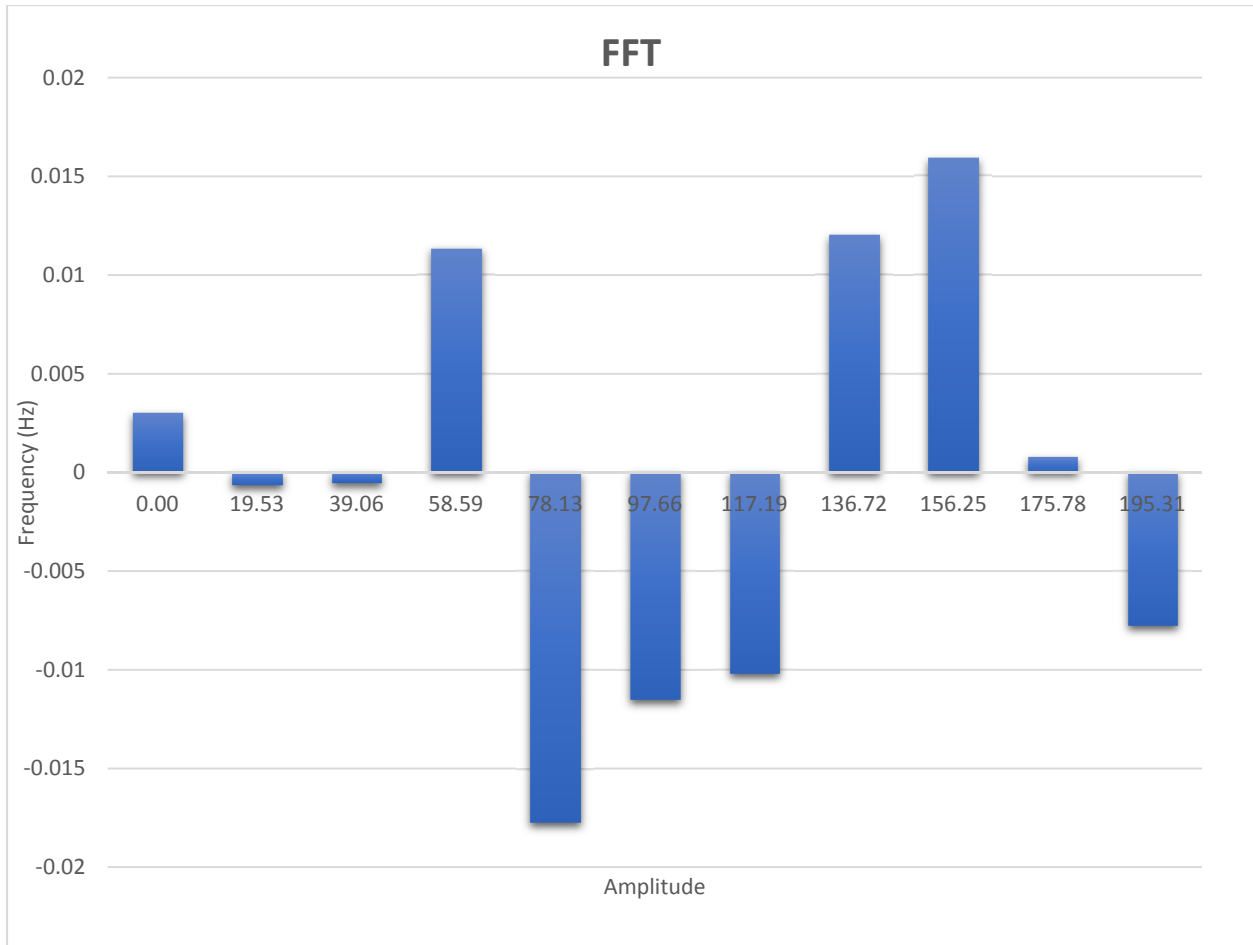
After many recordings were taken with light on and the pick up at the 0.00 mm distance from the light as an average data spread was calculated. This was done with the microphone sensor placed directly in front of the amplifiers loud speaker. With the use of logger pro a FFT chart was then created to represent the noise in a frequency vs amplitude chart. In order to make sense of this several recordings where done in the room with the light and amp off in order to calculate the back-ground noise in order to cancel it out. A chart was then created from the difference of the two conditions and it has shown that the interference lands on a 60Hz frequency as well as harmonic intervals from there.

Results

The data suggests that external sources have the ability to effect passive electromagnetic pickups. While testing the voltage received with the pickup it shows that moving close to an external source the pickup receives an exponential amount of voltage the closer you are.



Using the microphone sensor, it was able to show the frequency range that the signal was being produced on.



The FFT chart above shows that the frequency range that the pickup is receiving from the external source is primarily operating around 60hz as well as harmonic intervals of that.

Conclusion

Passive electromagnetic pickups show an ability to receive signals outside of what they are intended to. This is seen by the pickup receiving an outside voltage that produces a soundwave frequency creating interference in the instrumentation. If this experiment were to continue a wider range of sources would be tested and a more comprehensive FFT chart could be created. With this a better knowledge of the factors that create electromagnet interference would be developed and that would aid in finding ways to cancel out or eliminate the interference.

City of Cleveland Analysis of Crime to Income Relative to Police Stations

Student Researcher: Rosario J. Ceraolo, Jr.

Advisor: Bobby Oliver

Lakeland Community College

Department of Geography and Geospatial Technology

Abstract

The research project examined crime, income, and the relative location of the police stations for the municipality of the city of Cleveland. The information of crime was gathered from the city and the location of police stations was requisitioned from the county. The income information on median household income was gathered by the census. The information was analyzed on a census tract level for the year 2010. The Census gathers population data every ten years.

Crime is bound to occur within a city of nearly 400,000 residents plus visitors. Income can be regionally different amounts with different costs of living; however, with respect to crime it may be proportional. The location of police stations in high or lower income neighborhoods may deter or encourage certain types of crime or crime in general. Violent and property crimes are of different natures and may be affected by median household income of the area.

Objective

The objective of my research is to see if there is a direct correlation between where crime occurs with the respect of median household income with taking into consideration the location of police stations.

Methodology

This project was analyzed by using geographic information systems (GIS). The information used was collected by the city of Cleveland, Cuyahoga County, and United States Census Bureau. The information was distributed and provided by Case Western Reserve University, Cuyahoga county GIS department, and the Census website. The data provided had to be processed to display the results accurately and to be able to interpret the results. The year chosen for the project was 2010 for the municipality of the city of Cleveland. Crimes, population, and income that were measured on a census tract level is what was evaluated in this project. The crimes were examined as whole categories and specific crime types. The crimes examined were violent crimes categories, total violent crimes, illicit drug violations, and total property crimes. Mapping out individual crime types allowed me to see if there was one area that a certain crime touched or if all crimes shared common tracts. The crimes and income were mapped using a choropleth themed map to view the frequency of the crime and the amount of income for the year. The police stations and income layers were taken from a county level to a municipality level. The population layer was taken from the whole US to only include the tracts with in the city. Hot Spot Analysis (Getis-Ord G_i^*) tool is a Spatial Statistical toolbox (ESRI Arcmap) to analyze patterns of clusters. The analysis tool identifies statically significant hot and cold spots using the Getis-Ord G_i^* statistic. The tool categorizes its values on high, low, and average concentration to concise the map down to focus areas. This tool was useful because it highlighted the tracts and tract groups that were more likely or less likely for crimes to occur or had a greater or lesser average income. The information has to be layered in from foreground to background to ensure layers are seen.

Results Obtained

Downtown Cleveland was the main center of all crimes with a few outliers. The influx of crimes to the east or west of downtown varied depending on the nature of the crime. The population hot spot analysis map based on density shows the influx of crime happens in the more dense tracts. The income in the hot spots of the density map is neither hot nor cold. Based on the overall crimes, the population, and income the higher crime rates tend to happen in dense and average to low income tracts. The total violent crimes include domestic violence assault, robbery, homicide, aggravated assault, and rape. The other crimes viewed are liquor violations, illicit drug violations, and total property crimes. The crimes tend to be on the border on average to low income tracts. Domestic violence has higher rates in west Cleveland not following the location of total violent crimes yet following the middle range of income and population density. Homicide has only a few hot and cold spots around the city with not following general violent crime pattern. Robbery, aggravated assault, and rape have similar pattern that follows more of the total violent crimes which make up the core. Illicit drug violations were focus at the center of the city with a larger influx in north east Cleveland unlike any other crimes. Illicit drug violation crimes do follow the middle to low income surrounding the northern part of the cold area for income.

References

Cuyahoga County Open Data. Cuyahoga County GIS, n.d. Web. 16 Feb. 2017. <<http://data-cuyahoga.opendata.arcgis.com/>>.

Data Access and Dissemination Systems (DADS). "American FactFinder." United States Census Bureau. U.S. Department of Commerce, 05 Oct. 2010. Web. 16 Feb. 2017. <<https://factfinder.census.gov/faces/nav/jsf/pages/index.xhtml>>.

NEO CANDO (Cleveland and Northeast Ohio Indicator Data). Case Western Reserve University, n.d. Web. 16 Feb. 2017. <<http://neocando.case.edu/neocando/>>.

Wondrous Weather

Student Researcher: Ellie N. Conrath

Advisor: Dr. Sara Helfrich

Ohio University

Department of Teacher Education

Abstract

This lesson will be an introductory lesson to teach first-grade students how the sun warms the land, air and water. They will conduct several investigations, in groups of 3 to 4 and at rotating centers, that will lead them towards an understanding of this concept. The students will learn how to take measurements of water, air and land samples using an infrared thermometer. Conduct experiments using the scientific method, and use a hands-on approach to learn. The students will also use inference to build an understanding of the concept being taught.

Lesson

This lesson is designed to be an outside hour to an hour and a half lesson, set up in stations for students to rotate through. The students will be in groups of three to four people. This allows for students to work together and communicate to create a group consensus on what they notice at a given station. Students will have their science notebooks with them to write down any notes they feel would be helpful as well as what they notice at a given station. This lesson is meant to introduce students to the topic and is thus an open exploration with hands-on stations.

Each station will start with one or two groups, depending on one's classroom size. The stations are as follows; sun paper, water and land measurements, cardboard box solar oven and lastly, *Seeing the Invisible*. At the sun paper stations, students will be using wax paper, shaving cream, a few drops of yellow and red food dye, and a toothpick to mix together the food coloring into a circle or sun. The students will then lay their cardstock on top of the shaving cream and let it sit for a minute to soak up the coloring. When the paper is lifted off it will look like the burning surface of the sun. When they go to water, air and land measurements they will learn to use an infrared thermometer. They will use this tool to take measurements of samples of land and water both in the shade and the sun. Students will then go to the cardboard box solar oven. Each group will construct their own with the help of a teacher or a volunteering adult. When it is completed students will place four s'mores into the oven and use a timer to see how long it takes for the chocolate to melt and if possible the marshmallow to melt or brown. Lastly, at *Seeing the Invisible*, students will be given ultraviolet beads and a bracelet to put them on. Students will then conduct a section of a NASA lesson plan that has them complete a data sheet while observing what happens to the beads in different light.

After the lesson has been completed students will complete a prompt the next day, in the classroom. The students will spend time reflecting on their notes and writing a reflection on what they have learned, what they liked and disliked and their understanding of how the sun warms the land, air and water.

Objectives

Students will be able to explain that the sun can warm or cool down our land, air and water.

Alignment

The sun is the principal source of energy. Sunlight warms Earth's land, air and water. The amount of exposure to sunlight affects the amount of warming or cooling of air, water and land.

Resources

At the sun paper station, students will have a piece of wax paper in front of them and they will have an adult or teacher spray shaving cream onto the wax paper. They will then be allowed to add six drop of coloring to their shaving cream. It can be any combination they want of the red and yellow but only six drops altogether. Students will then use a toothpick to mix around the colors, blend them and shape the colors into a circle. Students will then use the paper and lay it on top of the shaving cream and let the color soak into the paper. Lastly, if needed students can use a piece of cardboard to scrape of excess shaving cream on their final picture. *At Seeing the Invisible* experiment #1, Students will create an ultraviolet bead bracelet to conduct a few experiments with and filling out the provided data sheet.

At the pizza box oven students, will use a cardboard box, aluminum foil, cling wrap, black paper and a stick to construct an oven to roast and make s'mores. Each s'more will be one half a graham cracker, a square of chocolate and a large marshmallow. Lastly, at land, air, and water temperature measurements station, students will take measurements of samples. The students will be using infrared thermometers to take the measurements. The samples will be of the ground around the playground, the air inside and outside the school and lastly of buckets, bowls or kiddie pools of water. The exact samples are up to the teacher and what their resources are at the time. =

Results

Due to the setup of my college program I was unable to test my lesson. This is a hands-on lesson so I am speculating that the students would have been highly engaged.

Assessment

The students would have been assessed by a prompt the next day. The students would be asked what they learned, what they liked and disliked and lastly how the Sun warms the land, air and water of Earth.

Conclusion

Although I was unable to implement the lesson in a first-grade classroom I believe that students would have been able to participate and be engaged in the lesson. Through the hands-on approach students would have been able to construct their own knowledge of what they think was happening and then discuss as a group what they thought. This helps students correct each other but in a non-threatening way. Lastly, assessing them with a reflection allows me to see exactly where a student has a misunderstanding, if there are any. =

Carbon Nanotubes Improvement of Granulated Activated Carbon as a Filter Media Abstract

Student Researcher: Chad A. Coolidge

Advisor: Dr. Regan Silvestri

Lorain County Community College

Department of Chemistry

Abstract

Carbon nanotubes have been grown on activated carbon and evaluated for use as filtration media. A novel process has been developed to grow carbon nanotubes whereby granulated activated carbon (GAC) is infused with catalyst, and carbon nanotubes (CNTs) are then grown with an alcohol precursor. The presence of CNTs was confirmed via SEM imaging and selected samples were further characterized by thermogravimetric analysis (TGA). Samples of activated carbon and activated carbon with nanotubes were evaluated for use as filtration media. Evaluation of the samples as filtration media was performed by testing for removal and recovery of various heavy metals via atomic absorption spectroscopy.

Introduction

Granulated activated carbon has been a media used for water filtration since the late 1800's. Carbon nanotubes are attributed to being discovered in 1991. Today there are multiple activated filters using various forms carbon (coal, coconut husks, nut shells). However, there are not as many for industrial applications and few, if any, where the contaminants can be recovered and the filter reused. One of the first goals was to repurpose coal for a more eco-friendly use. GAC alone has a large surface area. The idea of adding carbon nanotubes is not an attempt to merely add surface area but to create "fingers" of nanotubes that will be more effective in filtering of heavy metals.

Materials and Methods

Activation

A base product of sub-bituminous coal, activated at 950^oF, was received, ground and sieved to a specific particle size. This was then activated using a cartridge to suspend the 950^oF product allowed steam and carrier gas, nitrogen, to contact the maximum amount of surface area of the GAC. Water was injected for steam activation at a temperature greater than 1200^oF for one hour. After cooling, the product was weighed. Average weight loss was around 20-30%. All activated samples were kept in sealed containers to prevent the GAC from attempting to re-hydrate. It was discovered that keeping samples close to the activation state helped with nanotube growth.

Infusion

The newly activated material was then infused with a thin film of metals known to catalyze carbon nanotube growth. Multiple iterations of the infusion were tested before finding the correct amounts and composition for the infusion solution. During this process it was discovered that complete drying of the infused sample had an adverse effect on CNT growth quantity and quality.

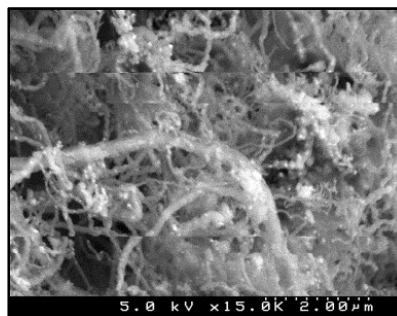
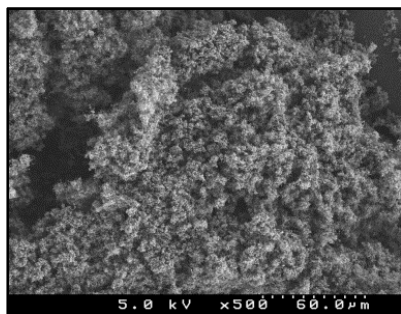
Growth

Using a Nanotech SSP-354, the GAC was placed on a quartz slide in a quartz tube in the furnace and growth conducted. As with the infusion, multiple alcohols were tested. The shorter chains produced no growth on the GAC. After many tests SEM imaging confirmed long chain alcohols worked the best for producing consistent growth of carbon nanotubes with the maximum coverage over the GAC particles. Experimentation showed there was a direct relationship between the temperature at which the GAC was activated and temperature used for growth. It was found the closer activation and growth temperatures were the better the growth. Shorter, faster alcohol injection times gave more amorphous carbon. Longer, slower injection times caused the sample

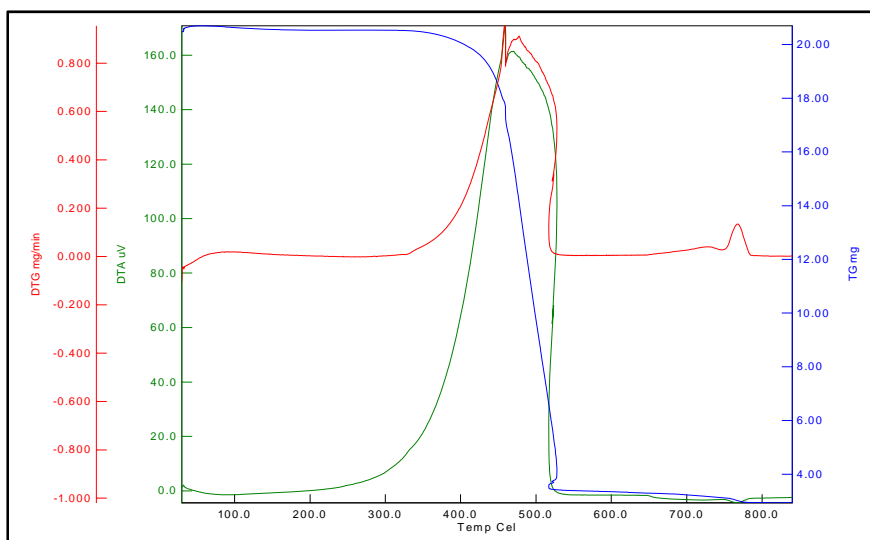
to cook the thin metal film off and decreased growth. SEM imaging was used to confirm growth and to measure nanotube length and width. Composition of the combined GAC/CNT particle was then categorized using thermogravimetric analysis (TGA). Finally, atomic adsorption (AA) and TGA were applied to test the adsorption of and the recovery from the combined particle.

Results

SEM Imaging showed thick forests of carbon nanotubes with unique shapes and structures.



TGA experiments were run to determine composition and purity of both the activated carbon and the activated carbon with carbon nanotubes. Below is GAC sample run in nitrogen gas.



Through atomic absorption spectroscopy it was shown the addition of CNTs to GAC improved the effectiveness of the particles in removal of zinc in solution.

GAC v. GAC with CNT Zinc Absorption				
	GAC		GAC & CNT	
Time	Final Concentration (mg/l)	% Removed	Final Concentration (mg/l)	% Removed
0	8.004		8.048	
20	5.957	25.57	0.032	99.6
30	2.084	73.96	0	100.0
40	0.680	91.50	0	100.0
50	0.492	93.85	0	100.0

Discussion

Unintentional and unexpected discoveries were made during the research and experimentation. One of the most important, but unfortunately not the first, was the relationship between activation temperature and growth temperature was important to optimize growth. Next was the infusion process. There was a lot of trial and error, along with SEM imaging, before a standard procedure for infusion and CNT growth was developed. In the end we found a solution that gave consistent results in terms of the amount of CNT mass added to the GAC. The type of alcohol used also changed the ability to grow and the quality of the carbon nanotubes. There were numerous iterations of infused versus not infused used with varied precursors before what is possibly the “sweet spot” was achieved. The addition of the nanotubes to GAC was in an effort to reduce or eliminate any possible water surface tension that may occur with the pores of the activated carbon. The nanotubes do improve absorption. Moving the project forward will require surface area analysis of the particle as it transitions from raw to final product. Testing of the adhesion of the CNT on the GAC particles will also be important if it can have industrial applications. One other important facet is the recovery of those metals once removed from the wastewater solutions.

Conclusion

The addition of carbon nanotubes “fingers” to activated carbon improves adsorption and allows the possibility of recovery for use in filtering heavy metals in industrial settings.

Can You Go the Distance?

Student Researcher: Hayley Crider

Advisor: James H. Tomlin

Wright State University
College of Teacher Education

Abstract

This multi-day unit called, "Can You Go the Distance?", covers principals of flight, including some materials from NASA, and some ideas I came up with. Students will learn the background on flight, and how the Wright Brothers created the first airplane. Students will master parts of the airplane that cause it to work together. They will also master the principals of flight that allow the plane to fly, and stay in the air for long periods of time. After they master those standards, they will design their own airplane out of a Styrofoam tray, milkshake straws, beans, tape, and scissors. This project will bring out the creative, and engineering parts of the student's brains. Following the design process, students will test their aircraft by measuring the distance it flies. The students will fill out their worksheet with the distance travelled, and calculate the speed of their aircraft.

Lesson

My series of lessons I created covers the topics of Principals of Flight, and how an aircraft is designed. I used some ideas out of NASA's unit lesson, "Right Flight", and I also added in my own ideas with ways to get the students intrigued, and to be able to understand the concepts they are learning. To give the students some background on planes in general the first lesson taught is about the Wright Brothers. After the video about the Wright Brothers the students will build a model of the Wright Brothers airplane out of candy. I think this is a fun introduction to all the things they will learn about aircraft.

Lesson two is the Design of the Aircraft. The students will make a six-door foldable, each fold will have a different part, and underneath will describe what it is. I know most students learn best doing hands on activities and creating their own study guides, so I think the foldable will be a fun way to learn these new concepts.

Lesson three is the Principals of Flight. Again, the students will make a four-door foldable and write the four principals of flight and what each does underneath.

Lesson four will bring out the creativity and brain power of the students. They will be given several materials, and told to build their own aircraft. Keeping in mind all the parts they learned, and the Principals of Flight. Remembering these things and looking back at their foldable will help them design an aircraft that will be able to fly! By creating their own aircraft with limited help, brings out the STEM concept in the lesson, students will fail, and then must try again. Failing is how we learn so it's very important students know it's okay to fail, they learn what to do, and not to do for it to work. They are using only their brains, and what they know about aircraft to make their own fly. After they have created their aircraft, there is a worksheet where they will measure the distance it flew, and the time it was in the air, then they will calculate the speed of their aircraft. This process engages the students, and helps them to strive to make the best aircraft possible. Once they finish their activity the students will feel accomplished, and proud of themselves that they each designed and built their own aircraft.

Students being proud of their work, and the educators praising them for a job well done is one of the most important things a student needs. These lessons and activities will be a fun and rewarding way for students to learn key concepts about aircraft and flight.

Development of a Haptic Joystick System for Human Interaction

Student Researchers: Michael C. Curtice and Lauren B. Pinder

Advisor: Dr. Augustus Morris, Jr.

Central State University
Manufacturing Engineering

Abstract

Haptics is derived from the Greek word haptikos, defined as “able to come into contact with”. A modern definition of haptics is “relating to or based on the sense of touch”. The field of haptics involves the knowledge of how kinesthetic interaction with the surrounding environment provides useful information toward improving human performance. Haptics can be involved with the improvement of human movement for artistic or athletic endeavors. However, haptics is more commonly useful in the areas of human rehabilitation and man-machine systems.

Research on man-machine systems investigates the physical limitations and control effectiveness of humans when interacting with or operating machine systems. Driving a vehicle, being part of a manufacturing assembly process, and remotely operating a first responder robot are all examples of man-machine systems. This research project will investigate the interaction humans have with a joystick type of device while performing a tracking task.

Project Objectives

The objective of this project is to utilize 3D modeling to assemble a Hapkit joystick assembly. This model will further assist us interpreting how Hapkits operate.

Methodology Used

There are many designs of haptic joysticks available. This project will utilize a popular open source device in kit form, called a Hapkit. The Hapkit is a one degree of freedom joystick driven by a DC motor and programmed to emulate the physical characteristics of conventional joysticks. However, the Hapkit can also provide sensations of touch or force otherwise not provided in virtual environments.

In the first phase of this project, a Hapkit will be built to interact with a compensatory tracking task viewed on a computer monitor. The Hapkit can be modeled through the computer to emulate a joystick with various spring constants, etc. The second phase of the project involves having human subjects performing the tracking task with the Hapkit emulated to having different physical characteristics. Data related to the tracking behavior and performance will be collected. Trends in how physical characteristics of the joystick affect tracking performance will be reported.

Conclusion

Currently the 3-D parts have been printed. The next step will be the assembly of the Hapkit and the programming of the microcontroller. Necessary hardware has been ordered in order to complete construction of the device. It is now understood that haptics is the sensation of touch and is used in technology within today’s society.

References

Dr. Augustus Morris, *Development of a Force Feedback Joystick for Manual Control Studies Based on a Novel Concept Using Magnetic Particle Brakes and DC Gearmotors*, 19 Mar. 2017.

"Build One." *Hapkit*. N.p., n.d. Web. 19 Mar. 2017.

Development of Formation Evaluation Program to Test Lithology Crossplot Hypothesis

Student Researcher: Charles E. Drennen, Jr.

Advisors: Professor Craig Rabatin, Professor Ben Ebenhack

Marietta College

Department of Petroleum Engineering and Geology

Abstract

Following Ben Ebenhack's development of the theoretical effective porosity vs bulk density crossplot, this study involves the development of a formation evaluation computer program that will provide various crossplots (including Ebenhack's) from raw well log data, while allowing the user to easily insert parameters to generate the desired plots. A colleague of Professor Ebenhack developed a FORTRAN 77 program to achieve this during his time in industry, and the objective is to develop a similar program viable for modern personal computers.

Such a program will be useful to petroleum engineers examining log data and students trying to understand how changes in the logs affect the crossplots. In addition to its usefulness as a general analytical and educational tool, the program will also display the elusive effective porosity vs bulk density crossplot. In a previous research project by Aaron Kurtz, this plot could not be fully developed when the data was highly influenced by gas effect and other natural sources of error. The attainment of this plot will enhance the petroleum engineer's understanding of the reservoir by displaying porosity and lithology in a novel way.

The methodology involves approaching the problem from two sides. First, using raw well data, attempts are made to recreate the program interface and graphing capabilities of the old program from verbal descriptions. The second arm of the approach involves combing through the FORTRAN code, specifically the clay, gas, and mineral effect corrections. By decoding these parts and comparing them to Aaron Kurtz's project, Ebenhack's lithology hypothesis will be tested. When finished, this formation evaluation program will not only provide a handy tool for students and log analysts, but also display the viability of the effective porosity vs bulk density plot as a potential new and interesting way to glean mineralogical information from well log data.

Project Objectives: The objectives for this project include reproducing a formation evaluation computer program capable of generating a variety of crossplots from raw log data and testing Ebenhack's effective porosity vs bulk density crossplot hypothesis. The computer program should have the same capabilities as the one used by Ebenhack's company in the 1980's, but work on modern computers. This means that the program must accept data from a spreadsheet and include calculations to create the various plots including Density Neutron (Figure 1), N vs Gamma, and a more reliable version of Effective Porosity vs Bulk Density plot (Figure 2).

Methodology Used: To delve into the project, learning FORTRAN became a necessity. *Introduction to Programming using FORTRAN 95* and a Silverfrost Plato compiler program were used to complete the exercises in the tutorial for familiarization with the language. This was sufficient to begin analyzing the old source code, since FORTRAN 95 is a more functional language that builds off FORTRAN 77. After careful review of Kurtz's research and attempt to replicate the hypothetical crossplot, the source code was searched for the clay, gas, and heavy mineral corrections. Kurtz believed these points were where

his program and the original differed. After uncovering the calculations to conduct these corrections, a program will be coded to display the theoretical plot and all other crossplots generally used for log analysis. This application may be created through Excel or programmed in another computer language. Results Obtained: In the current stage of the project, final results have not yet been obtained. Thus far, the student researcher has learned FORTRAN 95, an unfamiliar programming language. After this, a digital portion of the main program was reviewed for mention of density neutron plotting and corrections for clay, gas, and heavy minerals. Many lines of code were uncovered, and now the FORTRAN 77 subroutines for these sections must be decoded to find the more sophisticated correction calculations.

Significance of Results: Upon completion of this research project, Professor Ebenhack's hypothesis of the effective porosity vs. bulk density crossplot will be tested for viability as a useful tool to analyze mineralogy within an oil and gas well. This crossplot has only been used by Ebenhack in industry, and its validation would provide a new tool for well loggers. These findings will enhance the ability of petroleum engineers to glean more information from well log data and contribute new research literature to the well logging field.

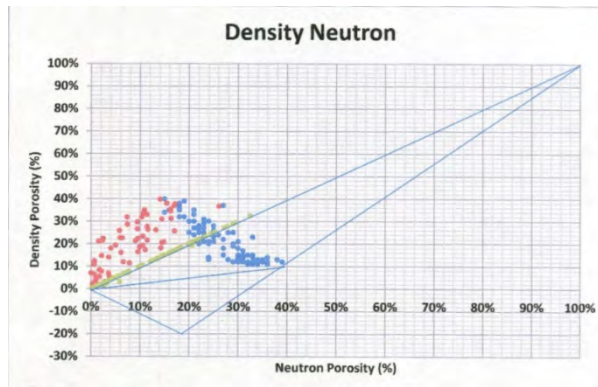


Figure 1. Density Neutron Crossplot (Kurtz 19)

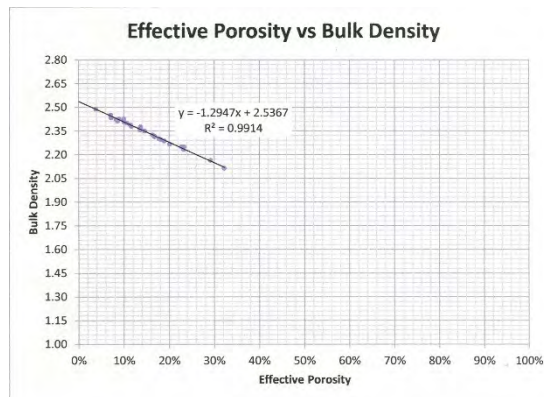


Figure 2. Effective Porosity vs Bulk Density (Kurtz from Ebenhack 21)

Acknowledgements

Ben W. Ebenhack; Associate Professor, Petroleum Engineering

References

1. Kurtz, Aaron. "Determining Mineralogy from Traditional Well Log Data". Marietta College: 2013. Print.
2. Ransom, Robert. *Practical Formation Evaluation*. John Wiley & Sons Inc., 1995. Print.

Design of Clothing Integrated with Circuitry to Regulate Body Temperature

Student Researcher: Solomon Ellison

Advisor: Professor Abigail Yee

Cincinnati State Technical and Community College
Pre-Engineering (Computer Engineering Focus)

Abstract

Traditionally “Performance Clothing” has worked to either retain heat from the body (Insulated clothing) or dissipate heat from the body. This has normally achieved body temperature regulation based on the molecular makeup of the materials alone; materials such as polyesters, or cotton, and sometimes poly-blends in an effort to achieve the desired goal. This basic reliance on the materials for temperature regulations present challenges. One of the major challenges presented is that the materials don’t allow a mechanism to increase or decrease temperature of the clothing itself, but rely solely on the body adjusting to the temperature and the construction of the clothing in order for regulation to happen. However, none of these options deal with actually “regulating” temperature with an option to vary the temperature depending on the desire of the consumer.

Project Objectives

The objective is to develop a multi layered shear suit that is very flexible (dry fit material) equipped with thin circuitry throughout the suit that regulates temperature variations. The suit must also be washable (able to withstand set number of washes before replacement), easy to charge (wireless charging capabilities), and equipped with a visual interface that is easy to understand.

Methodology Used

When looking at the construction of the suit, 3 categories have to be considered: Type of materials to use for the construction of the suit. How to multi-layer the suit, weaving the circuitry between the layers of the suit, while keeping it lightweight. What mechanisms to use in order to properly regulate the temperature of the suit.

The first thing to consider is the materials to use for the construction of the suit. The suit must be lightweight and very flexible and formfitting so as to achieve maximum functionality. Because the suit will involve sports application in nature, which will require a lot of movement and energy exertion, the materials will need to be very durable. I decided that the best material for this construction is a multi-layered polyester/rayon blend. This material is very flexible, and it already supports keeping the body warm and dry due to its construction.

For the multi-layered construction of the suit, it seems best to triple layer the garment in order to protect the circuitry of the suit. This includes the top layer, which is the layer visible to the person wearing the suit, the middle layer, which be the layer in which the circuitry is woven throughout the suit, and the back layer, which is results in a fully “sandwiched” layer of fabric that encloses the circuitry securely, while also protecting the user from direct skin contact with the circuitry and components.

The regulatory components of the suit are the most important part. These components are the what regulate the temperature of the suit. These include the Polyimide film, Lithium Polymer (Ultra Thin Battery), The PCM (Protection Control Module), and the Microcontroller. The Microcontroller is the main component out the four because this controls and computes the algorithms needed for the other three components to work. All of the sensors are contained in the microcontroller and allows the suit to transmit important information via a wireless chip onboard. It can also be programmed with other coding to allow different modes of functionality for the suit.

Results Obtained

Because the suit is in the concept stage, there are no results at this time. The next phase of this project is to being work on an official prototype of the suit.

LCC Parcel Ortho Mosaic Pixel Analysis to Identify Phragmites Plants

Student Researcher: Brett K. Enders

Advisor: Mark Guizlo

Lakeland Community College
Geospatial Technologies Program

Abstract

The purpose of the project was to identify invasive Phragmites plants here on the Lakeland Community College land parcel. By using remote sensing imagery and GIS analysis.

Methodology Used

Using 4 band 4" Ortho Mosaic imagery from 2014, clipped to the LCC land parcel. Then a reclassification of land use types using the national land cover database provided by the USGS. 60 classes were created and 4 land cover types were used to narrow down the land cover types here on the LCC land parcel. The 4 types are: 1- developed, open space, 2- developed, high intensity, 3- developed forest, and 4- a created type to represent Phragmites.

Results

The results obtained show likely spots of Phragmites growth. Then walking the likely spots I was able to ground truth and confirm their locations. The final result shows clear identification of the Phragmites plants. Also, red cars and the Phragmites plants appeared to reflect similar pixel values, tending to show more in the Near Infrared. As Phragmites has less chlorophyll that makes plants and trees to appear more red or green.

Conclusion

The project was a success in identifying how Phragmites shows up in relation to other land types. I feel that the use of more classes and land types would further help differentiate how this invasive plant appears, ultimately leading to easier identification and planning. The Phragmites plants usually reside along wetland areas, ditches, and fringe areas. Another conclusion was a surprise, that red cars within the parking lots were showing similar pixel values with the Phragmites plants. Both appeared in light blue and reflected similar outputs.

References (Data & Image Sources)

Lake County 2014 4" Ortho Mosaic Imagery, source data created by Pictometry International Company and Lake County GIS.

Background Image Source- Author: Johann Jaritz 21 Dec 2013

https://commons.wikimedia.org/wiki/File:Poerstshach_Halbinselpromenade_Phragmites_australis_21122013_745.jpeg

Image 1- US Army Corps of Engineers, Chicago District.

Image 2- <http://www.utahlake.gov/wp-content/uploads/2012/07/phrag.jpg>

Image 3- Photo by Randy Robertson <http://greatlakesphragmites.net/files/Phragmites-stands>

Image 4- Michigan Technological University

<http://cdn.phys.org/newman/csz/news/800/2012/followingphr.jpg>

Image 5- Photo by John Meyland <http://www.michigangardener.com/wp-content/uploads/Phragmites.jpg>

Modeling of a Bioinspired Water Filtration System: A Sustainable Approach

Student Researcher: Joanna A. Fadel

Advisor: Dr. Abinash Agrawal

Wright State University

Department of Biomedical, Human Factors, & Industrial Engineering

Abstract

The filtration, accessibility, and transportation of water is a challenge that affects both technologically advanced and under-developed countries. It is a necessity to all, but an efficient channel for the spread of disease and pollutants. Modern day water filtration systems seek to purify water, but may pose health risks of their own with the use of harsh chemicals to accomplish this task. This project seeks to use bioinspired methodology and biomimetic design to model a water filtration system, that utilizes sustainable processes, to produce drinking water out of waste water. The goal is to model this system with methods that can be used globally with decreased risk to human health and the environment.

Project Objectives

The goal of this project is to explore and assess various bioinspired mechanisms and their application in the filtration of polluted water. This project also attempts to offer preliminary models for a bioinspired water filtration system. These preliminary models come in the form of analysis on bioinspired techniques and a discussion on their potential applications in waste water treatment. This report does not only seek to give a literature study on the topic of bioinspired methods in regards to water filtration, but to also offer innovative connections between existing research in an exploratory way.

Water Pollutants

There are various pollutants in water that can make it unsafe to drink. Heavy metals such as zinc and arsenic serve as pollutants. Contaminants also include feces which carry disease causing bacteria and inorganic compounds such as nitrates and phosphates. Debris and industrial wastes such as dyes are likely contaminants, as well as many microorganisms. In the assessment of pollutant filtration methods, it is important to note the safe drinking water standards of these various pollutants to determine the effectiveness of the filtration method. Various guidelines for pollutants are stated in the World Health Organization's Guidelines for Drinking-Water Quality (Rosenboom, 2005). Chemical contaminants are sought to be reduced to the level specified in the guideline. Debris and disease causing microorganisms are sought to be completely eliminated from drinking water.

Current Water Filtration Methods

There is a lack in sustainable, efficient, and cost effective waste water treatment systems. Many people are without access to clean drinking water in developing countries and there are water contamination problems in many advanced countries as well. Current water treatment methods include the use of expensive synthetic coagulants (particularly aluminum-based) and chemical disinfectants such as chlorine that are impractical for use in developing countries, may compromise human health, produce large sludge volume, and greatly affect the pH of water when treated (Yin, 2010). Ultraviolet radiation and ozone are also used to disinfect treated water (Rosenboom, 2005), although they are effective, they are impractical for use in developing countries.

Nature's Mechanisms for Water Filtration

Nature has had 3.8 billion years to optimize the mechanisms behind water filtration, so it is intuitive to look to examples in nature to find sustainable methods for treating polluted water.

Phytoremediation

Phytoremediation is defined as “the use of plants and associated soil microbes to reduce the concentrations or toxic effects of contaminants in the environment” (Greipsson, 2011). There are four types of phytoremediation. This includes phytostabilization, phytodegradation, phytovolatilization, and phytoextraction. They each define different ways in which the pollutant is handled. Respectively, pollutants are either retained in the soil to avoid further dispersal, broken down into less harmful substances, converted and released as a gas, or accumulated in the plant’s biomass. Phytoextraction requires a continuous process of removing the biomass in which the pollutant is accumulated (Greipsson, 2011). An example of a plant with hyperaccumulation abilities is the ladder brake fern, which can accumulate high levels of arsenic in its fronds (Chen et al.; Indriolo, 2010).

Engineered wetlands use phytoremediation where water is treated and filtered naturally just by flowing from point A to point B through the rhizosphere of special hyperaccumulating plant species. Figure 1 depicts the phytoextraction of three different metals in regards to three different plant species. In the figure, species 1 is the hyperaccumulator of metal A, species 2 is the hyperaccumulator of metal B, and species 3 is the hyperaccumulator of metal C. This diagram shows how the flow of a fluid through the rhizospheres (root systems) of various hyperaccumulator plant species can filter out different contaminants. The Filter Component X in the diagram represents a general filter mechanism that can be used to disinfect the water or filter trace metals not captured during the phytoremediation process. This is a plausible system that can be implemented as an effective water filtration technique. Factors to consider in implementing this system are the metal accumulation rate of each species as well as the arrangement of species for optimized accumulation.

This method implements a step-by-step approach when dealing with multiple pollutants. Each pollutant is paired with a plant species that is specially attuned to alter the state of the contaminant or relocate it. This method is a system of solutions; to treat water it seeks to find a separate solution for the filtering of each pollutant and combining the solutions to make an effective system.

In addition to the previous approach, a region-by-region approach should also be taken into consideration. This implies that each region in need of water treatment requires that the system be specifically designed to cater to the pollutants present within that region.

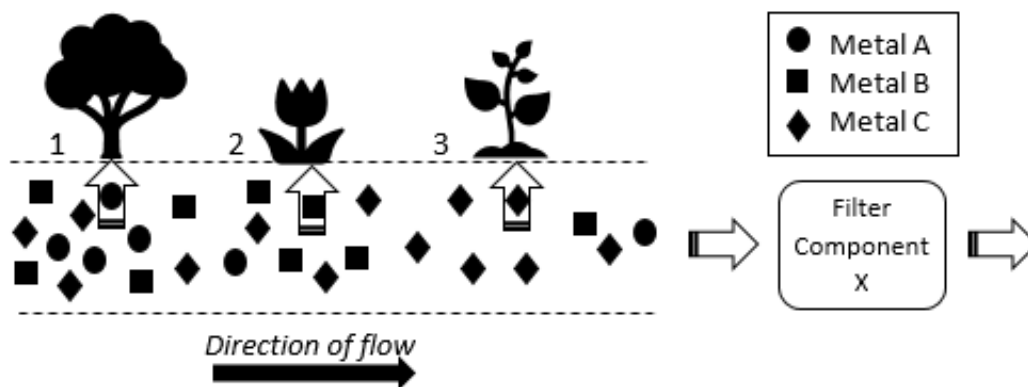


Figure 1. Phytoremediation of various metals

Hollow Fiber Bioreactor

Another bioinspired water filtration technique utilizes a bioreactor. Microorganisms naturally break down various substances and chemicals, some of which are considered pollutants in water. The purpose

of a bioreactor is to utilize microorganisms and their processes in a controlled environment to break down pollutants into less harmful substances. A new approach to the use of a bioreactor is to implement hollow fiber technology (Legazpi, 2016). Hollow fibers have microporous membranes and they are an efficient means to introduce air into the system. The microorganisms can thrive on the surface of these hollow fibers and the system would mimic a plant's rhizosphere where compounds are broken down and relocated. These microbes can be trained to acclimate to the food (i.e. contaminants in water) they are exposed to by mixing different cultures of microbes within the same system; those who can acclimate will live and reproduce more than those that cannot acclimate. Hollow fibers are an effective enhancement to a bioreactor system because they offer a high surface area to volume ratio which can be useful in providing more thorough filtration and aeration (Legazpi, 2016).

Plant-Based Coagulants

Plant-based coagulants are an effective technology for treating waste water in developing countries where elaborate treatment systems are lacking because they do not require expensive equipment or extensive methods. Plant-based coagulants are gaining popularity for their effectiveness and reduced health risks. The crushed seed of the *Moringa oleifera* tree serves as an effective coagulant. The seeds of this plant contain a positively charged protein that, when crushed and mixed in turbid water, stick to the negatively charged pollutants and sediment out (Jerri et al.). The driving force for this interaction is electrostatics. Most things in nature have a negative surface charge (i.e. pollutants). Due to electrostatic forces, the positively charged moringa protein is attracted to the negatively charged pollutants. Consequently, this combined clump of mass offers a difference in density with the surrounding fluid and sediments down. The moringa protein has another interesting feature within its structure. It contains positively charged glutamine contained in a helix-loop-helix structure that has a hydrophobic proline (Jerri et al.; Suarez, 2005). When attracted to the negatively charged bacteria, the hydrophobic protein acts as a "molecular knife" that penetrates the cell wall of the bacteria (Jerri et al.). This gives the *Moringa* coagulant antibacterial properties. It has also been proven to eliminate viruses and dyes in water, as well as reduce turbidity and sludge volume (Beltran-Heredia, 2009; Jerri et al.; Pritchard, 2009; Prasad, 2009; Suarez, 2005). The sediment moringa produces has the risk of providing microorganisms with food and increasing their growth in water, but Jerri et al. found that when the moringa seed is combined with sand, then the matter can be better filtered out rather than accumulated in the water.

Conclusion

Nature has provided many means in tackling water purification problems. This report has explored methods to model a system utilizing phytoremediation, a bioreactor coupled with hollow fibers to mimic root systems, and the use of plant based coagulants such as the seeds of the *Moringa oleifera* plant. These methods of water filtration provide a sustainable and effective way to attain clean drinking water out of waste water. Further investigation is recommended to produce effective filtration systems with optimal results using the methods discussed in this report.

References

1. Beltrán-Heredia, J., Sánchez-Martín, J., Delgado-Regalado, A., & Jurado-Bustos, C. (2009). Removal of Alizarin Violet 3R (anthraquinonic dye) from aqueous solutions by natural coagulants. *Journal Of Hazardous Materials*, 17043-50. doi:10.1016/j.jhazmat.2009.04.131.
2. Beltrán-Heredia, J., Sánchez-Martín, J., Delgado-Regalado, A., & Jurado-Bustos, C. (2009). Removal of Alizarin Violet 3R (anthraquinonic dye) from aqueous solutions by natural coagulants. *Journal Of Hazardous Materials*, 17043-50. doi:10.1016/j.jhazmat.2009.04.131.
3. Chen, T., Huang, Z., Huang, Y., & Lei, M. (n.d). Distributions of arsenic and essential elements in pinna of arsenic hyperaccumulator *Pteris vittata* L. *Science In China Series C-Life Sciences*, 48(1), 18-24.

4. Gonzalez-Perez, A., & Persson, K. M. (2016). Bioinspired Materials for Water Purification. *Materials (1996-1944)*, 9(6), 1-12. doi:10.3390/ma9060447.
5. Greipsson, S. (2011) Phytoremediation. *Nature Education Knowledge* 3(10):7.
6. Heredia, J., & Martin, J. (n.d). Removing heavy metals from polluted surface water with a tannin-based flocculant agent. *Journal Of Hazardous Materials*, 165(1-3), 1215-1218.
7. Indriolo, E., Na, G., Ellis, D., Salt, D. E., & Banks, J. A. (2010). A Vacuolar Arsenite Transporter Necessary for Arsenic Tolerance in the Arsenic Hyperaccumulating Fern *Pteris vittata* Is Missing in Flowering Plants. *The Plant Cell*, (6). 2045.
8. Jerri, H., Adolfsen, K., McCullough, L., Velegol, D., & Velegol, S. (n.d). Antimicrobial Sand via Adsorption of Cationic *Moringa oleifera* Protein. *Langmuir*, 28(4), 2262-2268.
9. Legazpi, L., Laca, A., Collado, S., & Díaz, M. (2016). Diffusion and Inhibition Processes in a Hollow-fiber Membrane Bioreactor for Hybridoma Culture. Development of a Mathematical Model. *Chemical & Biochemical Engineering Quarterly*, 30(2), 213-225. doi:10.15255/CABEQ.2015.2207.
10. Ndabigengesere, A., Narasiah, K. S., & Talbot, B. G. (1995). Active agents and mechanism of coagulation of turbid waters using *Moringa oleifera*. *Water Research*, 29703-710.
11. Prasad, R. K. (2009). Color removal from distillery spent wash through coagulation using *Moringaoleifera* seeds: Use of optimum response surface methodology. *Journal Of HazardousMaterials*, 165804-811. doi:10.1016/j.jhazmat.2008.10.068
12. Pritchard, M., Mkandawire, T., Edmondson, A., O'Neill, J., & Kululanga, G. (2009). Potential of using plant extracts for purification of shallow well water in Malawi. *Physics And Chemistry Of The Earth*, 34(9th WaterNet/WARFSA/GWP-SA Symposium: Water and Sustainable Development for Improved Livelihoods), 799-805. doi:10.1016/j.pce.2009.07.001
13. Rosenboom, J. W. (2005). Guidelines for drinking-water quality, Volume 1: Recommendations, third edition. *Waterlines*, 23(4), 30.
14. Suarez, M., Haenni, M., Canarelli, S., Fisch, F., Chodanowski, P., Servis, C., & ... Mermod, N. (2005). Structure-function characterization and optimization of a plant-derived antibacterial peptide. *Antimicrobial Agents And Chemotherapy*, 49(9), 3847-3857.
15. Yin, C. (2010). Review: Emerging usage of plant-based coagulants for water and wastewater treatment. *Process Biochemistry*, 451437-1444. doi:10.1016/j.procbio.2010.05.030.

Tri-C's Extreme Green Experience

Student Researcher: Steven A. Fairley

Advisor: Professor Terry Webb

Cuyahoga Community College
Engineering Technology

Abstract

The three most important global resources are water, food, and energy. We are researching a potential eXtreme Green solution that can potentially optimize the world's water and food resources. EXtreme Green is a concept originally developed at NASA's GreenLab Research Facility where renewable, alternative, and sustainable techniques were researched and implemented. We are utilizing two portable, self-sustaining renewable ecosystems containing three plant species (*Lima camelina*, *Salicornia europea*, and *Salicornia subterminalis*). We are also investigating a climatic adaption technique by salinizing each ecosystem from freshwater to beyond seawater levels and only use *Poecilia* species fish (Freshwater Mollies) as a natural fertilizer to provide essential nutrients for the plants. We are conducting a 30-week study with a goal of developing reliable, portable, self-sustainable, renewable ecosystems that can be implemented worldwide. What is presented are the results of the first 24 weeks of the project and recommendations for adapting our ecosystem lessons-learned into future eXtreme Green Concepts.

Introduction

Fossil fuels have played a major part of greenhouse gases being released in the atmosphere. Greenhouse gases could generate the world's climate change. Researchers are looking for ways to have energy without increasing carbon emissions. Many actions are needed and new technologies will play a major role. The energy and carbon deployed on earth play a big role in the picture by families. Understanding that picture will help us play our part in shrinking our carbon footprint. Greenhouse gases absorb heat when they interact with sunlight. They are the reason earth has a climate. The atmosphere has a natural carbon phase. Carbon is the constructing block of life and animal life, woodlands and the sea have a natural carbon phase. Carbon levels relate very closely to global temperature. The natural atmospheric carbon ranges between 180-280 parts per million. The amount of carbon that is released into the atmosphere, since the Industrial Revolution has been enormous. Meaning the carbon cycle is becoming increasingly out of balance. The more greenhouse gases are emitted into the air, the better chance of temperatures on earth will rise. We have an opportunity to start making a difference in our atmosphere, because we have a better understanding of what is going on today. Our use of fossil fuels contains carbon that has been outside of the natural carbon cycle. Therefore, every time we use fossil fuels, we are increasing the amount of carbon that is in the active carbon cycle.

Project Objective

To utilize Tri-C Metro's Greenhouse to expose students to a hand on STEM project that provides real-world laboratory experience as well as applying the "DO NOT RULE" in extreme green concepts; one do not use fresh water, two do not use food crops, three do not use arable land. We hope to climatically adapt our ecosystem to saltwater levels and have these ecosystems replicated in STEM classrooms across the United States to promote eXtreme Green Concepts.

Methodology

Utilize two portable, self-sustaining renewable ecosystems containing three plant species (*Lima camelina*, *Salicornia europea*, and *Salicornia subterminalis*). One ecosystem is in freshwater and the other ecosystem we applied climatic adaptation techniques. Climate adaptation means to take a plant species, where we start at freshwater add salt gradually over a period until the ecosystem has the same amount of salt content as the ocean. *Poecilia* species fish (Freshwater Mollies) was used as a natural fertilizer for the plants.

Data Collection Instruments

The Ph. Levels were measured with an ECO Tester PH 2. The pH of an aquatic environment is important and is used to monitor safe water conditions. Most aquatic life cannot live below a pH of 5 or above a pH of 9. Once the normal pH range for an aquatic environment has been established, a rise or fall in pH can indicate chemical pollution. The pH of natural waters typically ranges from 6 to 9. The pH of marine waters is close to 8.2, whereas most natural freshwaters have pH values in the range from 6.5 to 8.0. Pure rainwater and snow have a pH around 5.6. As such, one needs to know what conditions are best for each tank and maintain the tanks acidity within the acceptable levels

The phosphate levels were measured with a Milwaukee MW 12 Phosphate meter. Measuring phosphate levels can be a very important tool in understanding the water quality of an aquatic ecosystem. Excess phosphates can lead to eutrophication where the ecosystem has extensive algal growth and lead to low dissolve oxygen levels. The water quality can further deteriorate when bacteria use up dissolved oxygen to consume dead algae, suffocating other aquatic life. Monitoring phosphate levels in an aquatic ecosystem can help identify and minimize possible sources of phosphates before they threaten the health of the ecosystem and its inhabitants.

The Temperature levels measured were with a Hanna Temperature 93510. Temperature fluctuations can cause physical stress to fish, which leads to disease. Colder temperatures typically cause stress while high temperatures will lower the water's dissolved oxygen content, killing the fish. An aquarium heater and thermostat are used to keep the water temperature of aquariums constant. Larger aquariums may need multiply heaters. Usually, the larger a tank is, the more stable its temperature. For example, it would take a 50-gallon tank much longer to drop in temperature than a 10-gallon tank would take. However, this is not true for rises in temperature, because the water heaters used in aquariums scale with the amount of water they need to heat up.

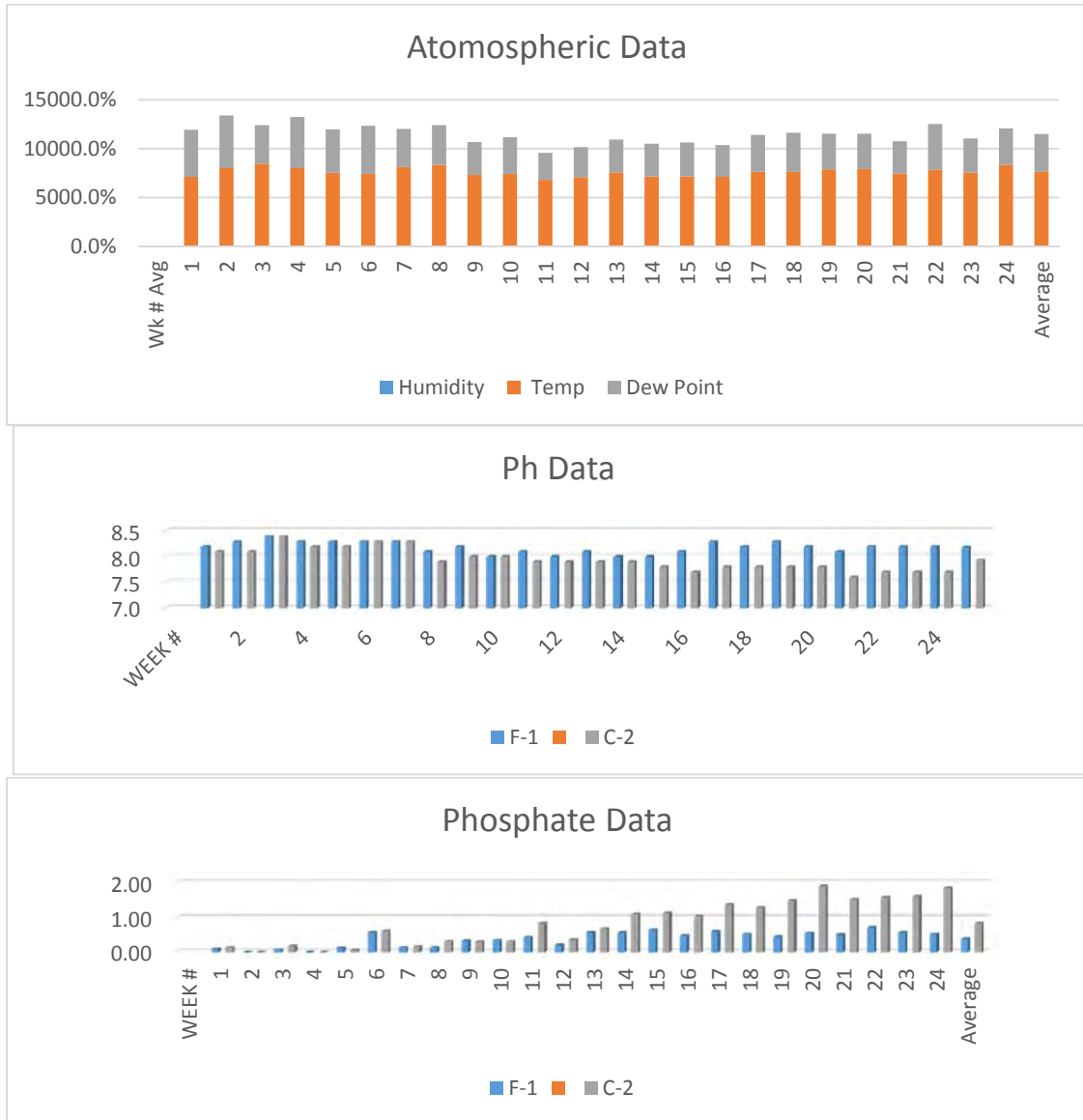
The Humidity and Dew Point levels measured ls were with the Humidity Meter by EXTECH. The dew point is the temperature at which air is saturated with water vapor, which is the gaseous state of water. When air has reached the dew-point temperature at a particular pressure, the water vapor in the air is in equilibrium with liquid water, meaning water vapor is condensing at the same rate at which liquid water is evaporating. Below the dew point, liquid water will begin to condense on solid surfaces (such as blades of grass) or around solid particles in the atmosphere (such as dust or salt), forming clouds or fog. Dew point is closely linked to relative humidity, which is the ratio of the pressure of water vapor in a parcel of air relative to the saturation pressure of water vapor in that the same parcel of air at a specific temperature. Relative humidity (RH) is expressed as a percentage.

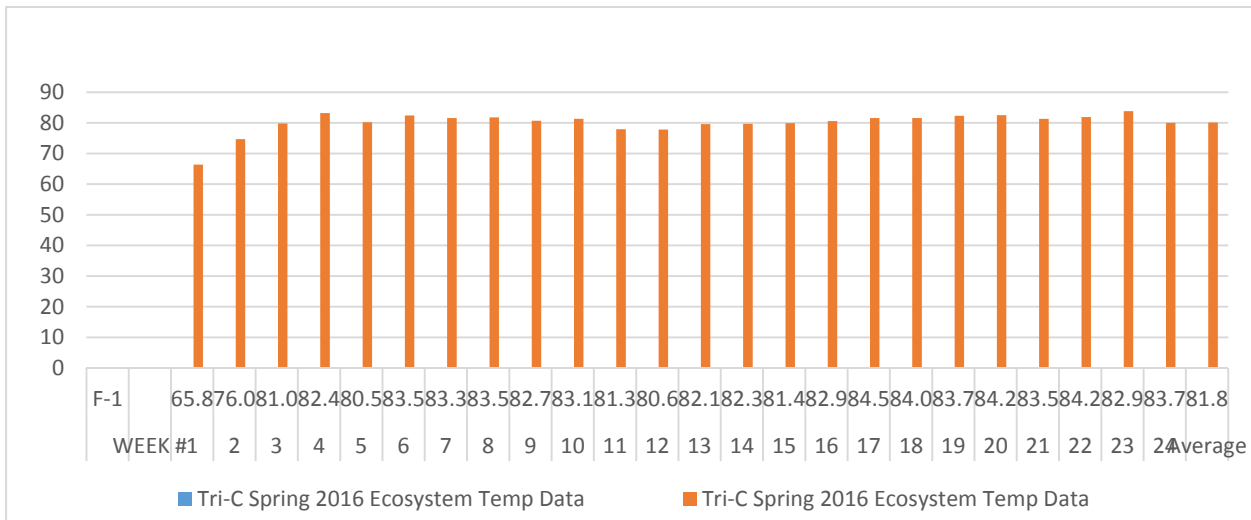
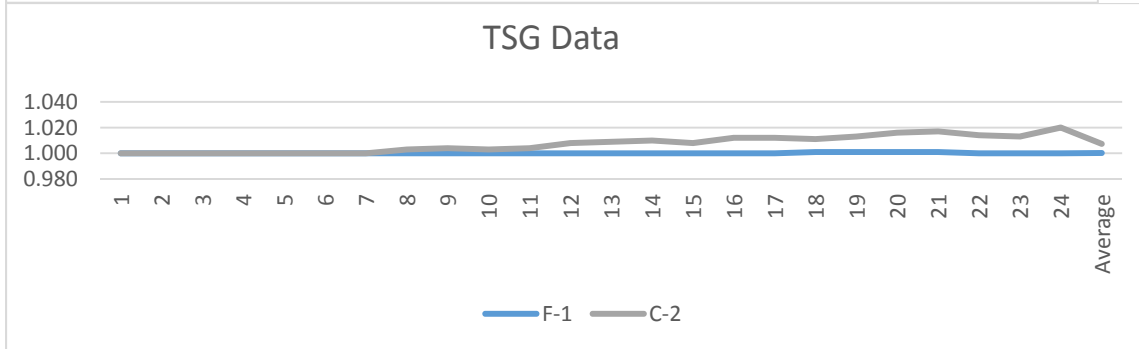
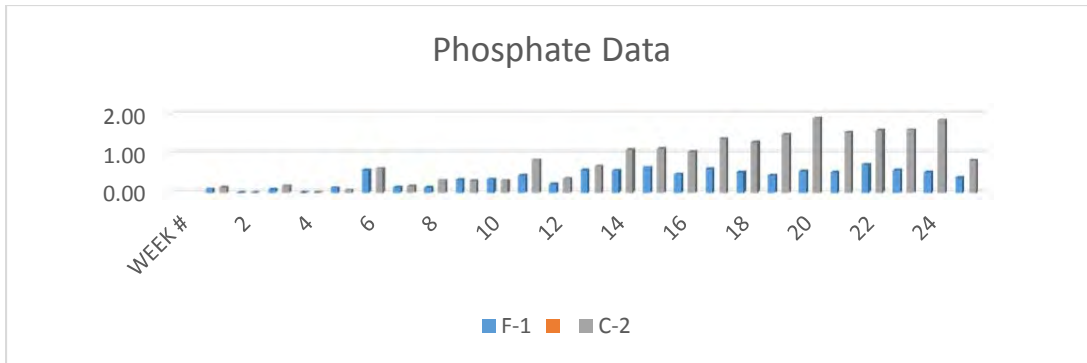
The TSG (True Specific Gravity) levels were measured with a digital refractometer. True Specific Gravity is measured in order to maintain a balanced ecosystem. The Green is dedicated to climatic adaptation from freshwater to seawater, monitoring and maintaining TSG is critical in order to make sure each tank has the right salinity level.

Observation

Initially there was no expectation of the study. There was no current evidence the three plants could in sand in an ecosystem. Also that *Poecilia* species fish (Freshwater Mollies) would be able to survive in water with the salt content of an ocean. The 24 week study proved that the plants could grow and the freshwater mollies could survive.

Figures





References

https://www.youtube.com/watch?v=7cJQ_8mwSew

https://www.youtube.com/watch?v=eCK_9TxR_q0

<http://nexsens.com/knowledgebase/article/10.htm>

Phosphorus: Sources, Forms, Impact on Water Quality: A General Overview, Minnesota Pollution Control Agency, 2007, <http://www.pca.state.mn.us/index.php/view-document.html?gid=8547>.

<http://animals.howstuffworks.com/pets/choosing-aquarium-equipment9.htm>

Salinity and Specific Gravity, Saltwater Aquarium Online Guide, 2007.

<http://www.saltwater-aquarium-online-guide.com/salinity.html>

Low Cost 3D Printing Using Vat-Free Photopolymerization

Student Researcher: Andrea L. Felicelli

Advisor: Dr. Jae Won Choi

The University of Akron
Mechanical Engineering

Abstract

Stereolithography, a process in which a 3D structure is formed by using light to cure and harden liquid polymers, is traditionally done using a vat to hold the polymer, photoinitiator, and additives needed to create the structures. This technique has several limitations, including its difficulty in producing structures with large horizontal areas and its lack of efficient use of photopolymer amounts compared to the structures formed. It's also limited by over curing and lack of depth control during the curing process. There is a possibility of replacing the vat used in the current technology with a "vat free" stacking mechanism using a liquid bridge, a common natural phenomenon generally formed between two solid bodies due to surface tension forces. This stacking mechanism can be implemented using two glass plates in between which a liquid bridge can be formed and maintained, and a 3D part can be cured within. The benefits of this approach include its simple configuration, material savings due to it being vat-free, and high-resolution layer formation.

Project Objectives

This research is based on previous work by an Akron PhD student on liquid bridge approach to microstereolithography (MSL). MSL has limitations when it comes to the fabrication process, many of which are increased by the traditional vat approach. Previously, a liquid bridge based microstereolithography was investigated as a means of improving the fabrication process of MSL. Our objective is to develop an LCD based MSL printer using the same liquid bridge technology. This printer would use an liquid crystal display panel with a backlight for generating light patterns and a liquid bridge formed between two glass plates. The expected cost of this printer is approximately \$500. The ultimate objectives of this project are to further understanding of the liquid bridge model in applications in 3D printing processes, and to make significant progress in developing a low cost, community accessible 3D printer using this model.

Methodology Used

A large part of this project centered around developing a design for this printer that met the four criterion: low cost, vat free using liquid-bridge, includes an LCD screen with LED light source, and simple enough for community accessibility. A schematic of the final drafted design is shown below in Figure 1. The main challenging components of this design were the z-axis, pump based design, LCD screen, and the restrictions of the liquid bridge itself. The z-axis was the most challenging aspect in terms of cost. Most prebuilt z-axes can cost upwards of several thousand dollars, especially for a precise, high-resolution application like MSL. To meet our low cost objective, it was decided to a from-scratch z-axis using a threaded rod and a micro-stepper motor for required high resolution. This significantly cut costs of this component and allows for movement as small as 20 μm .

As for the vat-free design, a pump syringe filled with liquid resin pumps a small amount of resin through a glass plate onto the print surface. Then, the z-axis moves the lower glass plate from its initial position touching the top plate, a distance of 3mm max, to form the liquid bridge. This is where the LCD comes into play. Our photopolymer resin needs light with wavelength of 470nm to cure. LED backlights have many wavelengths, including 470nm. Other wavelengths on the photopolymer may affect their curing. We solved this issue by incorporation a 470nm blue bandwidth filter over the LCD screen. Previously conducted experiments using water and a basic set up determined the maximum height an artificially created liquid bridge can hold is 3 mm. Past that, the bridge breaks, making it impossible to form a part within it. This limits the design to parts with maximum height of 3mm.

Status of Project

Currently, components are being accumulated to finish the construction of the printer, and a program will be written to control various components of the printer. Once the printer is constructed, we plan to conduct experiments using a water liquid bridge on the printer model to determine previously unknown limitations, as well as the performance of the printer. These experiments will also be conducted with our photopolymers that will be used to build 3D models.

Figures/Charts

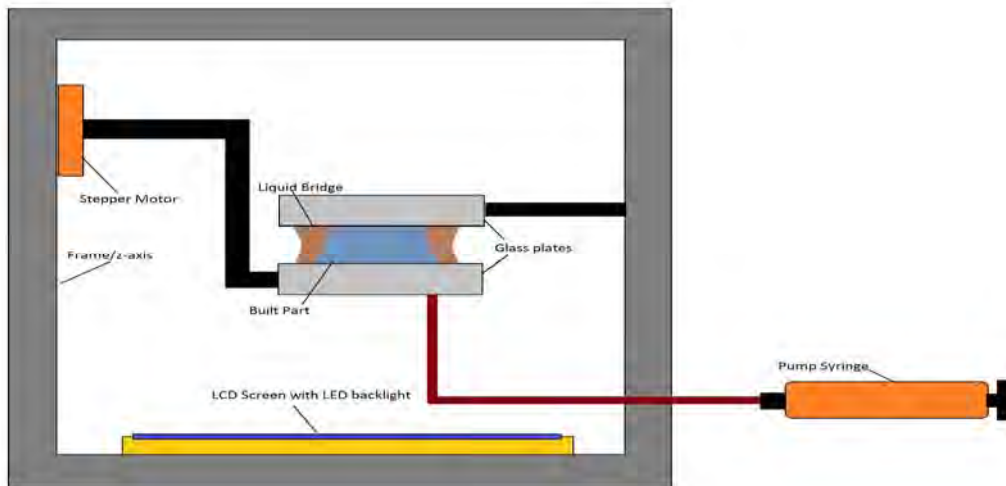


Figure 1. Low-cost MSL Printer Design Schematic

References

1. Yanfeng L., (2016) "A Study On Liquid Bridge Based Microstereolithography (Lbmsl) System", Doctoral Dissertation.
2. Yuan L., James E. S., (2016) "Capillary breakup of a liquid bridge: identifying regimes and transitions", Journal of Fluid Mechanics, Volume 797.

The Beginning of an Autonomous Robotic Hand

Student Researcher: Jeanette A. Gardner

Advisor: Professor Doug Bradley-Hutchison

Sinclair Community College
Electrical Engineering

Abstract

The study carried out was how electrical strain gauges could be used in the operation of a robotic hand that has the capability of sensing forces acting on it. A metal bar with strain gauges attached to the top and bottom was designated to represent a finger on the robotic hand. The strain gauges would be used to determine the tension and compression that occurred in the bar. The strain gauges were connected to a whetstone bridge circuit and the output voltages were measured with standard meters and a computer interface. The data collected from the computer interface can be used to recognize various "inputs", such as rubbing, pushing down and pulling up on the bar. The next phase of the study will be to create a computer program that can read the data from the computer interface.

Objective

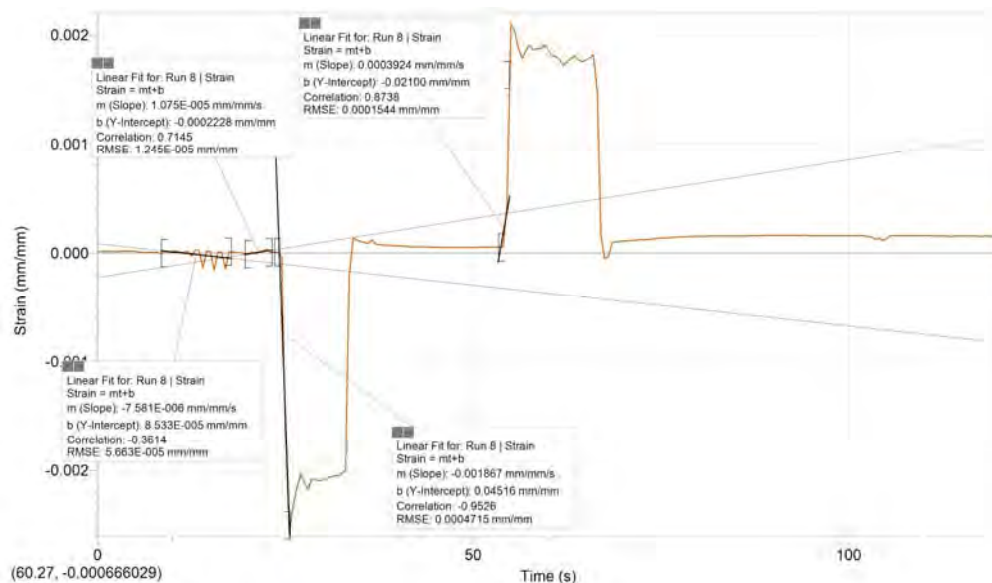
To create a robotic hand that can sense forces I needed to:

- Calibrate the strain gauges to be able to get reliable data that can be worked with
- Connect the strain gauges with a computer interface that can collect and graph the data collected
- Be able to interpret the data collected for the various ways the bar was manipulated.

Materials

- Vernier strain gauges
- Loggerpro software
- Aluminum bar
- Vernier bread board

Data



Conclusion

The conclusions that I have reached during this study has been quite insightful for when I fully build a robotic hand. The strain gauges tended to be very sensitive, meaning that they can be good indicators for when the material that the fingers are made of are no longer reaching the same equilibrium point from too much force being applied to the fingers. The strain gauges were able to pick up on different kinds of "inputs" like rubbing and bending the bar which the data collected could one day be used to program the hand to recognize if it applying too much or not enough force on the object it is holding, so that it does not break or drop the item.

Suggestions for Further Study

There are a few suggestions that I have to continue with this study. The first is to create a program that can read the data from the strain gauges through the computer interface and have it be able to tell the difference between the different kinds of inputs. The second idea is to find a way to connect multiple bars with strain gauges attached and be able to read them into the computer. The next phase after this suggestion would be to create a program that can read the data from all the strain gauges and be able to interpret them properly. Finally, would be to build the actual hand. The hand would have to be programmed to grip objects with the proper amount of force which it would be able to tell from the information being sent to it from the sensors.

Altitude Combustion Stand Low Power Thrust Stand Design, Fabrication and Integration

Student: Daniel G. Gerges

Advisor: Dr. Mounir Ibrahim

Cleveland State University

Department of Mechanical Engineering

Introduction

The Altitude Combustion Stand (ACS) at the NASA Glenn Research Center (GRC) is a one of a kind state of the art combustion research facility that is versatile and flexible enough to accommodate a variety of tests. The facility was initially designed to measure thrust of rocket systems that produced a large amount of thrust at different simulated altitudes. The ACS facility can accommodate a system that generates upwards of 2000 pounds of thrust at combustion chamber pressures of 1000 psia. Depending on the size, engines can be fired anywhere from a sea level altitude up to a simulated 100,000 feet altitude environment. One of the main objectives of the facility is to measure the thrust output of any given engine that it is testing. Built in 2009, the facility is fairly new, however, there are still some system issues that are being encountered on a daily basis and solutions are developed as they arise. One of the system issues/limitations that was recently identified was the need for the capability to measure thrust produced by low power engines. This issue was identified when a need to test “green propellant” engines became relevant. The green propellant engines in question produce thrusts in the range of 1N to 50N. This range is the equivalent of 0.25 pounds to 11.5 pounds. This quickly became an issue, since it is known that the lower limits of the current ACS thrust stand is about 50 pounds. Anything lower than 50 pounds tends to create a lot of distortion in the data and results become unclear. The reasons behind this problem will be investigated and discussed in the following report. The Design, Fabrication and Integration of a low thrust measurement stand for the ACS was assigned to the student and the progression of this project is the main topic of this report.

Project Objectives

The Altitude Combustion Chamber at the NASA Glenn Research Center is one of the nation’s newest and most versatile combustion testing facility. This facility is a valuable asset to GRC as it attracts national attention from government and private research institutions interested in testing new rocket engine technologies at different altitudes and with different propellant gasses at different temperatures. The flexibility of the facility in regards to propellant gasses, temperature control and pressure control makes it a unique facility with strategic resources that attract the multitude of customers. Some of the commercial applications of this stand include the following test subjects: Igniter concepts, Chamber/nozzle configurations, Ejector designs, integrated engine systems, engine performance studies and pulse and steady state firing behavior studies. In order to achieve the flexibility of this facility, there are many systems that have to work in unison in order to achieve the mission of the facility. One of the systems critical for the advancement of this facility is a low thrust measurement test stand that can extend the thrust measurement range into lower thrust readings.

Since the main focus of this study is the low thrust measurement test stand and how it interacts with the rest of the facility, only the main systems taken into consideration will be discussed in this paper. Other systems such as the cryogenic systems, cooling systems and fuel systems will not be discussed in this paper. The main systems to be considered for the purpose of this study will be the test stand and the vacuum chamber, in which the test stand will have to operate inside of.

The main objective of this project is to create a thrust stand that can measure thrust outputs lower than the current stand can measure. The current facility is only rated for a lower range of thrust output of 50 lbs. moving forward, Glenn Research Center would like to expand the capabilities of the facility to include lower ranges of thrust, as low as 1 N or 0.25 lbs of thrust. This would put the thrust measuring capabilities of the facility in the range of 0.25 to 2000 lbs, making it a very unique and impressive one of a kind facility! Seeing as this is a very large range of thrust output measurements, it is nearly impossible to be able to measure that range with one thrust stand. This is mainly due to the limits of thrust measurement devices and the sensitivity and stiffness of the current thrust stand. It is quite intuitive that a thrust stand designed to measure large amounts of thrust has to be structurally sound enough to handle the size of the engine. This robustness inherently stiffens the frame of the stand and makes it difficult to react to thrust produced by smaller engines. In addition to this, if the stand were to react to the thrust produced by a smaller engine, the load cell used on this test stand is not sensitive enough to register the thrust output clearly. This leaves us with the challenge of designing a more forgiving thrust stand with a sensitive force measurement devices for lower thrust ranges.

The low thrust measurement stand needs to meet a set of criteria to satisfy the mission goals. Of course the main objective is to accurately and clearly measure thrust outputs in the range of 1-50N. This is a critical capability of the project that must be met in order to satisfy the needs of the green propellant engines due for testing in the ACS facility mid-2017. In addition to this, this thrust stand must be fully compatible with all current systems in the ACS facility. The low thrust stand must be interchangeable with the current thrust stand, thus it has to be able to mount onto the same fixtures available at the ACS facility. Other requirements include calibration pre-test with minimal changes or movement of the stand. The stand must also be able to fully support the weight of test engines with no additional support or interferences. An important feature of the stand shall be the optimization of the damping ratio for the purpose of noise elimination without hindering the true thrust measurement. The optimization of damping is for the purpose of ensuring that there is minimal data loss and/or noise during pulse testing. The stand must be able to accommodate for pulse testing with frequencies ranging from 1-10 Hz and pulses lasting from 20 ms to 10 sec. Other considerations to keep in mind during the design process is the minimization of heat transfer from the engine to the test stand, as to not affect the measurement through material expansion and contraction.

Approach and Methodology

High thrust engines are typically measured with load cells. Since we are looking at designing a low thrust measurement stand, we have to consider low thrust producing engines. Typically, these engines are lighter and smaller, yet they still have a relatively low thrust-to-mass ratio. The design of this stand is very unique, as it is not used very often. Typically stands are designed for the typical high thrust engines, or very low thrust engines such as electric propulsion engines. This stand design will fall somewhere in the middle of this spectrum, making it more challenging to design, as it has to be sensitive enough, but not too sensitive either. In order to better understand how the stand must be designed to accommodate this need, we need to look at the characteristics and dynamics of a typical pendulum thrust stand.

Many characteristics of a pendulum thrust stand can be understood by studying two simple solutions of the equation of motion for an ideal pendulum. The equation of motion relates the sum of torques due to torsional springs, dampers and applied forces to the time rate of change of angular momentum of the pendulum arm as the thrust acts on it. The Equation of motion can be described as follows:

$$I\ddot{\theta} + c\dot{\theta} + k\theta = F(t)L$$

Where θ is the angular position of the pendulum arm relative to a specific position (for our case, it is easier to make this the equilibrium position). I is the moment of inertia, c is the damping ratio and k is the spring constant associated with the restoration forces. $F(t)$ is the force acting on the pendulum at a distance L from the pivot point. This is the force produced by the thrust in our scenario.

In the event that an active component such as an electronic damper is used on the system, the damping ratio becomes frequency dependent. In this case, we can re-write the equation of motion to accommodate for this:

$$I\ddot{\theta} + 2\zeta\omega_n\dot{\theta} + \omega_n^2\theta = F(t)L/I$$

And

$$\zeta = \frac{c}{2} \sqrt{\frac{1}{Ik}}$$

$$\omega_n = \sqrt{\frac{k}{I}}$$

Where ζ is the damping coefficient and ω_n is the natural frequency of the undamped system.

The guiding physical principals of a pendulum remain for the most part unchanged for an inverted pendulum. The primary difference between the two systems is the effect of gravity on the motion. In a hanging pendulum system, gravity acts as a restoring force, helping bring the system back to equilibrium. Essentially, a natural damper. In an inverted pendulum system however, gravity has the opposite effect, and acts as an additional torque on the pendulum, as it tries to bring it down to one side. The torque associated with the gravitational pull in the inverted pendulum is:

$$\tau_g = mgL_{cm}\sin\theta \cong mgL_{cm}\theta \text{ (Small Angle Approximation)}$$

In this equation, m is the mass, g is the acceleration due to gravity acting on the pendulum, and L_{cm} is the distance from the center of the mass to the pivot point of the pendulum. This can also be approximated using the small angle approximation for small deflection angles. The small angle approximation is typically valid for angles of 5 degrees or less with an accuracy of 0.13%.

Another issue that we have to deal with when considering an inverted pendulum is the fact that the torque inflicted on the pendulum by gravity must not exceed the spring torque. Otherwise the restoring force will be negative and the pendulum will be unstable. It is very important that the proper spring and support structure be designed correctly to ensure the stability of the inverted pendulum design.

Our equation of motion for a pendulum can be solved to give the response of the system to an arbitrary force input. There are three special cases with analytical solutions that are relevant for pendulum thrust

stands. The motion of the thrust stand subject to a torque produced by a constant force F_t from a steady state thruster applied at distance L_t from the pivot can be approximated. The deflection $\theta(t)$ normalized by the steady state deflection can be defined as:

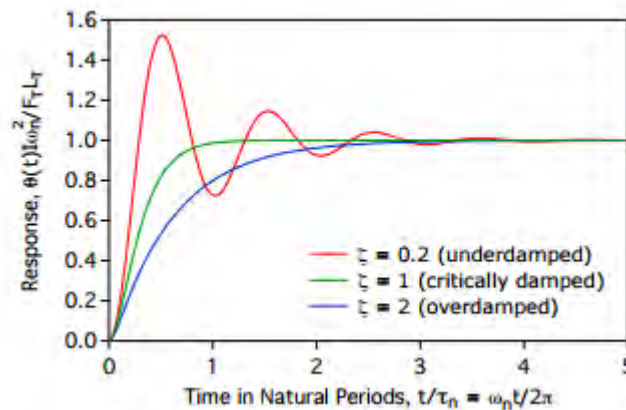
$$\theta_{ss} = \frac{F_t L_t}{I \omega_n^2} = \frac{F_t L_t}{k}$$

Dependent on the damping coefficient:

$$\frac{\theta(t) I \omega_n^2}{F_t L_t} = \frac{\theta(t)}{\theta_{ss}} \begin{cases} 1 - e^{-\zeta \omega_n t} \left[\cos(\omega_d t) + \frac{\zeta}{\sqrt{1 - \zeta^2}} \sin(\omega_d t) \right] & \text{for } \zeta < 1 \text{ (underdamped)} \\ 1 - e^{-\zeta \omega_n t} (1 - \omega_n t) & \text{for } \zeta = 1 \text{ (Critically damped)} \\ 1 + \frac{\zeta 1}{2\sqrt{\zeta^2 - 1}} \left[\frac{1}{d_1} e^{-d_1 \omega_n t} - \frac{1}{d_2} e^{-d_2 \omega_n t} \right] & \text{for } \zeta > 1 \text{ (Overdamped)} \end{cases}$$

Where $\omega_d = \omega_n \sqrt{1 - \zeta^2}$ is the frequency of the damped motion, $d_1 = \zeta - \sqrt{\zeta^2 - 1}$, and $d_2 = \zeta + \sqrt{\zeta^2 - 1}$

The time required to reach the steady state deflection depends on the damping coefficient and what type of damping it is. The graph below displays the different responses of the different damping types.

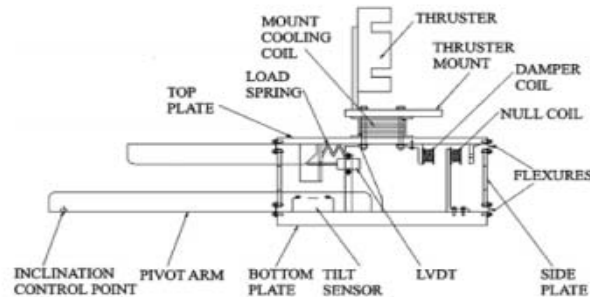


Using the knowledge discussed in this section, a few basic calculations can be completed to better understand the best damping ratio needed for a system of this sort. Through some iterative calculations and previous projects, it is understood that a damping ration in the range of 0.5-0.6 is ideal for this system. In this range of a damping ratio the system is in-between being critically damped and underdamped. In this range, the system is allowed some free oscillation in order to record the smaller forces that act on it, but at the same time it is still damped enough to be able to bring the system back to equilibrium. Having a system being underdamped will allow it to oscillate too much in response to any given force, creating a lot of noise data and making it hard to record the true thrust produced by any system. On the other hand, having a critically damped system will be too “stiff” and slow to any thrust response, especially in the lower ranges. This will prevent the system from recording those lower thrust data points, which would in turn negate the whole purpose of this project.

Since we have established the range of damping that we would like to be in, for the most part, all that is left to do is design and build a stand within these design parameters and fine tune it through a series of tests and experiments. We will use the theoretical knowledge to guide the design and work on improving it and idealizing it for the system it will integrate into. In the next section, the design, fabrication and testing parameters will be discussed.

Design, Testing and Fabrication Stage

The design of a basic inverted pendulum thrust stand does not vary much from stand to stand. Each system consists of the same basic subcomponents, but varies in the stiffness and damping ratios to accommodate for the types of tests that will be run. Each stand will consist of the base, which is the support structure or frame for the system. Inside the base, there will be 2 plates, a bottom plate and a top plate that are connected by flexures. The flexures are an important part of the design because they act as the springs of the systems. Depending on the thickness and material of the flexures, the desired spring constants can be achieved. The other important part of the stand is the damping coil. The damping coil is what helps the stand return to equilibrium in a reasonable amount of time, while also controlling how much noise and/or data gets filtered out. Every stand must also have a thrust measurement device. In our case, a Linear Variable Differential Transformer (LVDT) is most likely the best option for measuring the displacement of the pendulum, and therefore the thrust. Other components of the thrust stand include the engine mount and the mount cooling coil. Below is a Diagram of a basic inverted pendulum thrust stand.



Current Design Proposal

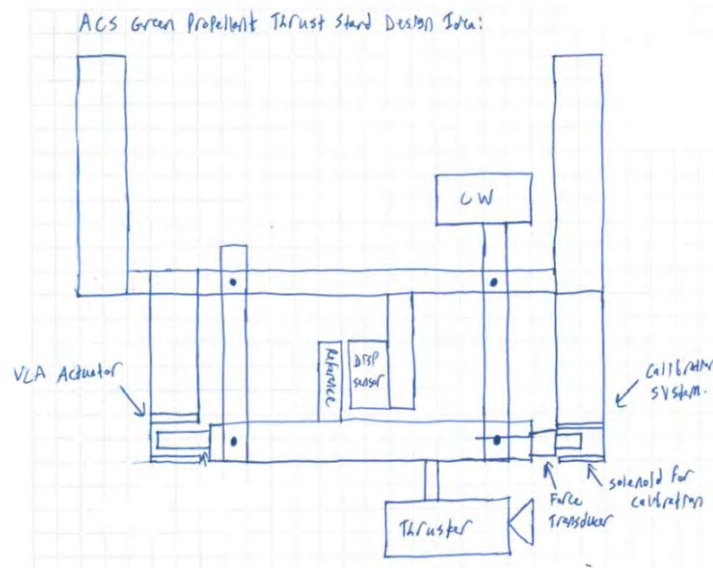
The first draft of an initial design, and the current design proposal under review, utilizes an electromagnetic high precision system to replace the traditional use of spring and damper mechanical systems. The proposed design uses an LVDT in conjunction with a Voice Coil Actuator (VCA) in a closed feedback loop to maintain the thrust stand in a null position. The thrust stand is maintained in a null position by the VCA providing enough force in the opposing direction of the thrust produced by the thruster. The VCA receives multiple distance readings from the LVDT at a high frequency rate and continuously corrects for the position to maintain a pre-defined delta, keeping the system in a null position. The voltage supplied to the VCA is proportional to the force it outputs, therefore the amount of force needed to keep the system null can be easily obtained as an output, and is equivalent to the force being produced by the thruster being tested.

VCAs are highly versatile and responsive devices that can handle impulsive changes quite well. The VCAs can also output displacements at a high rate, upwards of 100s of Hz. This makes it quite a good candidate for our thrust stand application, as it can adapt for pulse testing, with virtually no need for actual springs and dampers to help control vibrations created by the pulsing. The system would only be

limited in its response by the sampling rate of the LVDT and any present lag in the loop. This is an area of further investigation, however it is not expected that these factors will have a large impact on the response to impulse testing. From initial research, it is believed that the system will be fully capable of responding the pulse testing with minimal distortion in the data. In addition to this, vibrations due to the pulsing can be eliminated by correcting the stiffness of the stand through the use of flexures. A counter weight placed on top of the stand would also help dampen the vibrations caused by the impulse response.

Calibration of this proposed system would be quite simple and quick to execute. The idea would be to attach a force transducer to the opposite side of where the VCA would be located. This force transducer would be calibrated on a yearly basis to its rated force. At the beginning of each test run, the force transducer would be actuated, producing an acting force on the thrust stand. The LVDT would then sense a displacement greater than the set displacement and send a signal to the VCA to correct the displacement. The VCA would produce an opposite and equal force to place the test stand back into its null position. If everything is fully calibrated, the force produced by the VCA should be equal to or proportional¹ to the force produced by the force transducer.

Below is an initial “back of the napkin” hand sketch that demonstrates how the system would work:



Fabrication, Sourcing and Assembly of Thrust Stand Components

Fabrication of Thrust Stand Frame Components

Upon completion and validation of the thrust stand structure in solid works, it was time to break down the design into easily and cheaply Machin-able components. Each component was drawn separately in its own solid works file and an engineering drawing was created for each component so that the lab technicians can easily fabricate the parts to specs. Before handing over the engineering drawings to the

¹ If the VCA reads out a different measurement than the calibrated force transducer, then it should be proportional at a minimum. For example, if the force applied by the force transducer is 1N but the VCA reads 1.2N, then the calibration indicates that 1N of force will be read out as 1.2N. This should not be the case, as both devices should agree, however in the case this happens due to hysteresis or any other measurement inaccuracies, the VCA should at least be proportional to the force transducer reading.

technicians, tolerances were included and checked and an assembly of the components was created in solid works to ensure that they fit together. This was a very important step, as it ensures that all of the parts and pieces will fit together after being machined.

Sourcing of VCA and Solenoids

VCA Sourcing Parameters and Challenges

Once the drawings for the thrust stand frame were handed over to the technicians, it was time to spec and source the VCA and solenoids to be used on the thrust stand. There were multiple things to consider during the sourcing process of the VCA. Since this was the first time using such a device, lots of thought had to go into the technical specifications of the VCA. Such considerations included the stroke length, peak force and stall force of the VCA. In addition to the technical specification, the physical dimensions of the VCA had to be closely observed in order to ensure a proper fit onto the stand as well as proper clearance between the VCA push rod and the VCA plate on the stand. This dimension is of critical importance because if the VCA plate is too close to the push rod, it would cause difficulty for the VCA when trying to maintain a null position. This is because at a stroke close to “zero” the output voltage is lower, providing less power for the push rod to resist the thrust and maintain a null position. Inversely, if the VCA plate was too far from the push rod, it might not even touch the push rod, or if it does, the reading would be distorted as the VCA sensitivity would be lower than desired. The preferred positioning is for the push rod to be as close as possible to “mid-stroke” when it makes contact with the plate. At “mid-stroke” sensitivity is at its highest, allowing the VCA to sense and properly nullify any force within the resolution of the VCA. At “mid-stroke” the power output is also at a mediocre level, ensuring that the VCA has enough power to resist and nullify the force output from the thruster, but at the same time it is not too much power to the point of completely resisting the thruster output.

Solenoid Sourcing Parameters and Challenges

Sourcing of the solenoids posed similar challenges to that of the VCA, but with slightly more complications. The initial idea was to have 6 solenoids in total. 2 pairs that can provide 3 different thrusts for calibration purposes. The issue that this idea brought forth was that different force outputs meant relatively different sizes and lengths of the solenoid push rods. This would cause an issue with the positioning of the solenoid plate. A slight revision to the thrust stand design was implemented in order to help alleviate this issue; however, it still was not a perfect fix and allowed for only two different sizes of solenoids to work. Those sizes were the largest and second largest thrust outputs, leaving behind the smallest thrust output. The decision was made that this would be acceptable, but we ran into yet another issue. There was only enough room on the stand for 1 pair of solenoids once the VCA was to be installed. It was also discovered, after discussions with the NASA GRC Calibration lab started ensuing, that the solenoids could not be calibrated to the resolution we needed. In addition to this, the solenoids only had a force output accuracy of plus/minus 10% as per the manufacturer’s specifications. At this point, it was determined that the solenoids can no longer be used for an insitu calibration, but was decided to be kept as a VCA “health Check” mechanism to ensure the VCA is still responding during any portion of a test.

Future Works

In this phase of the project, we have a fully functional prototype that has proven that the VCA can successfully measure and counter-act thrust output from a thruster. The prototype has been run in both simulated test environments as well as real test environments. In addition to that, the system has been

“torture tested” through extreme conditions to ensure that under extraneous circumstances the thrust will survive and continue functions as intended with no harm to other systems or personnel.

- Completion of final prototype testing and review and design preparation for ACS Low Power Thrust Stand by May 2017
- Completion of fabrication of AVS Low Power Thrust Stand by July 2017

The above dates are the ACS Thrust stand milestones. On a personal note, as part of my commitment to the Mechanical Engineering Department at Cleveland State University, I have self-identified the following milestones:

- Completion of all necessary project requirements for the prototype along with completion of full design of ACS Thrust stand
- Completion of a final Master’s level report with details of design, fabrication and implementation of the Prototype stand and the completed and detailed design of the ACS Thrust stand.

Acknowledgments

Staying on track and being accountable has been a vital part of this project. I have been able to stay on track and stay accountable through weekly and monthly review meetings with the engineering staff here at the rocket lab as well as with my supervisor. I have received a tremendous amount of support so far during my time here with the space material and combustion group. In addition to this, I have received support and guidance from my College of Engineering Chair and Advisor, Dr. Mounir Ibrahim. His support and continuous push towards success have gotten me this far, and I am sure his continued support will empower me to accomplish all my goals for this Master’s Project.

Graphene and Energy Storage

Student Researcher: Amanda E. Gibson

Advisor: Professor Abigail Yee

Cincinnati State Technical and Community College
Pre-Engineering Program

Abstract

Energy production is a major contributor to the adverse effects inflicted by people on nature, something which scientists and engineers are seeking to correct. This will require massive changes to our energy infrastructure, therefore we must consider the practicalities of the existing technologies and the promise of new research. Renewable energy sources and electric vehicles are a path for the future, but require improvements in energy storage before they can be considered practical. Graphene is a recently discovered allotrope of carbon with a molecular structure such that it has many exciting properties, the exploitation of which could drastically change the field of energy storage. Despite some challenges, graphene has been shown to improve the performance of some batteries and supercapacitors. Many challenges are linked to defects in the quality of graphene when isolated during scalable production processes, but one recently developed method shows promise for eliminating this problem.

Objective

To identify the need for improved energy storage and summarize the challenges and promises graphene presents for these technologies.

Methodology

To identify the place of energy storage in the grid and its significance for renewable energy, I have drawn from the information presented in an extensive report from the National Renewable Energy Laboratory. Denholm et al. explain how renewable energies affect the grid and the potential applications of certain storage options in the future [1]. An article from the Brookings Institution explains the most promising batteries for electric vehicles [2]. A report from Raccichini et al. concerns the state of research involving different types of batteries and superconductors using graphene materials. They summarize graphene's properties and some production methods, as well as provide a thorough account of the results of some experimental batteries and supercapacitors incorporated with graphene materials as both an active and inactive component [3]. Finally, Ali Reza Kamali presents an experiment in which graphene is produced with an inexpensive and scalable method and is then used in the anode of an effective lithium ion battery [4].

Results

The introduction of renewable energies into the electric grid leads to difficulties in prediction and supplementation to meet the ever-changing demand [1]. Additionally, sometimes the renewables produce extra power when less is needed, and the emissions-free energy is curtailed and wasted [1]. In addition to other improvements in the grid system, energy storage is a method being considered to improve the incorporation of renewables into the grid [1]. Storage is also a concern for electric vehicles, a driving force behind the research of many batteries to develop a long-lasting, efficient, energy dense, and safe mechanism [2]. The top batteries being considered for this function are lithium-ion, solid-state, aluminum-ion, lithium-sulphur, and metal-air types [2].

Graphene is being studied in a large variety of technologies, including supercapacitors and various types of batteries [3]. It is a two-dimensional molecule consisting of six carbon atoms arranged in a hexagon, possessing fantastic electrical conductivity, high surface area, and is a potentially abundant resource [3]. It shows promise in playing a role in lithium-ion batteries (LIBs), as both an anode and cathode component [3], which can be applied to both the grid [1] and is favored for electric vehicles [2,4].

However, wider graphene proliferation is obstructed by its production method and certain technical issues within different devices [3]. The standard production processes that are considered economic and scalable result in graphene with defects, which can cause or exacerbate performance problems in batteries and capacitors [3]. For LIBs, anodes made of reduced graphene oxide show high initial capacities, but experience low Coulombic efficiency and energy storage after repeated cycles [3]. It seems to be more promising for LIB applications when used in the form of a composite, and as such this is an active topic in research laboratories around the world [3].

One example of results from this flourishing research comes from Kamali's work in which high quality graphene was produced from electrode-grade graphite within molten lithium chloride salt under an atmosphere of argon and hydrogen and an applied voltage [4]. This method is considered inexpensive, scalable, and environmentally friendly [4]. In his paper, Kamali uses this graphene product in a tin dioxide composite to produce an anode for a high performing LIB compared to those made with a standard graphite anode [4].

Significance and Interpretation of Results

For the field of materials science, the emergence of graphene is extremely exciting in many areas of research. Considering that graphene is a relatively new material, it shows great potential for use in energy storage devices like batteries and capacitors. Like many technologies in their infancy, there is still much to be discovered concerning how to harness graphene's properties, but it could play a significant part in the next and subsequent generations of energy storage devices. These improvements will be crucial to the transition of energy use in our nation and the world at large. For the major reduction of greenhouse gas emissions, it is imperative that renewable energies see greater penetration of the grid and electric vehicles become more affordable and attractive to consumers. Therefore, if an inexpensive and effective means to store energy can be derived from graphene in some form, it is worth exploring.

References

1. Denholm P, Ela E, Kirby B, Milligan M. The Role of Energy Storage with Renewable Energy Generation. National Renewable Energy Laboratory [Internet]. (2010, January), [cited March 27, 2017]. <<http://www.nrel.gov/docs/fy10osti/47187.pdf>>
2. West D, Karsten J. Five emerging battery technologies for electric vehicles. The Brookings Institution [Internet]. (2015, September 15). [cited March 27, 2017]. <<https://www.brookings.edu/blog/techtank/2015/09/15/five-emerging-battery-technologies-for-electric-vehicles/>>
3. Raccichinni R, Varzi A, Passerini S, Scrosati B. The role of graphene for electrochemical energy storage. Nature Materials [serial on the internet]. (2015, Mar), [cited March 27, 2017]; 14(3): 271-279. Available from: Academic Search Complete. <<http://www.nature.com/nmat/journal/v14/n3/abs/nmat4170.html>>
4. Kamali, A. Eco-friendly production of high quality low cost graphene and its application in lithium ion batteries. Green Chemistry [serial on the internet]. (2016, April 7). [cited March 27, 2017]; 18(7): 1952-1964. Available from: Academic Search Complete. <<http://rave.ohiolink.edu/ejournals/article/339397596>>

Computational Analysis of Pulsatile Flow in Abdominal Arterial Bifurcation Models

Student Researcher: Paul A. Goetze

Advisor: Dr. Jeong-Hoi Koo

Miami University

Department of Mechanical and Manufacturing Engineering

Abstract

A strong understanding of the human pulse profile is vital to the development of biomedical devices because accurate representations of the pulse must be used for training and simulations. Due to the fact that pulse profiles change with the body's health and age, the overall objective of this study is to determine what effects geometry variation of the abdominal bifurcation has on the blood profile. To accomplish this, simplified COMSOL models were created and parametric studies were done on several aspects of the geometry. These studies indicated that the bifurcation angle and radius at the split had a significant effect on the velocity profiles in the daughter branches and around the apex. These results will be incorporated into a more complex model that compares to a physical setup so that they can be validated empirically.

Project Objective

This study aims to experiment with bifurcation geometries to determine their effects on the blood flow profile. This is being done through the construction of both a computational and physical model of the bifurcation geometry. The computational model is being developed in the COMSOL Multiphysics Software where the fluid flow properties of the 2D geometry are explored. The physical bifurcation will be manufactured and used as an empirical comparison to the computational data. The goal is to validate the computational models developed with measured values created in the physical testing set up.

Methodology Used

The computational models created in the COMSOL software were developed so that parametric studies could be done easily. One model studied the laminar flow through the bifurcation, measuring the surface velocity and pressure profiles inside the geometry. In this model, the angle between the daughter branches and the fillet at the apex were varied parametrically. The angle sweep included values between 30 and 45 degrees and the fillet was varied from 0.05 to 0.15 in. In order to analyze the geometry, an input velocity flow curve was utilized that mimicked the human pulse. This was done with a periodic function developed for research done on aortas with a stenosis [1]. From this, point and surface plots were created to measure the velocity profile at certain locations in the daughter branches and around the bifurcation apex. These plots could then be used to compare different angles, radiuses, and locations within the parametric sweep.

The second model investigated material property variation through a Fluid-Structure Interaction Study (FSI) in COMSOL. This model utilized a singular geometry from the laminar flow study with a bifurcation angle of 60 degrees and a fillet radius of 0.100 in. Blood vessel walls and surrounding tissue were added to the geometry for this model so that material properties could be assigned.

The methodology used to create the simple bifurcation models were then utilized to create a more complex model that mimics a real world testing setup. This model incorporates both the laminar flows study and the material property investigation. The development of this computational model is ongoing.

Results Obtained

The parametric sweeps of the bifurcation angle and fillet radius within the laminar flow model produced velocity profile plots at locations within the daughter branches and around the apex of the bifurcation. These plots compared the different geometries and showed the effects on the velocity profiles.

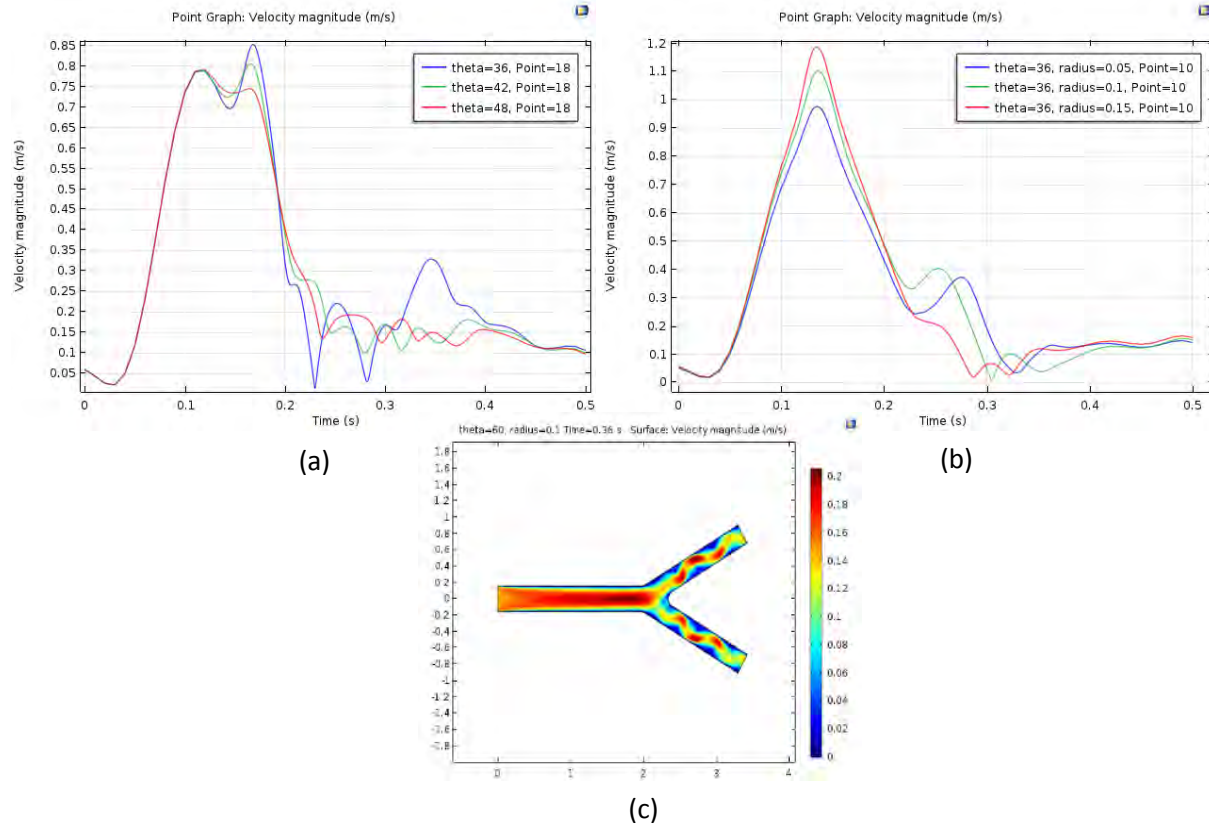


Figure 1. Velocity plots of (a) the changing bifurcation angle, measured in the daughter branch and (b) the changing bifurcation radius, measured immediately before the apex. (c) Shows a surface plot of the velocity magnitude @ 0.36 sec

The velocity plot of the changing bifurcation radius angle, shown in Fig. 1 (a), indicated that a second peak was present immediately after the initial peak at a certain location in the daughter branch. As the angle increased, the second peak became smaller in amplitude and closer in time relative to the first peak.

The velocity plot of the changing bifurcation radius, shown in Fig. 1 (b), shows the velocity profile measured immediately before the bifurcation apex. Again, there are two peaks present and the changing radius has an effect on the relative size and location of the peaks. As the radius increased, the magnitude of the first peak increased and the amplitude of the second peak decreased. Additionally, the second peak fell closer to the first peak in time as the radius increased.

The material property variation study through FSI produced results indicating that as the material stiffness increased, the deflection decreased as expected. This model is still being developed and is not fully functional. However, it may be used in the future to include blockages and stenoseds into the bifurcation geometry.

References

1. L Ying, L Xianwu, Z Mingkui, Z Yao, L shuhong and X Hongyuan, "Simulating the Blood Flow for the Aorta with a Stenosis", 4th International Symposium on Fluid Machinery and Fluid Engineering, 2008.

Determining the Minimum Distance Needed Between a Hip Implant and Knee Implant Using Finite Element Analysis (FEA)

Student Researcher: AlRitia J. Gore

Advisor: Dr. Brian Davis

The University of Akron
Biomedical Engineering Department

Abstract

The goal of this research project is to determine the required distance needed between a femoral fracture fixation rod and a knee implant. In order to find different stresses that occur between the beginning of a knee implant and the end of a hip implant, finite element analysis (FEA) will be used.

Project Objectives

The number of total joint replacements continues to rise at an ever growing rate, especially with an aging population^{3,4}, with total hip arthroplasty being the most commonly implanted prosthesis^{1,5}. With this also comes an ever growing patient population that has ipsilateral total hip and total knee arthroplasties². When a patient undergoes a knee replacement, there is a stem that typically protrudes proximally within the femoral intramedullary canal. In some cases, a patient who has undergone this procedure also suffers from a broken femur following a subsequent fall. In these cases, additional orthopaedic implants are needed to reconstruct the femur. The general rule is that the two implants cannot be closer than two cortical diameters^{3,5}. Spacing less than this is thought to lead to stress risers, although there is no quantitative evidence for this. The objective of this research is to determine there is no difference in strain and ultimate load to failure when a distal femoral plate is placed at varying cortical diameters in relation to the distal end of a total hip prosthesis as well as determine the required distance needed between a Smith & Nephew's Trigen Intertan long fracture fixation rod and a Smith & Nephew's Genesis II knee implant.

Methodology

A de-identified CT scan of a left femur was segmented to create a bony model. A femoral stem and distal femoral locking plates were modeled and incorporated into the bony model. All surfaces were converted into volumetric tetrahedral mesh. Abaqus CAE was used to perform simulations with varying amounts of torque applied to the model. Plate length was altered to vary the CDM from -2 to 3 (negative = overlap). Simulations were completed using varying bone densities. Maximal stress was obtained and correlated to a percent fracture risk (%FR) [Eq. 1]. The same de-identified left femur was used to model the fracture femoral rod and knee implant. All surfaces were converted into a volumetric tetrahedral mesh. The Trigen Intertan long fracture femoral rod and Genesis II were modeled in Solidworks. They were then imported into Abaqus CAE and were assembled with the femur.

$$\% FR = \frac{Stress}{Ultimate Strength} \times 100\% \quad \text{Eq.-1}$$

Results Obtained

The revealed in the 5 Nm simulation with mild osteoporotic bone, the control model had a %FR=9%. Highest %FR was 29% in the <1CDM model. With a 2 or 3 CDM the %FR was 6 and 8%. With overlap; the %FR was 14% and 9% for 1 and 2 CDM's of overlap. This trend was present in all simulations, with the greater the level of osteoporosis, the greater the %FR. This study was able to show that when the plate was left short of the femoral stem or overlapped by at least 2 cortical diameters, the percent fracture risk was equal to or slightly lower than the control model. Any distance in between the 2 cortical diameters of overlap or implant free bone led to increased risk of an interprosthetic fracture. In addition, when comparing the two groups, there was a higher percent fracture risk among all bone density levels when a higher torque (15Nm) was applied.

Acknowledgments

Dr. Brian Davis, Department Chair of Biomedical Engineering, The University of Akron

Dr. Brandon Jonard, Department of Orthopedics, Summa Health System

Piyush Walia, Department of Orthopedics, Cleveland, Clinic

Dr. Vanessa Falk, Department of Orthopedics, Summa Health System

Figures and Tables

Table 1. Results obtained from the 5 Nm torque simulation with a bone with density of 1.7gm/cm³ (OP-Med), showing the overall trend of the stress riser effect when the plate approached the tip of the stem.

Model:	CDM: (- = overlap)	Stress:	% Fracture Risk:
A (control)	N/a	4.8	9%
B	3.7	4.5	9%
C	2.3	2.28	6%
D	0.6	14.82	30%
E	-0.7	7.8	14%
F	-2.6	4.2	9%

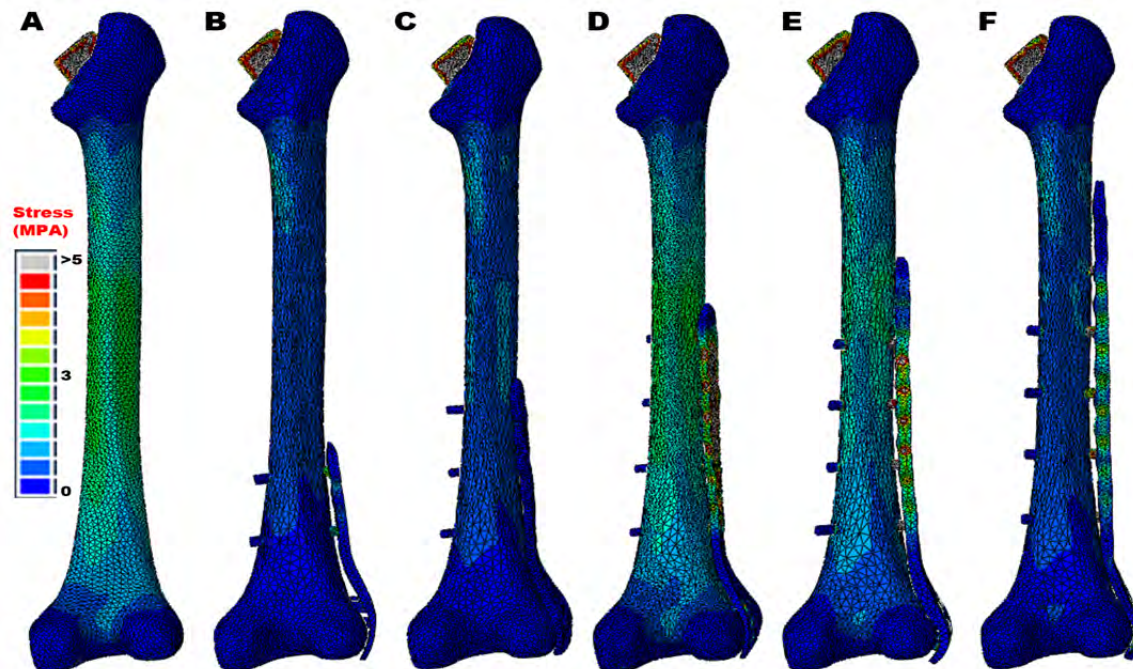


Figure 1. Shows the six simulations with the recorded stress values for varying plate lengths of 3 CDM (B), 2 CDM (C), 1CDM (D), -1CDM (E), and -2CDM (F). Image A is the control in which no plate was applied, only a femoral stem present.

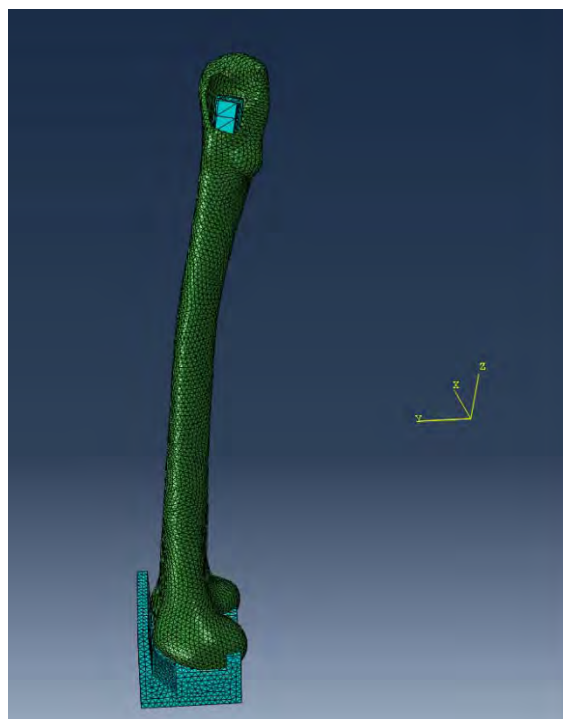


Figure 2. Shows the solid version of the bony femur model inserted with a Trigen Intertan long and size 6 Genesis II.

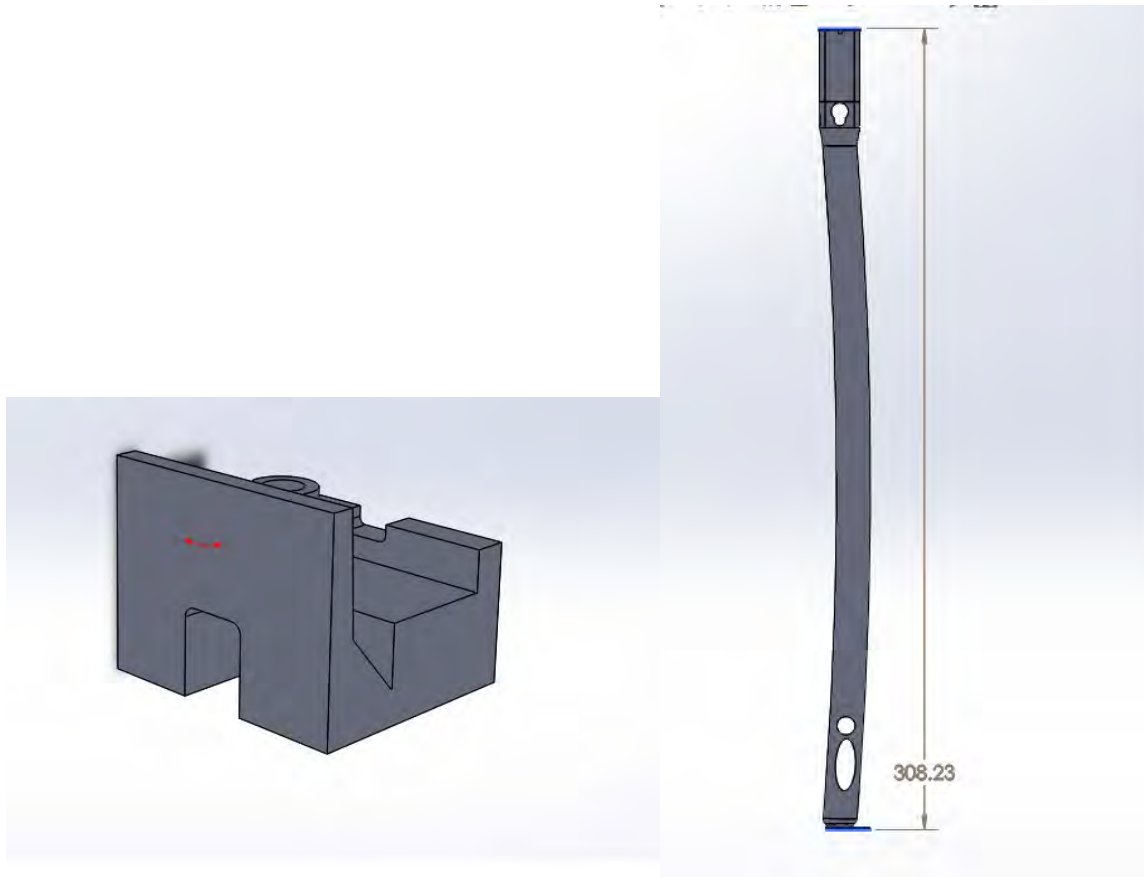


Figure 3. Trigen Intertan long and Genesis size 6 modeled in Solidworks

References

1. Graichen F, Bergmann G. Four-channel telemetry system for in vivo measurement of hip joint forces. *J Biomed. Eng.* 1991. Sept(13):370-74.
2. Hou Z, Moore B, Bowen TR, Irgit K, Matzko ME, Strohecker KA, Smith WR. Treatment of interprosthetic fractures of the femur. *J Trauma.* 2011. Dec;71(6):1715-9.
3. Rorabeck CH, Taylor JW: Periprosthetic fractures of the femur complicating total knee arthroplasty. *Orthop Clin North Am* 1999. 30:265-277.
4. McCrory JL, White SC, Lifeso RM. Vertical ground reaction forces: Objective measures of gait following hip arthroplasty. *Gait and posture.* 2001. (14)104-109.
5. Tsiridis E, Haddad FS, Gie GA. The management of periprosthetic femoral fractures around hip replacements. *Injury.* 2003. Feb;34(2):95-105.

ARGOS 8-Cable Suspended Robot Analysis

Student Researcher: Eric S. Graf, Jr.

Advisor: Dr. Robert L. Williams II

Ohio University

Mechanical Engineering Department

Abstract

The Active Response Gravity Offload System (ARGOS) is used at NASA's Johnson Space Center for experimental simulations of reduced gravity on humans and vehicles for planetary exploration. This research project aims to analyze the potential use of a cable-suspended robot system in place of the current single cable system, providing the system with additional capabilities for gravity simulation not possible with its current design. The potential of using this cable suspended robot system is evaluated by kinematic and pseudostatic virtual simulation. This project is to serve as the groundwork for future work in testing and evaluating a cable-suspended robot system as a replacement to the current ARGOS system.

Project Objectives

To assess the potential of using a cable-suspended robot system (Williams et al., 2003) in place of the current ARGOS design, certain aspects of the systems operation were analyzed. The main aspects of the robot system analyzed in this project were the operational robot workspace, cable tensions during various trajectories, cable interference, and the physical orientation of the robot end effector with respect to the stationary platform. For the more capable cable-suspended robot system to be a viable option in replacement of the current system, the operational robot workspace must be larger or equal in size to that of the current system, while also maintaining positive cable tensions through this workspace and avoiding cable interference in order to maintain control of the robot end effector during operation.

Methodology

The kinematic diagram of one orientation of the 8-Cable System is shown in Figure 1. Six design configurations of the cable suspended robot system were analyzed in this project. These different configurations correspond to the three different end-effector platform orientations with respect to the stationary structure, each with either crossed or uncrossed cables. The six different configurations analyzed in this project are detailed in the top views of the robot system shown in Figure 2.

Using MATLAB for virtual simulation of robot operation, each of the six different configurations of the robot system were tested and evaluated based on the size of their operational workspaces, frequency of cable interference, and their relative magnitude of cable tensions during two simulated trajectories. The Linear Trajectory simulates the robot moving from the bottom corner of the operational workspace to the opposite top corner of the robot workspace while rotating 20 degrees about all 3 XYZ axes. The Circular Trajectory simulates a circular XY motion while oscillating in the Z-direction and rotating about all 3 dimensional axes.

To evaluate the cable tensions of the different robot configurations, a representative pseudostatic model was developed, assuming small platform velocities and accelerations. The free-body diagram is shown in Figure 3 and defines the variables in the equations of static equilibrium that are used to solve the 8 cable tensions based on the end-effector position. The vector force and moment equations of

static equilibrium for the 8-cable system adapted from the 6-Cable RoboCrane (Albus et al., 1993) pseudostatic model (Williams, 2016) are shown in Equations 1 and 2:

$$\sum_{i=1}^8 t_i \hat{\mathbf{L}}_i + m\mathbf{g} + \mathbf{F}_{EXT} = \mathbf{0} \quad (1)$$

$$\sum_{i=1}^8 [{}^0_P\mathbf{R}]\{\mathbf{P}_j\} \times \{\mathbf{t}_i\} + [{}^0_P\mathbf{R}]\{\mathbf{P}_{CG}\} \times m\mathbf{g} + \mathbf{M}_{EXT} = \mathbf{0} \quad (2)$$

Where $[{}^0_P\mathbf{R}]$ is the $\alpha - \beta - \gamma, Z - Y - X$ Euler Angles (Craig, 2005) orthonormal rotation matrix representing the end effector frame $\{P\}$ with respect to the ground reference frame $\{0\}$; $t_i \hat{\mathbf{L}}_i$ is the tension applied by i^{th} active cable multiplied by the unit direction vector of that cable $\hat{\mathbf{L}}_i$; m is the moving platform mass; \mathbf{g} is the gravity vector in the negative z-direction; \mathbf{F}_{EXT} is the external force vector acting on the end effector by the environment; $[{}^0_P\mathbf{R}]\{\mathbf{P}_j\} \times \{\mathbf{t}_i\}$ is the moment due to the i^{th} active cable tension; $\{\mathbf{P}_j\}$ is the moment arm pointing from the end effector control point origin P to the j^{th} active cable connection point; $\{\mathbf{P}_{CG}\}$ is the position vector pointing from the origin of $\{P\}$ to the center of gravity of the end effector; and \mathbf{M}_{EXT} is the external moment inflicted on the end effector by the environment. During the analysis completed in this project both \mathbf{F}_{EXT} and \mathbf{M}_{EXT} were chosen to be zero and $\{\mathbf{P}_{CG}\}$ is 0 due to the center of gravity being located on the origin of frame $\{P\}$. Solving equations 1 and 2 simultaneously for $\{\mathbf{t}_i\}$ then yields the 8 cable tensions. To compare the relative cable tensions of each robot configuration during the 2 simulated trajectories, the 8 eight cable tensions norm was calculated and plotted against the robot motion duration.

To evaluate the effect of cable interference on the robot, a method for determining when two cables intersected was adapted from a method used for Two 6-DOF Foot Platforms (Otis et al., 2009). For simplicity, this model is represented in Figure 4 and Equations 3 and 4 as the intersections of cables 3 and 4. This method was also used in determining cable interference between cables 6 and 7.

$$\{\widehat{\mathbf{L}}_2\}L_{c2} + \{\widehat{\mathbf{n}}_{23}\}L_{MD} - \{\widehat{\mathbf{L}}_3\}L_{c3} = \{{}^0\mathbf{P}_1\} - \{{}^0\mathbf{P}_2\} \quad (3)$$

$$\begin{bmatrix} L_{MD} \\ L_{c2} \\ -L_{c3} \end{bmatrix} = [\{\widehat{\mathbf{n}}_{23}\}\{\widehat{\mathbf{L}}_2\}\{\widehat{\mathbf{L}}_3\}]^{-1} * [\{{}^0\mathbf{P}_1\} - \{{}^0\mathbf{P}_2\}] \quad (4)$$

Where $\{\widehat{\mathbf{L}}_2\}$ represents the unit vector in the direction of cable 2, L_{c2} is the length along cable 2 at which the shortest distance between cables 2 and 3 occurs, $\{\widehat{\mathbf{n}}_{23}\}$ is the vector in the direction of the shortest distance between cables 2 and 3, L_{MD} is the distance between cables 2 and 3, $\{\widehat{\mathbf{L}}_3\}$ is the unit vector in the direction of cable 3, L_{c3} is the length along cable 3 at which the shortest distance between cables 2 and 3 occurs, $\{{}^0\mathbf{P}_1\}$ is the moving platform point 1 in frame $\{0\}$, and $\{{}^0\mathbf{P}_2\}$ is the moving platform point 2 in frame $\{0\}$. Solving for L_{MD} from Equation 4 then yields the shortest distance between cables 3 and 4. This model represents cable interference occurring when the distance L_{MD} changes signs during a trajectory.

Results Obtained

Comparing the translational workspaces of the various robot designs showed all 6 robot configurations were able to maintain positive cable tensions through the entire current workspace of the ARGOS system. A representative workspace is shown in Figure 6 where each green marker represents an end effector position in the robot workspace where all 8 cable tensions are positive.

The 8 cable tensions norms for each robot design during the two simulated trajectories are shown in Figures 6 and 7. Figures 6 and 7 show the Square End-Effector with uncrossed cables, and Orientation 2 with crossed cables were the best suited to the linear trajectory while Orientation 2 with either crossed or uncrossed cables, and the Square End Effector with uncrossed cables were best suited to the circular trajectory. These orientations were best suited to their respective trajectories due to their relatively low magnitude of cable norms as well as their smooth plot shape corresponding to small overall changes in cable tensions over the course of the simulated trajectory.

Figures 8 and 9 represent the distance between cables 2 and 3 and 6 and 7 for all orientations of the robot that have crossed cables. It was concluded by visual inspection that the uncrossed cable orientations were not subject to cable interference in either of the two simulated trajectories. It can be seen that all 3 crossed cable orientations encounter cable interference while operating the circular trajectory, while avoiding cable interference during the linear trajectory. Orientation 2 had the smallest distance between both cables 2 and 3 and 6 and 7 corresponding to a limited range of motion before cable interference would occur.

The results from the cable tension norms and cable interference plots for the generated trajectories show that while some of the crossed cable configurations are better for cable tension optimization, their susceptibility to cable interference ultimately eliminate them as a viable option for an updated ARGOS system. The orientation that performed best considering the tested parameters was the Square End-Effector with uncrossed cables.

Acknowledgments

The author of this paper would like to thank Dr. Robert L. Williams II for all his support throughout the course of this project. The interest and advice of Asher Liebermann of NASA JSC are also appreciated.

Figures and Tables

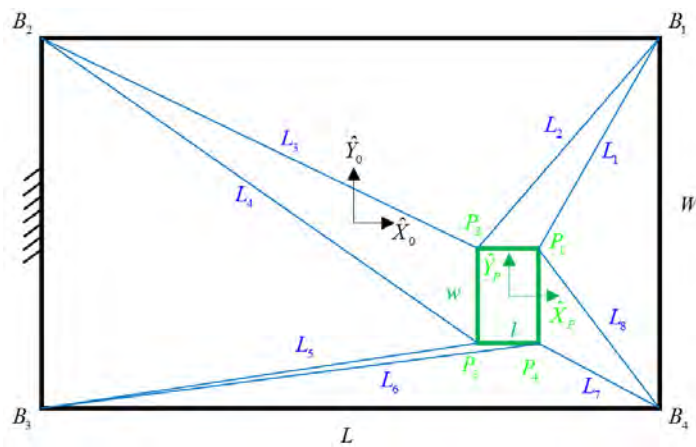


Figure 1. Kinematic Diagram of Orientation 1 – Uncrossed Cables

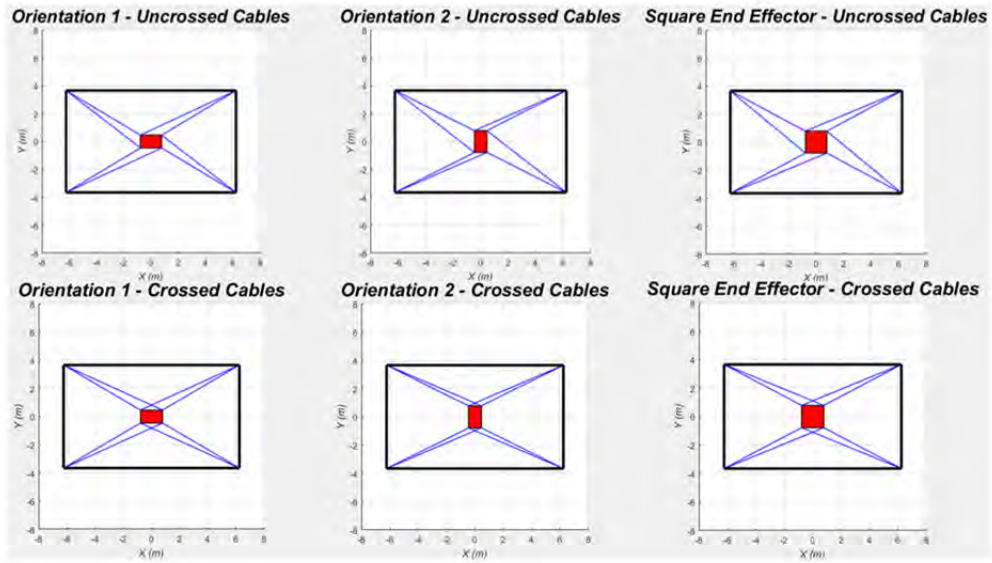


Figure 2. 6 Robot Orientations

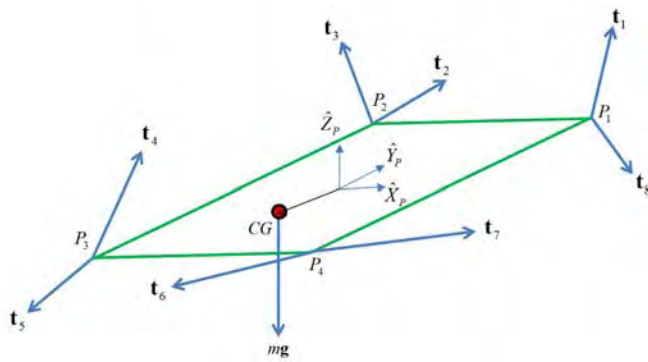


Figure 3. Pseudostatic Free-Body Diagram

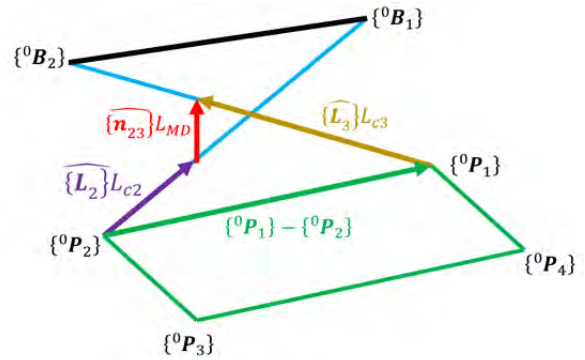


Figure 4. Cable Interference Model

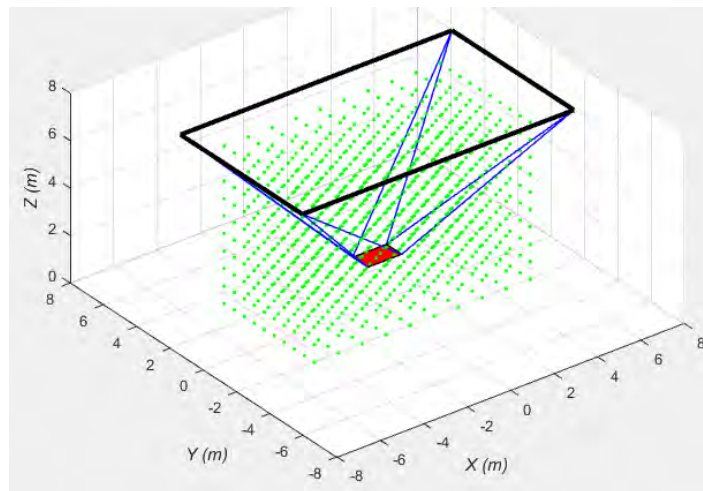


Figure 5. Robot Workspace

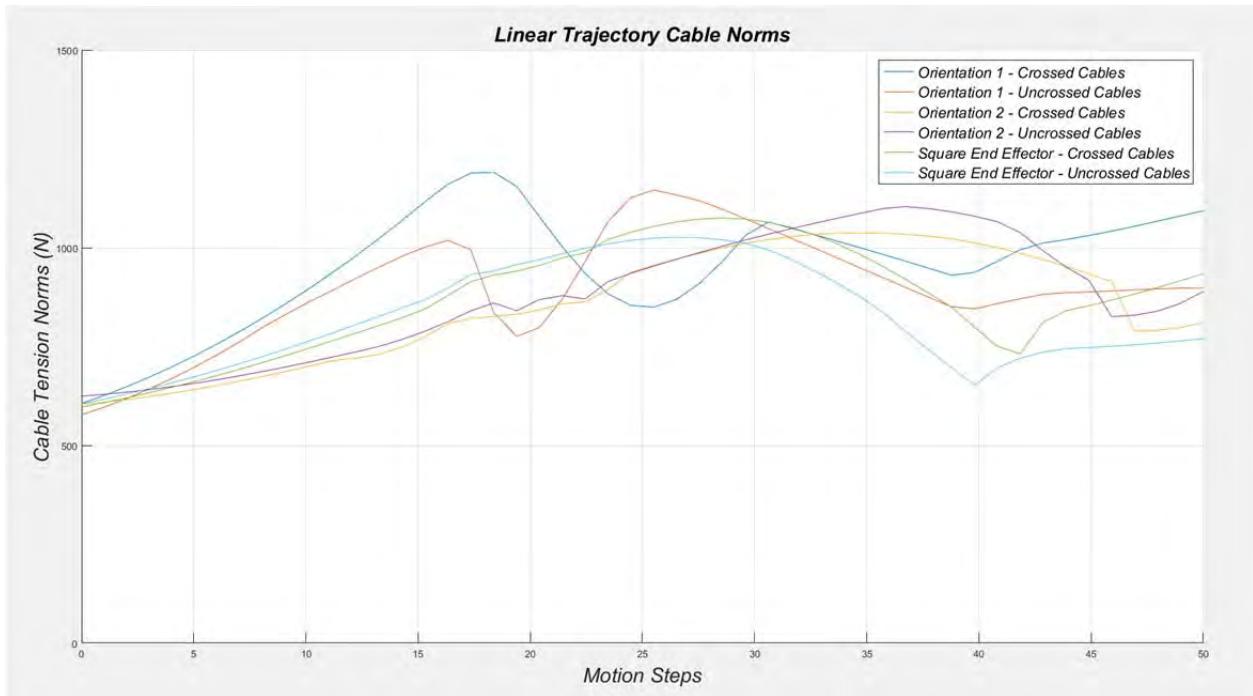


Figure 6. Normalized Cable Tensions during Linear Trajectory for Each Robot Configuration

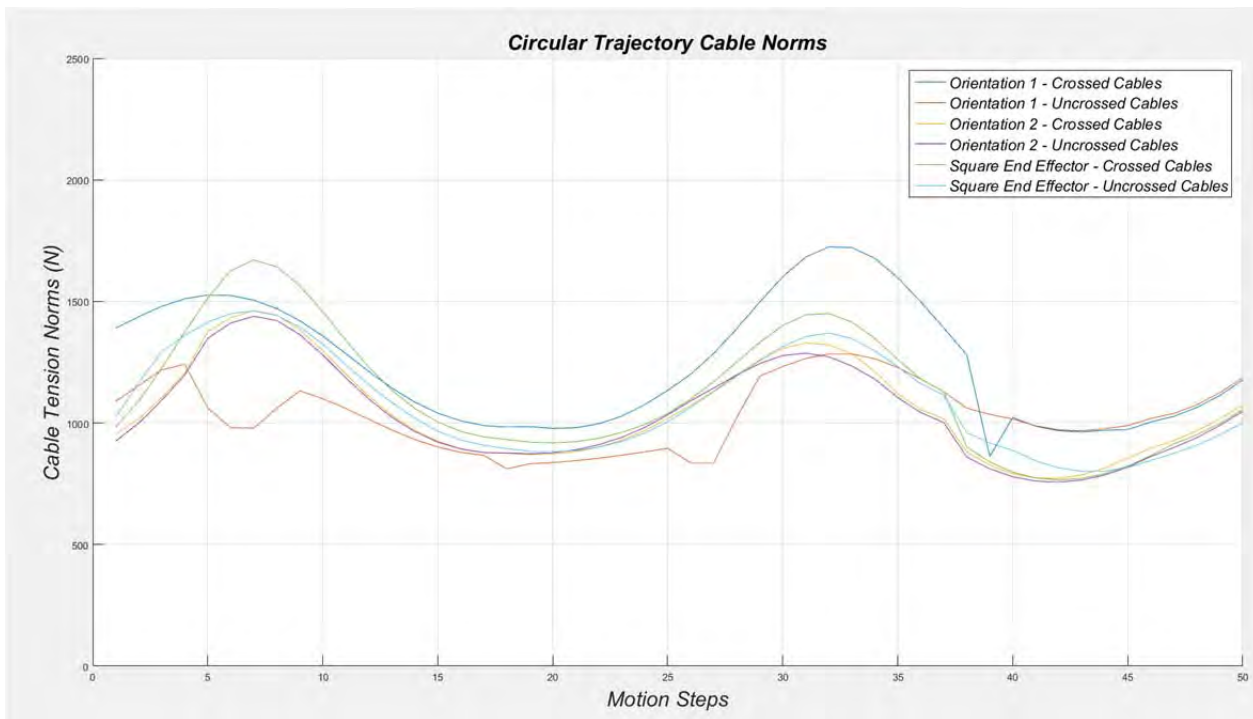


Figure 7. Normalized Cable Tensions during Circular Trajectory for Each Robot Configuration

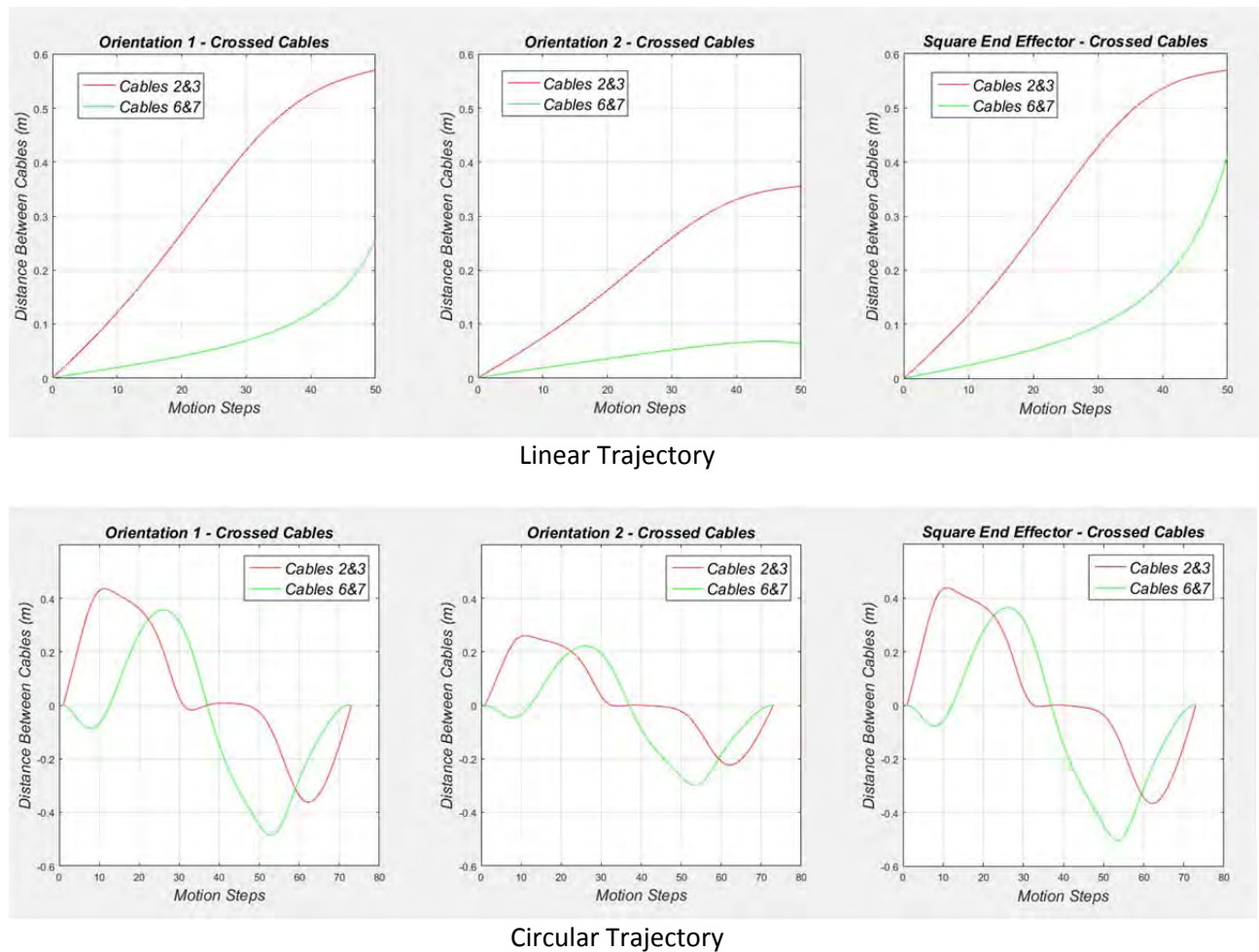


Figure 8. Distances Between Cables 2-3 and 6-7

References

1. J. Albus, R. Bostelman, and N. Dagalakis, 1993, "The NIST RoboCrane", *Journal of National Institute of Standards and Technology*, 10(5): 709-724.
2. J. J. Craig, 2005, *Introduction to Robotics: Mechanics and Control*, Addison Wesley Publishing Co., Reading, MA.
3. M. Otis, S. Perreault, T. Nguyen-Dang, P. Lambert, M. Gouttefarde, D. Laurendeau, and C. Gosselin, 2009, Determination and Management of Cable Interferences Between Two 6-DOF Foot Platforms in a Cable-Driven Locomotion Interface, *IEEE Transactions on Systems, Man, and Cybernetics – Part A, Systems and Humans*, May, 39(3): 528-544.
4. R. L. Williams II, P. Gallina, and J. Vadia, 2003, "Planar Translational Cable-Direct-Driven Robots", *Journal of Robotic Systems*, 20(3): 107-120.
5. R. L. Williams II, 2016, *NotesBook Supplement for ME 4290/5290 Mechanics and Control of Robotic Manipulators*, 2016 Dr. Bob Productions, Athens, OH, <https://www.ohio.edu/mechanical-faculty/williams/html/PDF/Supplement4290.pdf>
6. MATLAB (version R2015b). Windows. Natick, Massachusetts: MathWorks, Inc., 2015.

Heart Disease Awareness on a College Campus

Student Researcher: Katie S. Griffin

Advisor: Candice Jones, MEd, RD, LD, CDE

Cincinnati State Technical and Community College
Business Technologies

Abstract

According to the American Heart association (AHA), cardiovascular disease kills more than 801,000 people in the United States each year. Heart disease is a broad term used and includes coronary artery disease, hypertension and stroke. This accounts for 1 of every 3 deaths in the United States. Coronary Artery disease (CAD) is the most common type of heart disease and is the leading cause of death, accounting for 45.1% of deaths relating to cardiovascular disease. There are many risk factors that contribute to the development of heart disease, such as family history, smoking, hypertension, high cholesterol, diabetes, overweight/obesity status, physical inactivity, and simply getting older. All of these factors increase the risk for developing heart disease. Thus, 47% of Americans have one of three key risk factors for developing heart disease, yet most people don't know they have it until complications start to appear. Surprisingly only 27% of people are aware of the major signs and symptoms of a heart attack. As a prospective dietetic technician, and hopefully soon to be dietitian, the probability that I will be working with people who have heart disease is very high. Taking this into consideration, I would like to assess the college student's knowledge about the risks for heart disease and complications related to heart disease.

Project Objectives

One could hypothesize that the students in the health-related programs will have a better understanding of the risk factors associated with developing heart disease than the non-health related programs will. Based on these statistics, a campus wide study was conducted to gauge whether or not the students know their risk for developing heart disease in their lifetime. By conducting these heart disease surveys, the project's objective is to determine the knowledge and awareness about heart disease in both a health-related field of study and non-health related field. Based on the findings of this survey, "would students benefit from an information session, such as a lunch and learn, to provide them with potential lifesaving information about the risks associated with heart disease?"

Methodology Used

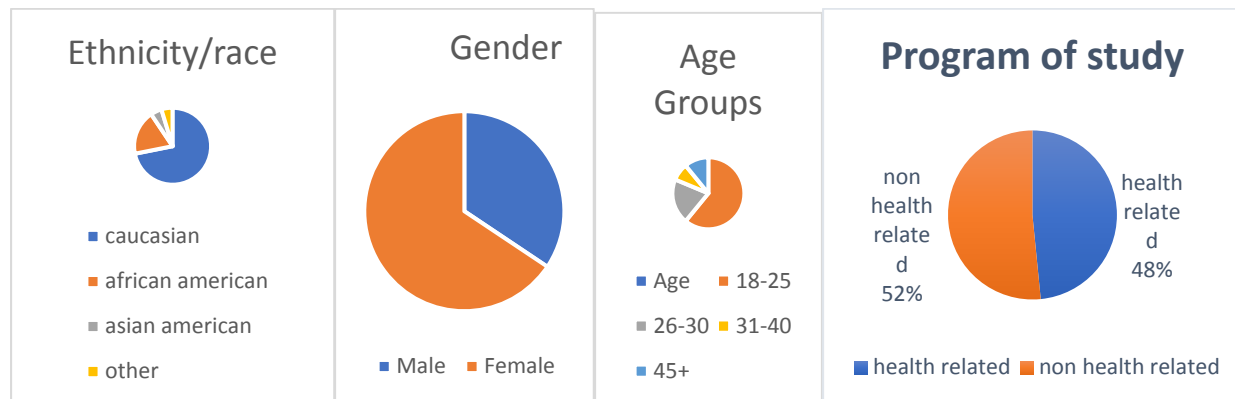
For the purpose of information gathering, the "Heart Disease Fact Questionnaire" (HDFQ) was used. This survey contains 25 questions related to heart disease awareness and risk factors associated with heart disease such as hypertension and diabetes. For the study, the health-related programs are those that concentrate on pursuing a career in the healthcare field, specifically Dietetic Technology, Nursing, and Health and Fitness majors. The non-health related programs are all other programs of study offered at Cincinnati State Technical and Community College. Due to accessibility, the programs specifically used for this study were; Pastry Arts, Culinary Arts, and Brewing Science. In addition to the obtaining the students field of study, we also obtained other demographic information from them such as; age, race/ethnicity and gender.

Results

This study surveyed 64 people; 31 were from a health-related program and 33 from a non-health related program. Out of the 64 people that were surveyed, most people answered the questions very similarly. Based on the results of the survey, it appears that the results may be skewed due to limited accessibility to students in other programs in the other three divisions on campus. Students from the Business Technology Division were more accessible, specifically students from, the Brewing Science, Culinary Arts and Pastry Arts programs. These programs still require an introductory nutrition course, except for Brewing Science, which may have influenced the findings. The sample size was small, which was due to the study being on a volunteer basis only. A notable limitation to this study was that they survey could only be completed in a paper form.

Significance and interpretation of results: Based on the results of this study, it appears that by increasing our sample size and including the other divisions on campus, such as automotive, accounting, business management and horticulture, would enable us to see a better end result, which should be less biased. The other programs do not require a basic nutrition course as part of their curriculum, which would provide a better look at how students with no health-related background view heart disease and the risks associated with heart disease. Upon reviewing the results from the expanded survey, there would be a better understanding of how college students from all programs view heart disease and the risks associated with it.

Figures



References

1. <http://www.heart.org/HEARTORG/>
2. "Development of a questionnaire to measure heart disease risk knowledge in people with diabetes: the Heart Disease Fact Questionnaire." Julie Wagner, Kimberly Lacey, Deborah Chyun, Gina Abbott.
3. A University of Connecticut School of Dental Medicine, UCONN Health Center, MC 3910, 263 Farmington Ave., Farmington CT 06030, USA Yale School of Nursing, USA Received 22 January 2004, Revised 25 May 2004, Accepted 13 July 2004, Available online 19 August 2004.

Development of a Shape Memory Smart Structure via 3D Printing

Student Researcher: James D. Harding

Advisor: Dr. Pedro Cortes

Youngstown State University

Chemical Engineering

Abstract

Current technological advances in the area of smart materials have impulse the development of morphing components to fulfill the multifunctional requirements of fully adaptive structures. Although considerable progress has been achieved in the area of intelligent materials, there is still a lack of integral properties able to act accordingly to a predetermined training to modify structural configurations. Thus, the integration of a shape memory alloy (SMA) into a 3D printed shape memory polymer (SMP) opens new opportunities in the area of morphing structures for upcoming responsive needs in the aerospace sector under unique designs. This research program proposes to investigate the mechanical and morphing properties of a 3D printed shape memory structure based on SMA and SMP. Indeed, it is widely known that whereas shape memory alloys are capable of acting as effective actuators, shape memory polymers are potential candidates to generate structural rigidity in their glassy state. Hence, the adaptive composite structure here proposed will take advantage of the rigidity imparted by the SMP and the high recovery stresses of the SMA as well as the degree of freedom on manufacturing convoluted designs through the 3D printing process. The main goal of this study is to develop a multi-functional shape memory structure endowed with shape memory effect (SME) via additive manufacturing. Through the innovative synthesis of shape memory alloys into 3D printed shape memory polymers, an original breed of adaptive engineering materials will be attained.

Project Objectives

The objectives of this project are separated into four phases.

Phase I: Manufacturing of SMP filament

This phase has concentrated on manufacturing a 3D printing filament by extruding SMP pellets. Here, investigation of the processing temperature has been a critical activity in order to produce a high quality continuous filament with shape memory effect properties. Additionally, the structural uniformity has been here investigated in order to ensure a reproducible filament. The diameter of filament has been studied in the 1.6-1.8mm range. Figure 1 shows the equipment used for the manufacturing of the SMP filament.

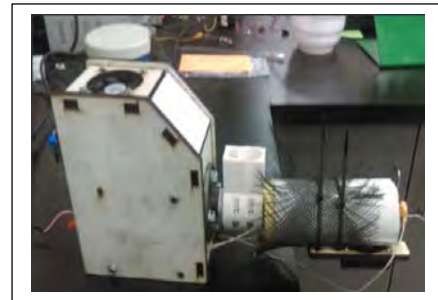


Figure 1. Extruder used to produce the SMP filament

Phase II. Synthesis of a SMA Truss

A SMA truss structures based on Ni-Ti alloy will be investigated as the core element of the smart structure here proposed. The SMA truss will be manufactured in a binder Jetting system using Ni-Ti powder. Here, different printing parameters such as: thickness layer, binder saturation and spreading speed will be studied, in order to ensure the manufacture of a robust SMA structure. Also, post-processing parameters such as sintering time and temperature will be investigates with the purpose to deliver a printed SMA coupon with SME features. Here, different truss configuration will be printed to study the appropriate weight-stress recovery ratio.

Phase III: Manufacture of the Smart Structure

Here, an SMP layer will be printed on the top and bottom of the SMA truss in order to actuate as the skin layer of the proposed morphing structure. Indeed, investigation on how to incorporate a printer SMP layer on the manufactured SMA will be a critical step for the success of the present project. A schematic of the proposed SMA structure should result in a morphing foil with the difference on having skin layers based on SMP and the core structure on 3D printed Ni-Ti alloy based on a truss configuration.

Phase IV Morphing Properties

Following the manufacturing process of the smart structure, the project will concentrate on testing the SME of the SMA/SMP system. This will be carried out in a wind tunnel, where an electrical current will be provided to the SMA with the purpose to activate the whole structure.

Methodology Used

Due to time restrictions only Phase I was carried out. After construction of an extruder was completed, pellets of SMP were added to the extruder, and the investigation of the processing temperature was investigated. Preliminary results have shown that the ideal extruding temperature for the investigated polyurethane SMO is between 190°C and 215°C. Extrusions were performed at 215°C, 205°C, and 200°C. Here, it was observed that at a temperature of 200°C, the extruder was able to produce an adequate filament with shape memory effect properties. Considering the die swell effect of the SMP, it was observed that an initial extrusion diameter in the nozzle of 1mm produced a filament diameter of 1.35mm. Indeed, the extrusion diameter was increased to 1.25mm and the resulted filament appear to have a diameter of 1.75mm, which is the adequate for FDM printing.

Results Obtained

At the present, a continuous uniform SMP filament has been manufactured (see figure 2). The current progress has concentrated on printing the SMP filament using a FDM system. Previous 3D printing of the SMP filament, have shown that it is possible to print SMP structures (see figure 3). These preliminary results suggests that the proposed concept of printing SMP skin on the SMA truss core is actually feasible.



Figure 2. Manufactured SMP filament



Figure 3. Preliminary 3D printing using a SMP filament.

References

1. Pilate, F.; Toncheva, A.; Dubois, P.; Raquez, J.-M. Shape-memory polymers for multiple applications in the materials world <http://www.sciencedirect.com/science/article/pii/S0014305716303767> (accessed Mar 3, 2017).

The Great Space Race: Thrust and Efficiency Rates of Burning Fuel

Student Researcher: Elizabeth L. Herting

Advisor: Professor Sarah Gilchrist

Cedarville University

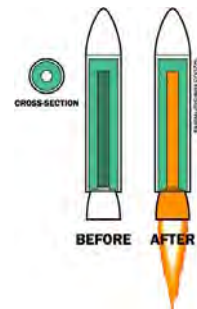
Department of Science and Mathematics

Abstract

In this lesson, we will focus rocket thrust and determining what method/container for burning fuel will produce the desired amount of thrust for rocket propulsion. Using NASA resources on thrust and fuel burn rate, students will get to explore surface area, volume, and unit conversions through the exploration of different fuel tanks and the burn rate that is desired to create the necessary speed in order to launch a rocket. The students will get to use an investigative approach to explore different fuel tank designs in order to ultimately achieve the results they desire. This activity will draw off of students' natural curiosity towards space and rocket propulsion and give them a real world application of how surface area could affect different areas of their lives.

Lesson

The foundation for this lesson comes from Solid Rocket Boosters problem 245 on the SpaceMath NASA resources page. As an introduction to this lesson, students will watch a 5.5 minute video from NASA. (NASA eClip: Launchpad: Liftoff with Solid Rocket Boosters). Students will complete the classroom challenges as competing "countries" (groups of four). In addition to helping with problem-solving, each team member will have a unique role that they must fulfill as calculator (records calculations), scribe (records all other ideas), time-keeper (checks for adequate progress), and leader (asks questions and balances input).



The challenges are related to rocket fuel burn rates and students are tasked with racing other groups to discover the most effective method for rocket fuel to burn. Students must then make a cross sectional model of the most efficient design.

Objectives

- Students will interpret data and perform calculations.
- Students will determine the relationship between fuel packing and burn rates.
- Students will explain the effect of exposed surface area on thrust created by a rocket.

Alignment

CCSS.MATH.CONTENT.7.G.B.6: Solve real-world and mathematical problems involving area, volume and surface area of two- and three-dimensional objects composed of triangles, quadrilaterals, polygons, cubes, and right prisms.

CCSS.MATH.CONTENT.7.G.B.4: Know the formulas for the area and circumference of a circle and use them to solve problems; give an informal derivation of the relationship between the circumference and area of a circle.

Underlying Theory

This lesson follows a constructivist approach. Through the activity students will apply their classroom knowledge of calculating area and surface area to solid rocket boosters and in the process will learn and grow in their knowledge of thrust and how fuel packing impacts thrust. The students may perform the calculations using any valid method. The teacher will provide the materials and desired outcome, but each team will create their own design. This approach gives students flexibility and also allows them to test the different methods to discover the information by themselves rather than through direct instruction.

Student Engagement

Each student has a particular role within their group. The groups then race the other teams (countries) to find out the best fuel packing method and to build their rocket so that they are the first to get their rocket to space. Students will be awarded points for how fast they complete the assignment, correct calculations and conclusions, and the quality of their rocket model. The group with the most points wins the race. This assignment combines group work calculations, explanations, and physical models to help engage learners with different interests and strengths.

Resources

Students will first watch the introduction video as a class and then will each be given an instruction sheet. Students will have to work in their teams to complete the calculations activity as well as to build the model. For the models they will have paper towel tubes, toilet paper rolls, and wrapping paper tubes of different sizes available as well as cotton balls, craft pom poms, feathers, scissors, glue, tape, paper, sticky felt, colored pencils, markers, cereal boxes, paper clips, snow cone cups, and pipe cleaners.

Assessment

Students will be pre-assessed on any misconceptions they hold on their exit slip the day before. At the end of the lesson, students will be assessed on their ability to work productively within their group, their accuracy in answering the discussion questions, and points in the exercise. For extension, students will look at the tubular, star, rod and tube, multi-fin, double anchor, and dual composition profiles and predict their burn patterns and thrust profile. They will provide a written response addressing their responses to the in class activity and discussion questions.

Conclusion

This lesson gives students an application of the material we are learning in class with surface area, volume and unit conversions. The group work is a fun, engaging, and informative way for students apply the material they are learning. This activity overall will help the students to see the wide variety of ways the concepts we are learning in class are applicable.

The Great Space Race

Grade 7/8 Math
Directions: Attach this activity on a separate sheet of paper.

Two solid rocket boosters (SRBs) for the Ares-V launch vehicle will each generate a total thrust of 3.8 million pounds. The SRBs from tip to ground are 193 feet long and have a diameter of 12.2 feet. The actual fuel occupies a cylindrical volume about 180 feet (60 meters) long and 11.5 feet (3.7 meters) in diameter. They will 'burn' for a total of 126 seconds.

Before You Begin- Thrust is created by burning the exposed surface area of the fuel in the SRB. Make a conjecture about which method of fuel packing will produce the most thrust in a rocket: from bottom to top (like an upside down candle) or from the central axis of the cylinder to the outside casing.

Problem 1- Thrust is created by burning the exposed surface area of the fuel in the SRB. To launch the 3.4 million pound Ares-V rocket, each SRB has to burn at a rate of 8,740 kg of fuel each second. The density of the fuel is 1770 kg/m^3 . If the exposed fuel area is just the circular cross section of the cylinder (see red area in the figure below), and the burn depth is 0.1 meters each second;



A) What is the total burn rate? Explain your approach to the first problem.
B) Is this enough to launch Ares-V? Explain.

Problem 2- Suppose, instead that a cylindrical core (red circle) with a diameter of 0.6 meters is cut out along the axis of the booster from top to bottom. The figure to the left show the red areas where the fuel is burning.



A) What is the surface area of the initial exposed fuel in the core region?
B) If the burn depth is 0.1-meter each second, what is the mass rate in kg/sec? Is this enough to launch Ares-V?
C) What is the mass rate in kg/sec after 5 seconds of burn?

(Problem 1 image taken from the NASA/Johnson Space Center/Johnson Space Center/Johnson Space Center)

Review and Design of Non-Axisymmetric Nozzles with Active Flow Control Capability

Student Researcher: Nicholas R. Horn

Advisor: Dr. Mo Samimy

The Ohio State University – Aerospace Research Center
Department of Mechanical and Aerospace Engineering

Abstract

Jet exhaust nozzle geometry has received a significant amount of research in recent years. The Gas Dynamics and Turbulence Laboratory at The Ohio State University has researched the flow field and noise effects of single and twin axisymmetric nozzles in the past. Future research could involve a shift to non-axisymmetric nozzles, as these nozzles are becoming more prevalent on tactical aircraft and they provide additional benefits in noise reduction and mixing characteristics. This project conducted a literature review of the characteristics of asymmetric nozzles to aid in the design of a nozzle to be used for future testing.

Project Objectives

The Gas Dynamics and Turbulence Laboratory (GDTL) at The Ohio State University has developed localized arc filament plasma actuators (LAFPAs) as an active flow control method to reduce jet noise and modulate natural instabilities in the flow. Previous studies have researched single axisymmetric nozzles and twin axisymmetric nozzles. However, many recently developed and conceptually designed tactical military aircraft feature non-axisymmetric jet nozzles to aid in their stealth capabilities as well as aiding integration of aerodynamic and propulsion components.

This project was selected to research the nozzle geometry used on tactical aircraft as well as the design and flow field effects of non-axisymmetric nozzles. A literature search was conducted to compare the physical parameters of various nozzle designs and to understand the impact of the nozzle geometry on the jet plumes and acoustic field. Different nozzle shapes as well as active and passive flow control methods implemented on these nozzles were reviewed. This review could aid the GDTL in confronting the challenge of designing non-axisymmetric nozzles implemented with LAFPAs.

Review of Rectangular Nozzles

Rectangular nozzles exhibit drastically different flow characteristics than circular nozzles. This is because a circular nozzle is axisymmetric and spreads evenly in all directions, whereas a rectangular nozzle is asymmetric. The sharp corners of a rectangular nozzle produce corner vortices in the flow. The vortices develop due to secondary flow in the nozzle, especially when there is a contracting transition from round to an asymmetric shape in the upstream flow geometry [1]. Axis switching occurs in rectangular nozzles and is governed by two different mechanisms: ω_{θ} -dynamics and ω_x -dynamics, where ω is the vorticity and x and θ are the streamwise and azimuthal coordinates. ω_{θ} -dynamics occurs because of induced velocity differences in various segments of a rolled-up azimuthal vortical structure. In a supersonic screeching jet, ω_{θ} -dynamics dominates and the axis switching occurs earlier in the flow. ω_x -dynamics occurs due to the induced velocities produced by pairs of streamwise vortices. The upstream contracting nozzle transition contributes to ω_x -dynamics [1].

Vortices can both promote or inhibit axis switching depending on their direction of rotation. The naturally developing corner vortices in a rectangular nozzle are of the outflow type: they rotate in the

direction such that the induced velocity is outboard on the minor axis of the nozzle. This type of vortex helps prevent axis switching; however, the natural vortices are not strong enough to overcome axis switching. Vortices of the inflow type result in induced velocity inboard along the minor axis, which promotes axis switching. Tabs can be placed along the perimeter of a rectangular nozzle, and depending on the tab's orientation, it can create either type of vortex. When the tabs are placed along the sides of the major axis, they cause two more pairs of vortices of the outflow type which combine with the original vortices to help prevent axis switching. Tabs along the minor axis created inflow type vortices which helped promote axis switching. Figure 1 shows the results of axis switching on a 3:1 rectangular jet without tabs, with tabs on the minor axis, and with tabs on the major axis. The crossover between the jet half-width (B/D) of the minor and major axes indicate axis switching has occurred [1, 2].

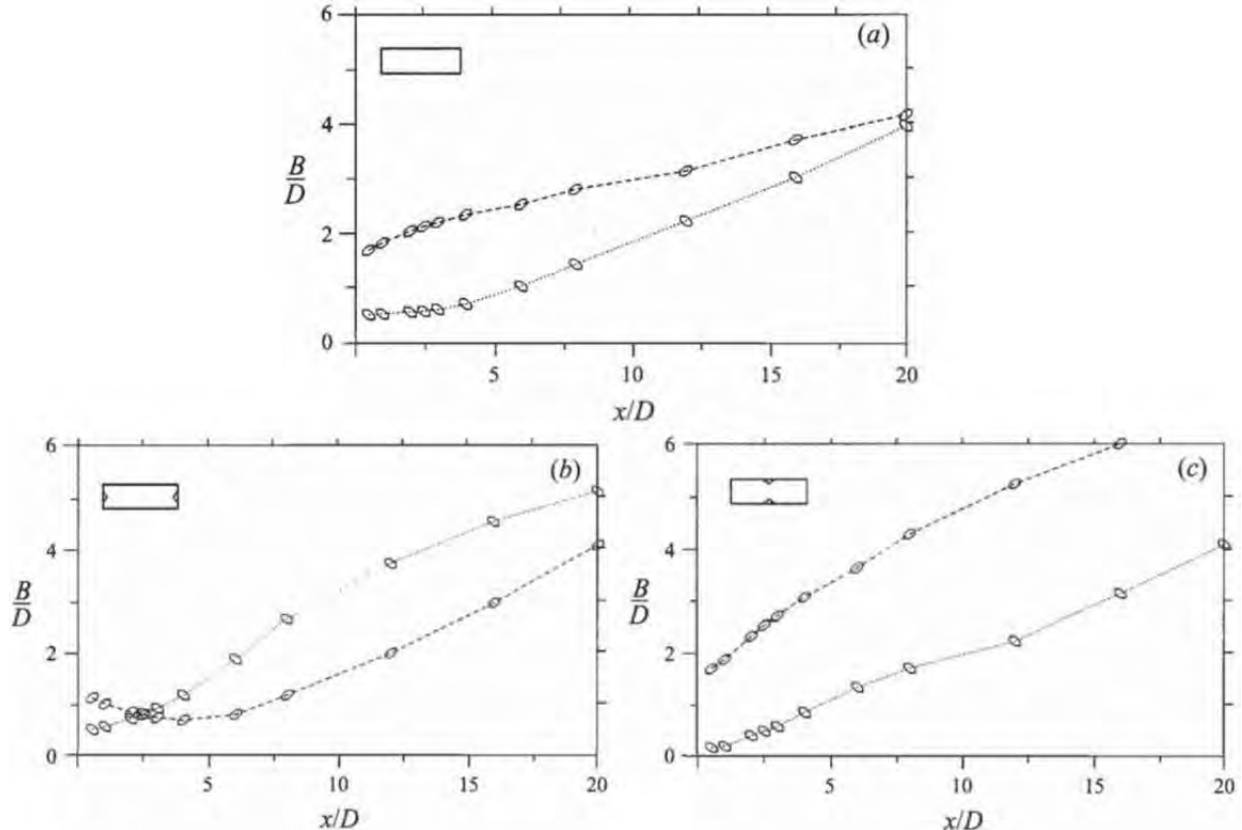


Figure 1. Streamwise variations of jet half-velocity-width; \circ , minor axis plane; \circ , major axis plane. (a) no tab, (b) two tabs on ends, (c) two tabs on sides (Replicated from Ref. [1])

Multiple studies conducted previously have shown that enhanced mixing rates contribute to a reduction in jet noise. Therefore, it is useful to determine which nozzles result in an increase in jet spreading and a reduction in jet noise. Asymmetric nozzles spread and mix faster than axisymmetric nozzles in supersonic screeching jets. In addition, most excitation modes (helical, flapping, etc.) result in an increase in jet spreading, with the largest increase occurring in the flapping mode. While these modes can all be excited in a circular nozzle, rectangular and elliptic nozzles only involve flapping mode screech. Tabs also play an important role in jet mixing and spreading. Tabs on the minor axis of a rectangular nozzle caused a drastic weakening of the shock/expansion structures in the flow and showed in an increase to the overall spreading and small scale mixing of the jet. This also resulted in a decrease in the amplitude of the screech tone and a frequency shift up the spectrum, as indicated in Figure 2.

Differences between Rectangular and Elliptical Nozzles

In many ways, elliptical nozzles have similar characteristics to rectangular nozzles. For example, they both shed vortices due to their asymmetry, they both exhibit axis switching, and they both have similar flow field effects when tabs are added. In addition, the screech tone spectrum is very similar between the rectangular and elliptical nozzles, as shown in Figure 2. However, the mixing characteristics of elliptical nozzles differ from those seen in rectangular nozzles. To promote mixing, the jet must have a combination of small and large-scale vortices in the correct proportion. Mixing characteristics are enhanced if the small-scale vortices consist of various sizes since it is these vortices which have mass transporting properties. Rectangular nozzles produce both small and large-scale vortices of various sizes at their corners, but the vortices are of similar length scale along the straight edges of the nozzle. The changing curvature of elliptical nozzles allows these nozzles to produce vortices of diverse scales all around the nozzle perimeter. This results in superior mixing and increased entrainment than is seen in axisymmetric and rectangular nozzles [3].

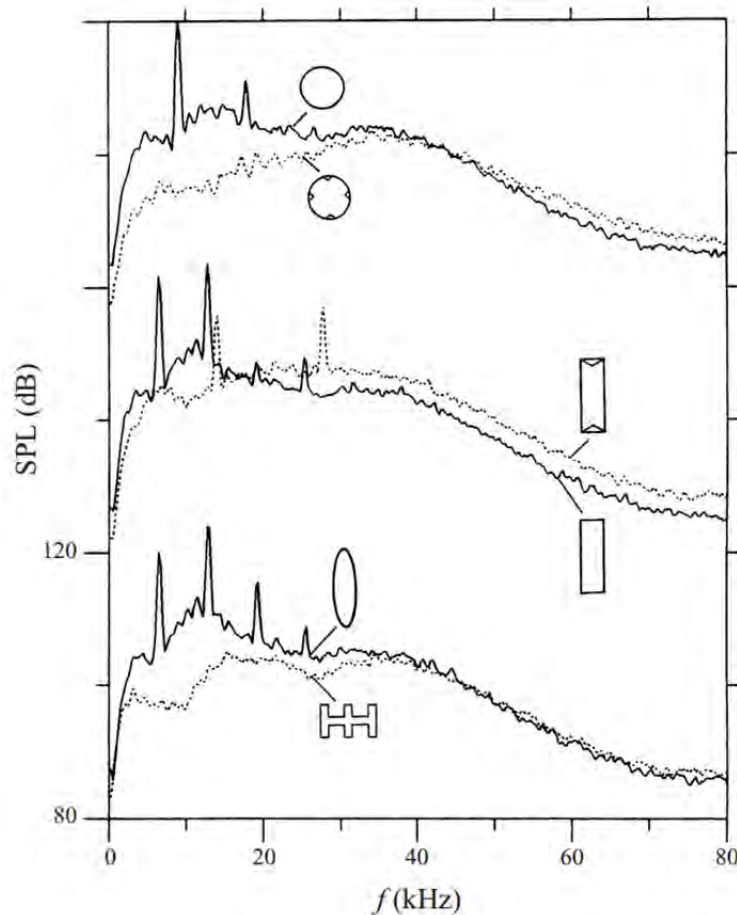


Figure 2. Far-field noise spectra for six nozzle cases at $M_j = 1.63$; the three pairs of traces are staggered successively by one major ordinate division. (Replicated from Ref. [2])

Tactical Aircraft Nozzle Design

Present and future aircraft designs can benefit from non-axisymmetric nozzle geometry. Tactical military aircraft thus far have received the largest benefit from these types of nozzles. This is because these aircraft require a large amount of thrust and often fly at supersonic speeds. Therefore, they typically involve low bypass turbofan or turbojet engines with an extremely high nozzle exit velocity. These engines produce a lot of noise. This is especially problematic in carrier-based aircraft where people must

work on the deck of the ship very close to the engines while they operate at maximum thrust. Hearing loss in the crew of these ships is not uncommon, and much research has been conducted to help prevent this issue. Asymmetric nozzles can help reduce the decibel level of the engine, helping to avoid hearing problems in crewmembers.

One of today's most successful fighter aircraft is the F-22. One of the main factors that led to the aircraft's success was the implementation of thrust vectoring nozzles with rectangular cross section. The straight sides of the nozzle can move like a hinge, which enable control of the flow angle. This would be significantly more difficult to design on a non-rectangular nozzle [4].

An additional benefit of asymmetric nozzles is their ability to help reduce radar and infrared (IR) signatures. Axisymmetric nozzles reflect radar in all directions, making it easier to spot. Asymmetric nozzles can be tailored to reflect radar away from the receiver, thus reducing the aircraft's signature. The IR signature can also be reduced using asymmetric nozzles because these nozzles provide enhanced mixing. This mixing helps to bring cool, ambient air into the hot jet plume, reducing the plume's temperature and thus its heat signature. The X-47B features a nearly elliptical nozzle (with aspect ratio of approximately 3.4) with a plate extending out the bottom of the nozzle. This nozzle might be designed to enhance mixing in order to reduce noise and the IR signature of the aircraft. The Gas Dynamics and Turbulence Laboratory at Ohio State would like to further investigate this type of nozzle as well as the possibility of implementing LAFPAs for active flow control on the nozzle. A preliminary design of the nozzle geometry that would be used in the future is shown in **Figure 3**. X-47B Nozzle [5] (Left) and Preliminary Testing Nozzle Geometry (Right)Figure 3, which is constructed based on the exhaust system of X-47B.

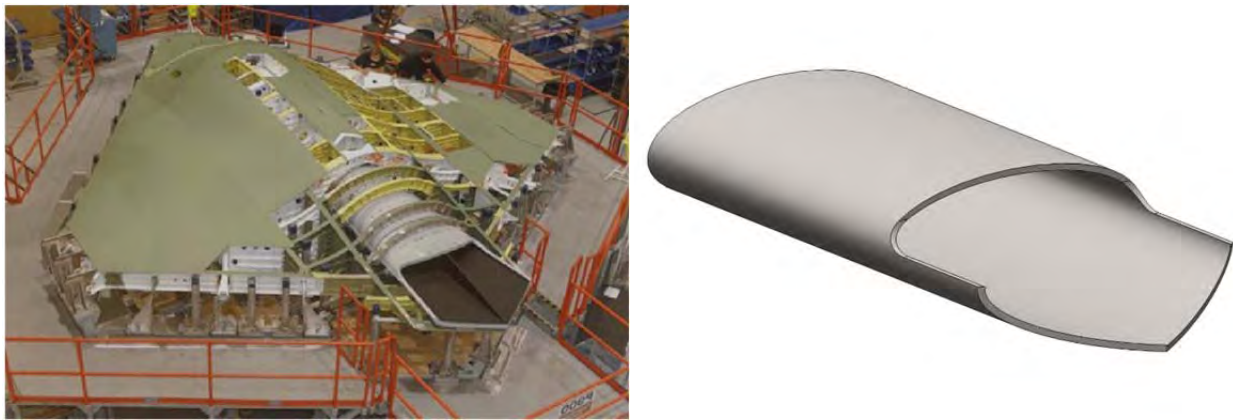


Figure 3. X-47B Nozzle [5] (Left) and Preliminary Testing Nozzle Geometry (Right)

References

1. Zaman, K. B. M. Q., "Axis switching and spreading of an asymmetric jet: the role of coherent structure dynamics," *Journal of Fluid Mechanics*, vol. 316, 1996, pp. 1–27.
2. Zaman, K. B. M. Q., "Spreading characteristics of compressible jets from nozzles of various geometries," *Journal of Fluid Mechanics*, vol. 383, 1999, pp. 197–228.
3. Kumar, S. A., and Rathakrishnan, E., "Characteristics of a supersonic elliptic jet," *The Aeronautical Journal*, vol. 120, Mar. 2016, pp. 495–519.
4. Gamble, E., Terrell, D., and Defrancesco, R., "Nozzle Selection and Design Criteria," *40th AIAA/ASME/SAE/ASEE Joint Propulsion Conference and Exhibit*, 2004, pp. 1–11.
5. Warwick, G., "Pictures: Northrop Grumman reveals X-47B UCAV," *Flightglobal.com* Available: <www.flightglobal.com/news/articles/pictures-northrop-grumman-reveals-x-47b-ucav-213091/>

Spacesuits of the Future: Adapting Technology for Further Exploration

Student Researcher: Kayla M. Hummell

Advisor: Dr. Jed E. Marquart

Ohio Northern University

Department of Mechanical Engineering

Abstract

Human space exploration was made possible with the invention of the spacesuit. Spacesuit technology has evolved to meet the changing demands of human space exploration over time. The technology must protect humans from the perils of space, while giving them the mobility to accomplish their research. This research will explore the environments on Mars and Venus, and propose how current spacesuits can be adapted for these extraterrestrial locations.

Project Objectives

The object of my research is to examine the environments of Mars and Venus and how they may affect the design of the spacesuits required to explore them. Both planets have special interest for further exploration in the coming years. Based on the information gathered about these environments, I will make recommendations on how the current spacesuits may need to be adapted to meet each location's unique challenges. Without spacesuits, humans could not survive in open space or on any known planet besides Earth. Spacesuits provide a regulated environment for astronauts by providing breathable oxygen, regulating air pressure, and protecting them against extreme temperatures, radiation and micrometeoroids.

Although the current spacesuit, also known as Extravehicular Mobility Unit (EMU), has been successfully implemented at the International Space Station for years, NASA has its sights set on further horizons. Mars and Venus have each been singled out for more research in the coming years. Rovers have found signs that Mars was once home to flowing water. Venus has been studied by orbiters to better understand the planet's "runaway greenhouse effect." If humans are ever going to be able to walk on Mars or Venus, the design of the EMU must be adapted to meet the challenges of these harsh environments.

Methodology Used

The first part of my research was identifying the functions of the spacesuit, and the material layers used to create it. Following this research, I accumulated known data about the surface conditions of Mars and Venus that an astronaut may encounter on a spacewalk. These environmental factors such as gravity, atmosphere, air pressure, temperature extremes, radiation and weather patterns, may warrant changes to the materials used in the EMU. The result of this research will be a set of recommendations for a designer creating EMUs that might explore Mars and Venus in the future.

The current space suit is constructed in material layers with different functions. The innermost layer of the EMU is the Liquid Cooling and Ventilation Garment (LCVG) which houses tubing full of liquid water that cool the astronaut's body. Following the LCVG, is the pressure suit. The pressure suit consists of a breathable nylon layer, a neoprene coated nylon layer to maintain pressure, and a nylon outer layer to

restrict the size of the other layers (1). If an astronaut were to enter space without this outer layer, the spacesuit would expand like a balloon due to the pressure difference. Layers 5 through 11 of the EMU make up the Thermal Micrometeoroid Garment (TMG) that provides tear protection, thermal protection, micrometeoroid protection and radiation protection. The 5 layers of aluminized Mylar insulation limit radiant heat from escaping the suit. The outer cover of the EMU is made of an ortho fabric which is a combination of Gore-Tex Kevlar and Nomex that are covered in Teflon. This layer reflects sunlight with its white color, as well as acting as a strong, tear resistant barrier between the suit and its environment (1).

The Martian environment is dry, dusty, and cold. Temperatures range from -120 to 20 degrees Celsius. The gravity on Mars is twice the gravity of the moon, but still $\frac{1}{3}$ that of Earth. Therefore, an EMU would feel like it would weigh nearly 100 lbs on Mars. The atmosphere is made up of 95.3% carbon dioxide, and the air pressure is less than 1/100th that on Earth at 0.7 kPa (1). The existing suit would be able to handle the pressure difference because it was designed for the vacuum of space, but the outer materials of the suit would need to be non-permeable and non-degradable in a carbon dioxide heavy atmosphere. The average temperature on Mars is -63 degrees Celsius, so materials would have to be chosen that will not become brittle at cold temperatures. According to the Southwest Research Institute, even the shortest Mars mission would expose astronauts to 0.66 Sieverts of radiation from the sun. 1 Sievert of radiation absorbed by the body results in a 5.5 percent increase in the risk of contracting a fatal cancer (6). Another unique characteristic of Mars are dust storms. During a dust storm, wind speeds may reach up to 60 mph which is less than half the speed of a hurricane on Earth (7). 60 mph winds, paired with the comparatively miniscule air pressure, would most likely not cause much damage to equipment on Mars (aside from covering solar panels in a layer of dust).

Venus is known as Earth's sister planet because the two planets are roughly the same size. The gravity on Venus is 90% that of Earth, so an EMU built for the planet would need to cut weight significantly. Today's spacesuit would weigh 252 lbs on Venus. For comparison, on the moon an EMU would weigh a little less than 47 lbs (8). The atmosphere is made up of 96% carbon dioxide, and the air pressure is 90 times that of Earth (5). The pressure would be equivalent to diving 3,000 ft under the ocean, a feat which no human has ever done in a suit. Aside from the huge obstacle of pressure, the average temperature on Venus is 462 degrees Celsius (8). Winds around Venus reach 224 mph, but on the surface they decrease drastically to only a few mph (5).

Results Obtained

The first issue that would need to be addressed for a Martian space suit is the weight. Ideally, the weight would need to be cut in half in order to be comparable to the suit used in the Apollo moon walks. Removing weight from the existing EMU is a complex design problem that will involve taking a critical look at the design of every element of the suit. All pieces with non-essential functions will need to be removed, and new materials with lighter weight and similar functions will need to replace the current materials.

Because the Martian atmosphere is mostly carbon dioxide, the suit would need to be non-permeable and non-degradable in a carbon dioxide atmosphere. The Mylar layers that make up the majority of the TMG are non-degradable in a carbon dioxide atmosphere, but they are not entirely non-permeable. Based on a surface area of a 6 ft tall astronaut's suit, carbon dioxide would permeate the Mylar layers at a rate of 24.76 cc/hr/atm/mil in a 25 degree Celsius testing environment (3). However, the Mylar becomes less permeable at cold temperatures, so the frigid Martian atmosphere would provide added protection against carbon dioxide penetrating the suit. Other layers such as the pressure garment would

also act as added protection to prevent the carbon dioxide from contaminating the astronaut's air supply.

Another concern about sending an EMU to Mars is the extremely cold temperatures on the surface. The average surface temperature on Mars is -63 degrees. The outer layer of the space suit is made of a special blend of ortho fabric made from Gore-Tex, Nomex, and Kevlar fibers specially made specially to maintain flexibility at low temperatures. These materials would need to be tested at extremely cold temperatures to ensure that the fabric will maintain flexibility and not become brittle on Mars.

An astronaut's best defense against extreme temperatures in space is the Liquid Cooling and Ventilation Garment (LCVG). The human body generates heat that enters the layers of the suit, and the LCVG is designed to remove some of this heat. The resulting heat deficit is emitted into space via radiation. Figure 1 illustrates this concept. An EES model based on a 6 ft tall astronaut at the average temperature on Mars was created in order to determine the rate at which heat would need to be removed from the suit. On the Apollo missions, the astronaut's average heat generation was 197 kcal/hr or 229 W. The range of acceptable temperatures inside the suit were 10 degrees Celsius to 45 degrees Celsius (1). Based on the computer model, the LCVG would need to remove 214-219 W of heat from the suit in order to remain in the range of acceptable temperature. The LCVG on the current EMU can remove up to 291 W for a 7 hour spacewalk (1). Therefore, the current LCVG is more than capable of meeting an astronaut's needs on Mars. The formatted equations used in the EES Program are included in Figure 2.

Similar to the Martian suit, any space suit designed for Venus will require a significant weight reduction. Ideally, the weight would be reduced by a full 80% in order to be comparable to the weight of the suits used for moonwalks. Like with the Martian suit, weight will need to be a primary consideration when designing all parts of the EMU.

The atmosphere on Venus is made of mostly carbon dioxide, so the suit would need to be non-permeable and non-degradable in this type of atmosphere. The small amount of carbon dioxide infiltrating the Mylar layers of the suit at 25 degrees Celsius would be amplified on Venus due to the extremely hot temperatures. Testing shows that as the temperature of the Mylar increases, more carbon dioxide permeates the layers (3). Testing has not been done on Mylar at temperatures as high as the surface of Venus. More testing would be required to know how the material reacts under these conditions. However, because the permeability will only increase at higher temperatures, new materials will most likely be required in a EMU fit for exploring Venus.

Perhaps the largest obstacle to sending humans to Venus is the extreme atmospheric pressure at the surface. The only place on Earth with pressures similar to the surface of Venus is 3,000 feet below the surface of the ocean. NASA engineers should look to deep sea divers when considering ways for humans to survive this type of pressure. Deep sea diving suits have a hard exoskeleton that resists enormous pressures that would crush the human body. However, even the most advanced deep-sea diving suits used by the U.S. Navy cannot dive deeper than 2,000 feet (2). NASA and deep-sea divers will need to collaborate to construct currently non-existent solutions that will enable a human being to survive the pressure on the surface of Venus.

The existing materials that make up the EMU would be insufficient on the surface of Venus. For example, the Teflon coating on the outer layer of the EMU has a melting point of 327 degrees Celsius, over 100 degrees *colder* than the average surface temperature of Venus (4). All materials used to create

a space suit for Venus will need to be able to remain flexible, but resist being melted by the extreme heat at the surface.

Using the same EES model as before, with variables changed to reflect the surface of Venus the rate at which the LCVG would need to remove heat from an astronaut's body on Venus was determined. Based on these results, the LCVG would need to remove 288-293 W of heat from the suit in order to maintain acceptable temperature. The LCVG on the current EMU can remove up to 582 W for a 15 minute space walk or a maximum of 465 W for a 1 hour spacewalk. However, for a 7 hour spacewalk the LCVG maxes out at 291 W which is not sufficient for maintaining safe body temperature in the suit. Therefore, the LCVG is adequate for sustaining body temperature for shorter space walks (up to 1 hour) with a factor of safety of over 1.5. However, if longer spacewalks will be required, the LCVG will need to be changed to increase the maximum amount of heat it can disperse.

Significance and Interpretation of Results

This research has highlighted several areas of the existing EMU that will be sufficient to reuse in a suit built for Mars or Venus. For example, the existing LCVG would be acceptable on both planets at average temperature. However, based on the EES model, the LCVG would need improved for space walks on Venus lasting longer than one hour. Some areas will need to be improved to send a space suit to either planet. For example, the weight of the space suit will need to be reduced for each planet based on the differences in gravity. Innovation in life support technology and in the materials used in the construction of the spacesuit will be required to enable such drastic weight reductions.

More testing is required in some areas in order to fully understand how the existing EMU materials would react to the environments of Mars and Venus. For example, some of the materials in the EMU have not been tested on extreme temperatures. On Mars, the cold temperatures may make the materials brittle and rigid. On Venus, the materials may be too permeable to carbon dioxide, and some of the materials will even melt. More testing is required on all EMU materials based on how they would react with extremely high or low temperatures. In regards to a space suit that can survive on Venus, pressure is the biggest obstacle. Though NASA should look to deep sea divers for innovation, more work is required on both sides before a spacewalk on the surface of Venus will be possible.

Figures

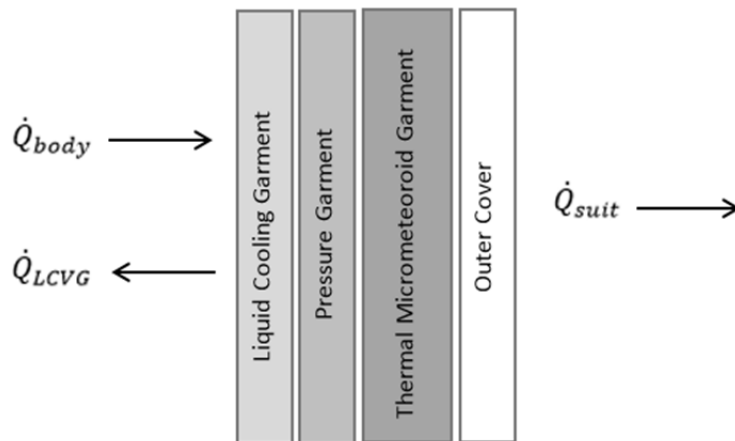


Figure 1. Model for Heat Transfer to and from the Suit

Constants

$$\varepsilon = 0.9$$

$$\sigma = 5.67 \times 10^{-8} \text{ [W/m}^2\text{K}^4\text{]}$$

Found Values

$$R_{\text{value}} = 17 \text{ [(K}^2\text{m}^2\text{W)}] \text{ based on 5 layers of Mylar in the TMG}$$

$$A = 1.31 \cdot 1.83 \text{ [m}^2\text{]} \text{ based on 6ft tall}$$

$$T_{\text{inside}} = 10 \text{ [deg-C]} \text{ lowest acceptable = 10 deg C, highest = 45 deg C}$$

$$T_{\infty} = -63 \text{ [deg-C]} \text{ -63 deg C for Mars, 462 deg C for Venus}$$

$$\dot{Q}_{\text{body}} = 229 \text{ [W]}$$

Temperature Conversions

$$T_{\text{surface,K}} = T_{\text{surface}} + 273 \text{ [K]}$$

$$T_{\infty,K} = T_{\infty} + 273 \text{ [K]}$$

$$T_{\text{inside,K}} = T_{\text{inside}} + 273 \text{ [K]}$$

Heat Transfer Equations

$$\dot{Q}_{\text{suit}} = \varepsilon \cdot \sigma \cdot A \cdot (T_{\text{surface,K}}^4 - T_{\infty,K}^4)$$

$$\dot{Q}_{\text{suit}} = \frac{(T_{\text{inside,K}} - T_{\text{surface,K}}) \cdot A}{R_{\text{value}}}$$

$$\dot{Q}_{\text{body}} - \dot{Q}_{\text{LCVG}} = \dot{Q}_{\text{suit}}$$

Figure 2. EES Program Used to Calculate Heat Transfer Rate to the LCVG

References

1. Gon, Debi Prasad, and Palash Paul. "Complex Garment Systems to Survive in Outer Space." *Journal of Textile and Apparel, Technology and Management* 7.2 (2011): 1-25. Web.
2. "Military Atmospheric Diving (ADS)." *Military ADS | OceanWorks*. OceanWorks International, n.d. Web. 25 Feb. 2017.
3. *Mylar: Polyester Film*. Rep. Hopewell: DuPont Teijin Films, n.d. Web.
4. "Properties of Teflon™ Industrial Coatings." *Properties of Teflon™ Coatings | Intech Services*. Chemours Company FC, LLC, n.d. Web. 25 Feb. 2017.
5. Reed, Nola Taylor. "Venus' Atmosphere: Composition, Climate and Weather." *Space.com*. Purch, 16 Nov. 2012. Web. 19 Feb. 2017.
6. Tate, Karl. "How Radiation in Space Poses a Threat to Human Exploration (Infographic)." *Space.com*. Purch, 30 May 2013. Web. 19 Feb. 2017.
7. "The Fact and Fiction of Martian Dust Storms." *NASA*. NASA, 18 Sept. 2015. Web. 19 Feb. 2017.
8. Williams, Matt. "Venus Compared to Earth." *Universe Today*. N.p., 07 Apr. 2016. Web. 19 Feb. 2017.

Projectile Motion: A Manned Mission to the Moon and Mars
Grade: 4 and up

Student Researcher: Kenton C. D. Jarvis

Advisor: Dr. Todd France

Ohio Northern University
Department of Education and College of Engineering

Abstract

This lesson plan will explore the topic of projectile motion on Earth, Moon, and Mars. It is primarily project-based learning with key engineering concepts incorporated.

Lesson

Over the course of a week groups of 3 or 4 students will work together to research, design, and prototype a rocket from supplied materials. Research should consist of materials used on actual rockets and planes, amounts of thrust each uses to sustain flight, and other forces acting upon rockets and planes. The designs will need to account for carrying a payload of varying size and weight. The varying weight will help simulate the difference in gravitational forces among the Earth, Moon, and Mars.

(Assuming one hour classes every day/ can be modified to accommodate block scheduling)

Monday

- Students should be told to do research the weekend before Monday class time so they can get together in groups and compare research.
- Monday's class should be used to introduce the project and talk about the objectives of the project. Monday's homework will be to individually design a rocket with dimensions.

Tuesday

- Tuesdays class will be spent discussing designs within the teams. Teams can then take the rest of class time and homework to finalize a design.

Wednesday

- Build day

Thursday

- Build day

Friday

- Friday's class time will be spent collecting mass and distance data. Each team will test its rocket 10 times with each of the three payloads, recording the distance their rocket traveled each time.
- The weekend will be used to create a brief summary of why that team thinks their project is the best. The summary should include things like:
 - What their research was focused on.
 - Materials used on real rockets.
 - Summary of their test data.
 - How their design could have been improved.

Objectives

By the end of this activity students will be able to:

1. Explain gravity and prototyping
2. Understand the differences in gravity among the Earth, Moon, and Mars.
3. Forces that affect projectile motion.

Alignment

MS-ETS1-4. Develop a model to generate data for iterative testing and modification of a proposed object, tool, or process such that an optimal design can be achieved.

RST.11-12.7 Integrate and evaluate multiple sources of information presented in diverse formats and media (e.g., quantitative data, video, multimedia) to address a question or solve a problem. (HS-PS2-1)

MP.2 Reason abstractly and quantitatively. (HS-PS2-1),(HS-PS2-2),(HS-PS2-4)

Underlying Theory

Using the universal design for learning as a template for this lesson plan, students will be able to use scaffolding to build off previously learned topics and apply them to this project. This project provides both hands-on learning for the kinesthetic learner and a brief summary for students that prefer more visual learning. Students will build teamwork and problem solving skills by having to communicate in a team based environment.

Resources/ Supplies

Reusable:

1. Rulers (1 per group)
2. Measuring tape (1 per launching platform)
3. Air compressor
4. Air hose (10ft minimum)
5. Air hose splitter
6. PVC/Metal piping
7. 3 ball valves
8. Scissors (1 per group)
9. NASA video
10. 2x2 Lego squares (6 blocks per group)

Non-reusable:

1. Printer paper
2. Construction paper
3. Masking tape



Setup Instructions: All connections should be sealed by thread seal tape.

1. Connect air compressor hose splitter to compressor valve
2. Connect air hose to splitter
3. Connect hand held launcher to air hose
 - a. Launcher build:
 - i. $\frac{1}{2}$ " diameter x 12" steel nipple connected to $\frac{1}{2}$ " diameter 45 degree steel elbow joint
 - ii. The elbow joint is connected to a $\frac{1}{4}$ " to $\frac{1}{2}$ " steel bushing
 - iii. The bushing is then connected to $\frac{1}{4}$ " x 4" Brass pipe nipple
 - iv. The brass nipple then connects to a $\frac{1}{4}$ " ball valve

Results

While some groups struggled with their designs at first, only a few did not launch on the first try. After a quick redesign, all students could launch their rockets. Distances varied between 2 feet and 20 feet. Students discovered that if they made the body of the rocket longer they could catch more air and achieve a higher velocity off the launcher. Some students made capsules inside the fuselage of their rockets to carry the payload. Other students put the payload inside the nose cone. Students could notice that the different payloads did cause changes in distance traveled.

Example Setup and Rocket



Assessment

Students test results should be recorded in the table provided. Then students are to graph their data points and calculate the average distance traveled for each payload. Students are then required to make inferences on how their design could be improved based on their research and data.

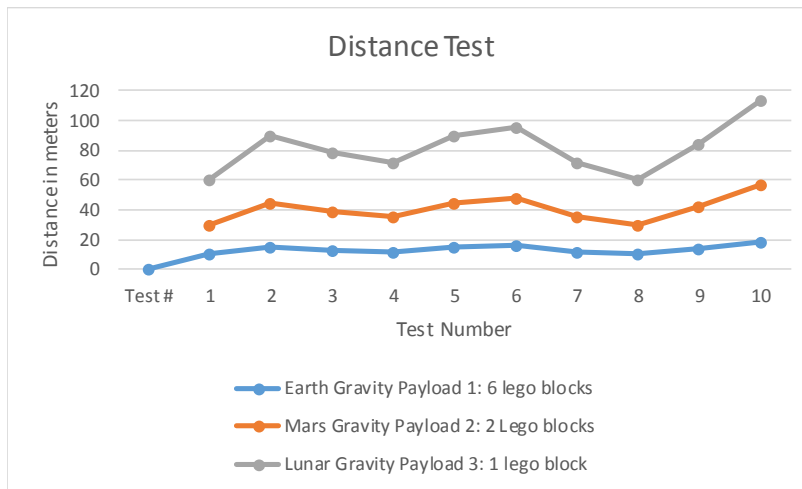


Questions to Ask

1. How is the mass of the payload related to the distance traveled?
2. How would mass of the payload relate to the rockets fuel consumption?
3. Which designs seemed to work better?

Example Diagrams

	Earth Gravity	Mars Gravity	Lunar Gravity
	Payload 1: 6 lego blocks	Payload 2: 2 Lego blocks	Payload 3: 1 lego block
Test #	Distance in Meters		
1	10	30.00	60
2	15	45.00	90
3	13	39.00	78
4	12	36.00	72
5	15	45.00	90
6	16	48.00	96
7	12	36.00	72
8	10	30.00	60
9	14	42.00	84
10	19	57.00	114
Average Distance (m)	13.6	40.8	81.6



Conclusion

At the end of the activity, students had a tangible way of representing projectile motion and observing the forces acting on the projectile as it flies. Students were able to see how different simulated gravitational forces changed distance traveled.

References

1. Exploring Your Weight Across the Solar System - NASA. (n.d.). Retrieved March 28, 2017, from <https://nasasearch.nasa.gov/search?query=11.1%2B%2Bspace%2Bmath%2Bexploring%2Byour%2Bweight%2Bacross%2Bthe%2Bsolar%2Bsystem%2B&affiliate=nasa&utf8=%E2%9C%93>
2. HS.Forces and Interactions. (n.d.). Retrieved March 28, 2017, from <http://www.nextgenscience.org/topic-arrangement/hsforces-and-interactions>
3. D. (2013, April 06). NASA Space Shuttle Launch from Onboard Camera, STS 112. Retrieved March 28, 2017, from <https://www.youtube.com/watch?v=ZFUm-HSPV5I>

Pipe Reconstruction and Water Flow on Central State University's Campus

Josephine Johnson

Dr. Krishnakumar Nedinuri

Central State University

Department of Water Resources Management

Abstract

In 1887, Central State University was born. With the construction of the University, they had to think of where all the water comes from. Central State had water coming in from 3 different distributions systems. The water was being supplied from Greene County, Xenia and of course their every own distribution system on the campus its self. Over the years Central State has expanded and stops using their own water Distribution center. Now in 2016 new buildings have been added and with that came their pipeline. The goal of this study is to figure out the amount of water pressure is used in each pipe along with how much water is being used throughout the campus. Figuring out if it is the best and most cost effective way.

Objective

Central State University (CSU) established in 1887, is one of 102 Historically Black Colleges and Universities (HBCUs) in the U.S. located in Wilberforce, Ohio (Figure 1.1). In 2014, CSU received designation as an 1890 Land-Grant Institution. CSU has a water system that serves a population of approximately 2,300 people (1800 students and 500 employees) including students and University staff. The water source consists of four groundwater wells, with iron and manganese removal and chlorine disinfection making up the water treatment process. Historically, the university used to supply its own water to the consumers. Four 10 HP submersible turbine pumps with a maximum capacity of 80 gpm and 250 ft total dynamic head each (three from a wellfield near Massies creek about one and a half mile from the campus and fourth inside the campus behind Center on Aging building) supplied water to the campus at from its four groundwater wells about 100 ft. deep. The university discontinued the existing system in 2015 and acquiring water from the City of Xenia using an existing auxiliary water supply via the 10 in. ductile iron main cross-connection. Two 20 HP high service submersible pumps distributed water to the campus using a 10 in. main feeder line and auxiliary 6 in. and 8 in. lines and pumped water to a 150 feet elevated storage tank about 50 ft. in diameter and 30 ft. deep. The university plans to increase its enrollment to 3000 in the next 10 years. A new student center has been added to the campus in 2015. The university also attained land grant status in 2014 which will allows it to make use of its current 500 acre land for experimental research in agriculture, food and natural resource conservation. The university will also expand its infrastructure to add an additional agriculture building, expand current building for extension activity, and build a new building for agriculture administration with an anticipated increase in staff by about 200. The anticipated need is to supply water for the proposed expansion projects in the most economical way satisfying different uses.

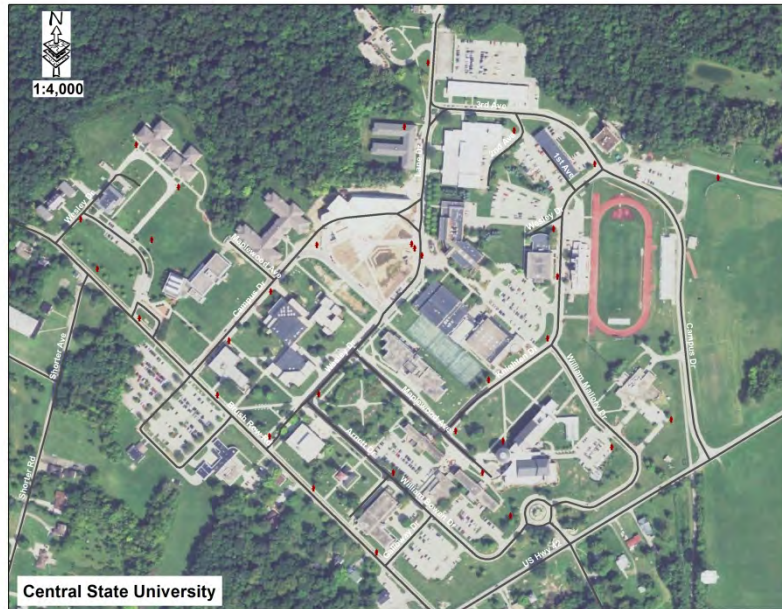


Figure 1.1. Aerial Map of Central State University

Methodology

The university neither has a digitized map of water distribution nor an updated paper copy of campus water infrastructure. Hence our first task was to develop for the first time in the campus a georeferenced water distribution system. The only available version of campus map with water distribution information is from an old 1987 map. The map was available in six pieces at a scale of 1 inch to 40 feet. This old map was taken to One Point Design Architectural Firm for scanning to the scale. All the six sections of the scanned map were digitally stitched using Photoshop which is shown in Figure 2.1.

All of the hydrants on the campus pipe distribution were located, their GPS coordinates and elevations were recorded as shown in Table 2.1 in Appendix B, and imported onto ArcGIS as a layer. The tank is about 165 feet from the ground, height of the stand pipe is 125 feet and that of the reservoir 40 feet. It has a storage capacity of 500, 000 gallons. The tank maintains a maximum pressure of 70 psi in the distribution. Two 20 HP high service pumps were deployed to pump water from the clear well to the elevated storage tank and the entire water distribution system when CSU plant was in operation. Currently, the campus receives water from the city of Xenia through a 10 inch cross-connection which connects to the campus network at the booster station. The booster station has pumps with a capacity of 275 gpm at 167 feet of total dynamic head. The distribution consists of 5600 feet of 6-inch, 1300 feet of 8-inch, and 12800 feet of 10-inch ductile iron pipes ranging from 60 year old pipes to newly replaced pipes that are two to five years old. The water distribution base map was updated through a field survey of current distribution system with assistance from CSU water plant operator Mr. Robert Oatneal. Figure 2.3 shows the updated pipe distribution.

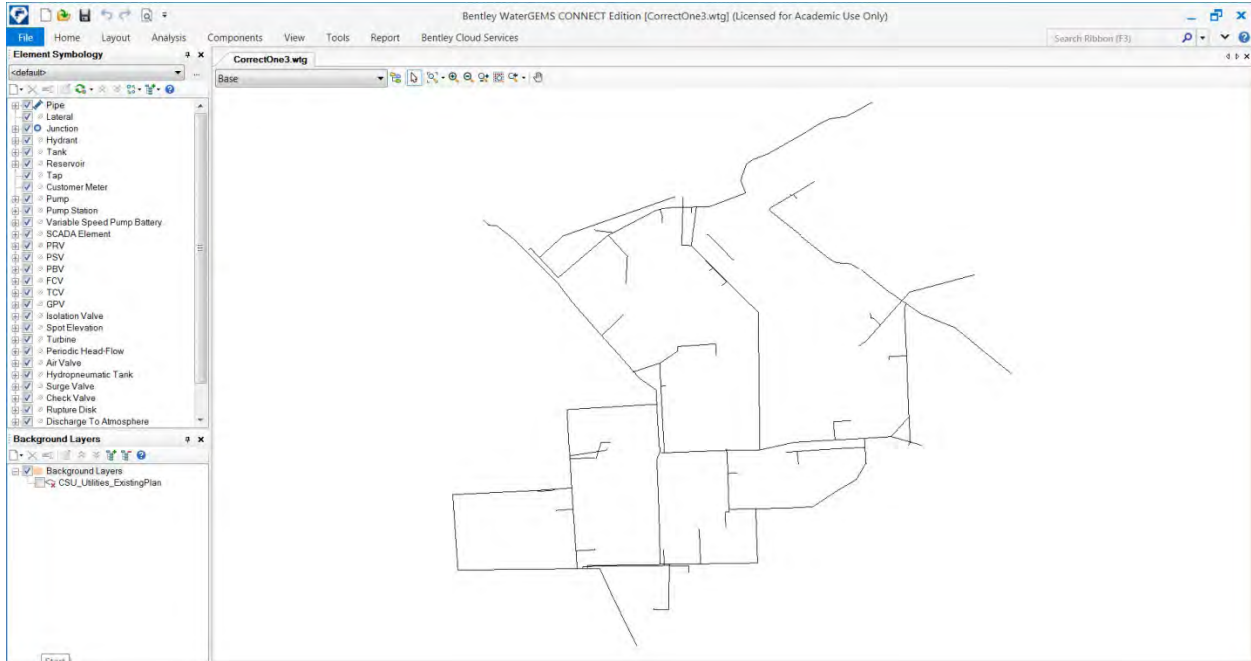
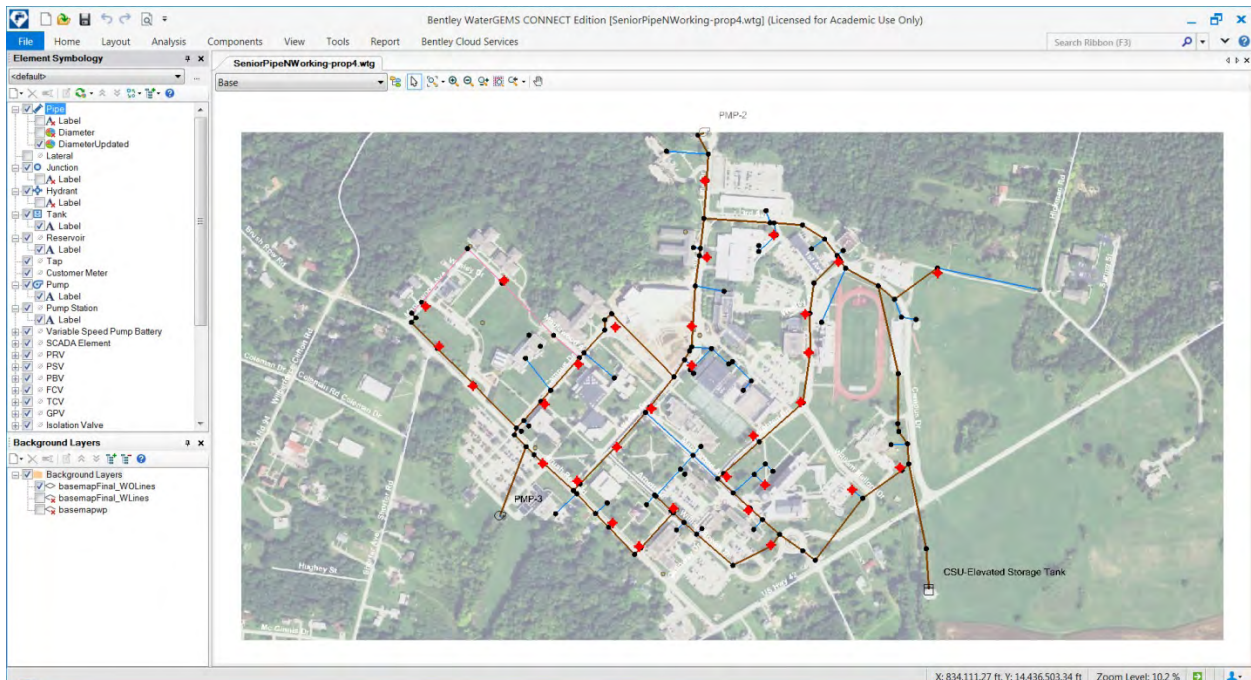


Figure 2.3. CSU water distribution updated on WaterGEMS from the traced 1987 distribution

The next step was to overlay the updated pipe network onto CSU campus layout. The updated pipe network CAD drawing was imported into ArcGIS through WaterGEMS to ArcMap conversion tool. It was then georeferenced using *editor* and *spatial adjustment* toolbars by taking GPS coordinates of eight actual locations on the pipe network. The CAD drawing was saved as a shapefile. GPS coordinates of hydrants, elevated storage tank, high service pump station, water treatment plant and booster statwere also recorded and saved as shapefiles. A screenshot of a campus map with pipe accessories is shown below:



Results

The entire campus was divided into three sections – academic units, administration buildings and residence halls. Students taking courses in each building was collected and classified into freshman, sophomores, juniors and seniors. The time spent by these students taking classes was estimated and equivalent number of students on an 8-hour shift calculated and added to the full time staff within the buildings working on an 8-hour shift to get the total daily occupancy. The occupancy was multiplied by per capita water consumption from IWR-Main to calculate daily demand. The daily demand for administration building and residence halls was estimated by multiplying the occupancy with the per capita consumption typical to these type of units. These calculations were shown in Table 2.2 in Appendix B.

The city of Xenia, OH Water Treatment Plant conducted hydrant flow test in 2015. Hydraulic calibration is achieved by comparing model predicted results with actual hydrant data obtained by the hydrant flow tests. Static pressure at a hydrant was first measured. The second hydrant was then opened to measure the flow in the pipe connecting the two hydrants and residual pressure at the first hydrant is measured. Hydrant data is collected through six pressure loggers that were placed around the distribution system and will be used for calibration. The hydrant tests were repeated using the campus pipe distribution in Bentley software. The pressures and flows were computed at the hydrants and compared with measured pressures and flows from the hydrant tests as shown in Table 2.1.

Model scenarios for each test were created and demands for each scenario scaled to the system demand of 220,000 gpd. The recorded hydrant flow for each test were added as a large demand to the hydrant location in the model. Pressure readings in the model before and after turning on the hydrant were compared to the results from hydrant flow tests.

The hydrant flow test procedure has several steps. Two hydrants, one flow hydrant with a diffuser and another residual hydrant with a pressure gage are a part of each flow test. Any closed valves, pipe breaks or other emergency pertaining to the water system that arouse from the testing should be reported to a BC representative.

The first step of a hydrant flow test is to synchronize watches of all personnel conducting the test with the City's SCADA system time. Next the set-up of a pressure gauge at the residual hydrant; this is done by removing the cap from the 2-1/2 inch nozzle and opening the hydrant valve to flush the barrel, then attaching the pressure gauge. The static pressure should then be recorded at the residual hydrant, the location of both hydrants and the time of the test should also be noted. Flush the flow hydrant to remove any debris that could be damaging to the diffuser or obscure the results of the test prior to installation of the diffuser to the flow hydrant. Once the pressure gage and the diffuser are in place, the test can proceed.

One hydrant test should be performed at a time. The test coordinator will ensure that only one test is being conducting at any one point of time. The test coordinator is responsible for instructing a fellow team member when to open the hydrant at a minimum 5 psi pressure drop flow. If 5 psi cannot be achieved, a second diffuser can be added and the step can be repeated. Once the residual hydrant pressure stabilizes, the test coordinator will ask for the flow from the flow hydrant and the pressure from the residual hydrant and record the information and the time. After the data is collected, the test coordinator will instruct the close of the flow hydrant. The flow hydrant must be closed slowly to prevent damage to the pipes that could be caused by water hammer. The test coordinator once again records the static pressure from the residual hydrant. The equipment can now be removed and the next

site can be tested. However, if a C-factor test is scheduled at any of the test locations, closing the system valves so that the water can be supplied to the hydrant through only one direction should isolate the pipe supplying the water to the hydrant. Afterwards, repeat the test and the equipment can be removed after the last record of the static pressure.

Acknowledgements

I would like to thank The Ohio Space Grant Consortium, Central State University, The city of Xenia and Greene County for allowing the project to be possible.

You Can't Handle the "Physically Correct" Truth

Student Researcher: Zachary Kordeleski

Advisors: Dr. Kristine Still and Paul Lockhart

Cleveland State University
Department of Physics, Mathematics, and Education

Abstract

Misconceptions in the sciences are especially numerous and of significant enough concern to warrant a special section in many curricula. We identify a main cause of this to be the portrayal of these misconceptions in popular media and film. With the prevalence of media increasing constantly in the tech-centric environments our students live in, exposure to these misconceptions grows increasingly larger. As such, we feel it both beneficial and culturally relevant to analyze physics in popular movies to identify artistic liberties writers and directors have taken portraying physical events.

Lesson

Students will analyze real-life footage of physical interactions involving the transfer of momentum between objects to derive the conservation laws and identify flawed movie physics.



- **Engage:** In the past, directors use clever filming tricks to make the impossible seem possible and C.G.I. has made this task ever simpler. Students select movie scenes that seem to violate the fundamental laws of physics and must explain why using Newton's three laws.
- **Explore:** Students explore real-life footage as they uncover the concept of momentum. By studying launch footage of the Juno space shuttle and more, students discover the law of conservation all while simultaneously learning to use video analysis software!
- **Explain:** The crux of momentum transfer is collisions. Students analyze footage of car crash tests to determine momentum transfers between objects and the role seatbelts play in impulse.
- **Elaborate:** Students analyze their flawed film scenes using the same video analysis software to spot errors in the film! Using their data, they must identify the laws being violated and how!
- **Evaluate:** The culmination of this project is a movie themed presentation format. Students present their findings to their peers and discuss their results with others. Multiple assessment types of available to choose from including the construction of scaled down model of the scene!

Objectives

- Students will use Newton's laws to describe the flawed physics in their scene of choice.
- Students will be able to analyze data in order to determine a relationship between the mass and velocity of two objects that are brought into contact.
- Students will be able to identify how conservation of momentum, elastic, and inelastic collisions and impulse apply to their movie scene and correct any flaws.

Alignment

Advanced Physics: *Momentum, Impulse and Conservation of Momentum with constant force*
Next Gen. Standards: HS-PS2-2 Motion and Interactions: Momentum Conservation

Underlying Theory

This unit was designed with as a project based learning (PBL) unit composed of many 5E lesson plans spanning the course of an entire unit on momentum. The 5E learning model is a lesson template based on the constructivist approach to learning. Each lesson contains an *Engage, Explore, Explain, Elaborate, and Evaluate* wherein students explore the physics just as true scientists would experiment and research.

Engaging the students in the learning process may be the most important role of an instructor and using film helps keep the content culturally relevant to the students. Students analyze real, observable events like the Juno shuttle launch to derive concepts such as the conservation of momentum. Each independent, student discovery builds upon the previous until students finally apply all of their gathered knowledge to a film of their choosing as they explore the artistic liberties taken by the film industry.

Student Engagement

The unit has proved to be incredibly engaging and enlightening for students. The lessons involving the crash test dummy analysis changed the perspectives of many students on seat-belt usage after they calculated the force of impact with and without protection. Moreover, analyzing real footage of events like the Juno shuttle launch and famous scenes from popular movies inspired students to experience films, videos and other popular media as more involved, less passive viewers.

Resources

- Computers are a necessity for the video analysis portions of this project
- Footage is required of: The Juno shuttle launch, a car crash test collision with and without seat-belts (available from most BMV's online), and scenes from popular films to analyze!
- Video Analysis: Free in several in-browser formats online or with Vernier's LoggerPro software
- Whiteboards, markers and erasers for lab presentations and data analysis

Results

Fantastic results were produced both in terms of student understanding and student output. In addition to student seatbelt usage rising significantly, the class has learned to watch interact with media in a much less passive way. When popular films were put under the microscope, students found very few examples of scenes which paid proper homage to the laws of physics.

Assessment

Students continually gather data and design whiteboards to portray and present their findings to the classroom. These ongoing assessments help instructors gauge the progress of the class as well as provide opportunity for the class to discuss each lab group's results. Multiple assessments are available as students may select from a more physically correct reenactment of their scene or a scaled down model of their chosen movie clip.

Conclusion

The use of culturally relevant material such as film is a wonderful way to give students the initial push necessary to continually drive their interest in the subject matter. We discovered, as a class, that we as scientists need to try and encourage truer depictions of physics in our media. Physics, perhaps more than any other field, is riddled with misconceptions and the film industry helps perpetuate this reality.

Eradicating Bacteria Using Ultraviolet Light

Student Researcher: Kayle L. Kornblum

Advisor: William Lane III, P.E.

Cuyahoga Community College
Electrical/Electronic Engineering Technology

Abstract

Using Ultraviolet light to eradicate bacteria has been increasingly used in many different applications over the past few years or so. Some experiments and studies have been conducted regarding the use and effectiveness of ultraviolet light. Without ultraviolet light, companies have resorted in using chemicals that are directly used in water to kill the bacteria in them. Not many see the resulting effects on using chemical in the water to kill the bacteria. From personal experience, our water (particularly the northern parts of the United States) have much more cholera and other chemicals used to kill bacteria in it and the result was hair loss and chronic dry skin. In contrast, changing the source of drinkable water can greatly improve the impact it has on the environment and on society.

Project Objective

My objective is to research and conduct a way of using ultraviolet light for drinkable water and research using photovoltaics as a source of energy.

Methodology Used

I used information that I have obtained when conducting my research involving the use of ultraviolet light for a water bottle, particularly the Camelback UV (ultraviolet) Water Bottle. This invention focuses on the effectiveness and use of ultraviolet light for the eradication of bacteria. This water bottle treatment can rid of any bacteria in a minute and it has been tested and proven safe for drinking after it has been treated in that water bottle. I decided to change the idea of that invention, making a water bottle sleeve instead of making a water bottle to use. Also, changing the source of energy to power the ultraviolet light so you do not need to worry about needing to charge the product before you plan to leave resulting that this product is safe to use with almost all water bottles and can be used for off grid exploration.

Results Obtained

Results from this data that I have researched and from the data I have gain from performing my own experiment provided needed information on the effectiveness and the use of using photovoltaics as a power source and the effectiveness of using ultraviolet light to eradicate bacteria and turning the water into a safe source. These results for my experiment have shown that using the water bottle sleeve is still just as effective than using the light to directly touch the water. It can be used in five minutes to eradicate the bacteria efficiently and effectively. The results to use ultraviolet light in industry is currently being conducted.

Significance and Interpretation of the Results

From performing my own experiment, I have proved that the use of ultraviolet light powered by photovoltaics is a safe and efficient way can lead way for huge developments in the future for industry and personal usage. With this data now known, research and future experiments can lead to new inventions for the future.

References

1. Mac. "CamelBak All Clear UV Water Purifier Review." *Halfway Anywhere*. N.p., 04 Jan. 2017. Web. 6 Mar. 2017. <http://www.halfwayanywhere.com/reviews/review-camelbak-all-clear-uv-water-purifier/>.
2. How does ultraviolet light kill cells? (2002, February 19). Retrieved March 6, 2017, from <https://www.scientificamerican.com/article/how-does-ultraviolet-ligh/>.
3. Ultraviolet germicidal irradiation. (2017, March 25). Retrieved March 7, 2017, from https://en.wikipedia.org/wiki/Ultraviolet_germicidal_irradiation
4. CONTAINERISED WASTEWATER SYSTEM TO PROVE 70% EFFICIENCY CLAIMS IN ALGERIA. (2017, March 15). Retrieved March 19, 2017, from <http://www.waterworld.com/articles/wwi/2017/03/containerised-wastewater-system-to-prove-70-efficiency-over-mbr-mbbr-in-algeria.html>

Searching for Brown Dwarfs and Ultra Cool Dwarfs in the Orion Molecular Clouds

Student Researcher: Heidi E. Kuchta

Advisor: Dr. Thomas Megeath

The University of Toledo

Department of Physics and Astronomy

Abstract

Studying the formation of very low mass objects, ranging from the lowest mass stars to the most massive planets, can provide new insights in to star and planet formation. This can help us understand the processes that determine the masses of stellar objects and can help us understand the formation of planets such as those in the newly discovered Trappist 1 system. By finding the ratio of the number of stars to brown dwarfs and to ultra-cool dwarf stars, we can look for variations in the relative numbers of brown dwarfs and stars formed in regions with different birth environments. This will help us understand the processes that determine the masses of young stars. For these reasons, I am looking for brown dwarfs and ultra-cool dwarfs in the less populated regions of the Orion Molecular Cloud. This is being done using data taken in the visible and infrared bands. We have 10 fields in the Orion A cloud taken with the Discovery Channel Telescope. Of these, 184 of the stars have I and z magnitudes. The data from these has been reduced and analyzed, and combined with infrared data taken with Spitzer and NEWFIRM. Once candidate brown dwarfs and ultra-cool dwarf stars are found from this list they will be the targets of spectroscopic observations with the DCT to confirm their identity.

Project Objectives

Brown Dwarfs have masses between the masses of planets and stars. Their masses are too low to start nuclear fusion, but unlike planets they float freely in space. Ultra-cool dwarf stars are stars that are just above the hydrogen burning limit. The ratio of the number of brown dwarfs to the number of stars is an important constraint on models of how stars and brown dwarfs form. This number can be best measured in young star forming regions where young stars and brown dwarfs are still relatively luminous. This ratio has been measured in clusters of young stars and is around 0.2, two brown dwarfs for every 10 stars. (Luhman et al 2012). However, the ratio may vary with the conditions in the birth environment. We are looking for those variations by looking at regions in the Orion clouds that are forming stars but which have much a lower density of stars than the clusters, and thus a different birth environment than stars in clusters. Variations would allow us to test models of how stars and brown dwarfs form. Furthermore, identifying young cool dwarfs with disks will provide us a sample of objects to study the formation of systems like Trappist-1.

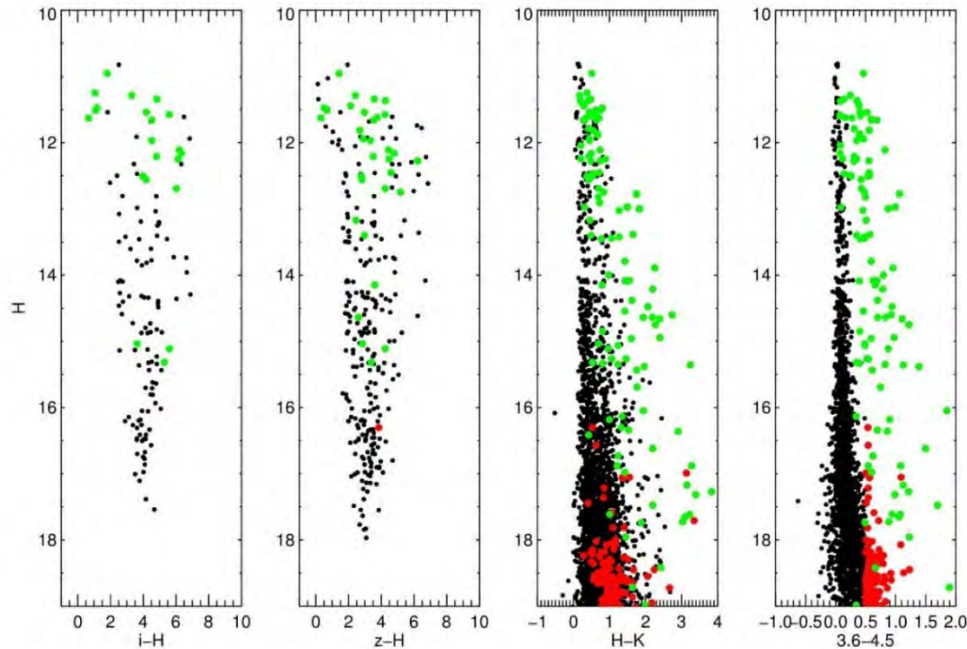
Methodology Used

The images taken with the Discovery Channel Telescope, hereafter DCT, were reduced using standard methods utilizing flatfields and biases. The reduced images were stacked together to form a mosaic. Then the mosaics were calibrated using standards from Smith et al. (2002). Using the program photvis, all the stars in the field were identified and then converted into a data array. The array of DCT data and was combined with the data arrays from Herschel and Spitzer Space Telescope.

Results Obtained

We have turned this array into the graph shown below. The graph shows color magnitude diagrams for four main bands that we are working with. The symbols are all of the stars that show up in all four color bands. The red symbols are the stars are the candidate brown dwarfs. These were chosen because they deviate from the main body of stars in the 3.6-4.5 band suggesting they have an infrared excess due to

the presence of a disk. The green symbols are confirmed infrared excess sources from Megeath et al (2012); these are young stars with dusty disks or infalling envelopes. This gives us a starting list of candidate Brown Dwarfs and Ultra-cool dwarf stars, but the list will still need to be modified. We will begin looking through the candidates throwing out objects in the foreground and background including background galaxies. Once the list has been reviewed we will apply for time at the DCT for infrared spectroscopy. By doing this we will be able to confirm whether these objects are bonafide brown or ultra-cool dwarfs.



Significance and Interpretation of Results

Both the newly found Trappist-1 system and the Initial Mass function, IMF, represent areas of astronomy that provide future possibilities for research of this type. The Trappist- 1 system is constructed of seven planets orbiting an Ultra-cool dwarf star congruent to the type of objects we are looking for (Gillon et al. 2017). If any such objects are found, they could be put under closer scrutiny to determine if they could form similar systems. The Initial Mass Function shows the distribution of stars based on their mass (Smith et al.). The IMF is uncertain for objects below the hydrogen burning limit. The data from this project in conjunction with other surveys across the Orion Molecular Clouds could be used to help determine the lower mass end of the IMF.

References

1. "Seven temperate terrestrial planets around the nearby ultracool dwarf star TRAPPIST-1" Gillon et al. 2017 Nature 456–460.
2. "The Formation and Early Evolution of Low-Mass Stars and Brown Dwarfs" Kevin L. Luhman, 2012 Annual Review of Astronomy and Astrophysics, 2012, 50, 65–106.
3. "The Spitzer Space Telescope Survey of the Orion A and B Molecular Clouds. I. A Census of Dusty Young Stellar Objects and a Study of Their Mid-infrared Variability" S.T. Megeath 2012 The Astronomical Journal, Volume 144, Issue 6, article id. 192, 27 pp.
4. "The u'g'r'i'z' Standard-Star System" Smith et al. 2002 The Astronomical Journal, Volume 123, Issue 4, pp. 2121-2144.

Aging of Photovoltaic Solar Panels

Student Researcher: Jeffrey M. Kudrna

Advisor: Joseph Arendt, Ph.D.

Cuyahoga Community College

Electrical / Electronic Engineering Technology

Abstract

This paper looks at why and how much Photovoltaic solar cells lose efficiency as they age.

Project Objectives

Solar panels typically degrade faster in the first couple of years of their life.[2] Three known methods of loss of efficiency are potential induced, light induced, and ultraviolet light degradation.[6] Nehme et al. have developed a mathematical model for loss of efficiency using these three known methods of degradation. [6] Solar panels are often constructed easier, faster and less expensively with amorphous silicon, but these degrade faster than the crystalline solar panels. [1] One cause of loss of efficiency of amorphous silicon solar panels is the Staebler-Wronski effect, but application of an electric field may slow this process. [5] For a study by the Electric Power Research Institute (EPRI), Southern Company has been experimenting with the process of controlling the heating and cooling of the solar panels to see how this process ages the panels. [3] This is being compared with solar panels that have aged naturally. This research can show whether an existing solar panel that has lost efficiency as the result of natural aging. [3] Dirt and pollen can reduce the efficiency of how solar panels produce, but this can be restored with cleaning. [2,3] For amorphous silicon solar panels that lose efficiency by the Staebler-Wronski effect, application of a strong electric field may slow this process. [5]

Methodology Used

We did a literature search. We used the Cuyahoga Community College library, The Cleveland State University Library, IEEE online resources, and other online resources.

"The rated power output of solar panels typically degrades at about 0.5%/year." [1,4] Using the average loss of 0.5% efficiency per year and assuming a warranty period of 25 years, it will still operate at 88% of its expectancy. Some solar panels do not degrade that quickly because examples exist that after over 30 years old still outperform their originally specifications, but investigation continues as to how to improve all solar panels to do likewise. [4]

Solar cell type Output loss in percent per year

Pre Post

Amorphous silicon (a-Si) 0.96 0.87

Cadmium telluride (CdTe) 3.33 0.4

Copper indium gallium selenide (CIGS) 1.44 0.96

Monocrystalline silicon (mono-Si) 0.47 0.36

Polycrystalline silicon (poly-Si) 0.61 0.64

Pre and Post refer to installations prior to and post 2000. Data is taken from Photovoltaic Degradation Rates — An Analytical Review NREL.[1]

Acknowledgments

I would like to thank Joseph Arendt, Ph.D. and Lam Wong.

References

1. National Renewable Energy Laboratory (NREL), [2] Renewable Energy World, [3] Inhabitat, [4] Kyocera.
2. Accessed 2/23/2017
The Real Lifespan of Solar Panels
Last updated May 7, 2014 by Mathias Aarre Maehlum
<http://energyinformative.org/lifespan-solar-panels/>
3. Accessed 2/23/2017
Research explores effects of aging on solar panels
Last updated February 9, 2017
<http://www.southerncompany.com/newsroom/2017/feb-2017/2017-02-09-researchon-aging-on-solar-panels.html>
4. Accessed 2/23/2017
How Long Will Solar Panels Last?
October 19th, 2015
<https://cleantechnica.com/2015/10/19/how-long-will-solar-panels-last/>
5. Andrea Scuto; Marina Foti; Cosimo Gerardi; Anna Battaglia; Salvatore Lombardo, Published in: Reliability Physics Symposium (IRPS), 2016 IEEE International
Date of Conference: 17-21 April 2016, Electronic ISSN: 1938-1891, INSPEC Accession Number: 16338093, Publisher: IEEE, <http://ieeexplore.ieee.org/document/7574524/>
6. Bechara Nehme; Nacer K. M'Sirdi, Tilda Akiki, Aziz Naamane. Contribution to the Modeling of Ageing Effects in PV Cells and Modules, Energy Procedia, Volume 62, 2014, Pages 565-575, 6th International Conference on Sustainability in Energy and Buildings, SEB-14
<http://www.sciencedirect.com/science/article/pii/S1876610214034493>

Arugula Plants and Their Various Responses to H₂O₂

Student Researcher: Maiya A. Kyles-Stewart

Advisor: Professor Douglas Bradley-Hutchison

Sinclair Community College

Biology Program

Abstract

This is a study of the possible effect(s) of hydrogen peroxide (H₂O₂) on the growth rate of arugula plants starting from seed germination to leaf production. The length of the stems, leaves, and cotyledons were measured for the control and experimental groups. *All of the seeds were grown in "Sta-Green" Moisture Max Potting Mix + Fertilizer and were given about ½ tea spoon of water 5-6 times each week. In addition, 5 drops of hydrogen peroxide were given to the experimental group 3-4 times each week.* Growth rates were based on the data. Our results demonstrate that the stem length in the control and experimental groups were not significantly different, but the length of the cotyledons greatly differed. The possible effect of the leaf length and the results from ongoing work are still in progress.

Project Objective

My objective is to determine if H₂O₂ will have an effect on the length of the cotyledons, leaves, or stems of arugula plants and if H₂O₂ will enable the plants in the experimental group to grow (sprout) at an earlier rate than the control.

Methodology Used

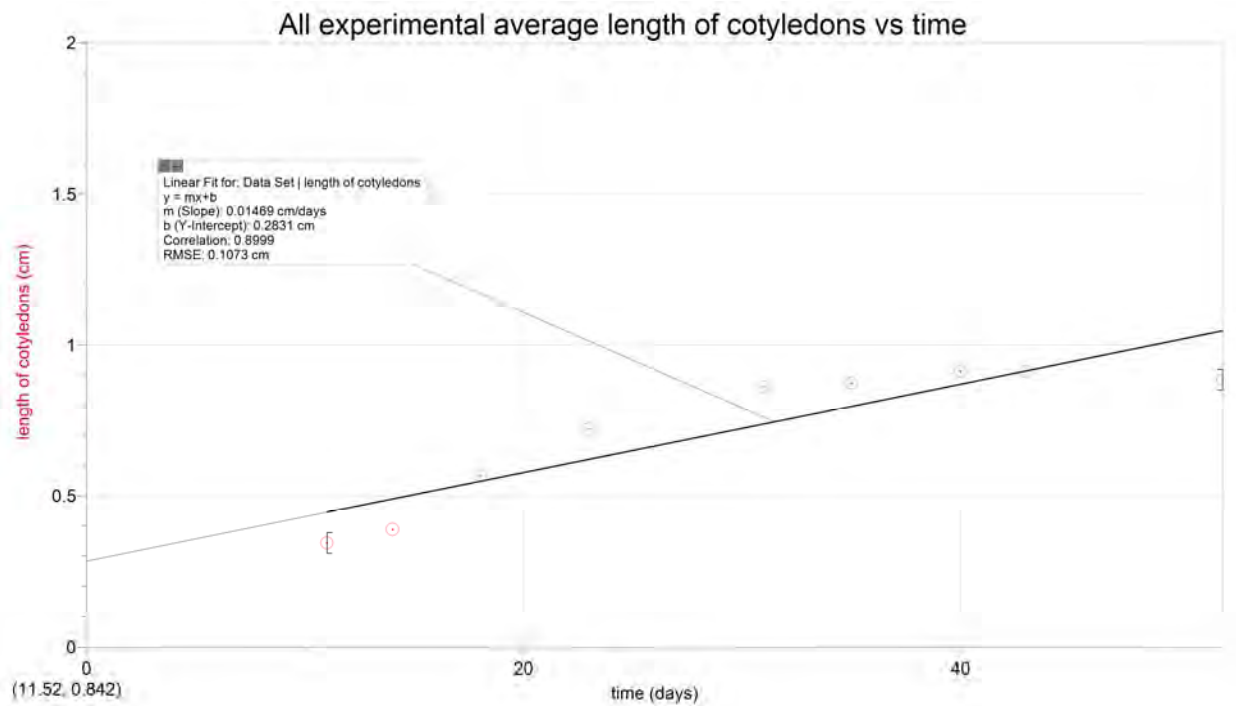
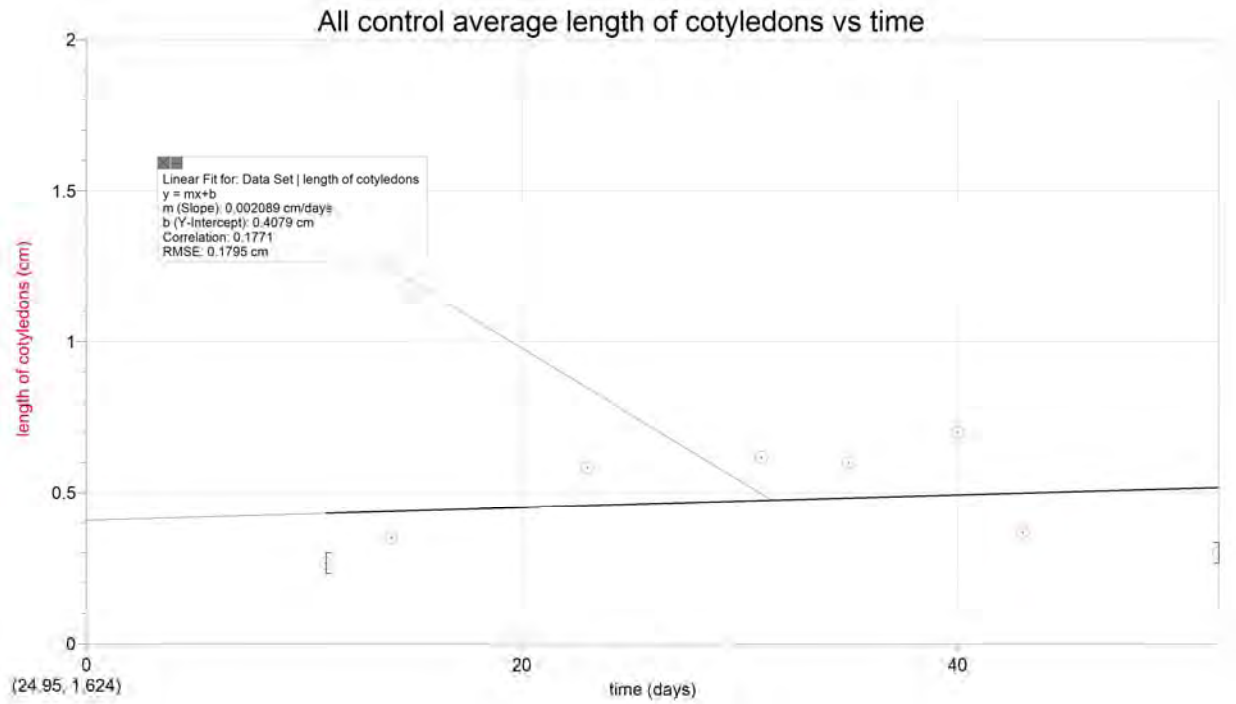
While researching the properties of hydrogen peroxide and determining a methodology, I used two journal sources. In the *Journal of Range Management*, Junqiang Hou and J.T. Romo germinated winterfat (*Ceratoides lanata*) and silver sagebrush (*Artemisia cana*) seeds to test if the weight of seeds and the time of fertilization influenced overall development. Also, in *Frontiers in Plant Science*, Wojtyla et al. thoroughly explained the important factors of hydrogen peroxide, its effects on germination, and its interactions between phytohormones such as Auxin. It was also noted that although H₂O₂ has many benefits, hydrogen peroxide is a part of the reactive oxygen species, which in turn can cause degradation to the plant's DNA. In summary, arugula seeds were labeled and grown in separate ice cube trays. For the first experiment, there were two groups- the control and experimental. Over time, the seeds in the control group only received water, while the experimental group were given five drops of hydrogen peroxide in addition to water. In the second experiment, there were three groups- the control, 5 drops of H₂O₂, and 10 drops of H₂O₂; each group were given water and the experimental groups were additionally given their corresponding amounts of H₂O₂ (please see materials and methodology).

Results Obtained

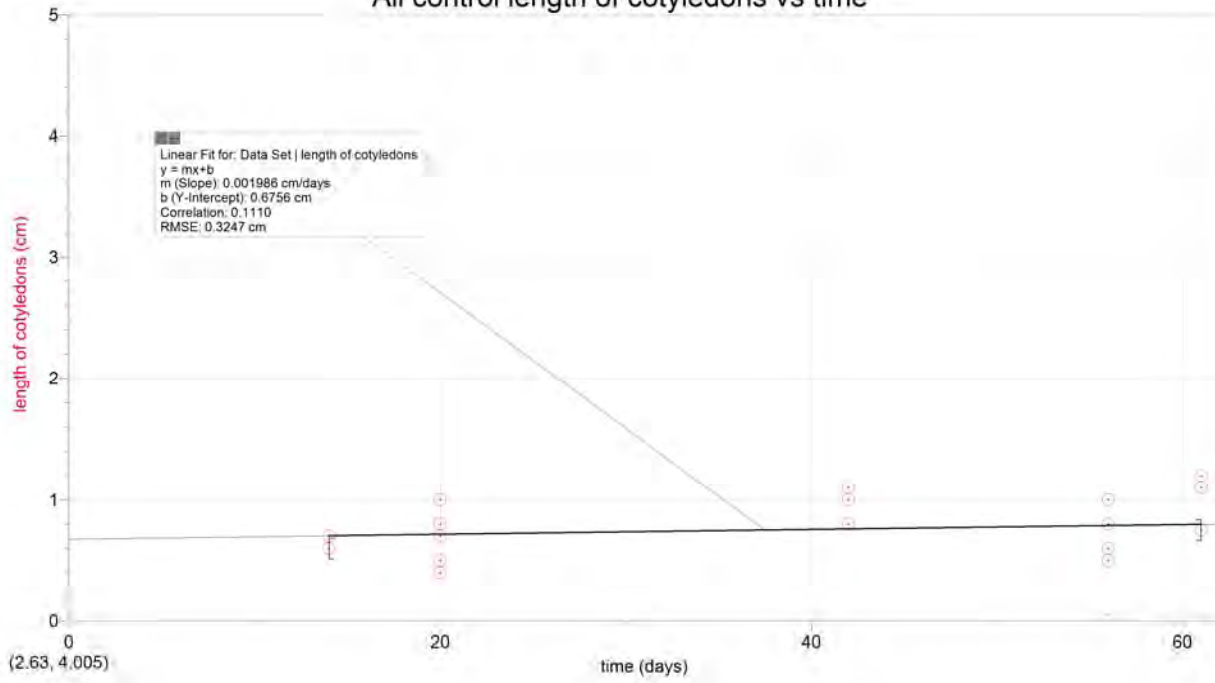
Based on the results of part 1 and 2, hydrogen peroxide does not seem to affect the length of the stems, however there is a significant difference in the length of cotyledons (possible effect of leaf growth is ongoing). In part 1, the overall growth of the stem is about 0.0389 cm/day and the overall for the experimental group is around 0.0385 cm/day. In contrast for the growth of the cotyledons, the control group has a slope (growth rate) of 0.002 cm/day, whereas the experimental group has a slope of 0.015 cm/day.

In part 2, the cotyledons in the 5 drops of H₂O₂ and the 10 drops of H₂O₂ groups have a 0.007cm/day slope, while the control has a slope of 0.002 (please see data). Additionally, for both part 1 and part 2,

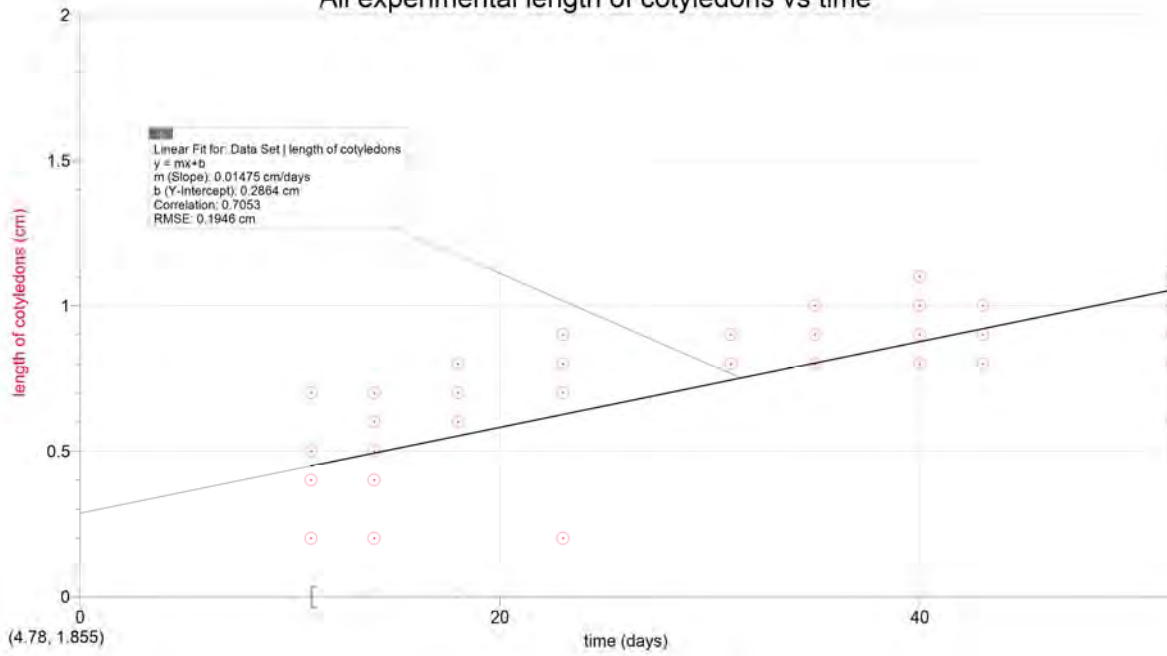
the plants in the experimental group(s) began sprouting at least 3 days earlier than the control group(s), however it would be best to continue the research.

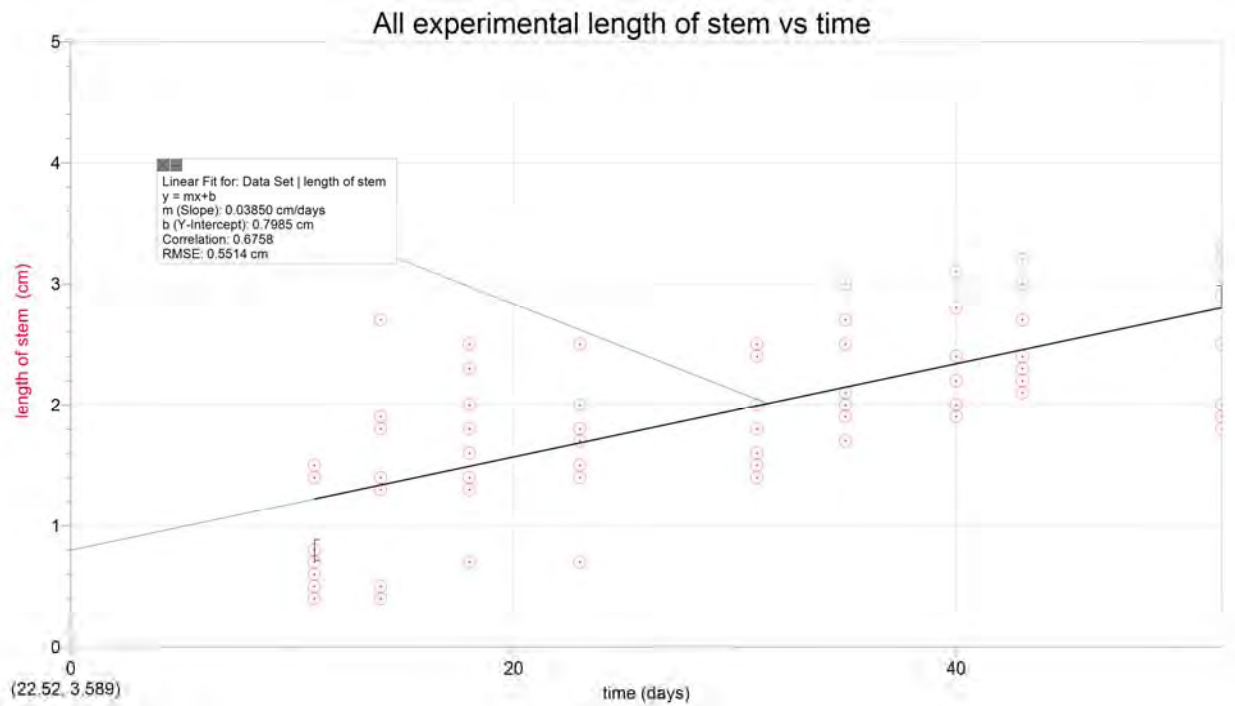
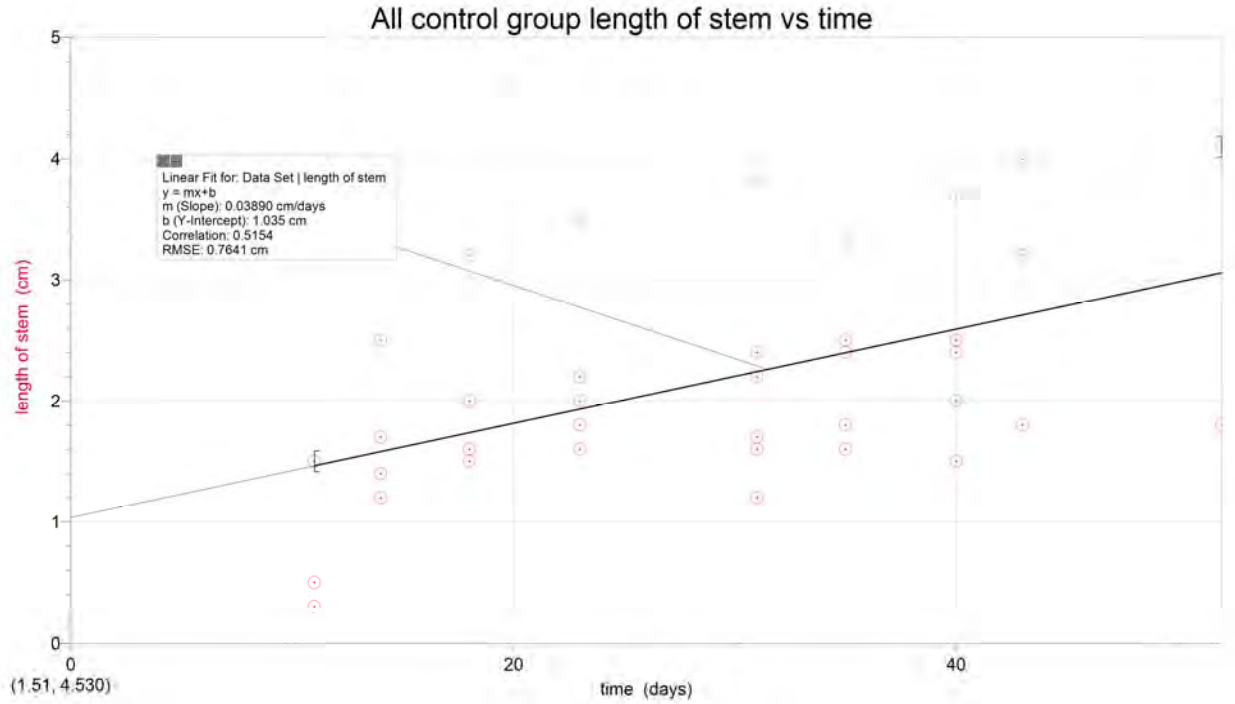


All control length of cotyledons vs time



All experimental length of cotyledons vs time





Significance and Interpretation of Results

My hypothesis based on these results would suggest that the hydrogen peroxide affects the cotyledons due to a possible relationship with photosynthesis, but in order to further determine this, further research on the leaves must be accounted. Since cotyledons transport nutrients to the leaves, perhaps the increase of the cotyledon length will correspond with the increase of leaf length; if so, then possibly plants given hydrogen peroxide will be healthier and stronger over time.

References

1. Junqiang Hou, and J. T. Romo. "Seed Weight and Germination Time Affect Growth of 2 Shrubs." *Journal of Range Management*, vol. 51, no. 6, 1998, pp. 699–703., www.jstor.org/stable/4003615.
2. Wojtyła, Łukasz et al. "Different Modes of Hydrogen Peroxide Action During Seed Germination." *Frontiers in Plant Science* 7 (2016): 66. *PMC*. Web. 14 Apr. 2017.

Catalytic Gasification: A Sustainable Waste Management Alternative

Student Researcher: Eric M. Lange

Advisor: Dr. Jorge E. Gatica

Cleveland State University

Department of Chemical and Biomedical Engineering

Abstract

This research focuses on advancing the current knowledge of a catalytic gasification process as a potential in-situ resource utilization and waste management system. This research has significance in a variety of engineering applications, but is of particular relevance towards municipal waste management and as an in-situ resource utilization alternative for advancing space exploration. A detailed analysis of an overall kinetics of the Sabatier reaction, the main fuel producing reaction in the catalytic gasification mechanism, is presented in this research. This research is an outgrowth to gas-phase kinetic literature data used to formulate a preliminary kinetic model. The analysis included a quantification of potential masking effects of the Reverse Water Gas Shift reaction, which could affect experimental data. Efforts on this project currently include completing the integration of the WGS reaction kinetics to expand the gas phase kinetics. Proof-of-concept experiments will be presented to illustrate the potential of the catalytic gasification system as a sustainable waste management alternative.

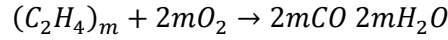
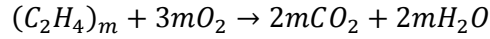
Introduction

Americans produce over 250 million tons of waste per year. Over 40 percent of this waste is composed of plastics and paper products (EPA, 2016), including materials such as polyethylene, polyethylene terephthalate, and cellulose, among others. Landfills are estimated to reach capacity in a near future as waste in large volumes continues to be un-recycled. Alternatives to landfills for the management of municipal waste must therefore be found. In Cleveland, Ohio, preliminary estimates suggest that municipal waste plastics contents can potentially produce 8000 tons of methane per year, i.e. enough fuel to power over 11,000 homes annually.

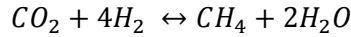
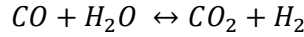
In addition to reducing municipal waste, catalytic gasification has the potential to benefit long-term space exploration. As the National Aeronautics and Space Administration desires to reach farther into our solar system, life support, mission support, as well as waste management in space must be improved. For long term space exploration, large volumes of fuel and life support supplies are required. However, storing the fuel and life support supplies necessary for the success of the mission prior to leaving Earth greatly increases the weight of the vessel. Increasing the weight of the vessel correspondingly increases the cost of launching spaceships into space. Furthermore, once in space, the management of waste creates additional problems. Existing solutions to space waste management include ejecting waste out into space or shipping waste back into Earth's atmosphere, where waste disintegrates on re-entry (Wright, 2013). These alternatives, however, are not without problems; ejecting waste out into space creates objects that can reach high velocities which have the potential to damage shuttles on impact (Mitchell, 2014). In addition, ejecting waste back into Earth's atmosphere does not utilize waste to create usable products and may have undesired environmental impact. Utilizing catalytic gasification as in-situ waste management system not only reduces the amount of fuel and life support required prior to departure, but also utilizes space exploration waste to create usable products.

The catalytic gasification reaction mechanism evolves through four reactions. The first two reactions are liquid phase oxidation reactions of long chain polymers. The liquid phase oxidation reactions produce

CO, CO₂, and H₂O. The liquid phase oxidation reactions are illustrated below for the case of polyethylene.



The oxidation reactions are complemented by two gas phase reactions: the Water Gas Shift (WGS) and the Sabatier reaction (Kulis et al., 2011).



These two reactions are the main stages in the pathway of producing H₂ and CH₄ in this “Trash to Supply Gas” technology. This work addresses the main fuel producing reaction of the catalytic gasification mechanism, the Sabatier reaction, also referred to as the Methanation of CO₂.

The main purpose of this paper is the formulation of a kinetic model for the Sabatier reaction, and estimating the corresponding kinetic parameters utilizing data from literature. Lunde and Kester (1974) developed one of the first kinetic models for the Sabatier reaction. Their simplified kinetic model equated the reaction rate to the change in partial pressure of CO₂ over the change in time. While these authors performed a kinetic analysis, their approach was simplified. In addition to Lunde and Kester’s model, several kinetic models have been proposed in the literature (Ohya et al., 1997). These kinetic models can be presented in a generalized form as follows,

$$-r_{CO_2} = \left(\frac{1}{RT}\right)^{5b} * A * e^{\frac{-E_A}{RT}} \left[p_{CO_2} p_{H_2}^4 - \frac{p_{CH_4} p_{H_2O}^2}{K_p} \right]^n$$

where the three most important parameters include the catalyst coefficient (n), the activation energy (E_A), and the Arrhenius pre-exponential factor (A).

Theory

The model developed by Lunde and Kester was simplified due to the assumption that the rate of conversion of CO₂ in the Sabatier reaction was equivalent to the change in partial pressure of CO₂ over the change in time, i.e.

$$\frac{-dP_{CO_2}}{dt} = A * e^{\frac{-E_A}{RT}} \left[p_A p_B^4 - \frac{p_C p_D^2}{K_p} \right]^n$$

However, if the expression is derived from a fundamental reactor general mole balance, a different expression is obtained, i.e.

$$\frac{-dP_{CO_2}}{dt} = 2RT\rho_b * A * e^{\frac{-E_A}{RT}} \left[p_A p_B^4 - \frac{p_C p_D^2}{K_p} \right]^n \left[\frac{1}{(1 + \varepsilon X_A)^2} \right]$$

One can clearly see that the simplified model’s fundamental equation lacks several important terms including: a temperature term and the compressibility term. Due to these simplifications, the kinetic analysis was reexamined in this work to validate and verify the kinetic parameters reported for the Sabatier reaction.

For a packed bed reactor, the reaction rate may be expressed in the differential form as follows

$$\frac{dF_A}{dW} = r_A'$$

The average reaction rate represents the integral of the reaction rate over the length of the catalyst bed, i.e.

$$\langle r_A' \rangle = \frac{1}{W} \int r_A' * dW$$

By substituting the differential equation of a packed bed reactor into the average reaction rate equation and integrating, the average reaction rate can be defined as follows

$$\langle r_A' \rangle = \frac{\Delta F_A}{\Delta W}$$

Two methods can be utilized to approximate the average reaction rate. The first method assumes that the reactor operates as a differential reactor. The second approximation technique assumes that the pressure can be approximated as a linear function along the reactor.

The first approximation assumes that a Perfect Mixing representation is a satisfactory model for the Differential Reactor. In other words, this approximation essentially considers the reactor to operate as an ideal continuously stirred tank reactor. The pressure function in the reaction rate can therefore be evaluated as a function of outlet partial pressures. This approximation is termed the Perfectly Mixed Approximation.

The second approximation is termed the Average Approximation. The Average Approximation assumes that the rate of change of partial pressures throughout the reactor is linear. In this scenario, the average partial pressures will correspond to the average between inlet and outlet partial pressures.

Upon completion of the preliminary calculations, a multi-parametric linear regression can be performed to determine the desired kinetic parameters: n , E_A , and A .

Reverse Water Gas Shift Analysis and Model Validation

Prior to validating the kinetic model, Lunde and Kester's Data was assessed for the occurrence of the Reverse Water Gas Shift (RWGS) reaction, i.e.



Figure 1 displays the equilibrium conversion for the RWGS and Sabatier reactions. In addition, Figure 1 displays the experimental conversion corresponding to Lunde and Kester's original experiments. At low temperatures, the RWGS equilibrium conversion is orders of magnitude smaller than the Sabatier equilibrium conversion; therefore, at low temperatures, it can be concluded that the RWGS reaction has little effect on the experimental data of Lunde and Kester. As higher temperatures are reached, the magnitude of the RWGS equilibrium conversion increases. At the highest temperature examined experimentally, 644 K, the conversion extracted from experimental data would seem to be higher than that corresponding to equilibrium conditions for the Sabatier reaction. Therefore, this experimental determination can be deemed as reflecting a significant extent in the RWGS reaction. Therefore, in order to ensure that the determined kinetic expression and its parameters were truly representative of the Sabatier reaction, the experiments potentially affected by the occurrence of the RWGS reaction were not considered in the kinetic determinations. In addition, to be conservative, two additional points were removed from the data set to ensure that none of the experimental data used to determine the Sabatier kinetics was subject to the RWGS reaction.

To validate the model, the literature data available (Lunde and Kester, 1974) was split in two groups: (i) a set of 21 points used in the parameter estimation, and (ii) a set of 21 points for validation purposes. The full model validation is not presented in this paper due to space limitations. One of the primary tools of comparison was the coefficient of determination, R^2 , defined as

$$R^2 = 1 - \frac{SS_M}{SS_{AVG}}$$

While both Approximations result in acceptable coefficients of determination, the Average Approximation yields a larger coefficient of correlation when attempting to predict the experimental conversion. The Average Approximation's correlation between the experimental and model conversions corresponded to a R^2 value of 0.93, whereas the Perfect Mixing Approximation's correlation corresponded a R^2 value of 0.78. In addition, the Perfect Mixing Approximation exhibited systematic deviations as higher values of conversion were reached. The primary assumption of the Average Approximation model; i.e., the presence of linear pressure profiles of all relevant species, was validated over the range of conversions observed experimentally. Therefore, the Average Approximation was selected to best represent the kinetic parameters for the Sabatier reaction, and it was utilized in all comparisons for the remainder of this paper.

Parameter Determination and Comparison to Literature Parameters

Upon completion of the model validation, all data points excluding the points contaminated by the RWGS reaction were used to calculate the Sabatier kinetic parameters in a multi-parametric linear regression. The parameters were calculated using the Average Approximation approach.

While the values for the activation energy, E_A , determined in this paper (67 kJ/mole) compares satisfactorily with those reported in the literature (ranging between 68-69 kJ/mole), the estimates for the catalyst coefficient (n) and the pre-exponential factor (A) found in this paper differ significantly from those reported by other authors.

The kinetic models were therefore compared in terms of their ability to predict the experimental data used in this paper. The primary comparison between the kinetic parameters was the model conversion versus the experimental conversion. The red line in Figure 2 represents the scenario in which the conversion predicted by the model matches the conversion estimated from experimental determinations.

The results in Figure 2 show that the kinetic parameters determined by Lunde and Kester systematically overestimate the experimental conversion. Significant deviations are observed even at low experimental conversion values. This is likely due to the simplifying assumption that the change in partial pressure of CO_2 over time can be used to correlate the extent of reaction in the Sabatier reaction. No correlation was found between the experimental conversion and the model conversion predicted by Lunde and Kester's kinetic parameters. When examining the model predictions for the kinetic parameters reported by Ohya and coworkers, one can clearly see that systematic deviations are also apparent. Even at low values of conversion there is significant overestimation of the experimental conversion values. No correlation was found between the experimental conversion and the model conversions predicted by Ohya et al.'s kinetic parameters. On the other hand, predictions found with the kinetic parameters found in this study show no systematic deviations for conversions below 20%. For conversion over 20%, the model systematically overestimates the experimental conversion. A coefficient of determination, R^2 , of 0.94 was found for the predictions based on the parameters found in this study.

Experimental Validation of the Catalytic Gasification Mechanism

Proof of concept experimental results are presented in Figure 3. Figure 3 displays both the CO₂ and H₂ mole fractions over time for a series of batch gasification experiments for polyethylene as the model polymer, and Ru on Al₂O₃ catalyst. In the case of H₂, one can see an increase in the H₂ composition from 2 to 5 hours. This signifies the occurrence of the WGS reaction. From 5 to 7 hours, the H₂ composition decreases; this signifies the occurrence of the Sabatier reaction. Furthermore, when examining the CO₂ composition versus time, one would expect to see a general trend in which the concentration of CO₂ increases over time. This phenomena is clearly visible from 5 to 8 hours. The gas mole fraction of CO₂ is expected to increase over time due to the fact that the Sabatier reaction only utilizes 1 out of every 4 CO₂ molecules produced by the WGS reaction.

Summary and Conclusions

The purpose of this work was to formulate a kinetic model for the Sabatier reaction using data from literature. Two approximations were proposed to approximate the average reaction rate of the Sabatier reaction. Prior to model validation, data from literature was surveyed for the occurrence of the RWGS reaction. The data showed that high temperature experiments may reflect the occurrence of the RWGS reaction, which reduced the data available for parameter estimation. Model validation showed that the Average Approximation resulted in a more reliable estimate of the average reaction rate for the Sabatier reaction. Upon validation of the kinetic model, all data points excluding the points contaminated by the RWGS reaction were used to estimate three fundamental kinetic parameters: the catalyst coefficient (n), the activation energy (E_A), and the pre-exponential factor (A). Comparison with alternative kinetic models reported in the literature suggests that the parameters determined in this study provide the best overall correspondence with experimental data. Proof of concept experiments were also completed; the results seem to support the proposed reaction mechanism for the catalytic gasification system.

Future work includes integrating the RWGS reaction into the kinetic model for the gasification of long-chain polymers. Laboratory experiments aimed to differentiate gasification via complete oxidation from that proceeding through partial oxidation are being conducted. A phenomenological model of the catalytic gasification process is currently under development.

Figures

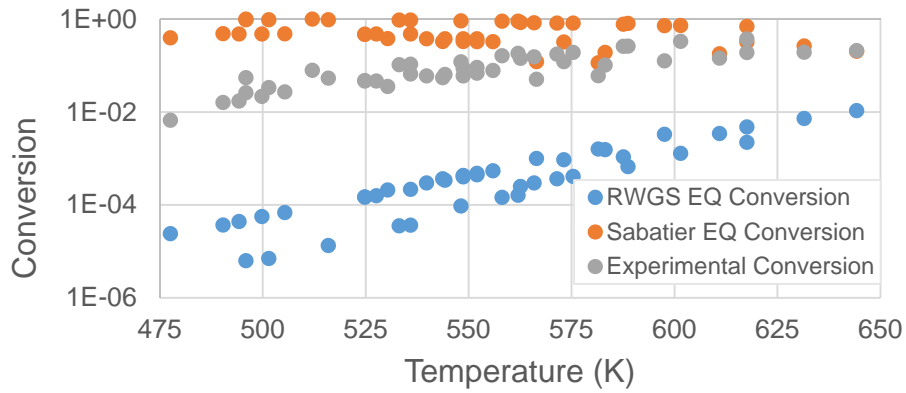


Figure 1. RWGS and Sabatier equilibrium conversion versus temperature

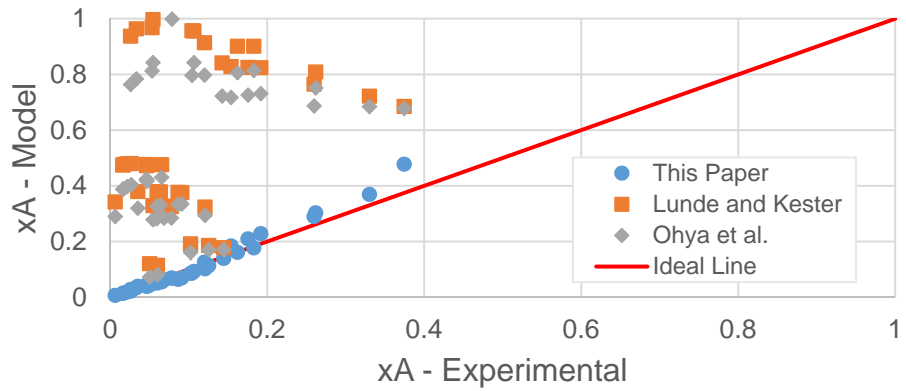


Figure 2. Model versus Experimental Conversion for This Paper, Lunde and Kester (1974), and Ohya et al. (1997)

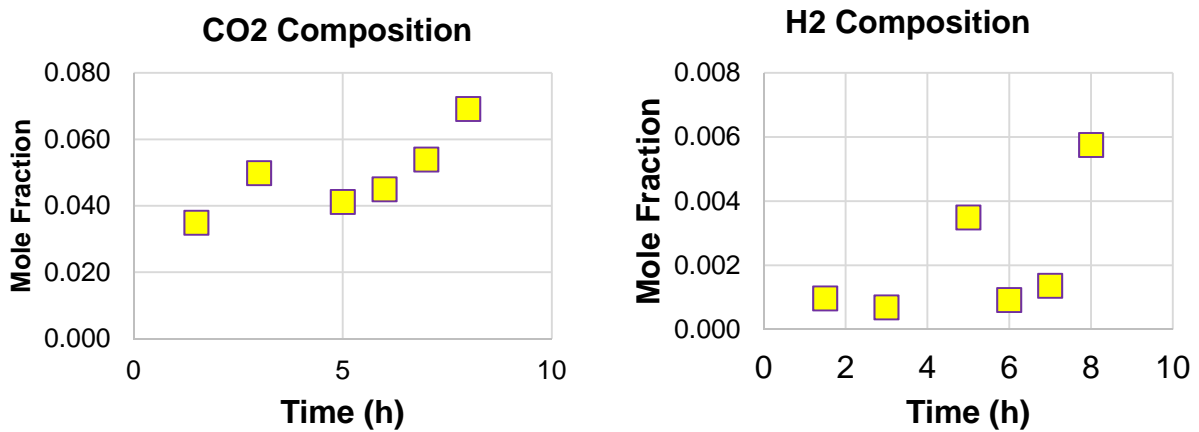


Figure 3. CO₂ and H₂ Composition versus Time for Polyethylene Substrate and Ru on Al₂O₃ Catalyst

Acknowledgments

This author would like to acknowledge the Ohio Space Grant Consortium, the National Aeronautics and Space Administration, the Ohio Department of Education Chose Ohio First Program, as well as the Washkewicz College of Engineering and the Jack, Joseph and Morton Mandel Honors College at Cleveland State University for providing support and resources for this research

References

1. EPA. (2016, March 29). Municipal Solid Waste. Retrieved from <https://archive.epa.gov/epawaste/nonhaz/municipal/web/html>
2. Wright, J. (2013, October 17). NASA - Automated Transfer Vehicle. Retrieved from http://www.nasa.gov/mission_pages/station/structure/atv.html#.Vq49SjbSk2w
3. Mitchell, R. (2014, January 10). NASA - Orbital Debris. Retrieved from <http://www.nasa.gov/centers/johnson/partnerships/orbital-debris/#.Vq4-uDbSk2w>
4. Kulis, M. J., Guerrero-Medina, K. J., & Hepp, A. F. (2011). Development of a Catalytic Wet Air Oxidation Method to Produce Feedstock Gases from Waste Polymers. NASA/TM-2012-217405, AIAA Paper 5739, E-18052
5. Lunde, P. J., & Kester, F. L. (1974). Carbon Dioxide Methanation on a Ruthenium Catalyst. *Industrial & Engineering Chemistry Process Design and Development*, 13(1), 27-33.
6. Ohya, H., Jun, F., Kawamura, H., Itoh, K., Ohashi, H., Aihara, M., et al. (1997). Methanation of Carbon Dioxide by using Membrane Reactor Integrated with Water Vapor Permselective Membrane and its Analysis. *Journal of Membrane Science*, 131(1-2), 237-247.

Investigating Our Climate System: Clouds and the Earth's Radiant Energy System

Student Researcher: Brittany A. Layden

Advisor: Dr. Mark Templin

The University Of Toledo
Judith Herb College of Education

Abstract

The basis of this lesson and its supplemental activities are rooted in concepts of the ideal gas law and Earth's radiation energy budget. Prior to conducting the activities, students should have a lesson or two of introduction to these difficult concepts. Introductory lessons would include instruction explaining background information about clouds, what they are made of, how they are made and why we scientist are interested in studying them. Based off of NASA's lesson plan, "Investigating Our Climate System: Clouds and the Earth's Radiant Energy System," students will create a cloud in a bottle and conduct an experiment that shows how clouds can affect our local weather and climate systems. These activities will allow students to better understand the ideal gas law and Earth's radiation energy budget.

Objectives

Students will: 1) Model and explain cloud formation. 2) Sketch and classify clouds according to height, shape, and optical thickness. 3) Calculate and compare incoming and outgoing radiation. 4) Describe how cloud properties affect the Earth's radiant budget. And 5) make climate predictions based on future increases or decreases of certain cloud types.

Lesson

The basis for these activities comes from NASA's lesson plan, "Investigating Our Climate System: Clouds and the Earth's Radiant Energy System". In the first activity, students will make their own cloud in a bottle. For this activity, I found it best to demonstrate the process then allowing the students to work in groups of 4-5 to conduct the activity on their own. The materials needed to make a cloud in a bottle are as follows; an empty two-liter bottle, a very small amount of water, a match or incense stick and a lighter. To make a cloud, add a small amount of water to the bottle. Coat the entire inside of the bottle with water drops then squeeze and release the bottle. A cloud does not appear yet because the water molecules have nothing to cling on to. Now open the bottle and add some smoke from the match or incense stick. After squeezing and releasing the bottle, voila, a cloud now appears!



In the second activity, students will design and conduct an experiment that shows how clouds can affect our local temperature. For this experiment, students will need the following materials; two empty 2 liter bottles, infrared heat lamp, two LCD thermometers (or similar), black and white construction paper, scissors and tape. Set up the experiment as shown in the image to the right. One bottle is representing a cloudy day, the other a clear day. Place both bottles on a piece of black paper; this will be acting as our Earth's surface. Use a heat lamp as a light source to heat up the domes. After a chosen amount of time, record the temperature in each dome and record in it your data sheet. Collect data from other groups and compare your results.

Alignment

Content Standards: 5-8

Science as Inquiry

Content Standard A: As a result of activities in grades 5-8, all students should develop: 1) Abilities necessary to do scientific inquiry. 2) Understandings about scientific inquiry.

Physical Science

Content Standard B: As a result of activities in grades 5-8, all students should develop an understanding of: 1) Properties and changes of properties in matter. 2) Transfer of energy.

Earth and Space Science

Content Standard D: As a result of activities in grades 5-8, all students should develop an understanding of: 1) Structure of the Earth system. 2) The water cycle. 3) Various types of clouds.

Underlying Theory

By using the Problem-Based method, students gain more than just knowledge of facts. They develop critical thinking skills while working in collaborative groups to try to solve a problem. When introducing the second activity, "Clear vs. Cloudy", I purposely gave the students very vague instructions on how to set up the experiment so that they could design the set-up as a group. This promoted collaboration among the groups and enhanced their problem-solving skills.

Results

In the first activity, students find that a cloud will not form with only water being present. They will understand that the water molecules need something to cling onto, so that by adding "dust" (smoke from incense stick or match), they have now provided the optimal environment for a cloud to be formed.

In the second activity, "Clear vs. Cloudy," students will see the effect that low-lying clouds have on our local temperatures. On a cloudy day, we will experience lower temperatures than we would on a clear day. The low-lying clouds are often brighter in color so they will reflect the sun's radiant energy, ultimately resulting in a cooling of the local surface temperature.

Assessment

With the scholarship I received from NASA and the Ohio Space Grant Consortium, I was able to purchase weather science kits for all the students in my after school service-learning program. After an introductory lesson and an additional lesson to complete the activities, I gave the students their kits and showed them how to utilize them. The students will use their kits to create a closed ecosystem. Using the principals we talked about in our lessons, they will write a report on their findings. I look forward to reading their reports in the next coming weeks.

Conclusion

When I asked the students to tell me what they learned from my lesson, I got some great responses! One student said that he now realizes that, "clouds are more than just puffy things in the sky, they can tell us so much about our environment". This student perfectly exemplified my goal for this lesson. I want my students to be able to understand all the natural processes that happen around us everyday so that they can better understand the world we live in. The students had so much fun with this lesson and enjoyed doing the hands-on activities.

Resources

NASA's lesson plan, "Investigating Our Climate System: Clouds and the Earth's Radiant Energy System".

Low-Cost Metal Printing

Student Researcher: Joseph V. Lonardo

Advisor: Dr. Eric MacDonald

Youngstown State University
Mechanical Engineering

Abstract

The goal of this project is to further develop a delta 3D-printer designed to print metal layers using a conventional MIG (Metal Inert Gas) welder that feeds molten metal wire onto a moving platform. This open-source printing method was originally developed by a team at Michigan Technological University under Dr. Joshua Pearce¹. The most appealing aspect of this research is the relatively low cost for using such a setup in comparison to commercial metal 3D printers that can exceed costs in the millions of dollars. The low-cost metal printer currently resides in YSU's Center for Innovation in Additive Manufacturing (CIAM) lab where work on printing firmware development is underway. Before the addition of the meta MiG welder platform, the movements of the printer must be fully operational. Once this occurs, the first tests using the MiG welder to act as the "extruder" for the printing material will begin. Once basic operations of the printer are underway, the final steps will be to add post-printing analysis elements. Such elements will include cameras to monitor each printed metal layer and provide adjustments (speed, distances, welder power magnitudes) throughout the printing process to optimize print quality. The end-goal will be printed parts of superior quality and development than past research conducted at YSU using this printer design.

Project Objectives

There are several components to this project, centered around the printer's development. Design of the printer, control of the printer, introduction of the welder system, and analysis of printing performance are all separate tasks to obtain a working prototype. First, the printer was designed originally by MTU under Dr. Pearce²; the printer replica at YSU is not complete in both hardware and software. Control hardware, such as sensors that orient the printer platform in 3D space (end stops) must be installed. The circuit boards used to control the printer's motors must be programmed before the printer can accept 3D models (in the form of G-code). The computer code (firmware) and software plays the role of communicating a CAD-drawn 3D model to a physical, printed part. Next, the MiG welder system must be incorporated into the printer, taking safety of both persons and equipment in consideration. Lastly, analysis of the printer's performance involves recording data while printing and adjusting as needed.

Methodology Used

Work began with research and review of both MTU's work on their design as well as prior teams at YSU on the replica that continued throughout the project. First steps included assessing the printer's current state. The printer was machined for end stops (sensors for orienting printer platform) to be incorporated into the printer. Work on printer control began early, but is still ongoing. Several open-source programs for control of a printer were tested. The uniqueness of this printer's design (inverted delta style) results in a lack in specialized firmware (computer code for communication of 3D drawings to the printer motors). Measurements for the printer's motors and geometric relationships that determine movement of the print surface were derived and incorporated into existing code. Work on the welding assembly consisted mainly of welder training. For implementation of the welder into the printer, a mount above the print bed is used to fasten the welding "gun" securely. It is proposed that

manual control of the welder (starting and stopping the flow of current and wire) will be used for safety during initial testing. Evaluation of printing performance was tested with normal cameras, protective filters, and a FLIR (Forward Looking Infrared) camera.

Results Obtained

Extensive testing with different software provided some degree of motion of the printer. Challenges with commanding the printer to make it move in the X, Y, and Z directions appeared to be related to the firmware adaptation for this unique design. Mechanical components such as the motors were ensured to be properly functioning. The welder assembly is ready for the printer, and recording welding (by hand, not with the welder inserted into the printer mount) resulted in both optical and thermal imaging of the welds.

Significance and Interpretation of Results

The proposed steps forward would be to continue researching and building custom firmware. The original printer by MTU uses a software derived from an in-house developed firmware³ (Franklin). However, it would be advantageous to develop firmware at YSU to enable separate development, as the planned closed-loop analysis conducted thus far will have to be incorporated into the firmware.

Figures



Figure 1. (Left) Parts of a weld.

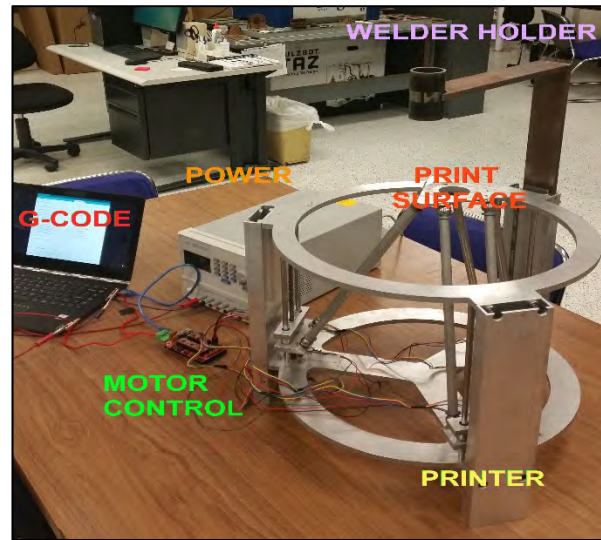


Figure 2. (Right) The printer.

References

1. G. C. Anzalone, C. Zhang, B. Wijnen, P. G. Sanders and J. M. Pearce, "A Low-Cost Open-Source Metal 3-D Printer," in *IEEE Access*, vol. 1, no. , pp. 803-810, 2013. doi: 10.1109/ACCESS.2013.2293018
2. "MOST open-source metal 3-D printer v2." *Appropedia: The sustainability wiki*. Pearce Research Group, 27 Jan. 2017. Web. 27 Mar. 2017. <http://www.appropedia.org/MOST_open-source_metal_3-D_printer_v2>.
3. "Franklin." *Appropedia: The sustainability wiki*. Pearce Research Group, 22 July 2016. Web. 27 Mar. 2017. <<http://www.appropedia.org/Franklin>>.

An Intelligent Fuzzy Sensor Based Motion Control System for Autonomous Mobile Robot

Student Researcher: Maxime Maisonnet

Advisor: Deok Hee Nam, Ph.D.

Wilberforce University
Computer Science

Abstract

Recently, the assessment and the suitable control of the attacked areas by the catastrophic natural disasters are very important issues in big data control fields. To provide the efficient and appropriate solutions, the accurate examination of the hazardous or contaminated areas is the most critical factor for the afterwards assessments. One of the desirable ways is adapting an autonomous mobile robot to navigate and explore the attacked area to reduce the risk of the safety comparing to the methods done by the human being. Since an autonomous mobile robot (AMR) has to cope with uncertain, incomplete or approximate information and control the deployed autonomous mobile robots to examine the hazardous or contaminated areas efficiently, it is essential to have more sensitive and efficient sensors for the autonomous mobile robots. The proposed work presents an intelligent fuzzy sensor-based motion control system for the autonomous mobile robots' navigation in unknown environments surrounded by the hazardous or contaminated conditions with the various input conditions for the system. The proposed system will also help a wireless sensor-based remote control of mobile robots motion. In addition, a fuzzy logic based intelligent control strategy has been developed through the proposed work to computationally implement the approximate reasoning necessary for handling the uncertainty inherent in the collision avoidance problem. Finally, the performance of the proposed fuzzy sensor based motion control strategy for autonomous mobile robots is demonstrated by the results of the motion control of the autonomous mobile robots with the obstacle avoidance behavior in unknown environments.

Project Objectives

The scope of the current project mainly deals with an aspect of autonomous and unmanned mobile robot control to navigate or explore the unknown and destroyed area by the catastrophic natural or man-made disasters under the restricted environments. The first task is how to navigate the mobile robot with predicting the mobile robot paths precisely under the unexpected environments with the unknown terrain conditions to find the targets or avoid the obstacles successfully with remotely controlling the mobile robots. Hence, the intelligent and autonomous control systems with applying fuzzy logic systems are proposed with finding the optimized path prediction of the unmanned mobile robots.

Methodology Used

In order to develop the intelligent system for the navigation of the unmanned mobile robots, four different fuzzy logic systems are deployed for the project to evaluate the optimized conditions for finding the unmanned mobile robot paths with avoiding all possible obstacles without any collision on the front way. The first fuzzy logic system is to evaluate the turning direction such as extreme right, right, no turn, left, and extreme left to avoid the possible obstacle in front of or near the unmanned mobile robots depending upon the input variables such as obstacle size, distance to object, and location of other obstacles. The second fuzzy logic system is to determine the mobile robot path (or course)

whether the current navigating unmanned mobile robot is supposed to proceed or not with one of two different decisions such as forward and backward. This system deploys three different inputs such as obstacle size, distance to obstacle, and other obstacle location. The third fuzzy logic system is about the detection of obstacles on the front mobile robot paths. The measurements of the detection of obstacles are separated by the following categories such as found and not found. To evaluate the detection of obstacles, three different inputs are used such as distance to obstacles, obstacle size, and other obstacle location. Through three developed fuzzy logic systems including the systems of turning angle, path direction and detection of obstacles, and an additional input, terrain slope, the decision of the speed of the current autonomous unmanned mobile robot will be determined for the possible next time frame as a fourth fuzzy logic system for the entire system.

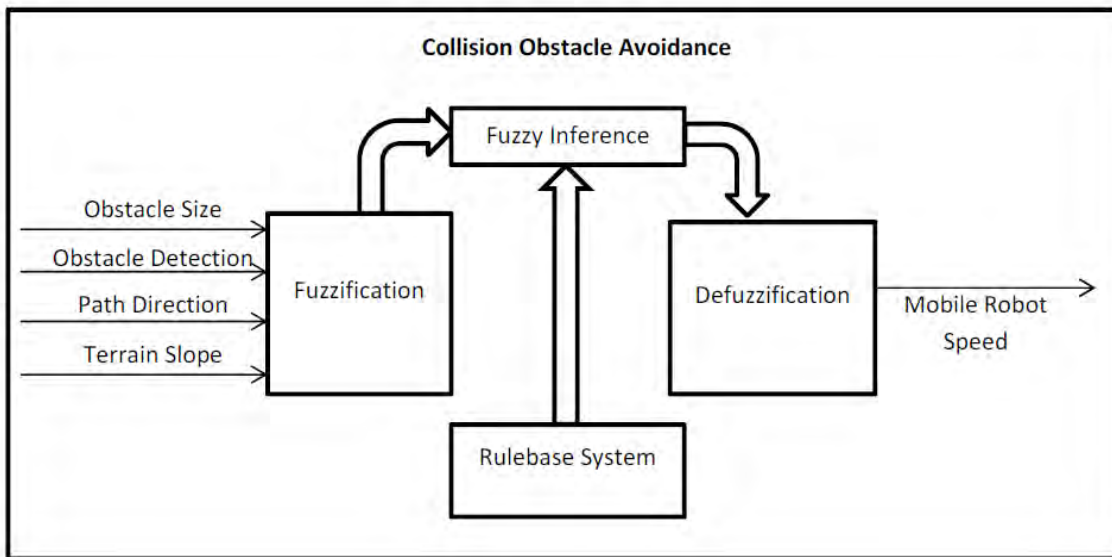


Figure 1. Overview of Proposed Fuzzy Logic Systems

Rule Base Systems for Fuzzy Logic Systems

The fuzzy logic system for determining the turning angle of the unmanned mobile robot in the environment is based upon the size of the obstacles, the distance from the obstacle and the other obstacle around the facing obstacle at that time. Mainly, if the obstacle is fairly far away from the unmanned mobile robot, no turning will be occurred. If the obstacle is relatively close to the unmanned mobile robot, except the locations of other obstacles which are placed at the sides of the unmanned mobile robot, the system provides the appropriate turning angle to avoid the obstacle in front. The fuzzy logic system for predating the future path direction of the unmanned mobile robot is developed by going forward direction for the relatively smaller obstacles, the further distance from the obstacle, and the clear view of the other obstacles. The fuzzy logic system for estimating whether the obstacle is found or not, is based upon the relatively closer distance from the obstacle, the larger size of the obstacles, and the location of other obstacles in the front area of the unmanned mobile robot for Found category in the membership functions of the obstacle detection system. The fuzzy logic system for Collision Obstacle Avoidance is composed by three pre-developed fuzzy logic systems with three inputs including obstacle size, obstacle distance, and location of other obstacles, and the condition of the terrain as an addition input to the system. Mainly, the speed of the unmanned mobile robot can be determined by the direction of the future path prediction and the existence of other obstacles with the condition of the terrain slope based upon the turning angles. To accelerate the speed of the unmanned mobile robot, the rules can be formed by the no appearance of any obstacle with the appropriate

turning angle for the next time frame. In addition, the going forward and the going backward are determined by the obstacle detection along with the decision of the terrain slopes.

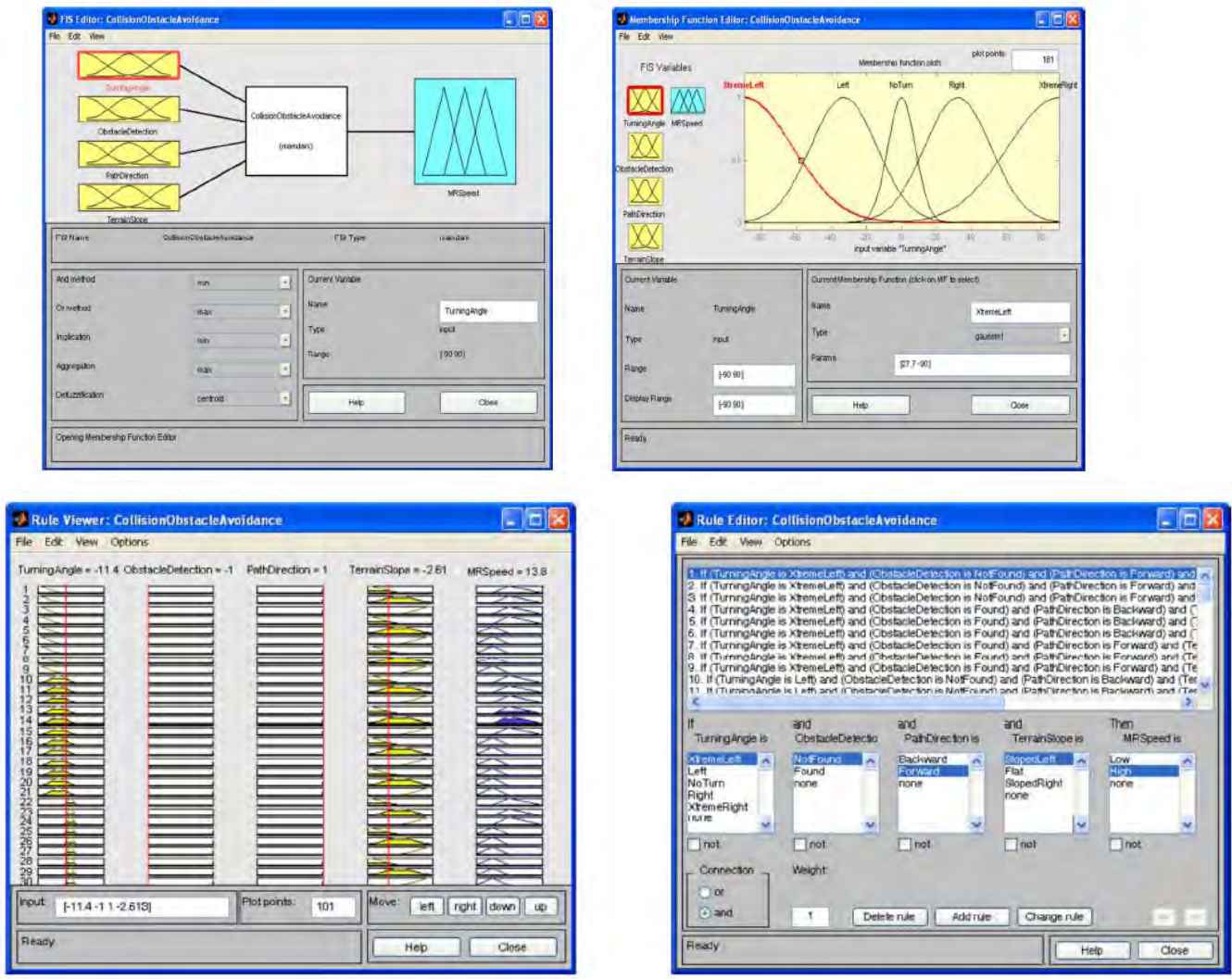


Figure 2. Developed Fuzzy Logic Systems

Conclusion

An intelligent fuzzy sensor based motion control system has been developed using the essential factors such as obstacle size, obstacle distance, other obstacle locations, terrain slope, turning angle, obstacle detection, path direction, and mobile robot speed to establish a system to avoid the collision of the obstacles. In the future work, another intelligent system needs to be developed with showing how efficiently to connect or communicate the distributed unmanned mobile robots in order to collect the required information in order to measure the afterwards assessment. To perform an intelligent system successfully, the efficient and continuous connection or communication methodology with the intelligent system between the main control unit and the exploring mobile robots in the disastrous area hitting by the catastrophic disasters will be developed.

Acknowledgments

Many thanks to Ohio Space Grant Consortium for the academic scholarship program. Special thanks to Dr. J. Marquart and Ms. L. Stacko at the OSGC Program, and Dr. J. Williams at Wilberforce University.

References

1. Mester G. and Rodić A., "Sensor-Based Intelligent Mobile Robot Navigation in Unknown Environments", *International Journal of Electrical and Computer Engineering Systems*, Vol. 1, No. 2, Dec. 2010, pp. 55- 66.
2. Rodić A., Addi K., and Jezdimirović M., "Sensor-Based Intelligent Navigation and Control of Autonomous Mobile Robots for Advanced Terrain Missions," *Scientific Technical Review*, Vol.60, No.2, 2010, pp.7-15.
3. Panigrahi P., Ghosh S., and Parhi D., " Intelligent Learning and Control of Autonomous Mobile Robot using MLP and RBF based Neural Network in Clustered Environment," *International Journal of Scientific & Engineering Research*, Volume 5, Issue 6, June-2014, pp. 313-316.
4. Hong T., Nakhaeinia D., and Karasfi B., "Application of Fuzzy Logic in Mobile Robot Navigation," in *Fuzzy Logic – Controls, Concepts, Theories and Applications* edited by Prof. Elmer Dadios, In-tech, 2012, pp. 21-36.
5. Mohanty P. and Parhi D., "A New Intelligent Motion Planning for Mobile Robot Navigation using Multiple Adaptive Neuro-Fuzzy Inference System," *Appl. Math. Inf. Sci.* 8, No. 5, 2527-2535 (2014), pp. 2527-2535.
6. Lafta, H., Hassan, Z., "Mobile Robot Control Using Fuzzy Logic," *Journal of Babylon University/Pure and Applied Sciences/ No.(2)/ Vol.(23): 2015*, pp. 524- 532.
7. Pandey A., Parhi D., "Multiple Mobile Robots Navigation and Obstacle Avoidance Using Minimum Rule Based ANFIS Network Controller in the Cluttered Environment," *Int J Adv Robot Automn* 1(1), 2016, pp. 1-11.

Analysis of Red-Tailed Hawk Breeding and Land Cover Change in Ohio

Student Researcher: Joanna C. Maniglia

Advisor: Bobby Oliver, GISP

Lakeland Community College

Department of Geography and Geospatial Technology

Abstract

The Ohio Breeding Bird Atlas divides the state into a grid comprised of survey blocks which are used to document the status and distribution of bird species in an area. In surveying a block, trained volunteers document the presence of bird species and record evidence of breeding or behaviors that suggest breeding, assigning each observation using a series of codes, Possible, Probable, and Confirmed. Two such atlas studies have been conducted in Ohio. This research focused on observations of Red-tailed hawk breeding in the First Ohio Breeding Bird Atlas (1982-1987) (OBBAI) and the Second Ohio Breeding Bird Atlas (2006-2011) (OBBAII). These data, along with land cover data, were used to study the location of breeding Red-tailed hawks and investigate the impact of land cover change on breeding location between the time of the two survey periods. The results demonstrate an increase in Red-tailed hawk breeding locations in the state of Ohio during this time period and thus, the assumption is made of an increase in the number of individuals of this species. Land cover change did not have an impact on Red-tailed hawk breeding locations for the three detailed study areas of interest in this research. Most of the land cover in the study areas remained the same and the largest percentage of change in each area from Agricultural Vegetation to Forest can be seen as favorable to breeding Red-tailed hawks.

Objectives

This research posed the following questions for study: What changes occurred in breeding location of the Red-tailed hawk between these two survey periods and what, if any, impact has land cover change had on the breeding location for this species?

Methodology

This research utilized ArcGIS to geoprocess both vector and raster data. Tabular data was joined to a shapefile and symbolized for the blocks held in common between both studies. Selections of data were made and exported to create new feature classes. Raster data was mosaicked, clipped, edited, reclassified, and converted to vector format. Spatial analysis tools and visual interpretation were performed to analyze changes over time in confirmed blocks and identify study areas of interest. Additional selections were utilized to create three feature classes for the detailed study areas of interest and gather statistics from their attribute tables for further analysis.

Results

The results showed an increase in the number of confirmed study blocks surveyed in OBBAII versus OBBAI. The results of the research concluded the majority of land cover type in each of the three detailed study areas remained the same. Results are available in Tables 1-7.

Interpretation

The results demonstrated an increase in Red-tailed hawk breeding locations in the state of Ohio between the two study periods and thus, the assumption is made of an increase in the number of individuals of this species. Land cover change did not have an impact on Red-tailed hawk breeding locations for the areas studied in this research. Most of the land cover in these areas remained the same

and the largest percentage of change, from Agricultural Vegetation to Forest, can be seen as favorable to breeding Red-tailed hawks.

Tables

Table 1 OBBAI block status		
Number of blocks with Possible status	206	28.93%
Number of blocks with Probable status	273	28.34%
Number of blocks with Confirmed status	233	32.72%

Table 2 OBBAII block status		
Number of blocks with Possible status	242	33.99%
Number of blocks with Probable status	183	25.70%
Number of blocks with Confirmed status	287	40.31%

Table 3 Percent change from OBBAI to OBBAII		
Number of blocks with Possible status	17.40%	
Number of blocks with Probable status	-32.96%	
Number of blocks with Confirmed status	23.17%	

Table 4 Analysis of Change in Land Cover between OBBAI and OBBAII	
Change From	Change To
Agricultural Vegetation	Forest
Developed	Forest
Forest	Developed
Water	Developed
Shrubland Grassland	Developed

Table 5 Study area 1 Percent land cover change	
Percentage of land cover change favorable breeding Red-tailed hawks	26.37%
Percentage of land cover change unfavorable to breeding Red-tailed hawks	8.35%

Table 6 Study area 2 Percent land cover change	
Percentage of land cover change favorable breeding Red-tailed hawks	13.54%
Percentage of land cover change unfavorable to breeding Red-tailed hawks	1.46%

Table 7 Study area 3 Percent land cover change	
Percentage of land cover change favorable breeding Red-tailed hawks	28.08%
Percentage of land cover change unfavorable to breeding Red-tailed hawks	5.71%

References

1. The Ohio State University. School of Environment and Natural Resources. (2005). *Breeding Bird Atlas II Volunteer Handbook*.
2. Peterjohn, B.G. and Rice, D.L. (1991). *The Ohio Breeding Bird Atlas* [Data file]. Available from http://www.ohiobirds.org/obba2/newsite/?page_id=534
3. Price, C.V., Nakagaki, N., Hitt, K.J., and Clawges, R.C. (2006). *Enhanced Historical Land-Use and Land-Cover Data Sets of the U.S. Geological Survey, U.S. Geological Survey Digital Data Series 240* [Data file]. Retrieved from <http://pubs.usgs.gov/ds/2006/240>
4. Rodewald, P.G., Shumar, M.B., Boone, A.T., Slager, D.L. and McCormac, J. (2016). *The Second Atlas of Breeding Birds in Ohio* [Data file]. Available from http://www.ohiobirds.org/obba2/newsite/?page_id=534
5. United States Geological Survey. Gap Analysis Program. (2010). *National Land Cover Gap Analysis Project* [Data file]. Retrieved from <https://gapanalysis.usgs.gov/gaplandcover/data/download/>

MiR-146a Upregulates Phagocytosis of Jurkats in a Human Macrophage Sjögren's Syndrome Model

Student Researcher: Ryan M. Marquardt

Advisor: Kaleb M. Pauley

Cedarville University

Department of Science and Mathematics

Abstract

Sjögren's syndrome (SjS) is an autoimmune disease that attacks exocrine glands such as salivary and lacrimal glands resulting in severe dryness of the mouth and eyes. Previous studies have linked increased microRNA-146a (miR-146a) expression in peripheral blood mononuclear cells to SjS patients compared to healthy controls. Like all microRNAs, miR-146a negatively regulates specific genes through binding mRNA, leading to degradation or translational inhibition. Further investigation into the role of increased miR-146a expression in SjS revealed links to several immune functions including cytokine production, cellular migration and phagocytosis. We have previously shown that upregulation of miR-146a in THP-1 human macrophages increases phagocytosis of *E. coli*. To find results more applicable to an SjS model, we set out to observe the effect miR-146a has on phagocytosis of Jurkats, cells of a human T cell line. Preliminary results have confirmed our hypothesis that upregulation of miR-146a in THP-1 cells results in an increase in phagocytosis of apoptotic Jurkat cells.

Project Objectives

Relatively little research has been conducted on Sjögren's syndrome (SjS), presumably because it does not directly cause death, but it does create severe quality of life issues for those affected in the form of chronic, severe dryness of the eyes and mouth, affecting approximately 4 million in the United States (Catanzaro & Dinkel, 2014). One previous study showed that miR-146a was upregulated in SjS model mice both prior to disease onset and after the disease was taking effect, and multiple studies have shown increased levels of miR-146a in Sjögren's patients (Pauley et al., 2011; Shi et al., 2014). Additionally, functional assays with human monocyte cell line THP-1 showed that increased miR-146a expression correlates with increased phagocytosis of *E. coli* and downregulation of pro-inflammatory cytokines (Pauley et al., 2011). Ultimately, these results show that there is a correlation between abnormal expression of miR-146a and Sjögren's syndrome, and that more research into the physiological role of this microRNA could be beneficial. The primary objective for this project is to answer the question of whether upregulation of miR-146a also upregulates phagocytosis of apoptotic human cells. The answer to this question would help us understand the effect of miR-146a on phagocytosis in a model more applicable to SjS. We hypothesized that increasing miR-146a levels would upregulate phagocytosis of apoptotic human cells, in accordance with the prior data involving *E. coli*.

Methodology Used

Experimental group THP-1 human monocytes were first transfected with manufactured miR-146a to increase expression levels, and a control group was mock transfected. Etoposide was used to induce apoptosis in Jurkats to be used as the phagocytic target. Phagocytosis experiments were carried out 3 days after transfection, and the day before the phagocytosis assay, the cells were harvested, washed, and treated with phorbol myristate acetate (PMA) to induce differentiation to macrophages. Apoptotic Jurkats were stained with pHrodo succinimidyl ester, a pH sensitive dye that emits light due to the drop in pH post-phagocytosis, and this allows quantification of phagocytosis (Miksa et al., 2009). Prior to using this assay in our experiment, we tested it under our experimental conditions. Mock-transfected

and miR-146a transfected THP-1 cells were co-incubated 2 hours with pHrodo-stained apoptotic Jurkats (4:1 Jurkat to THP-1 ratio). Cells were counterstained with DAPI nuclear stain and CD-68 to label macrophages. Phagocytosed Jurkats with positive pHrodo staining and THP-1 cells were counted.

The THP-1 human monocyte cell line was used for all experiments and was cultured according to ATCC recommendations in RPMI-1640 media supplemented with 10% FBS. All transfections utilized Lipofectamine 2000, a lipid-based transfection agent, following the manufacturer's protocol. A 40 μ M etoposide treatment overnight was used to induce apoptosis in Jurkats, and cell viability was determined using trypan blue exclusion, caspase-3 activity assay, and Annexin V staining. Phagocytosis of fluorescently labeled apoptotic Jurkats was observed using fluorescent microscopy and manual counting.

Results Obtained

We confirmed the success of our apoptosis assay by finding Jurkat cell viability. Trypan blue exclusion, caspase-3 activity, and Annexin V staining all showed optimal cell viability, shown in *Figure 1*. We also found that in our test of pHrodo dye, Jurkats fluoresced in low pH but not in normal pH, shown in *Figure 2*. After carrying out the phagocytosis assay, phagocytosing THP-1 cells were counted, and the data was normalized to account for discrepancies in the number of macrophages in a given sample. Full data from one trial are shown in *Table 1*. Cell counts of red (phagocytosed) Jurkats and THP-1 macrophages showed that miR-146a transfected THP-1 cells exhibited a 1.8-fold increase in phagocytosis of apoptotic Jurkats over mock transfected cells as seen in *Figure 3*.

Significance and Interpretation of Results

Our tests of the etoposide assay and the pHrodo dye both confirmed the validity of their respective use in our experiment. Cell counts after our phagocytosis assay revealed that miR-146a transfected cells performed more phagocytosis than mock transfected cells, which indicates that increased expression of miR-146a in THP-1 cells upregulates phagocytosis of apoptotic Jurkat cells. Due to staining issues and other setbacks, we were unable to run as many trials as we had hoped. Our data cannot be considered conclusive due to lack of repetition, but the limited data we obtained supports our hypothesis. More trials with similar results would confirm what our data indicates: increased expression of miR-146a in THP-1 macrophages upregulates phagocytosis of apoptotic human cells. This result corroborates previous findings and supports the hypothesis that miR-146a is involved in regulating phagocytosis as a part of innate immunity. Further research is needed to understand the underlying mechanism of how miR-146a is upregulating phagocytosis, what mRNA target(s) lead to this effect, and why this occurs in the context of Sjögrens syndrome.

Figures/Charts

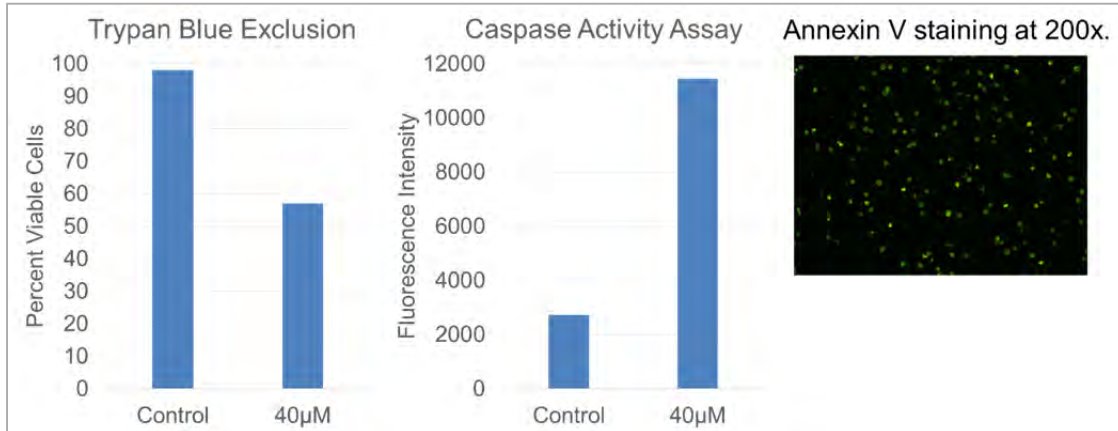


Figure 1. Jurkats given 40µM etoposide treatment overnight to induce apoptosis. Cell viability was determined using trypan blue exclusion, caspase-3 activity assay, and Annexin V staining.

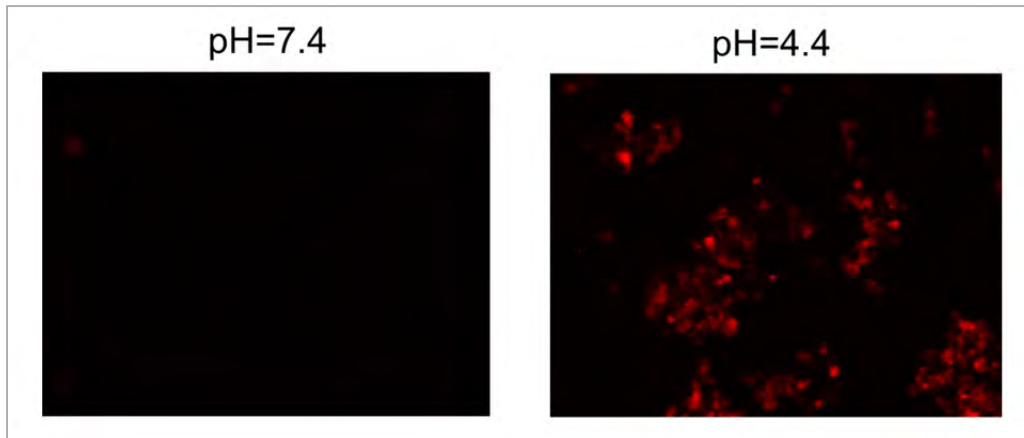


Figure 2. Jurkats were labeled with pHrodo succinimidyl ester, a pH-sensitive dye fluoresces red in low-pH environments.

Table 1. Count of red Jurkats and macrophages at 10x magnification reveals increased phagocytosed Jurkats in the experimental group.

	miR-146a transfected	Mock transfected
Jurkats	410	210
Macrophages	565	522
Jurkats per Macrophage	0.75	0.4

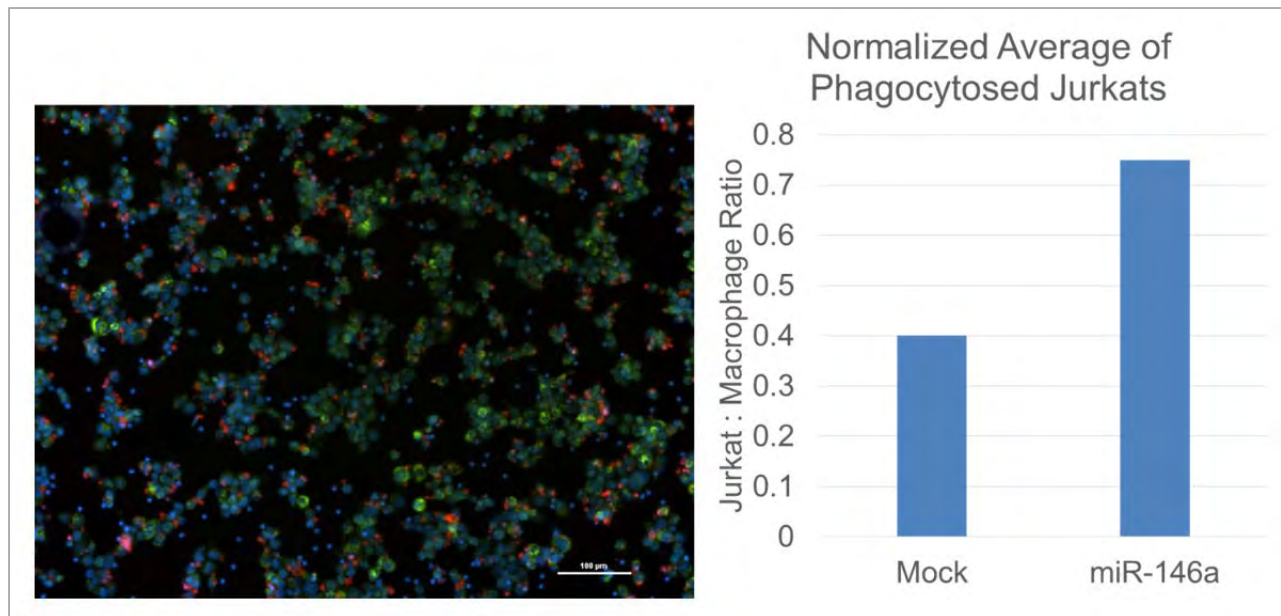


Figure 3. Mock-transfected and miR-146a transfected THP-1 cells were co-incubated and counterstained with DAPI (blue) and CD-68 (green). Phagocytosed Jurkats exhibiting positive pHrodo staining (red) and THP-1 macrophages (green) were counted. The ratio of jurkats to THP-1 cells was calculated for both mock and miR-146a transfected cells (see *Table 1*), and miR-146a transfected THP-1 cells exhibited a 1.8-fold increase in phagocytosis over that of the apoptotic Jurkats.

Acknowledgments

The author would like to thank Dr. Kaleb Pauley for her suggestion of the project and her guidance in completing it. The author would also like to thank Daniel Stank for his help carrying out experiments and maintaining cell cultures.

References

1. Catanzaro, J., & Dinkel, S. (2014). Sjögren's Syndrome: The hidden disease. *Medsurg Nursing*, 23(4), 219.
2. Miksa, M., Komura, H., Wu, R., Shah, K. G., & Wang, P. (2009). A novel method to determine the engulfment of apoptotic cells by macrophages using pHrodo succinimidyl ester. *Journal of immunological methods*, 342(1), 71-77.
3. Pauley, K. M., Stewart, C. M., Gauna, A. E., Dupre, L. C., Kuklani, R., Chan, A. L., Pauley, B. A., Reeves, W. H., Chan, E. K. L., & Cha, S. (2011). Altered miR-146a expression in Sjögren's syndrome and its functional role in innate immunity. *European Journal of Immunology*, 41(7), 2029. doi:10.1002/eji.201040757.
4. Shi, H., Zheng, L. Y., Zhang, P., & Yu, C. Q. (2014). miR-146a and miR-155 expression in PBMCs from patients with Sjögren's syndrome. *Journal of Oral Pathology & Medicine*, 43(10), 792-797.

Design and Performance Evaluation of a Miniature Haptic Actuator based on Electrorheological Fluid

Student Researcher: Alex J. Mazursky

Advisor: Dr. Jeong-Hoi Koo

Miami University

Department of Mechanical and Manufacturing Engineering

Abstract

Smart materials have adjustable material properties in the presence of an external stimulus. In this study, electrorheological (ER) fluid, a smart fluid with a viscosity and yield stress dependent upon the magnitude of applied electric field, is utilized in a haptic actuator to provide touch-based feedback to a user. For a device to provide complete haptic feedback, two key components must be present: tactile feedback and kinesthetic feedback. Tactile feedback consists of the sensations felt at the surface of one's skin and just underneath it. One such sensation is vibration, observed during vibrotactile feedback. Kinesthetic feedback is felt in one's joint and muscle nerves and provides information about position and movement. Thus, both sensations must be present to fully understand an object through touch. Most devices today use small motors to provide touch-based feedback. However, these motors are only capable of providing vibrational feedback and not kinesthetic feedback. This project aims to create a miniature button capable of providing both vibrational and kinesthetic feedback by manipulating the yield stress of the ER fluid with an electric field input. The button's performance will be evaluated under different electric field conditions. This project also explores cost-effectiveness by analyzing the performance of both commercially available ER fluid and a less-costly ER fluid made from silicone oil and cornstarch.

Project Objectives

The goal of this project was to produce a button device that is capable of producing both tactile and kinesthetic feedback through the application of ER fluid's tunable viscosity. To achieve this, the research first fabricated ER fluid samples at various concentrations of filler particles. Following fluid fabrication, an actuator based on ER fluids was designed and manufactured. Upon successful actuator assembly and noticeable haptic feedback observed during human evaluation, the actuator's effectiveness at generating haptic sensations was machine tested.

Methodology Used

ER fluid samples were fabricated using silicone oil as the electrically insulating fluid and three concentrations of cornstarch (15%, 30%, 45% by volume) as the particle suspension. These materials were selected for their desirable properties, such as the liquid's high activity (i.e., the magnitude of the change in flow properties caused by the presence of an electric field) and similar densities between the liquid and solids, as well as their low cost compared to commercially available ER fluid. Through observation, the 30% starch by volume fluid was found to exhibit the greatest response to an electric field input. Commercially available ER fluid was purchased for performance comparisons during testing.

A small button based on the adjustable yield stress of ER fluid was designed to provide haptic feedback to the user. The device contains a column of ER fluid between electrodes, which control the fluid's behavior through a voltage input. The haptic interface of the actuator is composed of an insulating membrane capable of being elastically indented 1-2 mm by the user. When indented, the user experiences a resistive force due to the ER fluid behind the membrane. This resistive force corresponds

to the properties of the electric field between the electrodes and was estimated during the design phase of the project. The pressure drop across the electrodes due to the yield stress of the ER fluid was estimated and applied to predict resistive force (Coulter, 1993):

$$F = \Delta PA = \frac{2\tau(E)(r_o - r_i)}{h} A$$

Where $\tau(E)$ is the yield stress, r_o and r_i are the outer and inner radii of the electrodes, respectively, h is the gap distance between the electrodes, and A is the surface area of the electrodes. Additionally, the actuator features a secondary fluid reservoir for the displaced fluid to flow into when the interface is pressed, rather than being forced out of the device at the membrane or the fitting. When the force is relieved, the fluid flows back into the main column due to change in pressure.

To measure the haptic performance of the device, mechanical analysis was conducted using a dynamic mechanical analyzer. This experimentation measured the total resistive force with respect to indentation depth over the button's stroke. The performance was evaluated under different conditions, such as input voltage and frequency. This testing was performed with giant ER fluid inside the device, which produces greater yield stresses than conventional fluid (Seo, 2013).

Results Obtained

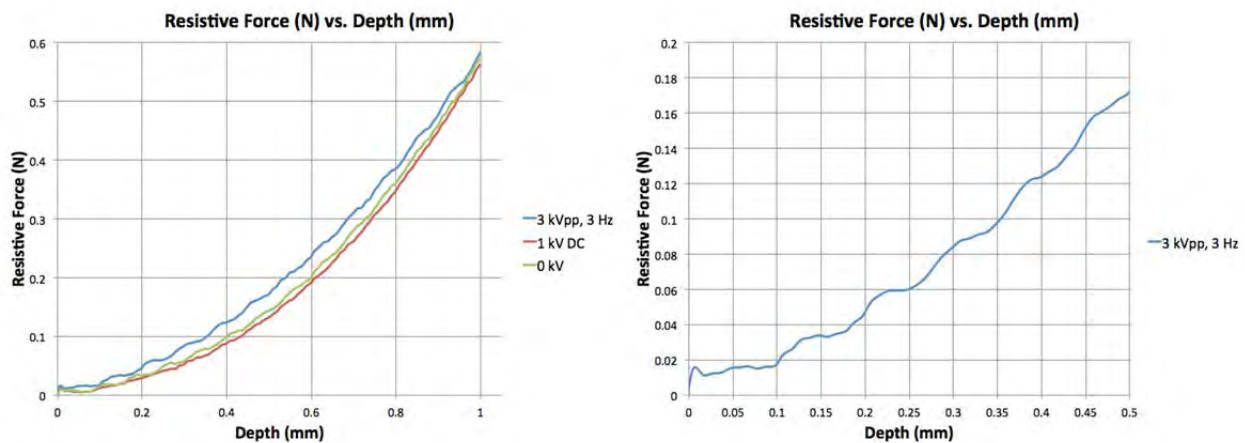


Figure 1. Resultant plot of resistive force with respect to depth.

Significance and Interpretation of Results

Indenting the button's membrane surface produced kinesthetic feedback. Vibrotactile feedback, seen in Figure 1, was observed when a low frequency voltage was supplied to the actuator. Therefore, the actuator is capable of yielding haptic feedback.

Acknowledgments

The author would like to thank Dr. Jeong-Hoi Koo for his guidance and mentorship throughout the project. Thank you to Paul Goetze and David Jacob for their assistance in design and manufacturing.

References

1. Coulter, John P., Keith D. Weiss, and J. David Carlson. "Engineering Applications of Electrorheological Materials." *Journal of Intelligent Material Systems and Structures* 4 (1993): 248-59. Web.
2. Seo, Youngwook P., and Yongsok Seo. "Analysis of Giant Electrorheological Fluids." *Journal of Colloid and Interface Science* 402 (2013): 90-93. Web.

Diabetes: The Community College Student's Perspective

Student Researcher: Joshua D. McIntosh

Advisor: Candice Jones

Cincinnati State Technical and Community College
Business Technologies Department

Abstract

According to the American Diabetes Association (ADA) and Center for Disease Control (CDC), 29.1 million people have diabetes, with 8.1 million people unaware that they have the disease. If current trends continue, it is predicted, that by 2050, 1 in 3 people will have diabetes (National Diabetes Statistics Report, 2014). As a prospective Dietetic Technician and, hopefully a future Dietitian, there is a high probability a new dietitian will be assessing, educating, counseling, and treating patients with diabetes. A campus wide information seeking venture was conducted and focused on attitudes towards diabetes. I want to see how college students perceive diabetes and components, such as blood glucose levels, medications, insulin and the dietary behavior changes that are important in diabetes self-management. For data gathering purposes, the Michigan Diabetes Research and Training Center's "Attitudes Survey" was used. Using a Likert scale, the survey contains 33 questions which address people's beliefs about diabetes self-management practices, including the role of health care workers, and dietary needs of the diabetic. From there, based upon my findings, there will be an attempt made to discover what programs or approaches could be utilized to improve the attitude and the knowledge level of college students about diabetes. Through this research project, the goal is to ultimately discover the knowledge level of the typical community college student and which program/approach can be utilized to lessen any knowledge deficit amongst community college students, whether through literature distribution, on campus lecturers, or a health and nutrition blog on the campus homepage. The data will be collected, analyzed, and conclusions will then be drawn as to the proper steps to be taken from that point forward.

Project Objective

The hypothesis is that health related students will have a more appropriate attitude towards diabetes than students in non-health related programs. With an increase of new diabetes diagnoses, attitudes towards diabetes among students on a community college campus have become an area of interest. Because of this interest, a campus wide information seeking pilot study was conducted. Its focus is on the attitudes of the community college student towards diabetes. Based on the findings of this venture, the question is "Would students benefit from an information session, such as a lunch and learn, to improve attitudes towards diabetes to initiate a lowering of risk of diabetes in this population?"

Methodology Used

For information gathering, the Michigan Diabetes Research and Training Center's "Attitudes Survey" was used. Using a Likert scale, the survey contains 33 questions which address people's beliefs about diabetes self-management practices, including the role of health care workers, and dietary needs of the diabetic. The question fell into 5 specific categories: Need for Special Training, Seriousness of NIDDM, Value of Tight Control, Psychosocial Impact of DM, and Patient Autonomy. Students were surveyed on campus that represented the populations in health-related programs and non-health related programs. Health related programs, for the purposes of this pilot study are programs that emphasize the healthcare system and preparedness for a career in the various facets of healthcare. Non-health related programs are simply all other programs of study offered at Cincinnati State Technical and Community

College. Because of easy accessibility, we focused our efforts in this initial pilot study on students in the Dietetic Technology, Nursing, and Health and Fitness majors for our health-related programs and Pastry Arts, Culinary Arts, and Brewing Science for our non-health related programs. Along with the 33 questions pertaining towards students' attitudes towards diabetes, the following demographic information was gathered: race/ethnicity, gender, and age group.

Results Obtained

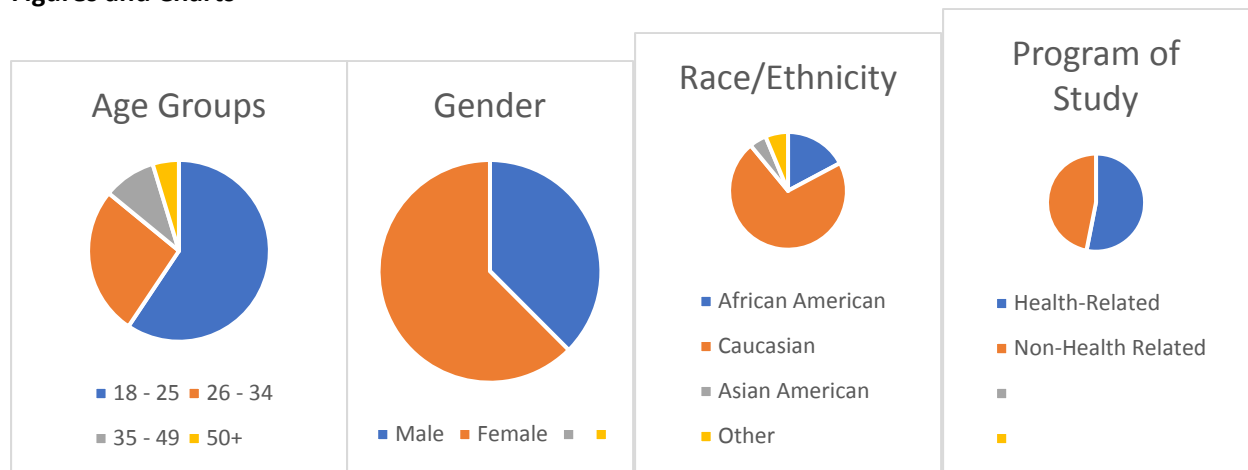
Many questions from the survey were answered similarly by both of the target groups. 64 surveys were obtained in total, 34 health-related students and 30 non-health related students.

Based on the results of this survey, the belief is that the conclusions are biased, based on the limited accessibility to other student responders. The students, both non-health related and health-related expect for those in the Brewing Science program, have taken a basic nutrition course as part of their curriculum. The belief is that this has positively affected their attitudes towards diabetes.

Significance and Interpretation of Results

Based on the results of this initial pilot study, the belief is that continuing this study and expanding the data collecting to student responders in programs such as horticulture, automotive, accounting, and business management, would provide us with a less biased end-result and provide us with greater insight into true attitudes of non-health related and health-related students. These programs do not require a basic nutrition course for their program's curriculum. Beyond obtaining a more diverse non-health related student pool regarding their program of study, it would be of great benefit to create and test a more focused survey to generate a clearer vision of the dichotomy between the non-health related students and health-related students.

Figures and Charts



References

1. Centers for Disease Control and Prevention. *National Diabetes Statistics Report: Estimates of Diabetes and Its Burden in the United States, 2014*. Atlanta, GA: U.S. Department of Health and Human Services; 2014.
2. Jones, C. N. (2011). Examining Racial Differences in Knowledge and Attitudes of Diabetes Management in Newly Diagnosed Type 2 Diabetes Patients. University of Cincinnati, Cincinnati, OH.
3. University of Michigan Diabetes Research and Training Center. (1998, December 18). *Diabetes Attitude Survey*.
http://diabetesresearch.med.umich.edu/peripherals/profs/documents/svi/das3_new.pdf

Analyzing Silicon Carbide as an Engineering Material

Student Researcher: Cameron R. McNair

Advisor: Professor Adele Wright

Columbus State Community College
Mechanical Engineering

Abstract

Silicon Carbide (SiC) is one of the strongest and most versatile engineering materials available. Silicon Carbide is an important compound. Why? Silicon Carbide is used in many different industries and applications: It's used in ceramic brake pads on vehicles, body armor, anti-slip flooring, and electronics just to name a few. Also, anything requiring high wear resistance and low thermal conductivity. The goal of this paper is to examine Silicon Carbide as an engineering material, and effectively examine SiC holistically through the research sources cited. To achieve this goal, this paper is divided into three different sections. The first section will cover in depth the different methods used to produce SiC, and understanding its natural state. Next, SiC's chemical and physical properties will be examined. The paper will conclude with an examination of the applications of SiC.

Production of Silicon Carbide

"Manufacture of Silicon Carbide," is a great source of information of how Silicon Carbide is produced. Silicon Carbide is produced through an exclusive process called the Acheson Process. The Acheson Process was developed by E.G. Acheson in 1891. Acheson process is a process which is used mainly for the manufacturing of silicon carbide (Indian Institute of Science or I.I.Sc.). Currently coke and quartz are used as major raw materials to produce SiC in bulk quantities. A schematic of a resistance furnace of the type used in the Acheson process is shown in Figure 1.

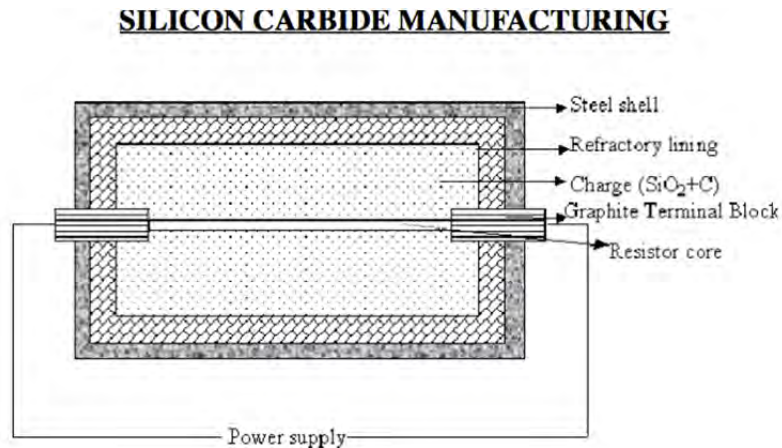


Figure 1 (I.I.Sc.)

In the Acheson Process at the ends are electrodes that supply the energy for the reaction. The electrodes heat the graphite in the reaction and cause the SiO₂ and the Carbon to react at temperatures from 1700- 2100 degrees Celsius to form SiC. After cooling, the SiC is crushed and

milled and sometimes chemically treated depending on the application. The disadvantage in this process is it is somewhat inefficient because all the materials in the cast do not fully react and change to SiC. More explanation on the manufacturing of Silicon Carbide: “The main raw materials are SiO_2 and C which are made to react at high a temperature. Saw dust and salt are also added, so that saw dust burns and provides pores facilitating escape of evolved gases (at high temperatures). Firing is done for about 40 hours and after cooling, the side walls are removed. An outer layer of uncombined mixture is broken away, exposing the cylindrical mass of sharp, brilliant crystals (I.I.Sc.)”

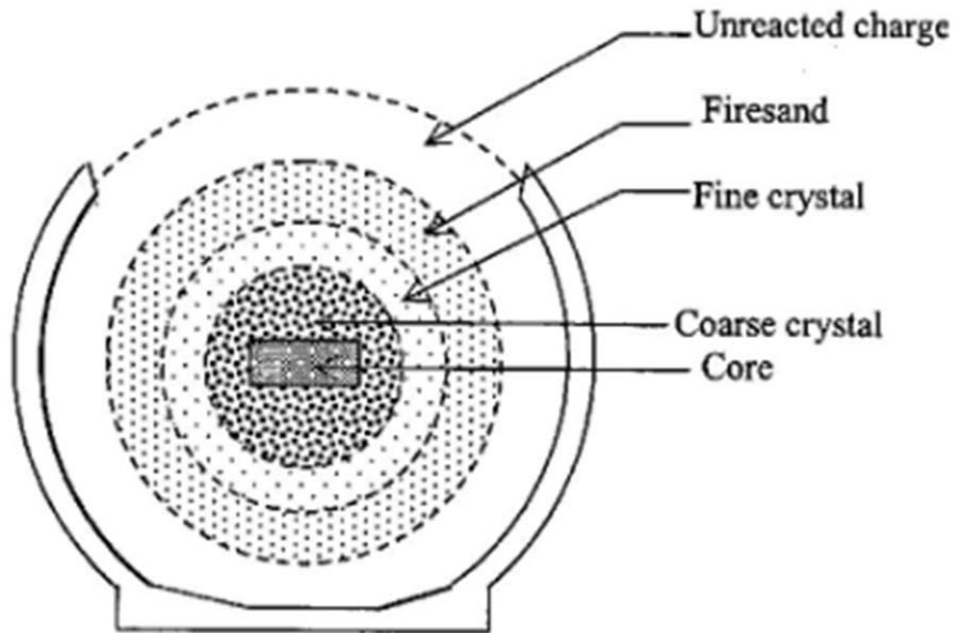


Figure 2 [I.I.Sc.]

SiC is also made via the Seeded Sublimation Growth method. (See Figure 3 below) “In the process polycrystalline SiC at the source sublimates at a high temperature, (1800-2600 °C) and low pressure (Råback). Sublimation is when molecules transition from the solid to the gaseous state. The crucible is heated through induction. The resulting gases travel through natural transport mechanisms to the cooler seed crystal where crystallization due to supersaturation takes place. The seed crystal is usually situated at the top of the crucible in order to prevent contamination by falling particles. “In the Seeded Sublimation Growth Method the crystals form thin 2” or 3” wafers, these wafers are used in the manufacturing of electronic devices (I.I.Sc.)” The advantage of this method over the Acheson Process is more control of the purity of the SiC formed.

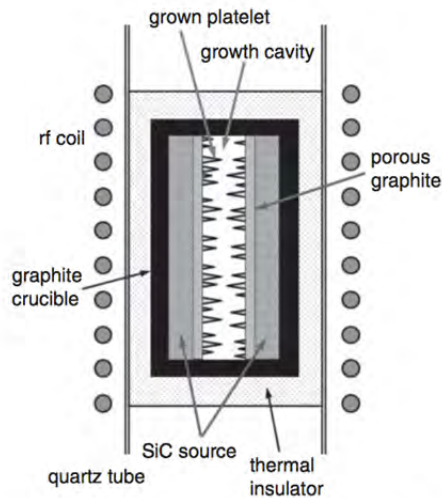


Figure 3.3 Schematic illustration of a crucible used in the Lely method.

Figure 3 [Kimoto 2]

Next, Silicon Carbide in its natural state will be discussed. SiC can be found in nature as a rock called Moissanite. It was discovered by a French Chemist name Henri Moissan in 1907 in the Canyon Diablo Meteorite (Barthelemy). Moissanite is 70.04% Silicon and 29.96 % Carbon. Moissanite's atoms are typically in the Hexagonal pattern, however they can exist in different crystal structures, making it polytypic. Polytypism is a phenomenon where a material can adopt different crystal structures, which vary in one dimension without changes in chemical composition.

Properties of Silicon Carbide

Silicon Carbide is one of the hardest engineering materials, with only osmium and diamonds being harder (I.I.Sc.) It has a Brinwell Test value of 2800 Kg/mm². Additionally, SiC has a yield strength of 21 GPa, a significant value. A few of the well-known advantages of SiC are its low thermal conductivity, hardness and elasticity at high temperatures. The low thermal conductivity indicates the material can resist over-heating. SiC's ability to remain hard and be elastic at high temperatures comes from it's unique combination of Carbon and Silicon. The Carbon atoms make the compound hard and the Silicon help the compound resist extreme temperatures. SiC has a Poisson Ratio value of 0.21 on a range from 0.00 to 0.50. (Kimoto 2) What this value indicates is that SiC will resist compression in the longitudinal direction.

Understanding SiC Phase Diagram (Figure 4 Below)

Between 0 to 49 % Carbon at or under 1400 degrees Celsius there exists Silicon and the compound Silicon Carbide. As the temperature increases, the Silicon dissolves into a liquid and the compound SiC remains. Above 2800 degree C there is only liquid and carbon left; the SiC compound dissolves. The eutectoid composition is at 50% Carbon and 1200 degree C to 2830 degree C. From 51 % Carbon to 100 % Carbon SiC compound and C carbon exist, with more Carbon existing toward the end of the diagram.

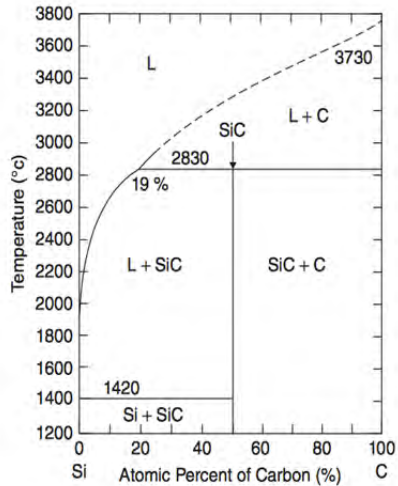


Figure 3.1 Phase diagram of the Si–C binary system [1, 2].

Figure 4 [Kimoto 2]

The Practicality of Silicon Carbide

As mentioned earlier, Silicon Carbide is a strong, durable and heat resistant material used in many different industries. The high surface hardness of the material lead to it being used in engineering applications where a high degree of sliding, erosive and corrosive wear resistance is required (Azom.com). This includes flooring, cutting tools, filters, bearings and incinerators in addition to the many other places where resistant parts are used. SiC is also a highly capable semiconductor. A semiconductor is a material that conducts current. SiC conducts current well because of the four outermost valence electrons that allow the formation of covalent bonds between atoms and consequently the flow of electrons. Silicon Carbide revolutionized the world of electronics (the circuit boards in which the integrated circuit chips are designed). The invention of integrated circuits (ICs) made by planar technology triggered rapid progress in *microelectronics*. Nowadays, Si-based large-scale integrated circuits (LSIs) are the key components in almost all electrical and electronic systems (Kimoto 1)

Conclusion

From examining SiC’s chemical and physical properties, manufacturing capability, and its applications we achieve a holistic view of the compound that has helped progress the world. Simply put, SiC is important because of its versatility and durability. Silicon Carbide will continue to be an effective and efficient engineering material in the applications it’s used in today, and for the future applications of tomorrow.

Notes

- (I.I.Sc)-Indian Institute of Science
- (Kimoto 1)- Chapter 1
- (Kimoto 2)- Chapter 2

References

1. "Manufacture of Silicon Carbide, Simulation Lab, Dept. of Materials Engineering, I.I.Sc. Bangalore, India." *Manufacture of Silicon Carbide, Simulation Lab, Dept. of Materials Engineering, I.I.Sc. Bangalore, India*. N.p., n.d. Web. 08 Dec. 2016.
2. Kimoto, Tsunenobu, and James A. Cooper. "Physical Properties of Silicon Carbide." *Fundamentals of Silicon Carbide Technology: Growth, Characterization, Devices and Applications*. Singapore: John Wiley & Sons Singapore Pte., 2014. 11-33. Print.
3. "Silicon Carbide Production Process." *Silicon Carbide Production Process | Saint-Gobain Silicon Carbide*. N.p., n.d. Web. 08 Dec. 2016.
4. Råback, Peter., et al. "Modeling of the Sublimation Growth of Silicon Carbide Crystals." *Staff.csc.fi*. N.p., n.d. Web. 8 Dec. 2016.
5. Barthelmy, Dave. "Moissanite Mineral Data." *Moissanite Mineral Data*. N.p., n.d. Web. 08 Dec. 2016.
6. Sponsored by INSACO Inc. - Machining of Hard Materials. "Machining Of Silicon Carbide - Process, Applications and Types." *AZoM.com*. N.p., 09 May 2016. Web. 08 Dec. 2016.

Active Exoskeleton for the Sit-to-Stand Transition

Student Researcher: Amanda M. Miller

Advisor: Dr. Manish Kumar

University of Cincinnati
Mechanical Engineering

Abstract

As of 2013, there are 40 million people over the age of 65, and it is projected to continue to increase in the coming years, resulting in more and more people needing assistance with activities of daily living, including the sit-to-stand motion. This motion is a key factor to one's independence, as it is the beginning and ending action for moving from one place to the next, and is involved in many other basic tasks, such as getting out of bed and using the restroom. This work presents the process of developing an active lower body exoskeleton and its controls, designed to assist with the sit-to-stand transition. This includes recording the motion for the sit-to-stand transition, analyzing the forces acting at each of the joints, and interpreting the data to determine a proper model for the exoskeleton and motors. The next step is to begin fabrication of the exoskeleton and test different control designs.

Statement of the Problem

In the United States, the number of people age 65 and older increased from 35 million to 40 million between 2000 and 2010 and is projected to increase to 72 million by 2030¹. As this population increases, more and more people will need assistance with activities of daily living including the sit-to-stand transition. Not only that, but muscle weakness can become an issue with astronauts. Muscle atrophy is an issue for astronauts in space. This atrophy is caused by the reduced amount of gravity, thus leading to muscle and bone weakness, which can become a problem once returned to Earth.

Background

ReWalk² and the Berkley Lower Extremity Exoskeleton³ assist in carrying weight while walking. Even though walking is the foundation of independence and has been studied and recognized in the development of exoskeletons, the sit-to-stand transition movement has not, despite being the beginning and end of almost every walking movement. The X1 exoskeleton developed by NASA and the Florida Institute for Human Machine Cognition provides both assistance and resistance to the user, which is key for physical therapy both in space and on Earth⁴.

Project Objectives

The Scope of this project deals with designing a 3D model and using force sensors to calculate the center of pressure for an active exoskeleton for the sit-to-stand transition. The planning and design of the exoskeleton must include multiple aspects: be modeled around an off-the-shelf leg brace, be self-supporting, and allow the mounting of series and parallel elastic actuators at the knee, hip and ankle joints. The second part of the project is to incorporate force sensors into the foot piece assembly. This will enable a computer to track and predict how the center of pressure will change, thus allowing a dynamic application of force for each of the six joints as needed.

The Design of the Exoskeleton

The design of the exoskeleton has three main elements: a foot piece assembly, adjustability, and the implemented actuation at the three joints. The foot piece assembly has four force sensors incorporated

into the footplate assembly. This allows for precise calculations of the center of pressure using the four force sensors. The foot piece assembly also incorporates tracks that allow wires to be guided along the foot piece, as well as enabling proper application of force from the user to the force sensors. The force sensors are calibrated with the equation listed below:

$$F_g = \text{analogread} * \frac{450N}{2} - F_{avg}$$

Equation 1: Calibration of a force sensor.

The *analogread* variable is the voltage that the microcomputer, Arduino Uno, interprets during the calibration run. Next, $\frac{450N}{2}$ is the maximum read of force for the force sensor over the maximum voltage the force sensor can interpret. Finally, F_{avg} is the net force that the force sensor initially measured. This includes the initial force that the user applies as well as the weight from the footplate sensor assembly. The center of mass is calculating using the equation listed below.

$$\text{Center of Mass} = \frac{F_{g1} \cdot x_1 + F_{g2} \cdot x_2 + F_{g3} \cdot x_3 + F_{g4} \cdot x_4}{F_{g1} + F_{g2} + F_{g3} + F_{g4}}$$

Equation 2: Calculation of the Center of Mass.

This equation is used to calculate the center of mass, used for both the x and y coordinates. This equation is used in each plate to calculate the center of mass as it changes throughout the sit-to-stand transition. This information will then be applied to predict the movement of the user and adjust the actuators accordingly.

The exoskeleton design itself must be adjustable in order to fit a variety of people. This allows for more people to wear one model and reduce the cost of modifications. This is key to ensuring that it is cost effective since it reduces the number of exoskeletons needed of varying sizes. This adjustability is modeled from an off-the-shelf leg brace. This leg brace allows for the exoskeleton to fit snugly on the user and correctly apply the necessary forces to the user for the sit-to-stand transition. And with the adjustability of both the exoskeleton and the leg brace, the torques can be precisely applied to the user, thus reducing their discomfort.

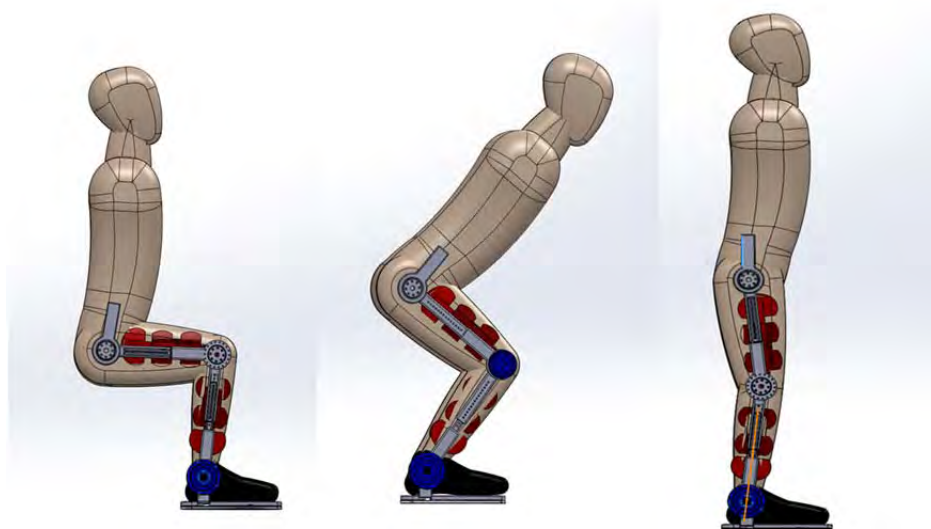


Figure 1. A 3D model of the exoskeleton with a human figure viewed throughout the sit-to-stand transition.

Figure 1 illustrates how the exoskeleton has adjustable links in the lower and upper leg links as well as incorporating a leg brace for the exact application of forces and torques to the user.

Finally, the exoskeleton needs actuation incorporated at the knee, hip, and ankle joints for the sit-to-stand transition. A rotary actuator is chosen to allow for precise control of torques and movement at the joints. Then, series and parallel elastic actuators are incorporated to reduce the power and torque required to be supplied by the actuator, as well as making the joints more flexible. This is necessary since it reduces the weight of the exoskeleton as well as increases comfort to the user.

Results

The results obtained from the design of the exoskeleton include precise calculations in changes in the center of pressure of the user from the foot sensors in the footplate assembly. In addition, the leg brace add-on will allow for a secure attachment of the exoskeleton to the user and correct translation of torques to the knee, hip, and ankle joints. Finally, a 3D model was designed that is adjustable and ready to begin simulation to determine the different types of materials that can be used.

References

1. Fowels , D. G., & Greenberg, S. (2011). *A Profile of Older Americans:2011*. Department of Health and Human Services.
2. ReWalk Robotics Inc. (2017). *About ReWalk Robotics*. Retrieved January 2017, from ReWalk : <http://rewalk.com>
3. Yang, S. (2004, March). *BLEEX*. Retrieved from Berkley Robotics & Human Engineering Laboratory :
4. Hall, Loura. (2015). *NASA's Ironman-Lie Exoskeleton Could Give Astronauts, Paraplegics Improved Mobility and Strength*. https://www.nasa.gov/offices/oct/home/feature_exoskeleton.html

An Electrochemical Analysis of Fretting Corrosion in Metal-on-Metal Hip Implants Subjected to High Impaction Loads

Student Researcher: Joseph R. Morin

Advisor: Dr. Timothy Norman

Cedarville University

Department of Mechanical and Biomedical Engineering

Abstract

The metal-on-metal total hip arthroplasty, a procedure where the hip joint is replaced by a femoral prosthesis with a metal femoral head and a metal socket, has been a popular option for patients requiring a hip joint replacement. Metal on metal hip implants have been a successful implant design until recently where there has been an increased number of failures of this type of implant due to fretting corrosion, believed to be caused from the use of large femoral heads. Fretting corrosion in hip implants results from cyclic micromotion at the taper-trunnion interface; this interface motion removes the protective oxidation layer from the metal allowing the fluid environment of the body to react with the metal and ultimately leads to the release of metal ions into the surrounding tissue and bloodstream. The objective of this research is to quantify the amount of fretting corrosion at the taper-trunnion interface after a static load of 991lbs is applied, and compare results to a previous study where 450lbs impaction force was applied. For both studies, all specimens are cyclically loaded between 10lbs and 460lbs while fretting corrosion data is collected. Fretting corrosion was characterized through the implementation of an electrochemical experiment in order to measure the amount of metal ions released from the implant during loading, which is directly correlated to the amount of fretting corrosion. Results from this study indicate that the specimens that were loaded a second to 991lbs produced more fretting area than those not loaded a second time. It is suspected that the second impaction disrupts the interface allowing for more fretting area to be done initially as compared to the 450lb specimen that were stable after the first test.

Project Objectives

When a hip implant is being installed in a patient, the surgeon attaches the femoral head to the stem by impacting them together. This experiment had the following objectives with regard to impaction load:

- Characterize fretting corrosion through an electrochemical analysis on hip implant specimens loaded to 991lbs
- Compare high impaction loads (991lbs) to low impaction loads (450lbs) for fretting corrosion
- Determine the relationship between impaction load and fretting corrosion in titanium hip implants
- Determine how a second loading affects fretting corrosion in a previously loaded hip implant specimen

We hypothesized that the increase in the impaction load would reduce the amount of fretting wear generated in taper-trunnion specimens loaded under cyclic loading because of the tighter press fit.

Methodology

In order to test how impaction load affects fretting corrosion, 15 Ti-6Al-4V specimens were collected from a previous study in which they were all statically loaded to 450lbs, and then dynamically loaded between 10lbs and 460lbs¹. The specimens differed by the taper angle and were divided into groups of three. Ten of these specimens were then statically loaded to a higher load of 991lbs, and the other 5 were left at the previous load level and not impacted any further in order to be used for control specimens. All load levels were chosen in accordance with ASTM 1875². Specimens were statically loaded using the Instron 3300 Floor Model Universal Testing System.

Once all the specimens were statically loaded to their respective impaction loads (991lbs or 450lbs), they were then cyclically loaded between 10lbs and 460lbs using an MTS 810 Servo-Hydraulic Universal Testing System. While the specimens were being cyclically loaded, they were situated so that the taper-trunnion interface was submerged in an electrolytic solution in order to perform the electrochemical analysis². A lead wire was then fixed to the specimen being compressed (acting as the anode) and was connected through a picoammeter to a cathode of the same material also submerged in the electrolytic solution. A diagram of this setup can be seen in Figure 1 below.

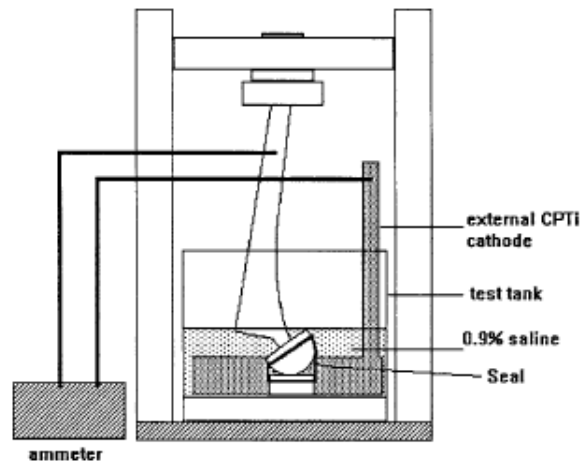


Figure 1. Electrochemical testing apparatus. Image taken from ASTM 1875-98²

During the cyclic compression of the specimen, metal ions wear off at the taper-trunnion interface and interact with the electrolyte, resulting in a current being produced and measured by the ammeter. The amount of current produced is directly correlated to the amount of metal ions interacting with the electrolyte, and is therefore directly related to fretting area. This method has been taken from and verified in ASTM 1875-98². The ammeter was directly connected to a computer and current data was recorded using TracerDaq Pro.

Once all the raw data is collected and stored in the computer, a MatLab Simulink model created in a previous study is used to calculate the amount of fretting area from the current measured¹. The Simulink model normalizes the raw data, and then integrates the current data and calculates the fretting area. It then outputs values for the total fretting area of each specimen tested and the results can now be compared for each of the impaction loads. The results will be evaluated by calculating the percent ratio (ratio of fretting area of new to old test), as well as calculating the percent change (percent difference) between the two tests.

Results Obtained

The values for fretting area can be seen in Table 1 in the Figures & Charts section of this report (note that 3 of the tested specimens were lost due to erroneous test data, or malfunctions in the experiments). The values for the new test are compared to a previously run test when all the specimens were compressed to 450lbs¹. Certain specimens that had already been previously loaded to 450lbs were loaded again without changing the impactation load to act as a control to be able to compare results of the new test to the old test. Results indicate that the fretting area for all of the new tests is less than the old test ($p < 0.0001$), as expected, regardless of whether or not a second high impactation load was applied.

The percent ratio between the new tests and the old tests was found by simply dividing the fretting corrosion of the new test by the old test, and multiplying by 100. These ratios are in the range of approximately 10-30%, which means that the second tests generated 70-90% less fretting area than the first test. Also, on average, but not statistically significant ($p < 0.2$), specimens that were impacted a second time had a higher percent ratio, which means that there was more fretting area than those specimens that were not impacted a second time. The implications of this will be discussed in the Significance and Interpretation of Results section.

The percent change between the two tests was also analyzed. Results indicate that on average, though not statistically significant ($p < 0.2$), there was less change between the two test when a higher impactation load was implemented, meaning that more fretting area was done in the specimens that were impacted again to 991lbs compared to the ones that were only impacted to 450lbs once. This is contrary to what was expected.

Significance and Interpretation of Results

It was expected that all of the new tests would yield lower fretting area values than the old tests because all the same specimens were loaded multiple times, so the majority of the asperities were broken and more wear was generated on first impact. This was observed in our tests. However, both fretting parameters indicated that, on average, the specimens that were loaded to 991lbs generated more fretting area than those only loaded to 450lbs. We hypothesized that the more the specimen is compressed to, the tighter the fit and the lower the fretting area generated, although that was not seen in this study. It is suspected that the second impactation disrupts the interface allowing for more fretting area to be done initially as compared to the 450lb specimen that were stable after the first test. In order to truly test higher impactation loads, new specimens should be acquired in a future study that have not been previously impacted and those fresh specimens should be impacted to 991lbs and compared with the study that impacted them to 450lbs.

Figures and Charts

Table 1. Fretting Corrosion in hip implants loaded to 450lbs and 991lbs

Specimen	Fretting Area		Percent Ratio	Percent Change
	Old	New		
1C	88.8	18.04	20.32	33.11
1D	85.5	14.509	16.97	35.49
2B	156.6	24.175	15.44	36.63
2D	158	44.163	27.95	28.15
2E	331.8	31.664	9.54	41.29
3B	172.7	16.895	9.78	41.09
3D	240.4	42.564	17.71	34.96
4B	111.4	54.209	48.66	17.27
4D	113.9	28.332	24.87	30.08
5B	187.7	24.61	13.11	38.41
5C	131.5	37.686	28.66	27.73
5D	149.8	35.137	23.46	31.00

Legend	
	450lbs Compression
	991lbs Compression

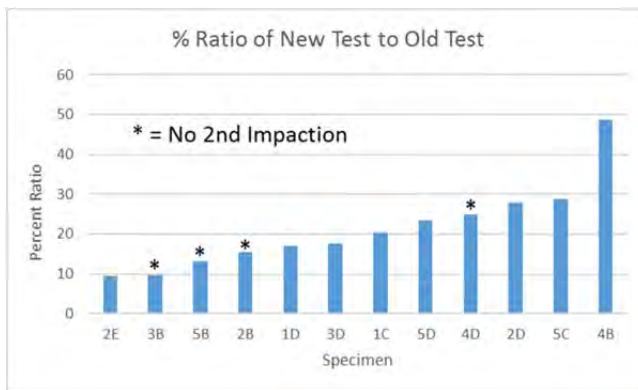


Figure 1a. Percent ratio analysis of fretting area

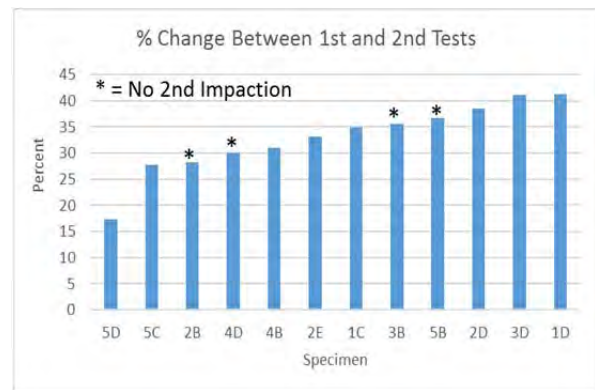


Figure 1b. Percent change analysis of fretting area

Acknowledgements

The author of this paper would like to thank Cedarville University for the means and equipment to conduct this research. The author would also like to thank Dr. Timothy Norman for his help on advising the project, as well as Dr. Thomas Fehring for clinical advice on the project. Finally, I am grateful to Dr. Bob Chasnov for his supervisor and administration of this program.

References

1. Bradley K, Harris S, Lawrence P, Lee A, Martin H. Design of Metal on Metal Hip Implants: Analysis of Taper-Trunnion Interface. April 2015. Cedarville University. Cedarville, OH.
2. ASTM F1875-98(2014), Standard Practice for Fretting Corrosion Testing of Modular Implant Interfaces: Hip Femoral Head-Bore and Cone Taper Interface, ASTM International, West Conshohocken, PA, 2014, www.astm.org

Waterless Fracturing Potential in the Appalachian Basin

Student Researcher: Sheldon P. Mullet

Advisor: Professor Craig A. Rabatin

Marietta College

Department of Petroleum Engineering and Geology

Abstract

The recent shale boom in the United States would not be possible without the ability to horizontally drill and hydraulically fracture wells in shale reservoirs that previously were not producible. As a result of these techniques enabling the shale boom, the U.S. has become one of the world's leading petroleum producers and is nearing energy independence. However, this new process is not free and comes with several potential drawbacks. One of the main drawbacks society sees with hydraulic fracturing completion techniques in Utica and Marcellus Shale wells in the Appalachian Basin is the large amount of water that must be used.

A large concern is that hydraulic fracturing uses too much fresh water. However, alternatives to hydraulic fracturing do exist, and this work shows the main alternatives and their viability in horizontal shale wells. The research includes case studies from other areas that have used waterless completion techniques and their economic outcomes. Also included in this work is a look into the net amount of water lost or potentially gained as a result of hydraulic fracturing. A conclusion, based on economics and the environment, is drawn on how petroleum exploration and production companies should fracture shale wells in the future.

Project Objectives

The project objective is to analyze the use of water in fracturing hydrocarbon-producing shales in the Appalachian basin from both an environmental standpoint and an economic standpoint. From the analysis, the objective is to form a recommendation for future fracturing operations in the Appalachian basin.

Methodology Used

The methodology used for this project consisted of four main research areas. First, evaluate the current use of water for hydraulic fracturing in Marcellus Shale and Utica Shale wells. Second, research potential alternatives to water for fracturing shale formations. Third, assess the economics of analogous formations that have undergone waterless or reduced-water fracturing and how that could affect the feasibility of trying alternative fracturing methods in the Marcellus and Utica shale formations. Finally, determine the environmental impact, specifically on fresh water, as a result of hydraulic fracturing.

Results

Current use of Hydraulic Fracturing and its Effects

Both the Marcellus and Utica Shale formations have very low permeability. As a result of the low permeability, oil and gas production companies must fracture the shale to allow the oil and gas to flow into the well. Most fracturing jobs in tight shales consist of pumping between three and five million gallons of water per well, along with chemicals and sand². This method usually has success, but some reservoirs do not respond very well when stimulated with water⁵. The water can cause clay in the shale

to swell and close pathways for oil and gas migration. Reservoirs can even trap the water in the small pathways and trap hydrocarbons from moving into the wellbore.

Fracturing reservoirs with water can also decrease the relative permeability of hydrocarbons and thus weaken oil and gas production¹³. The water can become trapped in the reservoir due to capillary retention and reduce the ability for oil and natural gas to flow¹³. In small pore spaces, the differential pressure between the reservoir and the well may not be large enough to push this water back out of the pore spaces. Figure 1 shows how lower permeability causes a much higher capillary pressure, which leads to retained water⁷. To the right of figure 1, figure 2 shows how an increase in the water saturation, due to the retained water, causes a decrease in the relative permeability to gas⁷. Finally, figure 3 shows how a hydraulic fracture (left) has a much smaller effective fracture length than a fracture that did not use water (right) due to the water left behind blocking the hydrocarbon production pathway.

Alternatives to Water for Fracturing

Because of the high volume of water used in hydraulic fracturing, an argument from an environmental standpoint could be made that oil and gas production companies should find ways to fracture their wells with a much smaller volume of water or even try to fracture without water at all. Reducing the water use could also potentially lead to better production from the wells. While waterless fracturing is not widely used, two main types of water-reduced fracturing do exist. The first is CO₂ fracturing. In CO₂ fracturing, companies pump CO₂ (as a super-critical fluid) into the formation along with sand as a proppant¹³. The second type involves using liquefied petroleum gas (LPG) in place of water¹¹. With this method, completion companies pump propane or butane (in liquid form) to fracture the shale, along with the chemicals and sand¹¹.

Economic Evaluation of Waterless Fracturing

Figure 4 shows the production rates of a sandstone reservoir in Texas with low permeability for a well fractured with LPG and a well fractured with water. The two production rates converge after about one year. This could mean a fracture with water and an LPG fracture end up with the same ultimate recovery, but companies cannot run economic analyses simply off of ultimate recovery. Table 1 shows the net present value (NPV) based only on revenue of the LPG fracture and the water fracture. The NPV, based on the revenue, of the LPG-fractured well is over twice as much after the first year as the conventional hydraulically fractured well using a 10% APY discount factor converted to an effective monthly discount factor. The difference in the values is around \$2 million, so this essentially means that the LPG fracture and its associated costs could be up to \$2 million more than the conventional fracture for it to be economical on an NPV basis.

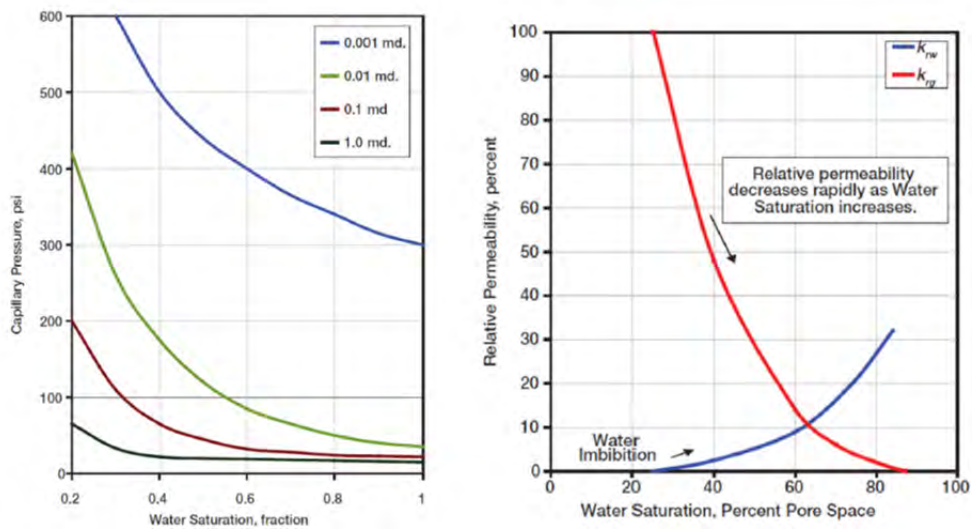
Environmental Impact (Specifically for Fresh Water)

From an environmental viewpoint, three to five million gallons of water used to hydraulically fracture one well sounds like a large amount of fresh water that could become a serious issue. However, taking a closer look at some information shows this may not be a problem at all. One way to look at this is to find the net amount of water used or released for each natural gas well. The chemical formula for burning methane is: $\text{CH}_4(\text{g}) + 2\text{O}_2(\text{g}) \rightarrow \text{CO}_2(\text{g}) + 2\text{H}_2\text{O}(\text{g})$. After working out the stoichiometry, 1,000 cubic feet of methane yields over eleven gallons of water. Using an average production per well per day of 2.8 million cubic feet of natural gas, each well (as a result humans burning its methane for energy) produces about 32,000 gallons of water per day¹². From this, a well only takes around 125 days to be responsible for releasing the same amount of water back into the atmosphere as the amount that was used to hydraulically fracture that well.

Significance and Interpretation of Results

Currently, from a fresh water usage standpoint, conventional hydraulic fracturing does not have a large impact on fresh water usage in a negative way. Transitioning to waterless fracturing methods only on the basis of reducing fresh water usage may not be justifiable. However, oil and gas companies need to keep fresh water usage in mind and do their own studies on how it could impact the specific area in which they are operating. From an economic standpoint, however, reduced-water fracturing methods and waterless fracturing methods could be advantageous. The potential to mitigate issues with clay swelling and reduced permeability due to retained water should give companies an incentive to test waterless fracturing techniques. The economic analysis from the tight sandstone reservoir in Texas discussed above and shown in table 1 below also give evidence that waterless fracturing techniques are worth exploring deeper and testing out in the Marcellus and Utica shale formations.

Figures



Figures 1 and 2. Capillary Retention and Reduced Relative Permeability⁷

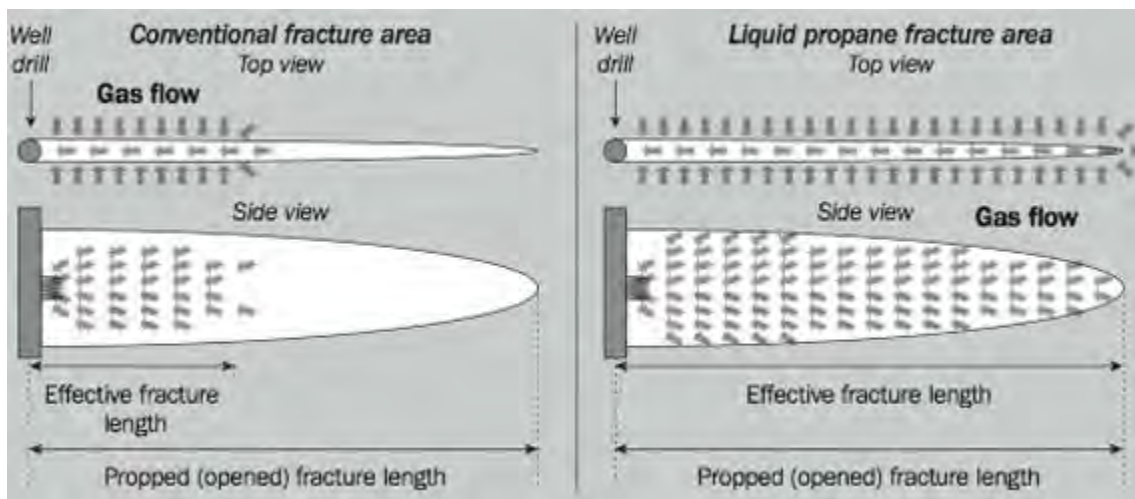


Figure 3. Effective Fracture Lengths⁵

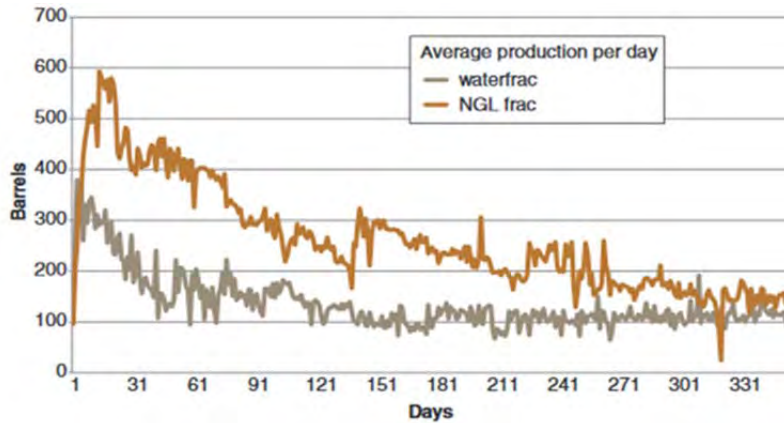


Figure 4. Flow Rate Comparison ¹¹

Month	Well 1 (bbl/day *30)	NPV Well 1 (i=10%) and \$40/bbl	Well 2 (bbl/day *30)	NPV Well 2 (i=10%) and \$40/bbl
1	15000	\$595,000	7800	\$310,000
2	12300	\$484,000	5250	\$207,000
3	10500	\$410,000	4800	\$187,000
4	8700	\$337,000	4500	\$174,000
5	8100	\$311,000	3450	\$133,000
6	7800	\$297,000	3000	\$114,000
7	7200	\$272,000	3000	\$114,000
8	7050	\$265,000	3000	\$113,000
9	5700	\$212,000	3000	\$112,000
10	5400	\$200,000	3000	\$111,000
11	4950	\$181,000	3000	\$110,000
12	4800	\$175,000	3000	\$109,000
	LPG Total NPV	\$3,739,000	Water Total NPV	\$1,794,000

Figure 5. Net Present Value Comparison ¹⁰

References

1. *Animation of Hydraulic Fracturing (fracking)*. Dir. Marathon Oil Corporation. *YouTube*. N.p., 26 Apr. 2012. Web. 3 Mar. 2017.
2. Bennett, Shawn. "Utica Shale Water Use." (n.d.): n. pag. 19 June 2014. Web. 9 Jan. 2017. "Golf's Use of Water: Solutions for a More Sustainable Game." *USGA*. N.p., 1 Nov. 2012. Web. 09 Jan. 2017.
3. Fei, Yang. "Simulation of Hydraulic Fracturing with Propane-based Fluid Using a Fracture Propagation Model Coupled with Multiphase Flow Simulation in the Cooper Basin, South Australia." N.p., June 2016. Web. 3 Mar. 2017.
4. Gurule, Kendall. "Nitrogen Gas Fracking." *Frack Wire*. N.p., 9 July 2013. Web. 09 Jan. 2017.
5. Gustin, Georgina, Lisa Song, Bob Berwyn, Zahra Hirji, Anthony Brino, Maria Gallucci, Elizabeth McGowan, and Phil Alexandra. "New Waterless Fracking Method Avoids Pollution Problems, But Drillers Slow to Embrace It." *InsideClimate News*. N.p., 6 Nov. 2011. Web. 10 Jan. 2017.
6. Khuwaja, Abdul, Abdul Basit, and Inamullah Haneef. "Waterless Fracking - a New Way to Frack Using Lpg Gel." *Search and Discovery*. N.p., 20 Nov. 2014. Web. 10 Jan. 2017.

7. Kong, Bing, Shuhua Wang, Shengnan Chen, and Kai Dong. "Minimize Formation Damage in Water-Sensitive Unconventional Reservoirs by Using Energized Fracturing Fluid." *OnePetro*. Society of Petroleum Engineers, 24 Feb. 2016. Web. 09 Jan. 2017.
8. "Marcellus Region Productivity Report." *U.S. Energy Information Administration (EIA)*. N.p., Dec. 2016. Web. 09 Jan. 2017.
9. ODNR Division of Oil and Gas Resources Management. "Ohio.gov / Search." *Shale Well Drilling and Permitting in Ohio*. N.p., 5 Dec. 2016. Web. 09 Jan. 2017.
10. "The Facts About Hydraulic Fracturing." *Ohio Department of Natural Resources*. N.p., 2009. Web. 9 Jan. 2017.
11. Rassenfoss, Stephen. "In Search of the Waterless Fracture." *In Search of the Waterless Fracture - OnePetro*. Society of Petroleum Engineers, June 2013. Web. 18 Feb. 2017.
12. "Utica Region Productivity Report." *U.S. Energy Information Administration (EIA)*. N.p., Dec. 2016. Web. 09 Jan. 2017.
13. Watts, Robin. "Oil and Gas Services." (n.d.): n. pag. *University of Wyoming*. 17 Apr. 2013. Web. 9 Jan. 2017.

Feasibility of Creating a Home Drone System Controlled by a Raspberry Pi

Student Researcher: Daniel Dennis Musci

Advisor: Dr. Jed E. Marquart

Ohio Northern University

Department of Electrical and Computer Engineering and Computer Science

Abstract

Drones are becoming increasingly influential in today's society, as they are often used in a wide range of areas including defense, research, and surveillance. With their increasing popularity, it would be beneficial to have a simple platform to implement drone control and testing, especially from a research perspective. This paper lays out the groundwork for this system by assessing the feasibility of creating a home drone control system controlled by a Raspberry Pi. Raspberry Pis are small, versatile, and inexpensive devices that function as low-powered computers. They provide a lot of functionality onboard, such as Bluetooth and 802.11n Wi-Fi capabilities, and work perfectly with a lot of well-developed software libraries. Because of their versatility and low cost, they are perfect for prototyping platforms, and thus are valid candidates for implementing a simple drone control system.

This paper assesses the feasibility of seven major categories in creating a home drone control system with a Raspberry Pi: Bandwidth consumption, Throughput/Data Rates, Security, Reliability, Power Consumption, Processing Power, and Ethics.

Keywords: Drones, Raspberry Pi, Ad Hoc Networks, Wireless Communications

Introduction

Autonomous unmanned aerial vehicles (UAVS), otherwise known as drones, are becoming increasingly popular in many different applications. They are often used in applications such as research, environmental monitoring, emergency assistance, border surveillance, and defense. Due to their increasing popularity and widespread usage, it would be beneficial to have a simple platform to test new drones and drone software, and this paper lays the groundwork for this platform.

In order to implement an inexpensive, simple, and versatile drone control system, a Raspberry Pi poses as a valid candidate for the platform hardware. Raspberry Pis are small, versatile computers that work well for rapid prototyping scenarios, and are thus perfect for this application.

The following seven major categories are assessed for their feasibility in creating a home drone system controlled by a Raspberry Pi: Bandwidth consumption, Throughput/Data Rates, Security, Reliability, Power Consumption, Processing Power, and Ethics. Once these are assessed the conclusion that this system is indeed feasible is drawn from presented results.

Bandwidth Consumption

The protocols in Table 1 were all considered for implementing the aforementioned drone control system with respect to bandwidth limitations and advantages.

Table 1. Considered Wireless Protocols and Available Bandwidths

Protocol	Maximum Available Bandwidth
<i>IEEE 802.11n</i>	<i>2.4 - 2.4835 or 5.15 - 5.35 GHz</i>
IEEE 802.11a/c	80 MHz
ZigBee	868 MHz in Europe, 915 MHz in US, 2.4 GHz worldwide
XBee	2.4 GHz
LTT	1.25 - 20 MHz
IEEE 802.16	10 - 66 GHz
IEEE 802.16d	2 - 11 GHz
IEEE 802.16e	2 - 6 GHz

The protocols in Table 1 all provide different advantages for different applications, and for the purpose of creating a drone control system for home use, IEEE 802.11n, a Wi-Fi protocol, was chosen as the best available protocol. This protocol operates within the 2.4 GHz industrial, scientific, and medical radio (ISM) band, which is desired for home use. This operating band is unlicensed and therefore free to use for legitimate reasons. It is not unregulated, however, but it is unlicensed and therefore makes this choice feasible for the purpose of a drone control system.

This protocol also provides bandwidth between the frequencies of 2.4 and 2.4835 GHz within the ISM band, which corresponds to $.0835 \text{ GHz} = 83.5 \text{ MHz}$ of available bandwidth. This is plenty of bandwidth for a standard controller, and is also shown to be sufficient for the proposed secure system described within the Security section. For these reasons the available bandwidth of the IEEE 802.11n wireless protocol was deemed feasible for implementing the drone control system [3].

Throughput/Data Rates

The protocols in Table 2 were all considered for implementing the drone control system studied with respect to maximum data rates.

Table 2: Considered Wireless Protocols and Maximum Data Rates

Protocol	Maximum Data Rates
<i>IEEE 802.11n</i>	<i>150 Mbps</i>
IEEE 802.11a/c	6.77 Mbps
ZigBee	20 kbps in Europe, 40 kbps in US, 250 kbps worldwide
XBee	250 kbps
LTT	326 Mbps
IEEE 802.16	32-134 Mbps
IEEE 802.16d	up to 75 Mbps
IEEE 802.16e	up to 15 Mbps

Since the IEEE 802.11n wireless protocol was determined to be the most feasible protocol for the project, the maximum data rates available were studied. Table 2 shows that this protocol supports maximum data rates of up to 150 Mbps. A simple calculation was performed in order to show an approximation of typical data rates required for a simple drone control system. Assume you are running a stability algorithm to keep the drone in one position and orientation despite disturbances. Assume you are sending 1000 commands per second (one per millisecond) to the drone, and each command contains a signal for each of the four motors present in a typical AR drone or quadcopter. Assuming 16 bit precision, then there would be $16 \text{ [bits/signal]} * 4 \text{ [signals/command]} * 1000 \text{ [commands/second]} = 64 \text{ kbps}$ which is well under 150 Mbps. Thus the maximum data rates available within the chosen protocol were deemed feasible for the drone control system [2-3].

Security

Drones are frequently flown in noisy environments, and are therefore exposed to intentional/unintentional interferences. In the case of a home system, there could likely be unintentional interferences, but there wouldn't likely be a huge threat of intentional interference. In either case, there is real danger of drone response to faulty signals. This could cause loss of control of the drone which could lead to crash and damage of nearby property. Also, security is of specific concern for a home drone network, because the network would have to operate in a small region surrounded by private property. This property should not be damaged, nor should it be recorded in the case of camera-enabled drones. For the above reasons, it would be beneficial for the raspberry pi controller to adopt Frequency Hopping Spread Spectrum (FHSS) in its communication links.

FHSS systems rapidly change channels using a pseudorandom sequence that is shared with the receiver. This rapidly changing carrier frequency makes the system highly resistant to narrowband interference. These systems are relatively robust, and would yield sufficient security unless deliberately attacked. Since deliberate attack is relatively unlikely in most home environments, an FHSS system on a Raspberry Pi should prove secure enough for a home drone controller. Table 3 shows a summary of the pros and cons of an FHSS drone control system using a Raspberry Pi.

Table 3: Pros and Cons of a Drone Control System using FHSS

Pros	Cons
Increased resistance to faulty signals such as general interference.	Requires much larger bandwidth. ¹
Allows system to safely operate in 2.4 GHz band. ³	More BW therefore less power efficient.
Protects against jammers/spoofers/hackers.	More complex system to initialize.
	Requires a complex receiver that can perform FHSS receiving. ²

1. BW required for an FHSS system should still be possible in 2.4 GHz operating band. A 47 channel FHSS system required 70 MHz and there is ~83.5 MHz available in that band [4].
2. The receiver would need to either have access to the frequency table indicating the pseudorandom sequence of carrier hopping, or it would need to listen in on all possible channels. Both of these are more complex and expensive solutions.
3. This is the ISM band that is globally unlicensed, but not unregulated.

Due to these reasons, implementing an FHSS drone control system with a Raspberry Pi is feasible in the sense of security [4].

Reliability and Power Consumption

Implementing an FHSS system as discussed in the Security section should greatly increase the drone's resistance to interference and would therefore increase its reliability. In order to gather further results the described system would actually need to be implemented and then tested.

Raspberry Pis are powered from a wall connection through a micro-usb port on the board. For this reason the power consumed by the device should not be of significant concern for a home control system, since the power delivered to the home is more or less constant. In order to gather further results the described system would need to be implemented and then tested using a wattmeter. For these reasons, although it is difficult to conclude, the system should be feasible in the sense of reliability and power consumption, but would require further testing.

Raspberry Pi Specs and Processing Power

The following is a list of notable specifications for the Raspberry Pi 3.0 model B, which was the device considered for this project: 1.2 GHz 64-bit quad-core ARMv8 CPU, 802.11n Wireless LAN, 1 GB RAM, Micro SD card slot, VideoCore IV 3D graphics core. Figure 1 shows an image of the Raspberry Pi 3.0 Model B as well.

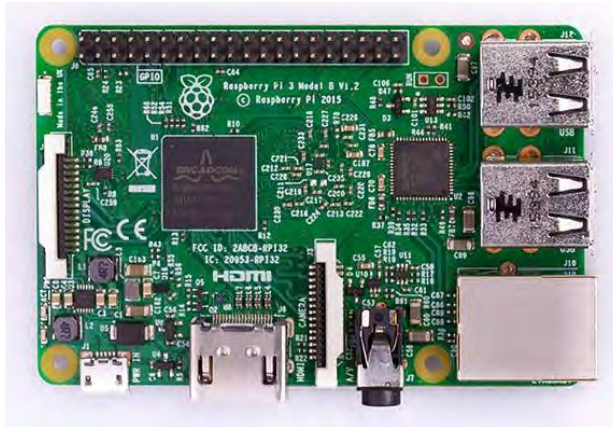


Figure 1. Raspberry Pi 3.0 Model B

The 1.2 GHz quad-core CPU on the device was determined to be fast enough to handle a simple command only control system. The available RAM should cause a limitation, but this would likely not be noticed unless active image processing was incorporated into the control system. For these reasons the Raspberry Pi was deemed a feasible hardware for implementing the drone control system studied [1].

Ethics

Ethics is always a concern within any project, and building a home drone controller is of no exception to this. This system introduces some ethical dilemmas due to the fact that it is to be implemented in a home environment. Home environments are limited to small ranges of motion, are surrounded by private property, and introduce privacy concerns. Table 4 summarizes the main ethical concerns with building a home drone control system that this research addressed.

Table 4. Ethical Considerations of Home Drone Control System using a Raspberry Pi

Concern	Solution
Crash and property damage due to loss of control.	Implementing an FHSS system would decrease the likeliness of losing control due to interference, hacking, or jamming.
Visual data causes privacy issues.	Visual data should not be incorporated for a home control system due to the very high probability of recording something private.
Limited range of motion due to private property.	Implementing an FHSS system would decrease the chances the drone would move off course and thus leave its valid range of motion.
Sudden loss of power to Raspberry Pi could cause the drone to crash.	Implementing a fail-safe algorithm on-board the drone will allow it to land safely if communication goes down.

Due to the above reasons, it would be ethically feasible to implement a Raspberry Pi controlled drone control system if proper precautions were taken (increased reliability and security, no visual data, fail-safe algorithms).

Conclusions and Future Considerations

Based on all of the presented research, using a Raspberry Pi to implement a home drone control system is feasible. Five of the seven major categories were shown to be feasible, and two of them were hypothesized as such, but require further testing. This conclusion implies it would be feasible to pursue this approach in creating a simple, inexpensive, and versatile drone control platform from Raspberry Pis. The next step would be to actually implement this system and test some of its features. The range of reliable ad-hoc networks that the Raspberry Pi can sustain, and the steady-state error to reference inputs (if any) could both be tested. Also, while it was not determined feasible in this project, it could be interesting to test the ability of the Raspberry Pi to handle active image processing in the control system.

Acknowledgment

This work was funded by the Ohio Space Grant Consortium.

References

1. Santana, L. V., Brandao, A. S., & Sarcinelli-Filho, M. (2016). Navigation and Cooperative Control Using the A.R.Drone Quadrotor. *J Intell Robot System*. doi:10.1007/s10846-016-0355-y.
2. Yanmaz, E., Quaritsch, M., Yahyanejad, S., Rinner, B., Hellwagner, H., & Bettstetter, C. (2017). Communication and Coordination for Drone Networks. *ADHOCNETS 2016*, 184, 79-91. doi:10.1007/978-3-319-51204-4_7.
3. Rahman, A. (n.d.). Enabling Drone Communications with WiMAX Technology.
4. Shin, H., Choi, K., Park, Y., Choi, J., & Kim, Y. (2016). Security Analysis of FHSS-type Drone Controller. *WISA 2015*, 9503, 240-253. doi:10.1007/978-3-319-31875-2_20.

Predictions of Human Arm Bone Strength from Measurements of Stiffness of Radii

Student Researcher: McKenzie L. Nelson

Advisor: Dr. Anne B. Loucks

Ohio University

Department of Biological Sciences

Abstract

Osteoporosis, a disease characterized by a decrease in bone strength and, therefore, an increased risk of fracture, affects over ten million people in the US, and this number is predicted to rise by 50% by 2025 [1, 2]. Currently, osteoporosis is diagnosed by measuring bone mineral density (BMD) by dual-energy X-ray absorptiometry (DXA), but research has shown that BMD does not predict fractures well [3]. About half of cortical osteoporotic fractures occur in the forearm, and forearm fractures are indicative of future fractures at the spine and hip [4, 5]. Dr. Anne Loucks with others at Ohio University have been developing a technology known as mechanical response tissue analysis (MRTA). MRTA measures the bending stiffness (EI) of the ulna, and previous studies in the lab have shown that ulna EI predicts ulna bending strength very accurately [6, 7].

This project used 23 cadaveric radius specimens, for which the associated ulna was previously tested by MRTA *in vivo* and by quasi-static mechanical testing (QMT) *ex vivo*. The purpose of the project was to test the accuracy with which radius bending strength is predicted by various mechanical tests of the radius and ulna and by DXA measurements of the radius. Linear regression analyses revealed that both radius EI and radius BMC at the clinical 1/3 site were the most accurate predictors of radius bending strength, though not significantly different from each other, and that the most accurate predictor of radius EI was radius BMC at the 1/3 site.

Project Objectives

The purpose of this study was to test the following null hypotheses regarding the accuracies with which radius bending strength and radius EI are predicted:

H₀₁: The Standard Error of the Estimate (SEE) in the regression of radius bending strength on radius bending stiffness (EI) is not less than SEE in the regression of radius bending strength on any other predictors.

H₀₂: The Standard Errors of the Estimate (SEEs) in regressions of radius EI on other predictors of radius bending strength are not different from each other.

Methodology

Cadaveric Human Arm Specimen Acquisition

The 23 fresh-frozen cadaveric human arms used in this study were obtained from the human tissue banks Science Care, Inc. (Phoenix, AZ) and AdvancedMed (Las Vegas, NV). In order to obtain a large range in bone stiffness and strength, donors with a wide range in age (17-99 years) and BMI (14-40 kg/m²) were selected.

Previous Research

Previous studies in Dr. Loucks' lab measured ulna EI non-invasively by MRTA, ulna EI and strength by QMT, radius BMC and BMD at the ultradistal (UD) region and 1/3 site, and UD radius compressive strength by QMT [6-8]. Between these steps in the process, specimens were stored at -20°C.

Radius Specimen Preparation

3-D models of each specimen were created using Avizo® image processing software (Visualization Sciences Group, SAS, Merignac, France) to determine that the clinical 1/3 site of the forearm is located, on average, at 40% of the length of the radius. To standardize end conditions, radius specimens were drilled while still frozen in a medio-lateral manner at 16% and 64% (i.e., $40\% \pm 24\%$) of the radius length. The specimens were then thawed in a saline solution until QMT bending tests the following day.

QMT Bending Tests

During testing, each radius specimen was pinned vertically with a steel pin through the holes drilled in the specimen and through a freely rotating horizontal steel roller seated on semi-cylindrical mating surfaces machined into steel supports. A guide held the pins vertical, and a metal overlay was placed at the loading site to prevent damage to the bone from the loading probe. Each radius specimen was subjected to three-point bending by QMT using a 10 kN load frame (QTest-Elite, MTS Systems Corporation, Eden Prairie, MN). The load was applied at the central 40% location at a strain rate of 0.00012 s^{-1} . Cyclic pre-conditioning loads up to 100 N were applied to the specimen until the coefficient of variation in repeated measures of radius EI was $< 1\%$. Then the load was increased monotonically until fracture occurred.

Data Analysis and Statistical Analysis

For most specimens, the QMT load vs displacement curves displayed no linear region. Therefore, as per ASTM D790, the measured transverse bending stiffness (k_M) was taken as the tangent to the load vs displacement curve at the inflection point between lower and higher load regions with positive and negative second derivatives, respectively. From k_M the specimen stiffness (k_S) was calculated by taking into account the measured stiffness of the test frame (k_F):

$$k_S = k_F \times k_M / (k_F - k_M) \quad \text{Eqn. 1}$$

in which k_F varied nonlinearly with load. Because the slenderness ratio of the radius specimens was low (9.0-5.4), shear stresses were taken into account in the calculation of radius EI as:

$$EI = (k_S L^3 / 48) \times (1 + 12 c (E_L / G_T) I / (AL^2)) \quad \text{Eqn. 2}$$

where L = the length of the span between end supports, c = a shape correction factor = 2 for a thin-walled tube, E_L / G_T = the ratio of the elastic and shear moduli = 4 for human bone, I = the cross sectional moment of inertia, and A = the cross sectional area of the specimen. It can be shown that the second term on the right hand side of Eqn. 2 reduces to:

$$12 c (E_L / G_T) I / (AL^2) = 6((D_o/L)^2 - (D_i/L)^2) \quad \text{Eqn. 3}$$

where D_o and D_i = the outer and inner diameters of the specimen, respectively. Specimen bending strength was taken as the maximum moment before fracture:

$$M_{\max} = F_{\text{peak}} L / 4 \quad \text{Eqn. 4}$$

where F_{peak} = the peak load before fracture.

Simple linear regression analyses were done to test the accuracy with which radius bending strength was predicted by radius EI, radius BMD and BMC at the 1/3 site and UD region, ulna EI by MRTA, ulna bending strength, and UD radius compressive strength. Simple linear regression analyses were also done to determine how accurately radius EI was predicted by the other predictors. The standard error of the estimate (SEE) was determined for each regression. The SEE values were then compared by F statistics ($F = (SEE_1 / SEE_2)^2$) to determine if they differed significantly from each other.

Results

In the regressions of radius bending strength on predictors, radius EI and radius BMC at the 1/3 site had the lowest SEE values that were not significantly different from each other (Figure 1). However, these SEE values were significantly smaller than those of any other predictor. The first null hypothesis was, therefore, rejected. In the regressions of radius EI on the other predictors, the SEE for radius BMC at the 1/3 site was significantly smaller than that of any other predictor. Therefore, the second null hypothesis was rejected, as well (Figure 2).

Significance

In this study, the clinical diagnostic criterion for osteoporosis, radius BMD at the 1/3 site, was not the most accurate predictor of radius bending strength. Radius EI and radius BMC at the 1/3 site were the most accurate. Ulna EI by MRTA was a more accurate predictor than radius BMD at the 1/3 site and similar to the remaining predictors. This study confirms previous studies that also found bone bending strength to be most accurately predicted by EI [6, 9, 10] and warrants further research into the use of EI as a predictor of fracture. Future research should increase the number of observations to confirm the original findings, and to distinguish a difference between the accuracies with which radius EI and radius BMC at the 1/3 site predict radius bending strength, if a difference exists.

Figures

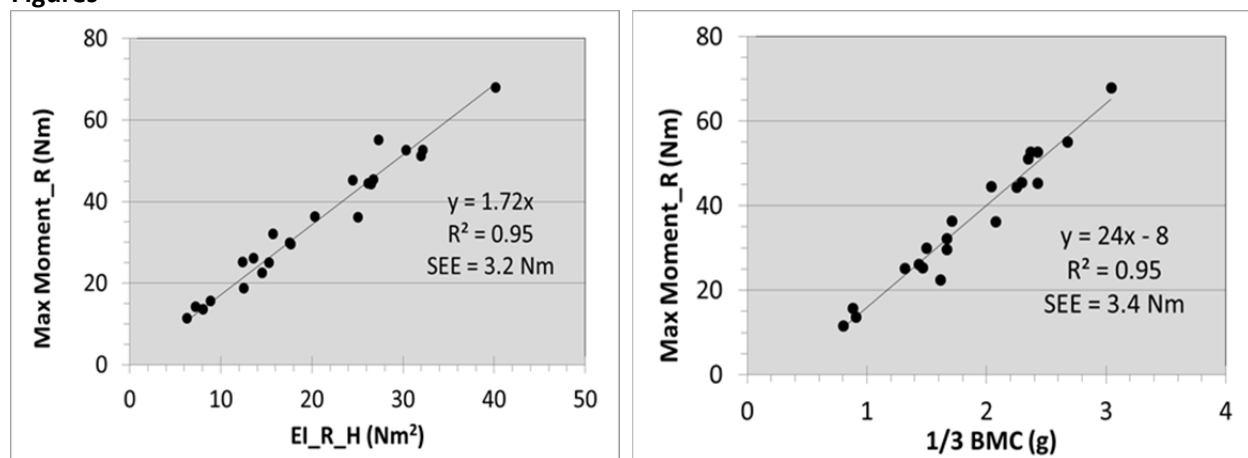


Figure 1. Predictions of Radius Bending Strength by Radius EI (Left) and by Radius BMC at the 1/3 site

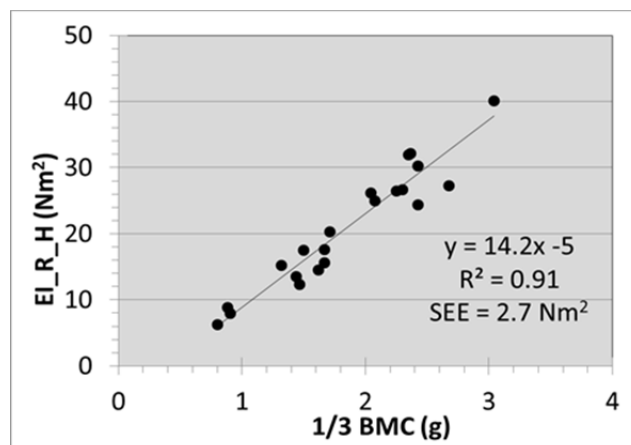


Figure 2. Prediction of Radius EI by Radius BMC at the 1/3 site

Acknowledgments

This project was made possible by funding from the Ohio Space Grant Consortium and Dr. Anne Loucks of the Department of Biological Sciences at the Ohio University. I would like to thank Dr. Betty Sindelar of the Ohio University Physical Therapy School for the use of her QMT system, and the human tissue banks, Science Care and AdvancedMed, for providing specimens for this project. I would also like to acknowledge the work done by previous students in the lab who provided data on certain predictors used in this project: Emily Ellerbrock, Jennifer Neumeyer, Tyler Beck, Gabrielle Hausfeld, and Maureen Dean. I would further like to thank Lyn Bowman in his help in developing the study protocol and educating me on how to analyze data. Finally, I would like to thank Dr. Anne Loucks for allowing me to work in her lab for the past two years, mentoring me, and giving me every opportunity to succeed in my project and education.

References

1. Ensrud, K.E., *Epidemiology of fracture risk with advancing age*. Journals of Gerontology. Series A: Biological Sciences and Medical Sciences, 2013. **68**(10): p. 1236-42.
2. NIH Consensus Development Panel on Osteoporosis Prevention, D., and Therapy, *Osteoporosis prevention, diagnosis, and therapy*. JAMA, 2001. **285**(6): p. 785-795.
3. Siris, E.S., et al., *Identification and fracture outcomes of undiagnosed low bone mineral density in postmenopausal women: results from the National Osteoporosis Risk Assessment*. JAMA, 2001. **286**(22): p. 2815-22.
4. Ohsfeldt, R.L., N.N. Borisov, and R.L. Sheer, *Fragility fracture-related direct medical costs in the first year following a nonvertebral fracture in a managed care setting*. Osteoporosis International, 2006. **17**(2): p. 252-8.
5. Lochmuller, E.M., et al., *Radius bone strength in bending, compression, and falling and its correlation with clinical densitometry at multiple sites*. Journal of Bone and Mineral Research, 2002. **17**(9): p. 1629-38.
6. Hausfeld, G.C., *Comparison of Cortical Porosity, Diameter, and Stiffness as Predictors of Ulna Bending Strength*, in *Biological Sciences*. 2015, Ohio University: Ohio University. p. 139.
7. Ellerbrock, E.R., *Accuracy of Mechanical Response Tissue Analysis Measurements in Cadaveric Human Ulnas*, in *Biological Sciences*. 2014, Ohio University: Ohio University. p. 65.
8. Dean, M.A., *Predictions of Distal Radius Compressive Strength by Measurements of Bone Mineral and Stiffness*, in *Biological Sciences*. 2016, Ohio University: Ohio University. p. 77.
9. Jurist, J.M. and A.S. Foltz, *Human ulnar bending stiffness, mineral content, geometry and strength*. Journal of Biomechanics, 1977. **10**(8): p. 455-9.
10. Borders, S., K.R. Petersen, and D. Orne, *Prediction of bending strength of long bones from measurements of bending stiffness and bone mineral content*. Journal of Biomechanical Engineering, 1977. **99**(1): p. 40-44.

Testing Game Design Choices in a New Genre of Educational Games

Student Researcher: Alexandra C. Oliver

Advisor: Noah L. Schroeder, Ph.D.

Wright State University

Department of Computer Science & Engineering

Abstract

This project focuses on developing a modular educational game framework within Unreal Engine 4. The Student-centered Interactive Modular Performance-based Learning Environment (SIMPLE) is a program that is designed to be modified by instructors and customized to their content domains. In this version of the software, the user must escape the level by using their “hacking” skill to open doors towards the exit by solving a series of math questions. As educational video games can be difficult to develop (Moreno-Ger, Burgos, Martínez-Ortiz, Sierra, & Fernández-Manjón, 2008), the mechanics, features, and appearance of both the gameplay and the virtual environment it lies in can potentially influence the users’ experiences during their use of the software. In this usability study, we compared three different versions of SIMPLE. The results suggest the game elements we tested did not considerably influence users’ experiences with the software.

Objectives

The objective of this study is to evaluate the user’s experience with different game features. We examined the influence of the user’s level of interactivity, as well as the addition of challenging gameplay elements, on the user’s experience. By altering these specific factors between versions of the game, we can discover which elements influence the user’s perception of the overall game.

Methodology Used

Participants were randomly assigned to one of three groups. Each group had different versions of the game (described below). During gameplay, the participant’s voice and gameplay were recorded, and upon completion of the game, the participant completed demographic questions, Likert scale surveys (Paas, 1992; Wiebe, Lamb, Hardy, & Sharek, 2014), and an eight question open-ended survey.

Group A held the basic features of the game which include a total of seven questions and one hint. Both the paths to each question and the order in which they can be encountered could vary per the in-game choices of each participant. The level that Group B played included all features of the standard level of Group A, but also included direct interaction and conversation with a non-player character through a constructed A.I. system. The level for Group C included all features of Group A and Group B while also expanding upon the inclusion of an A.I. system. This A.I. system differs in the behavior and purpose from the one found in Group B, as it added a challenge to the game in the form of a security system.

Results Obtained

Non-parametric tests indicate no significant differences between groups on measures of Mental Effort ($H(2)=0.96$, $p = 0.62$), Focused Attention ($H(2)=0.52$, $p = 0.77$), Perceived Usability ($H(2) = 1.18$, $p = 0.56$), Aesthetics ($H(2) = 0.07$, $p = 0.96$), or Satisfaction ($H(2) = 0.66$, $p = 0.72$). Table 1 shows the descriptive statistics.

Themes were found within the qualitative data collected through open-ended survey questions, and in many cases the responses were consistent among the three different groups. Elements that caused the game to be more immersive focused on the graphics, tone, and atmosphere of the game. A participant stated that “The game had a very good way of delivering a rather lonely atmosphere with a very quiet environment that was able to stay rather grim without reducing the color pallet. It is reminiscent of the same feeling one would get when playing [commercial game noted] or [commercial game noted]” which is a comparison to professionally published game titles. The main elements that caused the game to be challenging were the map and content layout within the level. Multiple participants suggested the addition of a mini-map because “While different types of rooms on the map are very distinct, hallways are in general fairly similar looking.” The best feature of the game was consistently seen as the game’s environment in all groups. When asked if they would use this game as an optional assignment, all groups responded yes and stated that it would be an entertaining method of studying or learning. One participant responded by saying “People play games online already on sites like [game website noted], and this game is a lot higher quality than those games, so I’m sure there would be lots of people like me who would love to have this game as an alternative.”

Inconsistencies between the three groups appeared within expectations in regards to the subject of engagement and immersion. The causes of engagement from Group A, B, and C within the game were labeled as the math application, the environment, and the level of challenge, respectively. The causes for feeling less engaged also differed among the three groups. Group A cited the length of the game as a concern. Group B referenced the difficulty of navigation as an issue, and Group C cited the difficulty of the questions. The elements that made the game less immersive to the participants were the simplicity of the mechanics, the limited interactions, and the glitches found within the game. One participant suggested more interactivity with other elements within the game because “it was also somewhat disappointing that the only thing you ever get to frequently interact with is the doors. There are all kinds of control panels and containers sitting around the level, but you never get to do anything with them.”

Overall, our results suggest that the game elements we tested did not profoundly influence the users’ experiences with the game.

Figures and Charts

Table 1. Results from Mental Effort (ME), Focused Attention (FA), Perceived Usability (PU), Aesthetics (AE), and Satisfaction (SA) scales. Note that lower scores on the PU scale are more favorable.

Group	ME		FA		PU		AE		SA	
	M	SD	M	SD	M	SD	M	SD	M	SD
A	6.00	1.41	28.50	7.78	15.00	2.83	22.50	2.12	30.50	2.12
B	6.50	2.12	29.00	1.41	18.00	0.00	22.50	0.71	28.00	1.41
C	5.00	1.41	32.00	5.66	16.00	8.49	23.00	2.83	30.00	7.07
	max - 9		max - 40		max - 40		max - 25		max - 35	

References

1. Moreno-Ger, P., Burgos, D., Martínez-Ortiz, I., Sierra, J. L., Fernández-Manjón, B, (2008) "Educational game design for online education," In *Comp. in Hum. Beh.*, Vol. 24, pp. 2530-2540.
2. Paas, F. G, (1992), "Training strategies for attaining transfer of problem-solving skill in statistics: A cognitive-load approach," In *J. of Ed. Psy.*, Vol. 84, No. 4, pp. 429-434.
3. Wiebe, E. N., Lamb, A., Hardy, M., Sharek, D, (2014) "Measuring engagement in video game-based environments: Investigation of the User Engagement Scale," In *Comp. in Hum. Beh.*, Vol. 32, pp. 123-132.

Plasma Controlled Cavity in a Transient Unstart Environment

Student Researcher: Dennis Omari

Advisor: Dr. Mo Samimy

The Ohio State University
Mechanical and Aerospace Department

Abstract

Scramjets can provide efficient propulsion for aircraft flying at speeds greater than Mach 5, however, they are susceptible to inlet unstart. Thermal choke in the combustor is a typical cause of unstart leading to loss of thrust and stalled engine operation. Isolators are generally employed to prevent unstart. The performance/stability of operation could be improved by increasing the isolator's unstart-prevention capabilities. It is hypothesized that a resonating cavity could supplement an isolator's capabilities by trapping the upstream traveling unstart shock train to prevent inlet unstart. As demonstrated previously, such a cavity's shock-trapping ability has been evaluated in a quasi-steady increasing back pressure environment (Webb and Samimy, 2015). The current study assesses the shock trapping ability in a more realistic, transient unstart environment. Based on results from the numerical simulations using techniques like tailored RANS calculations, a few selected cases that will be tested experimentally and compared to the simulation results. Scramjet flow path simulations like cavities as well as SBLIs will be conducted using RANS simulations. For the transient back pressure testing, a new mechanism was designed and built, to allow for rapid ramp motion, so that the shock trapping capabilities of the cavity can be experimentally investigated in a transient flow environment. Using the redesigned mechanism, the cavity's capabilities to prevent rapid inlet unstart will be demonstrated.

Project Objectives

This project will assess the effect of several parameters like the cavity geometry, resonance conditions, excitation conditions, and back pressure application rate on the ability of the cavity to support back pressure. The cavity's ability to support back pressure will be tested in a realistic, i.e. transient, environment to quantify the engine performance improvement it could theoretically provide.

Methodology

The supersonic wind tunnel used in this research is a blowdown facility at the Gas Dynamics and Turbulence Laboratory of the Aerospace Research Center at The Ohio State University. This research will use four cavity geometries; the rectangular, $\frac{1}{4}$ round, $\frac{1}{2}$ round, and 45° slanted cavity. The cavity will span the entire width of the test section. The cavity length will be varied between 1.5", 2" and 2.5" in the test section using various rectangular spacers of different lengths. Shorter cavity length meant more spacers stacked up together and longer cavity length meant fewer spacers were used. The experiments will seek to determine the optimal cavity geometry for shock trapping. The freestream Mach number is 2.24 and was confirmed using static/stagnation pressure measurements. Kulite pressure transducers collected data on the cavity floor, which was then low-pass filtered at a frequency rate of 25 kHz, and amplified using an in-built signal conditioner. All data collected was sampled at a frequency of 75 kHz. A Baldor Servo Motor BSM80N-375AF will be used to move the ramp in a transient fashion. The ramp will be moved at different speeds and to/from different angles to verify that the ramp is moving correctly and to ascertain how fast the shock moves. Schlieren photography will provide images that will define when unstart occurs and when the shock moves. This will be further validated by pressure measurements collected at the Kulite locations during the ramp motion. For all collected cases, one

block of more than 5000 points will be collected at 75 kHz for about 3 seconds to allow the shock location to be tracked.

Anticipated Results

The ramp will be moved at different speeds and to/from different angle locations to verify that the ramp is moving correctly and to ascertain how fast the shock moves. From previous work, unstart occurred with the ramp around 23° to 26° so there is a possibility a similar trend could be followed even in a transient environment. Furthermore, unstart typically occurs on the order of 10 -20 ms as demonstrated in literature, so time scales for the experiments will be set around that range to study a realistic unstart in a transient environment. Schlieren photography will provide images that will define when unstart occurs and when the shock moves. The change in pressure from two Kulite location will give an indication as to the shock moving and unstart happening. The Schlieren will act as an added proof of validation. In the long run, the Schlieren will become unnecessary because unstart will be detected using the pressure measurements and the Schlieren will only be used to validate the pressure measurements. The pressure measurements will however, be used to evaluate the shock-trapping abilities of various cavity geometries at various ramp speeds. The pressure measurements will provide metrics that verify how different cavity geometries affect the flow at different ramp speed and at what back pressure unstart occurs for each geometry. This will ultimately lead to an assessment of the shock-trapping abilities of the cavity geometry based on the location of the shock train and the change in pressure measurements for each cavity geometry.

Conclusions and Future Work

Ramp motion testing will help confirm that the ramp is indeed working properly and that the speed of the shock has being ascertained. Schlieren and pressure measurements will work in conjunction to show when unstart occurs. The future of this project is to perform more testing on a particular cavity geometry based on the results obtained from the computational portion of this project. The optimal cavity geometry will be determined based on the cavity that produces the lowest drag and has the highest supportable back pressure.

Acknowledgments

- Dr. Mo. Samimy and Dr. Nathan Webb
- Ohio Space Grant Consortium

References

1. Samimy, M., Kearney-Fischer, M., Kim, J.-H., and Sinha, A., "High-speed and High-Reynolds Number Jet Control Using Localized Arc Filament Plasma Actuators," *Journal of Propulsion and Power*, Vol. 28, No. 2, 2012, pp. 269–280. doi:10.2514/1.B34272.
2. Webb, N., Samimy, M. "Supersonic Cavity Control Using Plasma Actuators." 53rd AIAA Aerospace Science Meeting, 2015-19621, (2015). doi: 10.2514/6.2015-1961.

Effects of Anti-Gravity on Bone Formation in Coculture

Student Researcher: Olivia L. Petrey

Research Advisor: Dr. Marnie Saunders

The University of Akron
Biomedical Engineering Department

Abstract

It is well known that when bone is subjected to micro-gravitational conditions its density decreases significantly. The mechanism by which this bone loss occurs, however, remains unclear. Bone remodeling consists of two processes: bone formation and bone resorption. Bone formation is performed by osteoblasts, while bone resorption is performed by osteoclasts. Therefore, the goal of this research project is to characterize a cocultured system of osteoblasts and osteoclasts and use it to quantify the effects of soluble signals versus cell-to-cell contact in bone remodeling that has been induced via osteocyte unloading.

Introduction

It has been suggested that mechanical loading and unloading experienced by osteocytes is communicated to osteoclasts and osteoblasts via soluble signals to orchestrate bone remodeling. Under normal gravitational conditions, the osteocytes send signals to trigger osteoclastic bone resorption when unloaded and send signals to trigger osteoblastic bone formation when loaded. In space, bone density decreases since the bones are not being loaded by weight. However, does this still occur via the same soluble signals or by different ones? To promote a better understanding of this process, the media of osteocytes placed in a microgravitational environment will be introduced to a cocultured system of osteoblasts and osteoclasts. The soluble signals believed to be sent by osteocytes when they experience the unloaded environment of a bioreactor for an extended period should be communicated to the osteoblasts and osteoclasts through the osteocyte media. Therefore, how the cells respond in comparison to normal gravitational conditions will give better insight to the intricate steps of the bone remodeling process in space.

Methodology

Bone Formation Characterization

Mouse pre-osteoblastic (MC3T3-E1) cells were seeded onto polystyrene wells on a 26-well plate at a density of 2,500 cells/cm². The cells were then grown to 100% confluence, which takes approximately 5-6 days. While the pre-osteoblastic cells were reaching confluence, mouse pre-osteoclastic cells (RAW 264.7) were seeded onto a 100mm polystyrene plate and grown to 100% confluence, which takes approximately 2 days. The media within the RAW 264.7 plate was switched from D-MEM (osteoclastic media) to α -MEM (osteoblastic media) 24 hours before confluency was reached. After MC3T3-E1 cells and RAW 264.7 cells both reached confluence, the RAW 264.7 cells were seeded onto the same polystyrene wells at a density of 250 cells/cm², creating a ratio of 100:1 between the pre-osteoblastic and pre-osteoclastic cells respectively. 24 hours after the cells were placed in coculture, RAW 264.7 cells were induced to resorb using receptor activator of nuclear factor kappa-B ligand (RANKL), and the MC3T3-E1 cells were induced to mineralize with β -glycerophosphate (β -GP) and L-ascorbic acid (L-AA). Cells in coculture were fed osteoblastic culture medium containing RANKL, β -glycerophosphate, and L-ascorbic acid every 3 days for 9 days total. Then they were fed culture medium containing β -GP and L-AA every 3 days for the remaining 17 days. Control wells containing only osteoblastic cells were fed culture

medium containing only β -GP and L-AA every 3 days for 26 days. For all wells, only half of the medium (0.5mL) was replaced for each feeding. After 26 days, mineralization of osteoblastic cultures with conditioned media was observed qualitatively via Alizarin Red staining, which shows calcium, and von Kossa staining, which shows phosphate, and quantified by Alizarin Red quantification and calculation of area covered by stain.

Anti-Gravitational Bone Formation

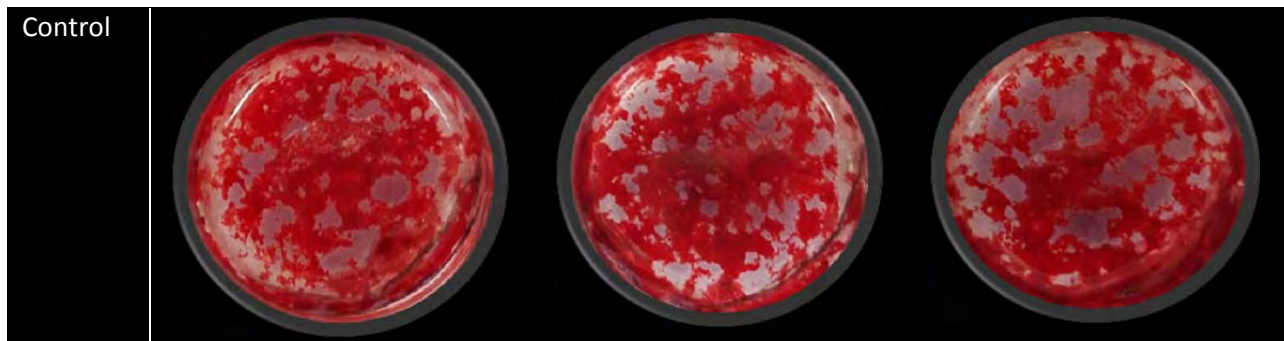
Once this characterization process was completed successfully, the process was repeated but with a microgravitational element. Osteocytes were placed in a bioreactor for 24 hours in an unloaded environment. Their media was then collected and stored in a -180°F freezer for experimental use. For this experiment, MC3T3-E1 cells were seeded at the same density. Upon confluence of both the MC3T3-E1 and RAW 264.7 cells, the RAW 264.7 cells were seeded onto the same 26-well plate as the MC3T3-E1 cells at the same 100:1 ratio as used above. 24 hours after the cells were placed in coculture, RAW 264.7 cells were induced to resorb using RANKL, and the MC3T3-E1 cells were induced to mineralize with β -GP and L-AA.

Cells in coculture were fed osteoblastic culture medium containing RANKL, β -glycerophosphate, and L-ascorbic acid every 3 days for 9 days total. Then they were fed culture medium containing β -GP and L-AA every 3 days for the remaining 17 days. Control wells containing only osteoblastic cells were fed culture medium containing only β -GP and L-AA every 3 days for 26 days. For all wells, half of the medium was replaced for each feeding (0.5mL). To simulate a microgravitational environment, 10% of the medium for the experimental wells and half of the control wells were replaced with osteocyte medium from the bioreactor. After 26 days, mineralization of osteoblastic cultures with conditioned media was to be observed qualitatively via Alizarin Red and von Kossa staining and quantified by Alizarin Red quantification and calculation of the area covered by the stain.

Results

Bone Formation Characterization Experiment

After 26 days, Alizarin Red and von Kossa stains were each applied to half the wells. Images were taken using a light microscope for mineralization quantification. Total areas of bone formation were to be quantified using imageJ. Calcification levels were measured using spectroscopy. A graph was to be compiled using Microsoft Excel. However, due to technical error, the data was lost and could not be recovered. Images of the stains were also taken using a camera, but were not of high enough quality for quantization. These images are depicted below.



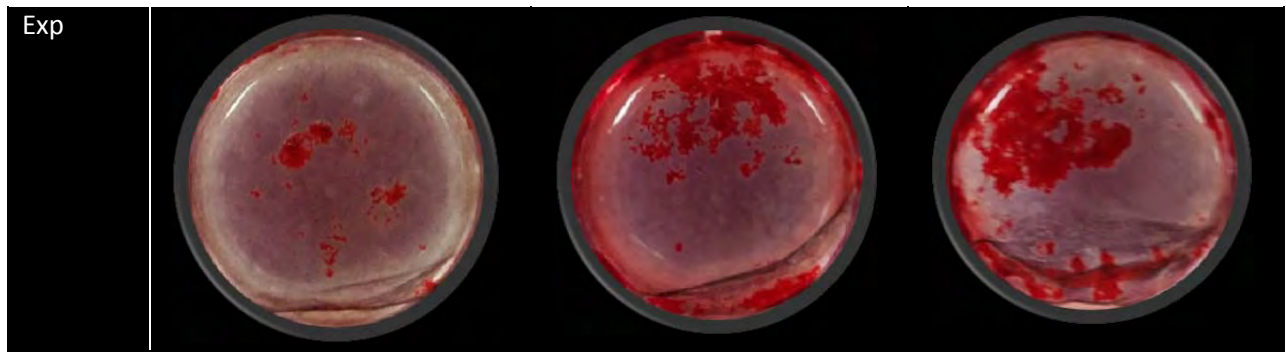


Figure 1. Alizarin Red staining of control and experimental wells for calcium quantification. Top row: MC3T3-E1 cells. Bottom Row: MC3T3-E1 cells in coculture with RAW 264.7 cells.

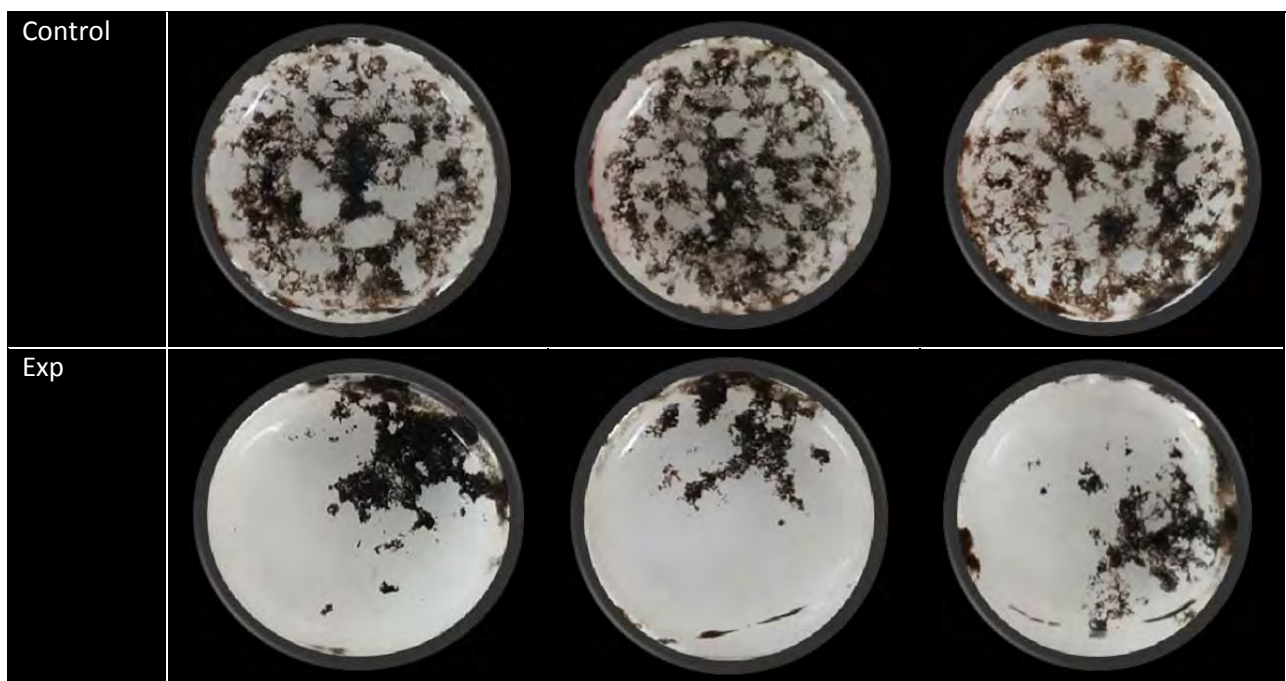


Figure 2. von Kossa staining of control and experimental wells for phosphate quantification. Top row: MC3T3-E1 cells. Bottom row: MC3T3-E1 cells in coculture with RAW 264.7 cells.

Anti-Gravitational Bone Formation Experiment

After 26 days, Alizarin Red and von Kossa stains were each applied to half the wells. However, the cell layers in many of the wells had lifted off prior to day 26. The rest lifted off from the washes during the staining protocols. Images were taken of the cells every 3 days over the 26-day period. One of the images was saved to a personal computer, while the rest were lost due to technological error. This image is depicted below. It was taken on day 15 out of 26 and clearly depicts both the osteoblasts and osteoclasts.

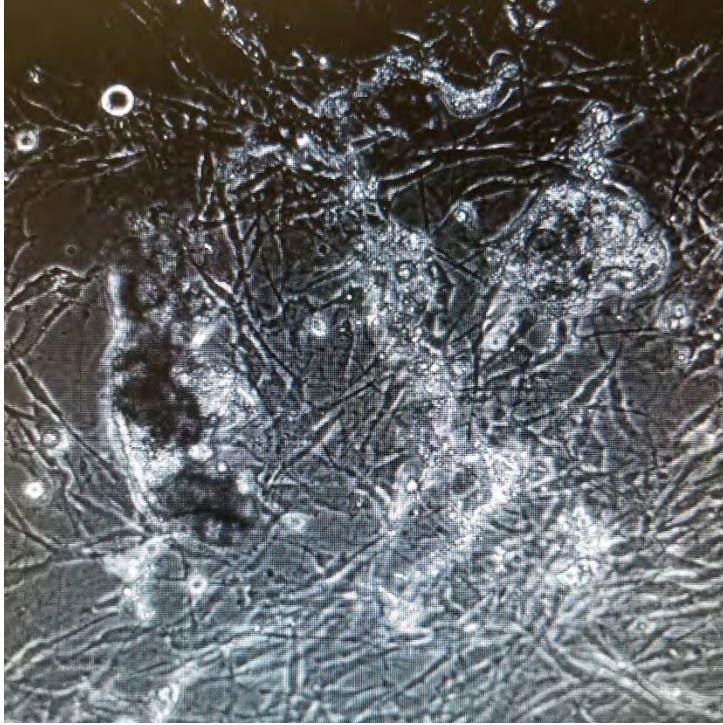


Figure 3. Osteoblasts in coculture with osteoclasts on day 12 out of 26.

Conclusion

Bone Formation Characterization Experiment

There is a noticeable difference in the mineralization levels of the control and experimental groups. If the differences in data would have been found to be significant, it could have been concluded that the presence of osteoclasts dampen the osteoblastic bone formation process.

Anti-gravitational Bone Formation Experiment

Since the cell layers lifted off from the polyurethane surface, the cell density ratio needs to be altered. If cell ratio alterations are unsuccessful, it may be that the well material needs to be changed in order to promote better cellular adhesion. Another issue that arose from this experiment was that the RAW 264.7 cells are not maturing as they should be. Osteoclastic resorption is an 11 day process that is induced by RANK'L. This ligand triggers the maturation of pre-osteoclastic cells. Pre-osteoclastic cells fuse together to form mature, multinucleated osteoclasts. Therefore, RAW 264.7 cells can be determined capable of resorption when they fuse to form large cells with multiple nuclei. Since the RAW 264.7 cells in this experiment never became multinucleated, it can be determined that they were incapable of resorption. Therefore, the osteoblast to osteoclast density ratio may not need to change. Instead, the entire protocol regarding the media for this experiment may need to be altered.

References

1. Greiner, S., A. Kadow-Romacker, G. Schmidmaier, and B. Wildemann. "Cocultures of Osteoblasts and Osteoclasts Are Influenced by Local Application of Zoledronic Acid Incorporated in a Poly(D,L-lactide) Implant Coating." *Journal of Biomedical Materials Research Part A J. Biomed. Mater. Res.* 91A.1 (2009): 288-95. Web. May 2015.
2. Kim, Chi Hyun, Lidan You, Clare E. Yellowley, and Christopher R. Jacobs. "Oscillatory Fluid Flow-induced Shear Stress Decreases Osteoclastogenesis through RANKL and OPG Signaling." *Bone* 39.5 (2006): 1043-047. Web. May 2015.
3. Kitazawa, Sohei, and Riko Kitazawa. "Epigenetic Control of Mouse Receptor Activator of NF- κ B Ligand Gene Expression." *Biochemical and Biophysical Research Communications* 293.1 (2002): 126-31. Web. May 2015.
4. Jones, Gemma L., Antonella Motta, Mike J. Marshall, Alicia J. El Haj, and Sarah H. Cartmell. "Osteoblast: Osteoclast Co-cultures on Silk Fibroin, Chitosan and PLLA Films." *Biomaterials* 30.29 (2009): 5376-384. Web. May 2015.

Lake Erie Water Quality Investigation

Student Researcher: Abigail E. Recker

Advisors: Dr. Bridget Mulvey and Dr. Joseph Ortiz

Kent State University

¹ School of Teaching, Learning, and Curriculum Studies and ² Department of Geology

Abstract

This series of lessons will help grade 3-5 students to understand how natural resources are impacted by human actions through observation, inference, and the use of scientific tools and data. Students will act as Dr. Ortiz's assistants to help find out why the water in Lake Erie is polluted. They will examine real water samples from the lake, using tools to see how they compare to other bodies of fresh water. NASA satellite images will be used to help the students make observations and inferences about water quality. Students will research and evaluate their predictions, using technology and NASA articles. Finally, the students will create an action plan to make a difference and share their findings with Dr. Ortiz. This hands-on approach to science content will support a high level of engagement and intrinsic motivation to learn. Language arts standards are integrated with science standards in this problem-based science unit. Student learning will be assessed through work samples and an observational checklist, updated throughout the unit of inquiry.

Alignment

This series of lessons was designed to align with the following national science standards (Next Generation Science Standards) and integrate language content from the Common Core Standards: 3-LS4-4 - Make a claim about the merit of a solution to a problem caused when the environment changes and the types of plants and animals that live there may change.

CCSS.ELA-LITERACY.W.3.B - Write opinion pieces on topics or texts, supporting a point of view with reasons. Provide reasons that support the opinion.

Objectives

- Students will be able to use tools to explore and measure the properties of water.
- Students will be able to make observations and inferences about the water they explore, in relation to water quality and pollution.
- Students will be able to use the information obtained from observations and informational texts to explain why water becomes polluted, and explain one thing that could be changed to reduce our use of resources.

Educational Theory

This five-day unit of inquiry was constructed using the BSCS 5E Instructional Model, centered around student inquires and student construction of their own understandings of content through tactile experiences and explorations. Montessori's influence is in the hands-on approach involving real, accurate materials, with real, meaningful work as a driving force for young children's learning. Students need to know that their work is contributing to something greater than themselves and will make a difference. This core theory contributes a great deal to the effectiveness of this unit of inquiry.

Abbreviated Lesson Plan

Engage: Students were introduced to Dr. Joseph Ortiz, a local researcher at Kent State University. Students learned of a basic summary of Ortiz's work through a PowerPoint presentation. The teacher shared that Dr. Ortiz needed students' assistance figuring out why the water quality in Lake Erie was changing. Students then were invited to examine water samples from Lake Erie, Cuyahoga River, and the classroom sink. Students engaged with the materials and began to develop questions about water quality, water properties, and what causes differences in water clarity. Students documented their observations and inferences. Finally, students discussed their observations and inferences, summarized on a class T-Chart. All students completed an exit slip with their questions. In a different classroom, the teacher might choose to find a local scientist or researcher to drive the learning in that setting.

Explore: On Day 2, students explored water through two activity centers. At Center 1, students examined the Engage phase water samples again, but now used tools perform simple tests. They were given a secchi disk, thermometer, flashlight, and pre-setup microscope to explore simple properties. At Center 2, students looked at a set of Lake Erie images: a close-up of the water, an aerial photo of an algal bloom, a satellite photo of all the Great Lakes, and a map of the Great Lakes region. The teacher monitored the centers and supported student learning with high order questions and scaffolding. Once complete, they engaged in a whole class discussion about their observations, what those observations might mean, and how they could learn more moving forward.

Explain: On Day 3, students read informational texts about Lake Erie in mixed-ability reading groups. Their findings from the articles were recorded in personal graphic organizers. Once all the groups completed the reading, the class met on the rug for discussion. The ideas from all of the texts were combined on chart paper to form one large graphic organizer. Students noted connections made across articles and how the data from these texts related to their ideas from work the days prior.

Elaborate: On Day 4, students applied and extended their understanding of Lake Erie water quality by constructing an action plan. After brainstorming possibilities as a class, students worked in their table groups to construct and illustrate a way that they could have a positive impact on the water quality in Lake Erie. Finally, we discussed the upsides and challenges of each possibility. The students' work was then posted in the hall, from which all classes could learn.

Evaluate: On the last day, students summarized all of their learning in a final letter to Dr. Ortiz. In these letters, students shared their unit experiences and articulated their present understanding. This real and meaningful framework led to a high intrinsic motivation to share knowledge. Students were highly motivated to share their ideas with Dr. Ortiz. After the letters were written and shared out, Dr. Ortiz responded, and students had the chance to read the letter back from him the next week.

Data Sources

Student learning was documented through work samples taken from various activities throughout the unit. The final summative assessment, the letters to Dr. Ortiz, show a student's overall understanding, as well as their ability to articulate that understanding. An observational checklist also was used by the teacher to document student learning expressed orally during class discussions or displayed through tactile experiences.

Student Results

Students showed a high level of engagement and intrinsic motivation to learn. Through the hands-on experiences, appropriately leveled informational texts, and high order teacher questioning, ~3/4 of the students were able to construct a valid and deep understanding of why algal blooms occur in Lake Erie. They developed an understanding of the relationship between agricultural methods and water quality. Students also showed a basic understanding of how they could make a difference moving forward. Although a few students could have benefitted from more time to develop the deep understanding desired, all students showed at least a foundational understanding by the end of the five-day period.

To access the full lesson plan, student work samples, and supplemental resources please visit:
www.abigailrecker.wordpress.com

Bibliography

1. Bybee, R. W., Taylor, J. A., Gardner, A., Scotter, P. V., Powell, J. C., Westbrook, A., & Landes, N. (2006). *The BSCS 5E Instructional Model: Origins, Effectiveness, and Application*. BSCS. Retrieved January 29, 2017, from <https://www.bscs.org/>.
2. Mooney, C. G. (2000). *Theories of Childhood: An Introduction to Dewey, Montessori, Erikson, Piaget, & Vygotsky*. St. Paul, MN: Merrill/Prentice Hall.

Dynamic Responses of Bending Actuators Based on Magneto-Rheological Elastomers

Student Researcher: Adam L. Reece

Advisor: Dr. Jeong-Hoi Koo

Miami University

Department of Mechanical and Manufacturing Engineering

Abstract

This study investigates the dynamic properties of Magneto-Rheological Elastomers (MRE) with hard magnetic particles used as bending actuators under an alternating magnetic field. As earlier studies demonstrated, a dispersion of hard magnetic particles in polymeric materials, aligned in a preferred orientation, cause rotational motion in the sample when a magnetic field is applied perpendicularly to the magnetization direction of the particles. They focused on static responses of MREs with hard magnetic particles. The primary goal of this study is to characterize the dynamic behavior of a flexible bending actuator based on MREs under alternating magnetic fields. In this study, samples from a previous study, consisting of barium hexaferrite particles at 30% concentrations by volume, were tested. A C-shaped electromagnet was constructed to apply alternating magnetic fields along the length of the sample. By securing only one end of the sample to the electromagnet, the sample is free to bend similar to a cantilever beam. Using this setup, the tip displacement of the sample under various input magnetic field strengths and frequencies was recorded using a laser displacement sensor. The results show that increasing the voltage output or the magnetic field strength increases the displacement of the sample. The results also show that, as the frequency of the sinusoidal voltage input increases, the amplitude of the tip displacement of the sample decrease.

Introduction

Smart materials are materials with properties that can be altered using controlled external stimuli. Magnetorheological (MR) materials are a branch of smart materials with properties and responses reliant on an applied magnetic field. Types of MR materials include, but are not limited to, fluids, foams, and elastomers. An elastomer containing dispersed ferromagnetic particles is called a magnetorheological elastomer (MRE). The response of MREs is dependent upon the concentration of the dispersed particles, the size of the particles, the type of particles, the properties of the material that the particles are dispersed in and whether or not the particles are aligned in chains or are randomly dispersed [1]. Conventional MREs contain a dispersion of soft magnetic particles, such as iron. The elastic modulus of the resulting material is magnetic field dependent [2]. Possible applications of soft MRE materials include variable stiffness elements in vibration control of engineering structures and mechanical systems [1].

As an alternative to using iron ("soft" magnetic particles) as the dispersed particles, a hard magnetic material, such as barium hexaferrite, can be used. Aligning the hard magnetic particles under a magnetic field produces an anisotropic, magnetically poled MRE. Von Lockette et. al. investigated the behavior of four classes of MRE materials with respect to magnetic symmetries and filler particle types [3]. Hard magnetorheological elastomers (H-MREs) have properties that differ from traditional MREs (soft or S-MREs). When subjected to a magnetic field, the hard magnetic particles embedded in the material will cause rotational motion because the particles create a torque due to the cross product of the particles' internal magnetization and the applied magnetic field [2, 3]. As a result, the H-MRE material can be used as a magnetic field controlled bending actuator. Research on traditional MREs has been focused on

maximizing the MR effect by experimenting with different types of particles and elastomers as well as different concentrations, shapes, sizes, and orientations of the particles.

Koo et al., studied characterization of MRE beams embedded with different types of hard magnetic materials [2]. This research has further helped to model the static responses of H-MRE materials. Studies have previously been conducted on magnetorheological elastomers as bending actuators, and the results have shown how the strength of the applied magnetic field and the use of different magnetic materials affect the stiffness of the material, the block force, and the tip displacement. As a new application of MREs, Von Lockette et al., studied folding actuation and locomotion of magneto-active composites [4].

The previous studies focused on fabrication of MRE actuators and characterization of their “static” actuation properties. In other words, the blocked tip force and the tip displacement of an MRE bending actuator were measured at a discrete magnitude of the input magnetic field. Expanding on the study of the static responses of MREs, the current study intends to study the dynamic responses of MREs. The response of the sample subjected to an alternating sinusoidal magnetic field. This report outlines the preparation of samples, the experimental setup, and the results that were obtained.

H-MRE Samples

The samples were fabricated by mixing barium hexaferrite particles in a liquid resin. This mixture was placed in a rectangular prism mold and was allowed to solidify under a strong magnetic field generated by an electromagnet. In a previous study, it was determined that the optimal concentration of magnetic particles is 30% [3]. Therefore, the concentration of particles in the samples was 30% by volume. The silicon rubber acts as a binding agent, which contributes to the flexibility of the sample. Samples were fabricated from high strength silicon elastomer resin (Dow Corning Corp.). The size of the particles used was pre-determined by the commercial availability of the particles. The size of the barium hexaferrite particles was $\sim 44 \mu\text{m}$. The samples were cured for 1 hour under a magnetic field of 2 T. The total curing time was 24 hours at room temperature. It is important for the particles to be uniformly aligned because if they weren't, the torque generated by each particle would be in various directions instead of a single desired direction. Further information on the sample preparation can be found in [2]. For the current study, a sample with the dimensions of 3.5 cm x 0.5 cm x 0.25 cm is used.

Experimental Setup

The purpose of this work is to study the dynamic behavior of H-MRE samples under an alternating magnetic field. The displacement of the sample and the magnitude of the applied magnetic field needed to be recorded over time in order to analyze the dynamic properties of the sample. In order to produce a controlled electromagnetic field, an electromagnet consisting of a horseshoe shaped iron core with 18-AWG wire coiled around one side of the electromagnet was constructed as seen in Figure 1. A voltage is supplied to the wire, which creates a current in the wire. This current in the wire is what creates the magnetic field. The number of coils around the iron core affects the strength of the magnetic field.

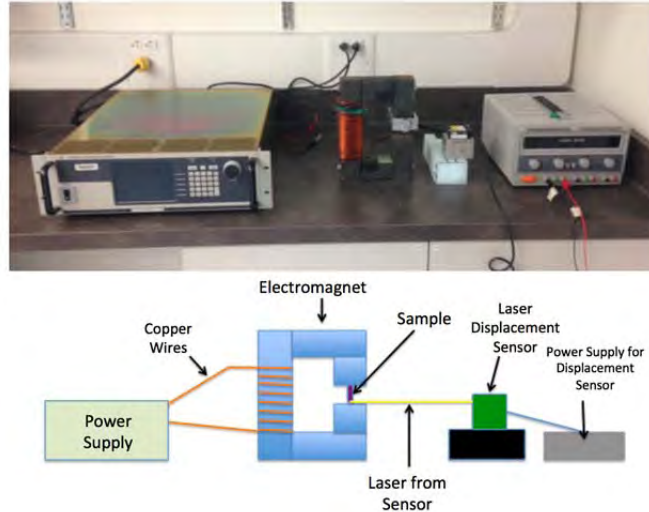


Figure 1. A schematic of the experimental setup used to collect data

Voltage was supplied the wires using a Kepco Model ATE 36-15DM power supply. This device is modeled as the power supply in Figure 1. A sinusoidal voltage of different magnitudes was supplied to the electromagnet in order to generate an alternating magnetic field.

The relationship between the input voltage and resulting magnetic field is linear. In this study, the maximum output voltage was limited to 20 V. The magnitude of the magnetic field did not change when the frequency was changed.

In order to secure the sample in the gap of the electromagnet, an aluminum square clamp was fabricated. The samples were positioned so that one end was fixed and the other end was free to move. The sample was positioned such that the length of the sample was parallel to the applied magnetic field and the width of the sample was perpendicular. When a magnetic field passes through the sample, the sample deforms similar to a cantilever beam. When an alternating sinusoidal voltage was supplied to the electromagnet, the sample moved in a back and forth motion with the magnetic field.

A high-resolution laser displacement sensor was used to measure the tip displacement of the sample. The laser sensor orientation relative to the electromagnet and sample can be seen in Figure 2. The laser sensor was focused on the moving tip of the sample. A Gauss/Tesla meter was used to measure the magnetic flux in the gap of the electromagnet. The Gauss/Tesla meter was also connected to the data acquisition system so that the displacement and the magnitude of the magnetic field could be recorded simultaneously. The Gauss/Tesla meter was used to measure the magnetic field at different positions in the gap of the electromagnet to ensure that the magnetic field was uniform throughout the sample.

Experimental Results and Discussion

Using the electromagnet, laser displacement sensor, and Gauss/Tesla meter, experiments were conducted to test the effects of magnetic field magnitude and frequency on the response of the H-MRE sample. The same sample was used for each experiment to ensure the only variables being changed were either magnitude or frequency of the magnetic field. The magnetic field is applied perpendicular to the magnetic dipole of each particle creating a torque.

Effect of Magnetic Field Strength

In order to study the effect of the peak-to-peak amplitude of the voltage input, the tip displacements of the sample for low (5 V) and high (10 V) inputs are compared in Figure 2. As shown in figure, for the input frequency of 1 Hz, the maximum tip displacement of the sample under the 10 V input is about 0.55 cm, and that of the 5 V case is about 0.25 cm. For the range of input voltages, the displacement of the tip of the sample is increased as the voltage is increased.

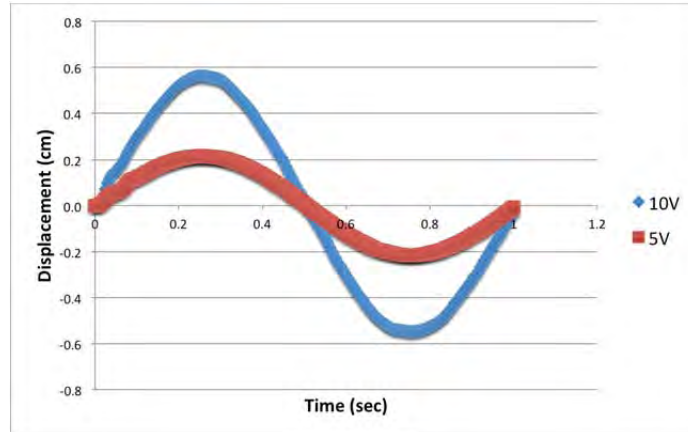


Figure 2. Displacement versus time at a frequency of 1 Hz and voltage inputs of 5V and 10 V

At the maximum input voltage considered in the current study (20 V), the sample displaced out of range of the laser displacement sensor. The laser was focused near the bottom of the sample. When the tip of the sample is displaced, it moves horizontally, but also vertically, displaying highly non-linear hyperelastic behaviors. This limited the maximum magnitude of the magnetic field that could be studied.

Effect of Frequency

For the displacement experiments, a sinusoidal voltage output was varied from 5V to 20V peak-to-peak amplitude. The output frequency was varied from 0.1 Hz to 10 Hz. The sample was allowed to move freely on one end and the distance of the bottom tip of the sample from the laser sensor was recorded using a data acquisition system. The magnetic field was also recorded using a Gauss/Tesla meter and the data acquisition system. First, the peak-to-peak amplitude was held constant and the frequency of the applied magnetic field was varied. The displacement of the sample was recorded versus time and the results were plotted.

Figure 3 shows the time history of the tip displacement of the sample under various input frequencies (0.5 Hz, 1 Hz and 2 Hz). For these sample responses, the peak-to-peak input voltage was fixed at 5 V. As the output frequency was increased, the maximum displacement of the sample decreased slightly. This trend continues for higher frequencies as well.

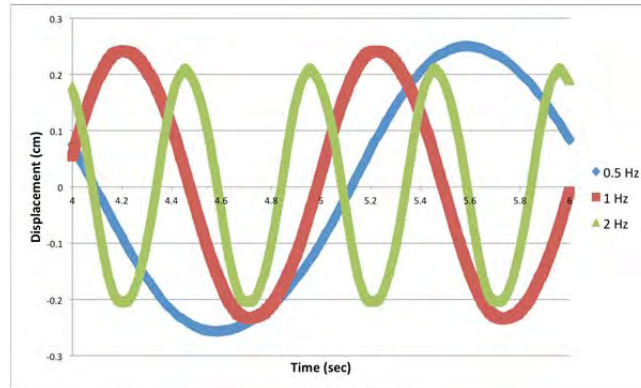


Figure 3. Experimental displacements with 5 V peak-to-peak output and 0.5 Hz, 1 Hz, and 2 Hz frequencies

Similar to previous “static” studies, the results in this study show that, as the output voltage was increased, the maximum displacement of the sample also increased. However, it is noteworthy that the dynamic response results show that, as the frequency of the alternating magnetic field is increased, the displacement of the sample decreases, while the maximum value of the magnetic field did not change with the increasing frequency. The displacement decreased at higher frequencies because the sample was not able to reach its maximum deformation in one direction before the magnetic field changed to the opposite direction. In other words, the sample is lagging. To further investigate this, the tip displacement of the sample and the input magnetic field are compared for low and high frequencies considered in this study (0.5 Hz and 10 Hz).

Conclusion

In this study, the effect of magnitude and frequency of an applied, alternating magnetic field on the response of an H-MRE sample were analyzed. As the magnitude was increased, the displacement of the sample also increased. As the frequency was increased, the displacement of the sample decreased. At high frequencies, a slight delay occurred between the maximum displacement of the sample and the maximum value of the magnetic field. When using this material as a displacement actuator, the response delay at higher frequencies and as well as the resonant frequency.

In the future, samples will be created that have magnetic particles embedded in only parts of the sample such as the end. Active control of the sample will be studied so that a desired response can be achieved. Finally, applications for this material will be investigated.

References

1. Ruddy, C., E. Ahearne, and G. Byrne. "A review of magnetorheological elastomers: Properties and applications," Proceedings of the International Manufacturing Conference (IMC) 24, Waterford Institute of Technology, August 2007, pp. 999-1005.
2. Koo, Jeong-Hoi, Alexander Dawson, and Hyung-Jo Jung. "Characterization of Actuation Properties of Magnetorheological Elastomers with Embedded Hard Magnetic Particles." *Journal of Intelligent Material Systems and Structures* (2012): 1049-054.
3. P. R. von Lockette, S. Lofland, J. Mineroff, J. Roche, and M. Babock, "Investigating new symmetry classes in magneto-rheological elastomers," *Smart Materials and Structures*, 20, 105022, 2011.
4. P. R. von Lockette, R. Sheridan, "Folding Actuation and Locomotion of Novel Magneto-Active Elastomer (MAE) Composites," Proceedings of the ASME 2013 Conference on Smart Materials, Adaptive Structures and Intelligent Systems (SMASIS2013-3222), September, 2013, Snowbird, UT, USA.
5. Lokander M and Stenberg B, "Improving the magnetorheological effect in isotropic magnetorheological rubber materials," *Polymer Testing* 22: 677–680, 2003.
6. Young, W. C., Budynas, R. G.(2002). Roark's Formulas for Stress and Strain . 7nd Edition, McGraw-Hill, Chapter 16, pages 767-768.

Augmented Reality and Virtual Reality in the Construction Industry

Student Researcher: John A. Reynolds

Advisor: Dean Bortz

Columbus State Community College
Construction Management

Abstract

My experiments and studies harnessed around the effects augmented reality and virtual reality have on the construction industry. The process at which humans build a structure has changed tremendously just over the last fifty years. However, many of the same problems have survived the test of time. Many general contractors and contracting companies use drawings and blueprints to acquire the detailed information needed to erect a building or structure. Nevertheless, this seemingly old method tends to cause some confusion with analyzing data and being able to clearly communicate it with architects and other contractors to confidently complete the project with smooth operations. Although there are software's out there that allow 3D rendering of projects during the constructing stages, potential flaws may still arise during highly complex stages in the building process. This in return causes major delays in the planning and scheduling aspect of the project, causing a prolonged finish date. Lastly, safety has become a major issue over the years. In 2015, out of the 4,379 deaths among workers in private industry, 937 were in construction, which comes out to 21.4%. The leading cause of death was falls (38.8%). Also close behind falls were struck by objects (9.6%), electrocution (8.6%), and caught-in/between (7.2%). These areas are continuously growing problems in the construction industry to this day. Luckily, technology in construction is growing at an exponential rate. Due to the progression in new technology being invented, this continuous problem may be minimized at a vast rate, or possibly even diminished permanently.

Project Objective

My objective is to research the causes of the problems surrounding planning and scheduling, mid construction flaws, and health and safety in the construction industry. Also researching how augmented reality and virtual reality technology can reduce these effects, they have on the construction process and improve a multitude of issues infecting these problem areas.

Methodology Used

I used information involving statistics from the Occupational Safety and Health Administration. I have also used research done by global consultancy firm McKinsey & Company and the Institute for Computer in Engineering at the Ruhr-Universitat Bochum located in Germany. Mckinsey Global Institute industry digitization index of 2015 available data shows that construction is among the least digitized sectors with relatively low digitization in assets, usage, and labor. Companies like Microsoft and PlayStation are designing technologies that can address these issues. Microsoft is coming out with a device called the HoloLens that superimposes a computer-generated image on a user's view of the real world. In construction, this will enable contractors to help project managers be able to view schematics and specific details overlaid with an actual structure right in front of them. This can open the doors to allow adjustments or foresee potential problems before the building phase has even started. Thus preventing any schedule changes and potentially producing a sooner finish date. Another device is the PlayStation VR. It is a virtual reality headset designed by PlayStation that can convert with a Building Information Module (BIM) to a virtual reality simulation. This can help with communicating the design aspect of a job to an investor or owner. The study done by the Institute for Computer in Engineering at the R.U.B.

provides construction employees a virtual experience of real life hazardous situations before it happens on the site. By doing this, it can potentially help lead to less accidents on the job site.

Results Obtained

Results from the combination of data and information collected will provide a better understanding of how augmented reality and virtual reality usage in construction can be genuinely useful. Construction companies today are using technologies such as McCarthy Building Companies. The PlayStation VR was used to design a critical care facility in Los Angeles that was completed in 2013. The results were seen in an increase in positive client interaction, client satisfaction, project approval time, and a sooner project finish date. In the German study done at the Institute of R.U.B., it showed that workers can engage in health and safety training more than they would in paper based training. The Virtual Human Interaction Lab at Stanford University studies the impact of exposing humans to an alternate reality. By doing so, they found that experiencing a virtual event could change ones behavior.

Significance and Interpretation of Results

From a residential construction employee standpoint, I feel that augmented reality and virtual reality could be a significant change for the better within the industry. It will help lead to a positive client interaction and understanding of the project at hand. It will also help identify problems before construction of the structure that may have otherwise occurred during the building process. By bringing this new technology to the industry, companies can have a clearer communication with their contractors in the understanding of the drawing details or blueprints. Out of all the benefits these different devices can bring, one of the most important is it can help save lives by preventing fatalities or accidents that could have otherwise been avoided on the job site. I look forward to seeing the growth and evolving in technology, as well as, digitization in this industry and will continue my own study and usage of these augmented and virtual devices.

References

1. Johnson, Mark L. "Are You Ready for Virtual Reality?" AWCI. E-Media & Publications, 22 June 2016. Web.
2. McEachran, Rich. "Augmented Reality Is Driving Construction's Creative Reinvention." The Guardian. Guardian News and Media, 28 Oct. 2016. Web. 29 Mar. 2017.
3. United States. Occupational Safety and Health Administration. Department of Labor. Commonly Used Statistics. OSHA, 1 Oct. 2015. Web. 30 Sept. 2016.
4. Friedman, Emily. "Augmented and Virtual Reality for Architecture, Engineering and Design." BrainXchange. Emily Friedman https://brainxchange.events/wp-content/uploads/2016/06/bx_logo_340x156.png, 22 Sept. 2016. Web. 29 Mar. 2017.
5. "German VR Safety System Lets Workers Have Accidents before They Arrive on Site." GCR - Innovation - German VR Safety System Lets Workers Have Accidents before They Arrive on Site. N.p., n.d. Web. 29 Mar. 2017.

Applying Genetic Fuzzy Systems to Time-Optimal Control Problems

Student Researcher: Nathaniel L. Richards

Advisor: Dr. Kelly Cohen

University of Cincinnati
Aerospace Engineering and Engineering Mechanics

Abstract

This project attempts to apply novel Machine Learning approaches to optimal control problems. The 1990 ACC Benchmark Problem, proposed by Wie and Bernstein, is investigated; this problem is well researched for both linear and nonlinear attempts at robust control under parameter uncertainty [4]. Training data is generated by GPOPS-II, a MATLAB toolbox developed by Dr. Anil Rao and Dr. Michael Patterson, that solves the open-loop optimal control and state time histories [3]. A Genetic Algorithm (GA) trains a series of Fuzzy Logic Inference Systems (FISs), resulting in a Genetic Fuzzy System (GFS) that attempts to stabilize the system with an unknown spring constant.

Project Objectives

Optimal control problems are ubiquitous throughout the Aerospace field and engineering abroad. From determining minimum time-to-climb maneuvers or minimizing fuel burn for an engine, the systems involved can be controlled in such a way that reduces time, effort, and cost under certain constraints in state and control. Traditionally, optimal control problems are solved with a fixed plant with known parameters, and the resulting control is open-loop. Time-optimal control has been shown to be bang-bang in nature, where the control switches between maximum and minimum values, hence the name “bang-bang.” This type of open-loop control is obviously not robust to plant changes, uncertainty, or sensor noise; closed-loop control is desired. However, determining analytic models for closed-loop control of complex systems may not be possible.

The goal of this research is to train a GFS to map closed-loop state feedback to the optimal control based on the time-optimal control and state histories for the ACC Benchmark Problem generated by GPOPS-II. A custom Fuzzy Logic module was developed for this project, as well as the GA that optimizes the GFSs represented as chromosomes.

Methodology

Fuzzy Logic involved multi-valued logic, where statements take on degrees of truth on a continuum [0,1]. Crisp numerical inputs are “fuzzified” to linguistic variables via membership functions (MFs) and linguistic rules; several rules can be activated at once. These rules are then aggregated and “defuzzified” into a crisp output. Fuzzy Logic has been applied to several controls problems in recent history, such as the classic inverted pendulum. A Genetic Algorithm is a derivative-free optimization method based on the principles of biology and natural selection. Fuzzy Logic membership functions can be represented by real numbers and the rules as integers; the GFS individuals can be encoded as strings within the GA. The individuals are evaluated by a cost function, and better-performing individuals survive to breed and pass on their genetic information. Mutations inject new genetic information into the population, thus making GAs relatively robust against local optima.

The ACC Benchmark Problem is described as a double mass-spring system, where control only acts on m_1 , shown in Figure 1. The spring constant is uncertain and can vary: $0.5 \leq k \leq 2.0$. Control constraints

are imposed, where $|u| \leq 1$. The system must be settled to where all the states fall within the window $|x| \leq 0.1$. The nominal system is described by $m_1 = m_2 = k = 1.0$. The system dynamics are as follows:

$$\begin{bmatrix} \dot{x}_1 \\ \dot{x}_2 \\ \dot{x}_3 \\ \dot{x}_4 \end{bmatrix} = \begin{bmatrix} 0 & 0 & 1 & 0 \\ 0 & 0 & 0 & 1 \\ -k/m_1 & k/m_1 & 0 & 0 \\ k/m_2 & -k/m_2 & 0 & 0 \end{bmatrix} \begin{bmatrix} x_1 \\ x_2 \\ x_3 \\ x_4 \end{bmatrix} + \begin{bmatrix} 0 \\ 0 \\ 1/m_1 \\ 0 \end{bmatrix} u$$

Fuzzy Logic has been applied to this problem previously by several authors. Cohen et al. stabilized the system by introducing a virtual cart with damping, allowing the system to be settled to the origin [1]. Settling time was further improved by allowing a fuzzy controller to vary the damping control effort. However, the full control authority of $u = \pm 1$ was not used, hence the control could not be bang-bang. Linder et al. cascaded FISs, where separate FISs controlled stability and tracking characteristics [2]. Both methods were hand-tuned and yielded better settling times and robustness compared to linear control approaches.

GPOPS-II was used to generate the optimal control and resulting state time histories for 100 randomly sampled values of k . Figure 3 shows that decreasing spring constants increase the settling time; this is due to the lag introduced between the two carts as a result of a non-stiff spring. Figure 4 shows the optimal control for the nominal system; the control generated from GPOPS-II is indeed bang-bang in nature.

The GFS controller trained by the GA on the GPOPS-II training data attempts to emulate bang-bang control, which is the mathematically-proven optimal control. Figure 2 demonstrates the cascaded structure of FISs within the GFS. Cascading FISs reduces the number of overall rules, compared to a single FIS with 4 inputs and 1 output; this shortens the number of genes on the chromosome and reduces the search space of the problem. A custom Fuzzy Logic Python module was developed, which uses trapezoidal membership functions and the weighted mean-of-maximum defuzzification method to map 4 state inputs to 1 control output. The GA and dynamics simulations were also developed in the Python programming language.

Results

The GFS was first trained only on the nominal system ($m_1 = m_2 = k = 1.0$); Figure 5 shows that the GFS successfully settles the system within 10.0s. The GFS settles the system in 5.110s, where the optimal settling time is 4.083. However, when this controller is applied to other values of k , the GFS does not settle the system within 10.0s. For higher spring constants, such as $k=2.0$, the system's behavior is promising – the states approach zero but do not settle within 10.0s. Conversely, the system's behavior is quite poor for low spring constants, such as $k=0.5$. The system does not appear to drive the states to zero, and some states appear to diverge.

A controller trained on one set of parameters cannot be expected to generalize to a whole range. Stochastic training attempted to expose each GFS controller to several k values in each generation. These k values were randomly sampled from the 100 data sets over the full range of spring constants. The cost returned for the GFS was a weighted average based on how quickly it settled the system, or it was penalized for not settling within 10.0s.

Unfortunately, a single GFS was not able to generalize over the entire range of spring constant values. The stochastic sampling training method was able to train a GFS to partially generalize, trending towards

higher k values that are easier to settle. Because the GFS did not generalize over the range of spring constants, there is no guarantee of stability or robustness.

The implications of closed-loop intelligent systems that emulate optimal control are huge. This research provides the groundwork for future experiments with varying training methods for GFSs and optimal control. Future work will include varying the number of membership functions for each FIS, cascading the FISs differently, and potentially including recurrent connections.

Figures

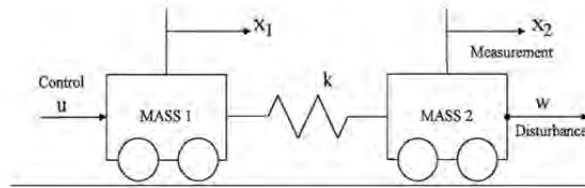


Figure 1. ACC Benchmark Double Spring-Mass System

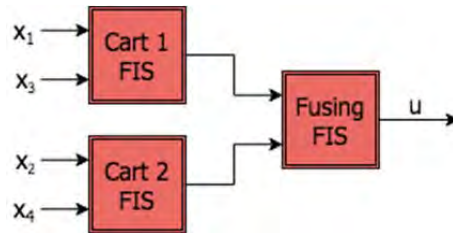


Figure 2. Cascaded GFS Architecture

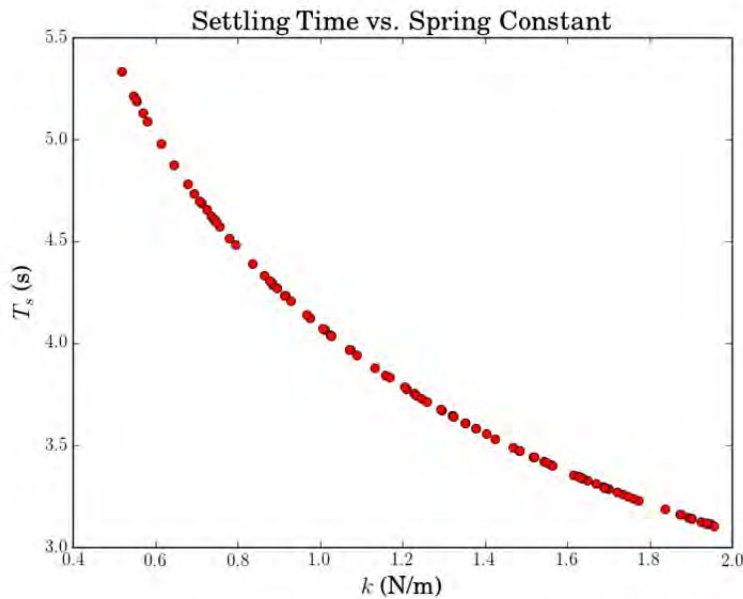


Figure 3. GPOPS-II Training Data Over Range of Spring Constants

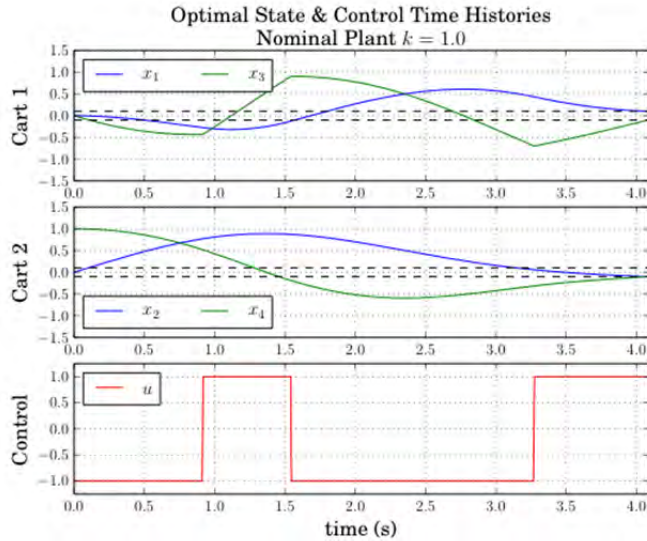


Figure 4. GPOPS-II Time-Optimal Control of Nominal System

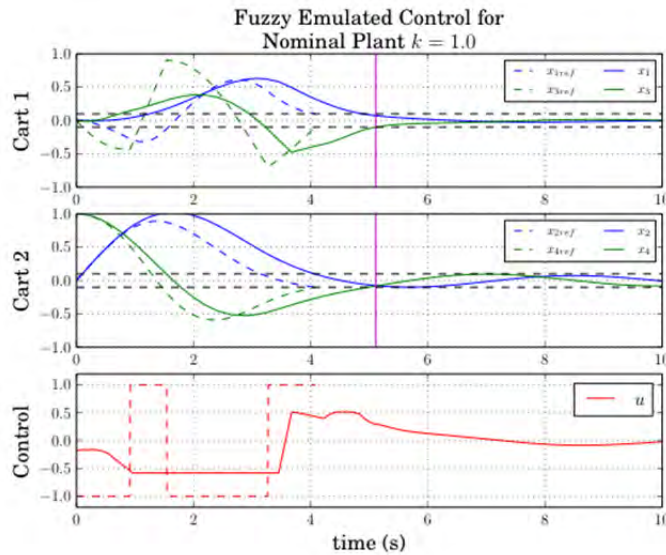


Figure 5. Fuzzy Control of Nominal System

References

1. Cohen, K., Weller, T., and Ben Asher, J. Z., "Control of Linear Second-Order Systems by Fuzzy Logic-Based Algorithm," *Journal of Guidance, Control, and Dynamics*, Vol. 24, No. 3, May 2001.
2. Linder, S. and Shafai, B., "Qualitative robust fuzzy control with applications to 1992 ACC benchmark," *IEEE Transactions on Fuzzy Systems*, Vol. 7, No. 4, 1999, pp. 409–421.
3. Patterson, M. A. and Rao, A. V., "GPOPS-II: A MATLAB Software for Solving Multiple-Phase Optimal Control Problems Using hp-Adaptive Gaussian Quadrature Collocation Methods and Sparse Nonlinear Programming," *ACM Trans. Math. Softw.*, Vol. 41, No. 1, Oct. 2014, pp. 1:1–1:37.
4. Wie, B. and Bernstein, D. S., "Benchmark Problems for Robust Control Design," *Journal of Guidance, Control, and Dynamics*, Vol. 15, No. 5, September 1992.

Characterization of Massive vs. Laminated Texture of the Coconino Sandstone (Permian), Arizona from the Study of Thin Sections

Student Researcher: Sarah C. Rouse

Advisor: Dr. John Whitmore

Cedarville University

Department of Science and Mathematics

Abstract

This project seeks to contribute to the work of Dr. John Whitmore and Sarah Maithel on the Coconino Sandstone (Permian) of Arizona. More than one hundred thin sections are available for study from this sandstone. Each thin section was examined both macroscopically and microscopically to determine if the sample is “laminated” or “massive.” The purpose of this project is to define what “laminae” are and then develop reliable quantitative criteria that can differentiate between the laminated and massive samples. These criteria might then be applied to distinguish patterns that occur across the deposit, which in turn may provide insight into the depositional conditions of the sandstone.

Project Objectives

The primary purpose of this project is to explore the causes of lamination, a sedimentary structure consisting of fine parallel layers. While the appearance of layers can be caused by compositional or textural changes, this project focuses on the textural characteristics of the sandstone. These characteristics are explored through macroscopic visual examination as well as microscopic analysis. The results of such study may then be used to search for patterns of deposition across large areas. These patterns may contribute to an understanding of the conditions under which the Coconino Sandstone was formed.

Methodology Used

This study began with an initial visual examination of thin sections which had previously been taken from 14 locations in northern and central Arizona. This allowed for a distinction between compositional and textural lamination. The thin sections that displayed evidence of textural lamination, as well as those with no apparent lamination whatever, were then compared using data provided by Dr. Whitmore. This data, which was collected through the measurement of 400-600 randomly selected grains within each thin section, was then analyzed in an attempt to determine the causes of lamination and to discover regional trends based on the presence of such causes.

Results Obtained

Statistical analysis of rounding, grain size, and sorting data suggested that sorting is the primary characteristic that causes lamination. While sorting data cannot provide a definitive classification of “massive” or “laminated” for individual thin sections, it can substantiate visual characterizations and support regional trends. For example, the outcrops in this study appear to be grouped into poorly sorted in the north and more moderately sorted further south. This indicates a change in the depositional environment which is probably related to a decrease in velocity. Collectively, sorting data along with visual inspection can be used to draw conclusions about the laminated or massive nature of an outcrop and can contribute to an understanding of depositional conditions.

References

1. Campbell, Charles. "Lamina, laminaset, bed and bedset." *Sedimentology* 8 (1967): 7-26.
2. Friedman, Gerald and John Sanders. *Principles of Sedimentology*. John Wiley & Sons, 1978.
3. Johnson, M.R. "Thin section grain size analysis revisited." *Sedimentology* 41 (1994): 985-999.
4. Whitmore, John; Strom, Raymond; Cheung, Stephen; and Garner, Paul A., "The Petrology of the Coconino Sandstone (Permian), Arizona, USA" (2014). Science and Mathematics Faculty Publications. 307.
5. Whitmore, John; Strom, Raymond. "Textural trends in the Coconino Sandstone, Central and Northern Arizona." Geological Society of America, 2 Nov 2010, Colorado Convention Center, Denver, CO. Poster Presentation.

Detection and Analysis of Biogeophysical Factors Influencing Local Water Quality and Coral Reef Health in the US Virgin Islands

Student Researcher: Hannah L. Schlaerth

Advisor: Joseph D. Ortiz

Kent State University
Geology

Abstract

Nearly a quarter of ocean species are constrained to coral reefs, making them important economic resources in terms of tourism and fishing (Grimsditch, 2005). In recent years, climate change, agricultural runoff, and overfishing have started to degrade the coral reefs of the US Virgin Islands (USVI). This study aims to integrate data obtained from NASA satellites with field measurements using a hand held spectroradiometer (ASD) in order to determine bio-optical properties and to quantify water quality parameters that effect coral reef health in the coastal waters of the USVI. Landsat-8 (L8) images from August 2016 through February 2017 were systematically analyzed by taking the derivative of the measured visible/near infrared spectra and then using Varimax-rotated principal component analysis (VPCA) decomposition to identify the main contributors to the signal (Ortiz et al., 2013). Results from this data decomposition were then matched to libraries of standard reflectance derivative spectra for known pigment and mineral standards. To verify these results and provide *in situ* data for satellite image verification, a week-long, research campaign was conducted in and around the coastal waters of St. Thomas Island of the USVI (Ortiz et al., KSU NASA EPSCoR Annual Report 2016). The results from the Landsat data processed here are compared with the data from the field campaign. Using VPCA-decomposition, it may eventually be possible to identify algal species and the mineralogy of detritus from satellite images alone, making near real-time water quality monitoring a possibility.

Project Objectives

The coral reefs of the Caribbean Islands are known for their scenic attributes, making places like the USVI lucrative tourist destinations. Increases in development and docking large cruise ships has created an influx of sediment and nutrients entering the coastal waters of the USVI, causing detrimental effects on water quality. As consequence, coral reefs have started to degrade, particularly those located within nearshore waters (Ocean Conservancy). In situ water quality monitoring is costly and time intensive. Past research projects in the USVI have laid the groundwork for water quality monitoring via remote sensing (Kerrigan 2015; Hollister et al 2016), which offers a spatial advantage and cost effective alternative over traditional water quality monitoring. We use VPCA decomposition on L8 images from August 2016 through February 2017 to identify color producing agents (CPAs) in the water column. Coupled with spectroscopy performed in the field and ongoing coral reef monitoring around the USVI, this project contributes a multidisciplinary approach to understanding the biogeophysical factors influencing local water quality and coral reef health in the USVI.

Methodology

L8 surface reflectance images dating from August 2016 through February 2017 were systematically analyzed using VPCA decomposition (Ortiz et al., 2013). Water pixels in each image were isolated by creating masks that cover land, clouds, and cloud shadows, following Hollister et al (2016). The centered, first derivative of each valid water pixel was calculated and a VPCA was performed using the computer software ENVI/IDL. Principle components were ranked, with the first component accounting for the greatest percentage of variance in the data matrix and each successive component contributing

less. The loadings for each principal component were then plotted against wavelength and identified by their spectral patterns. Our spectral library of known, standard CPAs was averaged to the spectral range of L8 sensors and stepwise multiple linear regression was used to determine the combination of CPAs associated with each component for identification.

Bio-optical properties were sampled at eleven field locations (figure 1) around St. Thomas Island (USVI) from December 5-10, 2016. At each site, surface reflectance was measured from 350-1075 nm using an ASD Fieldspec HH2. The spectra were averaged to 10 nm resolution and analyzed with VPCA decomposition (Ortiz et al., KSU NASA EPSCoR Annual Report 2016).

Results and Discussion

VPCA decomposition of the L8 images revealed matching spectral signatures across dates, with four major patterns emerging, here defined as VPCA Match 1,2,3, and 4. VPCA Match 1 shows a steep decrease between 500 and 550 nm wavelengths (figure 2). Decomposed satellite imagery corresponding to VPCA Match 1 has a plume of high intensity extending from Magen's Bay and grading to low intensity seaward. VPCA Match 2 has a maximum loading at 480 nm and a minimum at 655 nm. Highest surface reflectance can be seen north of Savana with near shore environments displaying lowest loadings. VPCA Match 3 shows a maximum loading at 440 nm and minimum at 560 nm. This component is most intense in the coastal areas of Magen's Bay and Coculus Rock, and dramatically decreases beyond coastal waters. VPCA Match 4 has relative maxima at 440 nm and 655 nm. Two plumes are evident- one west of Magen's bay and the other from the south coast of St. Thomas extending towards Buck Island.

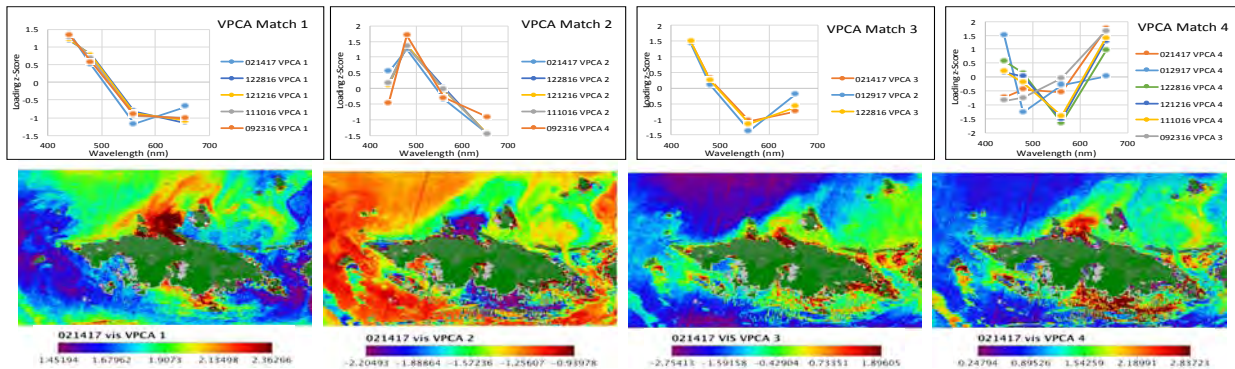
Five major components were revealed from the VPCA-decomposition of the *in situ* hyperspectral measurements, which are graphically similar to the spectral patterns described above. Future efforts will be targeted at identifying the CPAs present in each principle component and quantitatively comparing spectral signatures of L8 images to ASD measurements. By using handheld spectroradiometer measurements in conjecture with satellite imagery, we hope to contribute to future efforts in real-time, qualitative and quantitative analysis of water quality.

Figures



Figure 1. Locator Map: St. Thomas Island of the USVI, showing eleven sampling sites where biooptical characteristics were measured from December 5 through December 10, 2016.

Figure 2 (below): Varimax principal component analysis of Landsat-8 images revealed the four spectral patterns below, matched on the basis of loading z-scores (top row). Corresponding, sample satellite imagery is shown below each component, with land masked in green and clouds in grey.



References

1. Grimsditch, G. (2005). A study of potential coral reef bioindicators in the Mamanucas region, Fiji, using Coral Cay Conservation Reef Check data. (Unpublished doctoral dissertation). UCL, London.
2. Hollister, K., Ortiz, J. D. (2016). Historic Water Quality Trends in the US Virgin Islands and Future Implications on Coral Reef Health (Unpublished McNair Scholars Report). Kent State University.
3. Kerrigan, K. (2015). Development of a regional bio-optical model for water quality assessment in the US Virgin Islands (Master's thesis).
 - a. Ocean Conservancy. (n.d.) The state of the coral reefs of the U.S. Virgin Islands. Retrieved from http://act.oceanconservancy.org/site/DocServer/Reefs_USVI_part2.pdf
4. Ortiz, J. D., Schlaerth, H., Hollister, K., Avouris, D. (2016). Annual Report, 2016 for Using NASA's Ocean Color Sensors to Identify Effects of Watershed Development and Climate Change on Coastal Marine Ecosystems of the US Virgin Islands. Grant number NNX15AM74A. (p 1-18).
5. Ortiz, J. D., Witter, D. L., Ali, K. A., Fela, N., Duff, M., and Mills, L., Evaluating multiple color producing agents in Case II waters from Lake Erie, International Journal of Remote Sensing, 34 (24), 8854-8880, 2013.

Control of Dynamic Stall over a NACA 0015 Airfoil using NS-DBD Plasma Actuators

Student Researcher: Achal Singhal

Advisor: Dr. Mo Samimy

The Ohio State University

Department of Mechanical and Aerospace Engineering
Aerospace Research Center

Abstract

Dynamic stall is found in numerous applications, including sharp maneuvers of fixed wing aircraft, biomimetics, wind turbines, and most notably, rotorcraft. The associated unsteady loading can lead to aerodynamic flutter and mechanical failure in the system. The present work has demonstrated the ability of nanosecond pulse driven dielectric barrier discharge (NS-DBD) plasma actuators to significantly reduce the load hysteresis in dynamic stall over a NACA 0015 airfoil. The flow Reynolds number, airfoil oscillating reduced frequency, and excitation Strouhal number were varied over large ranges: $Re = 167,000 - 500,000$, $k = 0.025 - 0.075$, and $St_e = 0 - 10$, respectively. Surface pressure measurements were taken for each combination of Re , k , and St_e . Phase-locked particle image velocimetry results were acquired for select cases. It was observed that the trends of effect of St_e were similar for all combinations of Re and k . Excited resulted in several positive effects, including the suppression of the dynamic stall vortex. The decrease in the strength of the dynamic stall vortex is achieved by the formation of large-scale structures induced by the excitation that bleed the leading-edge vorticity prior to the ejection of the dynamic stall vortex. At sufficiently high excitation Strouhal numbers ($St_e \approx 10$), the dynamic stall vortex was completely suppressed.

Introduction

The primary focus of this work is exploring flow physics and control in dynamic stall. In rotorcraft, dynamic stall occurs when the rate of change of the angle of attack (α) is fast enough to maintain attached flow past the static stall angle of attack. As the airfoil motion slows and begins to pitch down, a vortex is formed at the leading edge, convected over the airfoil, and shed. This dynamic stall vortex momentarily increases the lift production. Once it has convected past the airfoil and shed, the flow is fully stalled. This process results in large oscillatory loads that can significantly reduce the life of the blade [1]. As such it is desirable to eliminate the oscillatory loads, and this problem has attracted much attention in the rotorcraft community.

Previous research has focused on the use of flow control devices to mitigate the dynamic stall vortex. These devices consist of both passive (such as geometric modifications to the airfoil) and active (such as momentum injection) techniques [2]. Geometric modifications have a narrow operating range, and may be difficult to incorporate into an existing fleet. Active techniques aim to provide efficacy over a broad operating range. Active techniques typically involve momentum injection [2]. The primary disadvantage of momentum injection techniques is that at high speeds more momentum is required to maintain efficacy. Meeting this increasing demand for high Reynolds number application flows is often impractical.

The focus of this paper will be on the use of nanosecond pulse driven dielectric barrier discharge (NS-DBD) plasma actuators. These actuators consist of two copper electrodes separated by a dielectric barrier. DC pulses are used to create localized, rapid heating that results in the formation of a

compression wave at the DC pulse frequency [3]. If introduced in the proper location and frequency, the localized heating can be used to excite natural flow instabilities. In static tests, NS-DBD plasma actuators have been shown to reattach flow at post stall angles of attack for a NACA 0015 airfoil at high flow velocities [3].

Experimental Arrangement

Experiments were performed in the recirculating wind tunnel located at the Gas Dynamics and Turbulence Laboratory, within the Aerospace Research Center at The Ohio State University [3]. A NACA 0015 airfoil undergoing sinusoidal motion with reduced frequency ($k = \pi f c / u_\infty$, where f is the physical oscillation frequency of the airfoil) was used in the experimentation. Although not a typical cross section for rotorcraft blade, it has been well characterized in static flow. The experimental arrangement used in this work is briefly recalled here. More details are found in Singhal [4].

Two coordinate systems are used throughout this paper. The axis of the first system lies along the chord line and the coordinate is normalized by the chord length, denoted x/c . A positive coordinate indicates the aerodynamic suction side and a negative coordinate indicates the aerodynamic pressure side. The second coordinate system is a two-dimensional grid aligned with the test section. These coordinates are also normalized by the chord, denoted x/L and y/L (L instead of c is used to distinguish between the two normalized x coordinates). This system is in the test section reference frame and is used to define the location and direction of velocity data. The origin of this coordinate system is at the point of rotation, or $x/c = 0.25$.

A single actuator, powered by a custom, in-house manufactured pulse generator, was placed on the airfoil to evaluate the efficacy of excitation. The actuator is constructed of two 0.09 mm thick copper tape electrodes; the exposed high-voltage electrode is 6.35 mm wide and the covered ground electrode is 12.70 mm wide. The dielectric layer is composed of three layers of Kapton tape, each 0.09 mm thick with a dielectric strength of 10 kV. The total thickness of the entire actuator is 0.45 mm. The actuator was placed on the suction side of the airfoil with the electrode junction at $x/c = 0.01$ and covers the entire span of the airfoil. The position of the actuator was based on static results [3].

Static pressure measurements on the airfoil surface were acquired using three Scanivalve digital pressure sensor arrays (DSA-3217). A total of 35 taps are located on the surface of the airfoil. The pressure coefficient was phase averaged over 4 sets of 16,384 samples acquired at 400 Hz near the airfoil centerline. The sectional lift and moment coefficients (C_L and C_M) were calculated from this data and used to determine the effect of excitation on the dynamic stall process.

Particle image velocimetry (PIV) was the primary diagnostic technique. Olive oil seed particles were injected upstream of the test section. An approximately 2 mm thick laser sheet illuminated the measurement plane at 60.4% of the airfoil span. Two commercially available LaVision cameras (Imager Pros) and software (DaVis) were used to acquire 5 sets of 100 images pairs for each excited cases. For the baseline cases, a single set of 500 images was acquired. Acquisition was locked to the airfoil motion to provide phase averaged flow field information. Swirling strength was used as the vortex identification technique, as detailed by Adrian et al. [5], and was non-dimensionalized by the freestream velocity divided by the chord. In the presentation of the PIV results, the airfoil is plotted in black along with an arc. The arc is a manifestation of an optical obstruction and is not indicative of any flow features.

Results and Discussion

Before examining the effect of excitation, the baseline flow was documented. Although the actuators are thin ($0.0022c$), the physical presence of the actuator near the leading edge does impact the flow. Thus, excited data will be compared to data acquired with the actuator mounted to the airfoil but turned off (referred to as baseline or $St_e = 0$) throughout this paper.

Flows were investigated for various Reynolds numbers ($Re = 167k, 300k, 500k$) and reduced frequencies ($k = 0.025, 0.05, 0.075$). Twenty excitation Strouhal numbers were tested for each combination of Reynolds number and reduced frequency. The only motion profile tested was a sinusoidal waveform with an amplitude of 10° and a mean of 10° . The results presented herein are at $Re = 300,000$ and $k = 0.05$. The trends for each combination of Reynolds number and reduced frequency are similar with respect to the excitation Strouhal number and no significant information is lost by the omission of the other combinations of Reynolds number and reduced frequency.

PIV data was acquired at one combination of Reynolds number and reduced frequency. This case was $Re = 300,000$ and $k = 0.05$. Three excitation Strouhal numbers were tested, $St_e = 0, 0.3, 9.9$. These conditions were chosen as representative cases after an analysis of the pressure data. Phase-locked PIV data was collected at 17 phases for the baseline case, and 9 phases for the excited cases.

Baseline Results

Figure 1 shows the baseline phase-averaged lift and moment coefficients. In this figure, the five stages of dynamic stall, as outlined by Corke et al. [2], are numbered. The process of dynamic stall begins as the airfoil begins pitching up. In this stage, the flow is attached and the lift increases steadily with α . When α exceeds the static stall α , the lift continues to increase; this is the second stage of dynamic stall. The delayed separation is a consequence of the airfoil motion and the formation of a closed separation bubble near the leading edge of the airfoil.

In the second stage, the vorticity at the leading edge accumulates and the dynamic stall vortex begins to form. This accumulation of vorticity is better visualized by the PIV results, shown in Figure 2. In this figure, the phase of motion (ϕ) and angle of attack are shown in the bottom left of each image.

As α increases, the airfoil undergoes the third stage of dynamic stall [2] – the ejection of this vorticity in the form of the dynamic stall vortex. Figure 3 shows the dynamic stall vortex convecting over the airfoil at $\phi = 73.5^\circ$ ($\alpha = 19.6^\circ$). However, the vortex does not appear to be well defined. The shape of the dynamic stall vortex in the PIV results is attributed to the stochastic nature of dynamic stall process. As the dynamic stall vortex does not shed at the same phase with respects to the airfoil motion, phase-averaging results the appearance of a more diffuse and oblong vortex.

The convection of the dynamic stall vortex results in an additional increase in lift, as shown by the lift peak near $\alpha = 19^\circ$ in Figure 1. The vortex shedding also results in a sharp decrease in pitching moment, since the vortex moves the airfoil center of pressure downstream as it convects. It is known that moment stall precedes lift stall [2]; however, due to the limited temporal and spatial resolution of the pressure taps, they appear to occur simultaneously. After the dynamic stall vortex has convected, the airfoil is fully stalled. This marks the fourth stage of the dynamic stall process [2], and corresponds to the sharp drop in the lift observed in Figure 1. The final stage of dynamic stall is flow reattachment.

Excited Results

After characterizing the baseline flow, a sweep of different excited cases was collected to perform an assessment of the NS-DBD actuator's potential as a dynamic stall flow control device. Figure 4 displays the phase averaged lift coefficient for the baseline and excitation results for $Re = 300,000$ and $k = 0.05$. Although a total of twenty different excitation Strouhal numbers were tested only four representative cases ($St_e = 0, 0.3, 0.96, 9.9$) are shown to keep the figures uncluttered.

The trend of the effects of excitation on the overall progression of dynamic stall appears to be similar for different combinations of Reynolds number and reduced frequencies. Each combination follows three primary trends:

1. Low excitation Strouhal numbers ($St_e < 0.5$) result in oscillatory lift and drag after the dynamic stall vortex has shed. This behavior smooths out, as the excitation Strouhal number increases.
2. All excited cases observe earlier flow reattachment than the baseline.
3. Excited cases (in general) observe reduced lift and moment hysteresis and decreased dynamic stall vortex strength.

In order to maintain brevity, only trend three will be discussed further. In particular, this section will only focus on the decreased dynamic stall strength. A thorough discussion is provided in Singhal [4].

Shown in Figure 5 is the normalized swirling strength for various phases (angle of attack near the peak lift) at $Re = 300,000$, and $k = 0.05$ for the pitch up motion. The images are ordered by the excitation Strouhal number column-wise – that is, the left, middle, and right columns contain the data for $St_e = 0$, $St_e = 0.35$, and $St_e = 9.9$, respectively. Baseline lift curves on the right of the data provide a reference for when the PIV data was acquired with respect to the lift and moment coefficients.

As discussed previously, the ejection of the dynamic stall vortex is preceded by the accumulation of vorticity at the leading edge. This is shown by the high swirling strength in Figure 5 at $St_e = 0$, and $\phi = 44.5^\circ, 53.0^\circ, 64.2^\circ$ ($\alpha = 17^\circ, 18^\circ, 19^\circ$). At $\phi = 73.5^\circ$ ($\alpha = 19.6^\circ$), it is seen that the dynamic stall vortex has been ejected and is convecting downstream. Due to the unsteady nature of dynamic stall, the vortex is not well defined. However, when coupled with pressure results it is apparent that the vortex is convecting over the airfoil at this time. Compared to the baseline case, the accumulation of vorticity is much smaller in the excited cases, particularly for the high excitation Strouhal number. At $St_e = 9.9$, this accumulation of vorticity is replaced by a stream of small, coherent vortices which appear to remove the accumulating vorticity near the leading edge. Thus it follows that as the number of vortices increases (i.e. as St_e increases) more vorticity is removed from the leading edge and the dynamic stall vortex should be weaker (as observed in the results).

To an extent, this is also observed in Figure 5 at $St_e = 0.35$ and $\phi = 73.5^\circ$ ($\alpha = 19.6^\circ$), where the swirling strength of the dynamic stall vortex is considerably weaker than its baseline counterpart. But at the highest excitation Strouhal number, $St_e = 9.9$, the formation and ejection of the dynamic stall vortex is not observed.

Closer examination of pressure results (Figure 4) indicates that there is a fairly monotonic relationship between the excitation Strouhal number and the lift peak. This is consistent with the prior discussion of the formation of vortices, namely, that the formation of structures due to excitation removes accumulated vorticity from the leading edge, thereby weakening the dynamic stall vortex and reducing the magnitude of the lift and moment peaks.

Due to the poor temporal resolution in the phase-locked PIV data, it is difficult to directly determine the strength of the dynamic stall vortex. As a simple alternative, the reduction in the magnitude of moment stall due to excitation is shown in Figure 6. The reduction in the moment coefficient is normalized by the baseline value. The figure indicates that, in general, as the excitation Strouhal number increases, the magnitude of the peak moment coefficient decreases. This continues until the formation of the dynamic stall vortex is suppressed at which point the moment coefficient value plateaus with respect to the excitation Strouhal number.

Conclusion

Dynamic stall is present in many applications, including rotorcraft, MAVs, and wind turbines. Associated unsteadiness and the potential for aerodynamic flutter has made it a problem of interest to the aerodynamics and flow control communities. NS-DBD plasma actuators have previously demonstrated the ability to reattach separated flow in a variety of static stall conditions. This work has sought to explore the use of these actuators to control dynamic stall in an airfoil.

A single NS-DBD plasma actuator was mounted to the airfoil near the leading edge, and pressure was taken for each combination of three Reynolds numbers and three reduced frequencies. Phase-locked PIV measurements were acquired at $Re = 300,000$ and $k = 0.05$. The baseline pressure and PIV results compare well with the stages of dynamic stall in the literature.

Over all the combinations of Reynolds number and reduced Strouhal numbers the observed trends were remarkably similar. From these results, three major trends were observed. The first was that excitation at low Strouhal number results in the formation of large-scale flow structures in the stalled regime, which result in unsteadiness in the lift and moment curves. In second trend, excitation resulted in earlier reattachment due to the formation of coherent structures that entrain the high momentum free stream flow and reattach the flow. Lastly, excitation results in the reduction of the lift and moment hysteresis due to the decreased dynamic stall vortex strength. The decreased strength of the dynamic stall vortex is attributed to the decreased vorticity accumulation at the leading edge during the pitch up motion. Excitation results in the formation of vortices prior to the ejection of the dynamic stall vortex. These vortices remove some of the accumulated vorticity. At high excitation Strouhal numbers, this results in the suppression of the dynamic stall vortex.

Figures

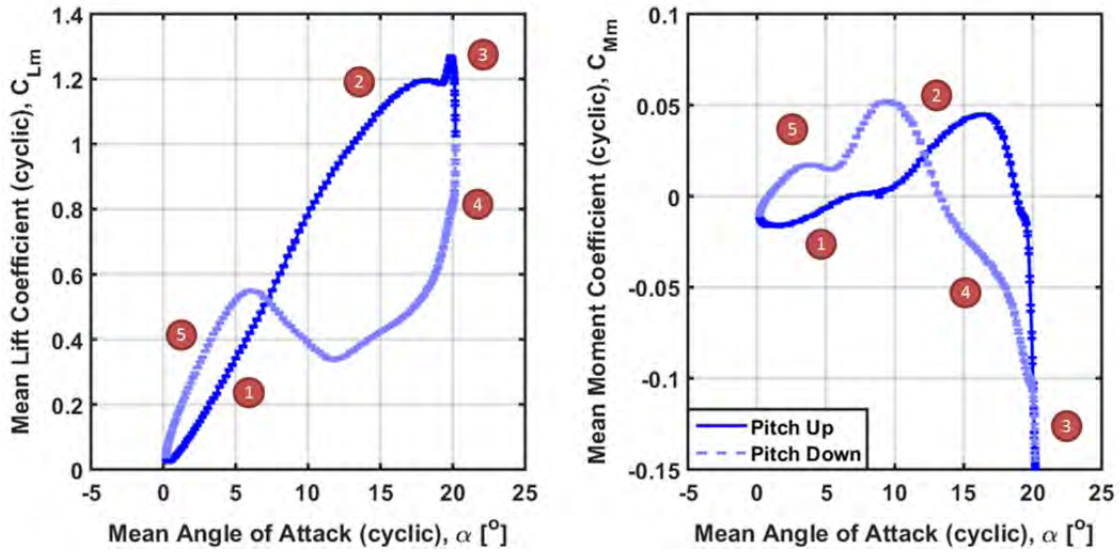


Figure 1. Baseline phase-averaged lift and moment coefficients at $Re = 300,000$ and $k = 0.050$.

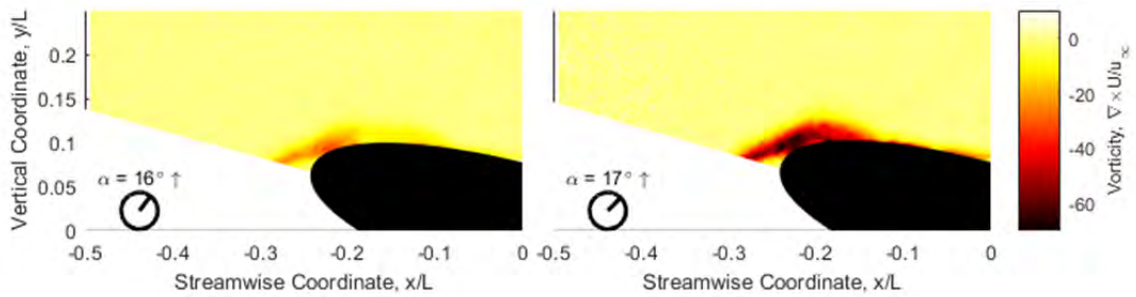


Figure 2. Close up of baseline phase-averaged vorticity maps at $Re = 300,000$ and $k = 0.050$.

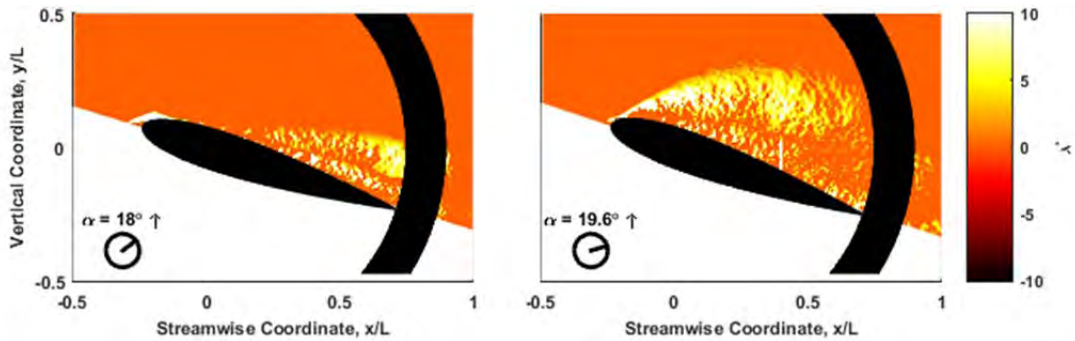


Figure 3. Baseline phase-averaged normalized swirling strength at $Re = 300,000$ and $k = 0.050$.

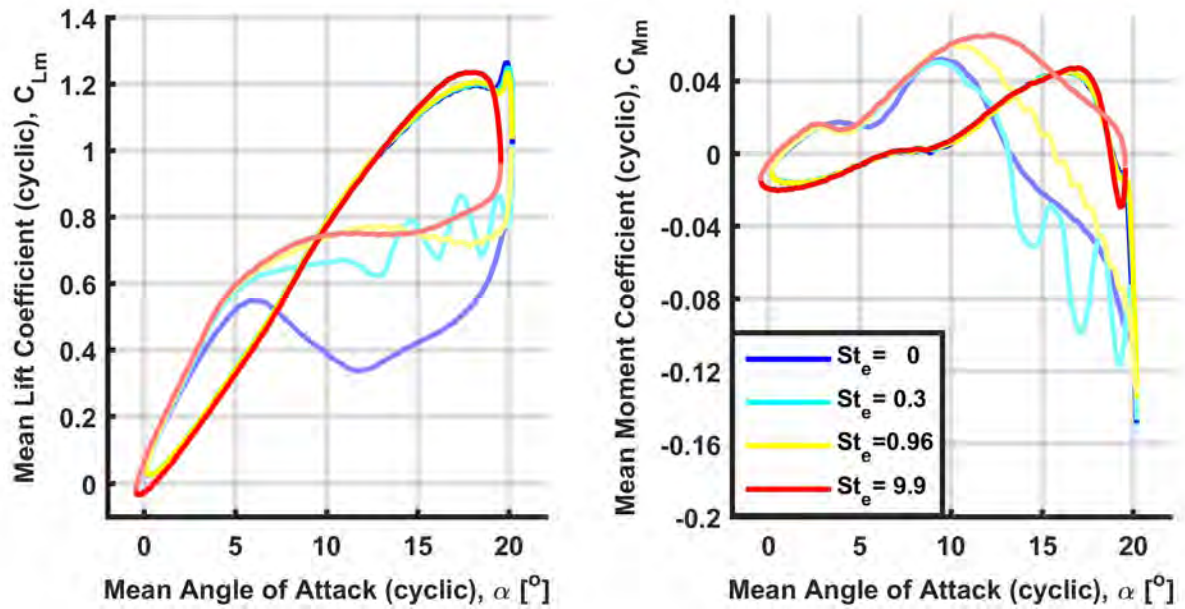


Figure 4. Phase-averaged lift coefficient and moment coefficient for various excitation Strouhal numbers at $Re = 300,000$ and $k = 0.050$.

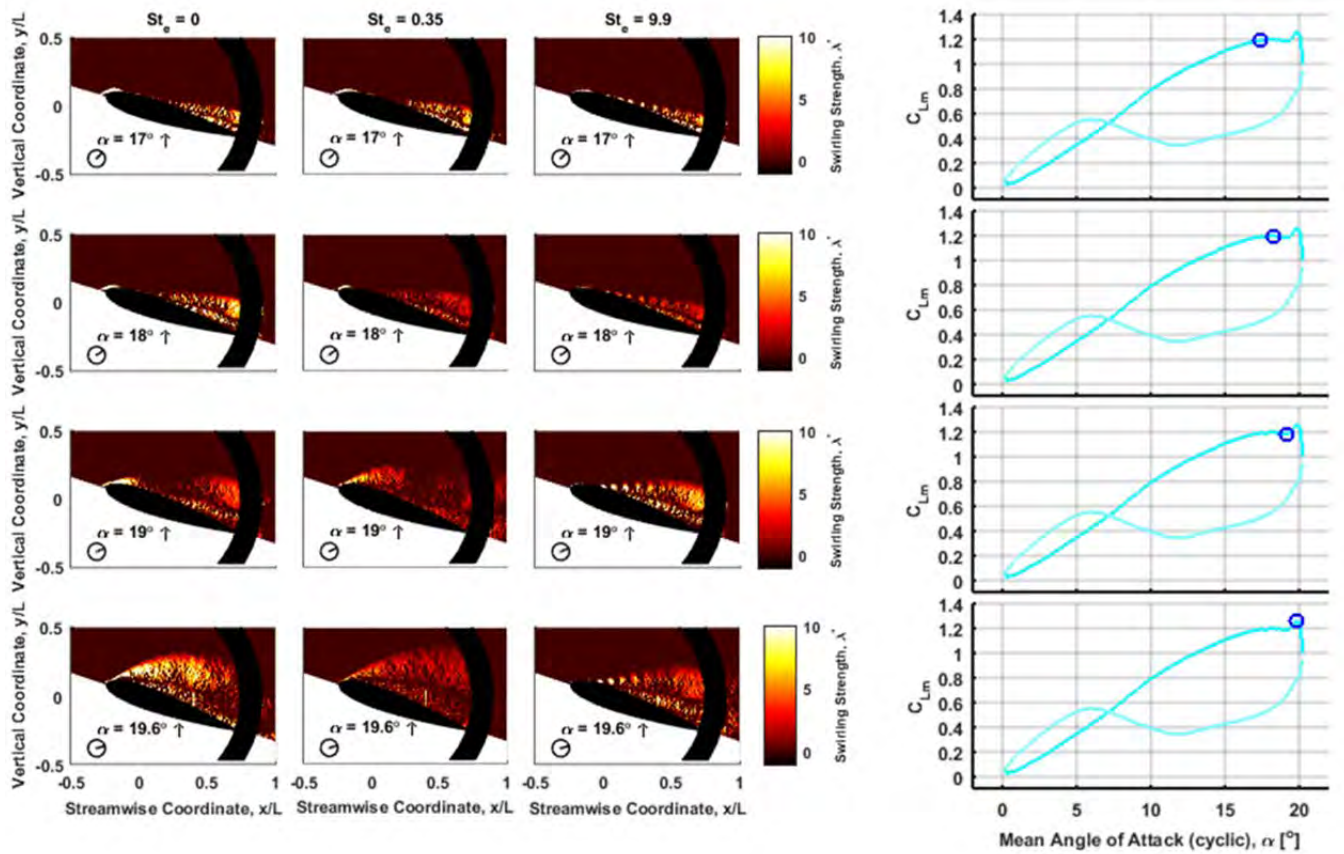


Figure 5. Phase-averaged normalized swirling strength at $Re = 300,000$, and $k = 0.050$.

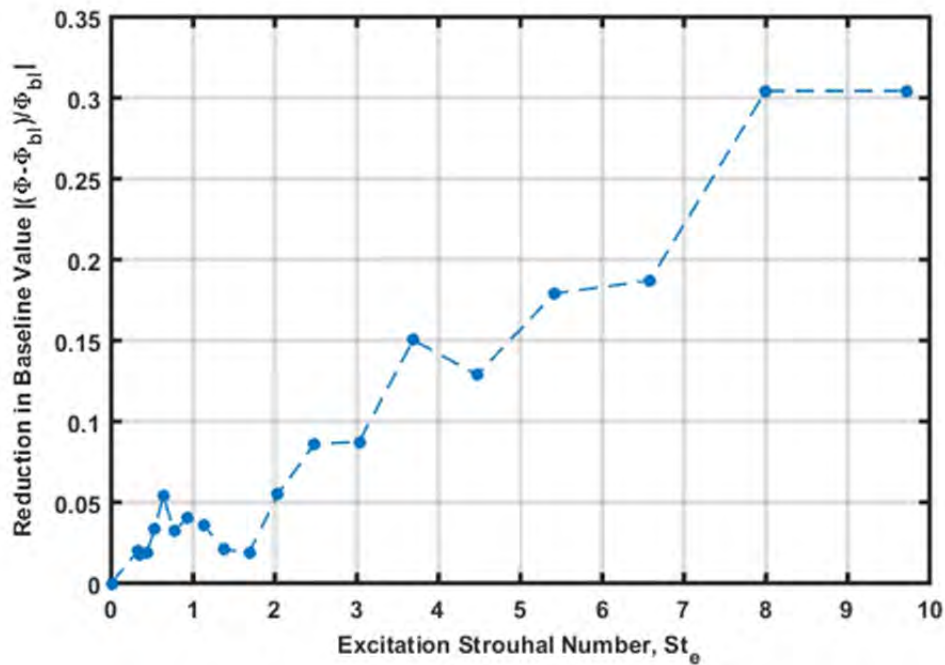


Figure 6. Reduction in moment stall versus excitation Strouhal number at $Re = 167,000$ and $k = 0.05$.

Acknowledgments

This study is sponsored by the AFRL Collaborative Center for Aerospace Sciences (CCAS) at the Ohio State Aerospace Research Center with Dr. Miguel Visbal. The fellowship support for Achal Singhal from the NASA/Ohio Space Grant Consortium is much appreciated.

References

1. N. D. Ham, "Aerodynamic Loading on a Two-Dimensional Airfoil during Dynamic Stall," AIAA Journal, vol. 6, no. 10, pp. 1927-1934, 1968.
2. T. C. Corke and F. O. Thomas, "Dynamic Stall in Pitching Airfoils: Aerodynamic Damping and Compressibility Effects," Annual Review of Fluid Mechanics, pp. 479-505, 2015.
3. C. Rethmel, J. Little, K. Takashima, A. Sinha, I. Adamovich and M. Samimy, "Flow Separation Control Using Nanosecond Pulse Driven DBD Plasma Actuators," International Journal of Flow Control, vol. 3, no. 4, pp. 213-232, 2011.
4. Singhal, "Unsteady Flow Separation Control over a NACA 0015 using NS-DBD Plasma Actuators," M.S. Thesis, Department of Mechanical and Aerospace Engineering, The Ohio State University, Columbus, 2016.
5. R. J. Adrian, K. T. Christensen and Z. C. Liu, "Analysis and Interpretation of Instantaneous Turbulent Velocity Fields," Experiments in Fluids, vol. 29, no. 3, pp. 275-290, 2000.

Wide Area Sampling Prototype

Student Researcher: Anthony Smoktonowicz

Advisor: Dr. Lesley M. Berhan

The University of Toledo
Electrical Engineering Technology

Abstract

The motivation for the project stems from a need in both environmental categories for a system that can conduct initial scans of an unknown contaminated zone and from the growing problems resulting from seasonal algal blooms. The robotics system is inspired by the dragonfly, which with its dual wing design is able to fly rapidly and has a high degree of mobility. The insect is able to hover and fly backward making its design very desirable for a mini aerial vehicle (MAV).

Project Objectives

The project involves the design, construction, and programming of an autonomous robot that utilizes the aerodynamic design of a dragonfly. This prototype is being designed with the intentions to be used as a first entry robot, plus to function in the agricultural arena as a chlorophyll scanner. The later has promise, giving farmers a more accurate determination of the status of the crop. This will in turn indicate when fertilizing is necessary, thus reducing cost and reducing over fertilizing resulting in runoff which promotes algal bloom formations.

Status of Project

The conversion from terrestrial to an autonomous flying drone created new challenges in the form of aerodynamics, collision detection, and coordinate location. Aerodynamics has presented more complications than this student researcher was initially aware. The features of lift, and thrust alone presented mathematics and engineering problems that afford new learning experiences. The second feature is the power systems; the size of the proposed MAV involves size issues that conventional battery power does not accommodate. The third feature is the motor action, traditional 5 volt to 24 volt motors are larger than the proposed prototype size, thus adding considerable weight to the prototype. The power consumption of the motors also adds an undesirable element for prolonged usage. Locomotion is the initial issue that is being addressed at this time. While still in the early stages, this project will develop as the student researcher continues the university education.

Locating Abandoned Wells; Using Historical Documents and Records with Practical Physical and Technical Methods

Student Researcher: Jennifer A. Starkey

Advisor: Professor Craig Rabatin

Marietta College

Department of Petroleum Engineering and Geology

Abstract

Abandoned oil and gas wells can be found anywhere drilling for oil and gas has occurred, but can often be difficult to locate. ODNR estimates that 270,000 wells have been drilled in Ohio in the past 150 years with 49,000 currently in production across the state. Since 1977, when the Orphan Well Program started, Ohio has been plugging 40-50 old wells per year. At this rate it would take over 500 years to plug only 10% of the wells drilled in Ohio. Current standards require that wells not producing at an economical rate be plugged but in the early days of the oil and gas industry, these wells were simply loose ends due to lack of standards and became orphaned. With such a large volume of orphaned and abandoned wells, ODNR does not have the man power to efficiently find and plug all the wells that need attention. An efficient method for locating problematic abandoned wells needs to be designed. This paper highlights methods to locate orphaned and abandoned wells in Ohio using historical documents and records with practical physical and technical methods with a focus on drone based magnetometry.

Objectives

Even though the regulations and documentation of oil and gas wells has become stricter over the years, older wells have fallen off the map. It is estimated that 270,000 wells have been drilled in Ohio in the past 150 years with 49,000 currently in production across the state. Some orphaned wells go back more than 150 years, were improperly abandoned and discovered decades later, when the companies that drilled them no longer exist. The Orphan Well Program was established in 1977 to plug improperly abandoned oil and natural gas wells. Funded by a portion of the Ohio state tax on oil and gas production, Ohio's Orphan Well Program has plugged over 2000 wells. Even though it is recognized as one of the best in the nation, with such a large volume of abandoned wells across the state, ODNR does not have the man power to efficiently find and plug all the wells that need attention. An efficient method for locating problematic abandoned wells needs to be designed.

Methodology

There are many different methods for locating wells, including using historical documents and records combined with physical and technical methods. This paper focuses on locating specified abandoned wells that are known to exist in a specific area. Technical methods are suggested when looking over broader areas.

Surveying People

The best way to quickly find an abandoned well is to talk to people who might have come in physical contact with it. This includes landowners and people inside the petroleum industry. Landowners or people inside the petroleum industry might have stumbled upon the well or might have personal records of old well locations. Other people to ask are production/operation supervisors that are active

on or around the specific area. It is also likely that a company active in the area may have already looked for old wells near their drilling locations.

State Records

Currently, states require drilling permits and records on the precise well location. These practices were only established in most states during the 1930s to the 1980s. Now all drilling permits and leases are documented in the respective county. County records also include tax assessments, ownership records, survey maps, and chain-of-title records. These records are not commonly online and can be tedious to search through. It is also possible for an older well to not have an official paper trail. In this case, other documented wells can be helpful because the configuration of known wells will often reflect those of undocumented wells. Most wells drilled in a certain area will reflect the wells drilled around them. Even after a well is located, this type of in-depth research must be conducted to determine if the well has a fiscal party or not.

Historical Records

Historical photos, maps, and company records are sometimes in local museums or library collections. Most maps of older wells are hand drawn, as they were drilled, mapped and abandoned before computers. These can give a general idea where wells were once drilled but will not be entirely accurate. Company records are also usually more complete and better documented than county or state records. Company records are harder to find but could also include “potentially drilled” wells which might have been drilled but never reported. Old photos could show the surrounding buildings or landmarks in relation to where the well head would have been. Some old wells might still have the derrick intact above the well head after completion. Historical aerial photographs from the 1930s to the present are available from Federal, USGS, State and county agencies and private companies.

Physical Methods

There are many different physical (non-technical or research) methods to find an abandoned well if it is known where one or more should exist on a reasonably-sized portion of land. After conducting research to narrow down the search area, visual inspection is required to determine the well’s exact location.

Manual Labor

Using volunteers or hired employees to physically walkthrough the area of interest while using line-of-sight is a straightforward method. This is best done when vegetation is low so the ground is visible. The most visible paraphernalia associated with well sights are abandoned production equipment, metal pipes sticking out of the ground with or without surface equipment or well head, concrete well pads, or wooden casing sticking out of the ground. Open wellbores at the surface can range from 5 inches to 24 inches in diameter. Unfortunately, surface equipment will not be present at all well sites as it could have been removed for scraps. Also, over time, the well head could have been buried under sediment or natural debris.

Surface Indications

ODNR lists physical signs for polluting wells as: water containing salt, oil or natural gas, areas where vegetation won’t grow and natural gas odors. Water characteristics are affected as well; salt might prevent water from freezing and oil will present as a rainbow sheen on the water’s surface. Not all abandoned wells are currently polluting the area around/above them, so there isn’t always an obvious way to know that a well exists. Using volunteers or hired employees to physically walk through the area of interest while using line-of-sight is best done during seasons when vegetation is low so the majority of the ground is visible. Abandoned production equipment, metal pipes, surface equipment, a well head

or concrete well pads stand out. Open wellbores at the surface can range from 5 inches to 24 inches in diameter. Unfortunately, surface equipment might not be present at all well sites as it could have been removed or buried under sediment or natural debris.

Technology

There are many technical methods to locate abandoned wells, but most require an experienced lab technician to run equipment and interpret data and are only applicable if the search area is very small. These are a few practical technologies that can aid in determining location.

In a small area, a chemical sniffer can be used to confirm the location if there is a methane leak. Chemical sniffers are handheld devices that detect specific amounts of chemicals in the air. This reveals how dangerous or polluting the well is. Many well programs, such as ODNR's Orphaned Well Program, use chemical data to determine how immediately the well needs to be plugged. A hand metal detector can also locate a well head or metal debris if it cannot be found by visual inspection alone. These methods are useless if there is no surface presence of the well, but are the cheapest and easiest technical methods available.

Magnetometry

A magnetometer finds magnetic anomalies in relation to the earth's magnetic field. Magnetometers can be boom mounted on a helicopter, built into a special drone or can be carried on a person's back. Aerial magnetometers can locate buried well casings, cover a large area, and have a relatively low cost compared to other methods. This method would be best used in a rural setting where the search area is too large to be done by foot. Helicopters can be expensive and have to be rented for every use, while a drone can be purchased if commercial use is desired. Backpacks are of use too, but limit an area that can be checked on foot.

The key factors with using magnetometers to locate well heads are the range and quality of the equipment being used and the background magnetic noise caused by the landscape and geology of the area. There are many naturally occurring magnetic signatures, as well as other sources of magnetic material, including trash, pipelines, debris, sediments, buildings and manmade features. This can be good if the material found is a pipeline or discarded surface equipment that will lead right to the well head, but more often than not, it will distort the exact well location.

Results

Not every abandoned well is a threat, but many were plugged with lower standards than are required today or not plugged at all. When undocumented, these wells need to be located so they can be assessed and cataloged. The biggest problem of past regulations is the same as the one that is faced today. The industry rapidly evolves over time and standards need to be in place to accommodate whatever can happen down the road. Before more problems are created, the old ones need to be cleaned up by locating, documenting and plugging old abandoned wells that are missing from public databases.

As many of these wells need to be found as possible, this paper highlights more straightforward methods that can be practically applied. The main methods for location are searching through records for documentation or using physical methods to find the actual well. Both methods can be used practically and either recreationally or commercially.

Significance and Interpretation of Results

The danger imposed by oil and gas wells is immense during the life of a well, and continues after the well is plugged. Abandoned and plugged wells still have fluids, pressure and risks associated with them. Unplugged and improperly plugged wells can leak methane and other natural gases into the atmosphere. Since these wells are not monitored, the amount of gas potentially leaking is unknown but is significant because of the vast number of known abandoned wells across the country. Other pollutants are oil and brine water, both of which can kill vegetation and harm wildlife. The uncontrolled release of hydrocarbons into the environment can be catastrophic and should be reduced as much as possible.

Acknowledgments

Thank you to Professors Rabatin and Ebenhack for their help and guidance throughout this project and thank you to the OSGC for giving me the chance to present my research.

References

1. Abandoned Well. PetroPedia.com, <https://www.petropedia.com/definition/4365/abandoned-well>. September 10, 2016.
2. Arthur, J, Hoschheiser, H. 2011. PLUGGING AND ABANDONMENT OF OIL AND GAS WELLS. Working Document of the NPC North American Resource Development Study Made Available September 15, 2011.
3. Jordan, P, Hare, J. 2002. Locating Abandoned Wells: A Comprehensive Manual of Methods and Resources. No. 2002-1-SMRI. Solution Mining Research Institute. June, 2002.
4. Orphan Well Program. <http://oilandgas.ohiodnr.gov>, <http://oilandgas.ohiodnr.gov/orphanwellprogram>. September 10, 2016.
5. The Well Plugging Program. Pennsylvania Department of Environmental Protection <http://files.dep.state.pa.us/OilGas/BOGM/BOGMPortalFiles/AbandonedOrphanWellsWellPluggingProgram.pdf>. September 10, 2016.
6. Williams, M, Matthews, C, Garza, T. 2011. Well Plugging Primer. Railroad Commission of Texas, January, 2000.

The Earth, Sun, Stars, and Math?

Student Researcher: Lindsey A. States

Advisor: Dr. Todd Edwards

Miami University

Mathematics and Education Department

Abstract

This lesson connects Common Core State Standards for geometric proofs with NASA resources to provide a rich and intellectually challenging problem for high school students. Students will be asked to discuss the direction of the setting sun, moon, and stars in both a scientific and mathematical context. Students will be encouraged to research this topic with various NASA websites and search engines. The lesson helps students understand that Earth rotates from west to east, but the sun, moon and stars and planets rise in the east and set in the west. Students can prove this scientific fact utilizing geometric theorems and properties gleaned from the standard high school mathematics curriculum. Some review of proof-writing and theorems may be required to ensure the successful completion of this activity. Students will collaborate in groups of four to construct a geometrically correct proof. These groups will then work together to turn their proof into a mathematical argument supported with scientific facts discovered earlier in the lesson. Groups will present their arguments and mathematical proofs to the whole class. During this time, other students will have the chance to evaluate their peers' work and provide feedback, promoting greater conceptual and procedural understanding amongst students.

Alignment

This lesson was created to meet the following Common Core Standards:

CCSS.MATH.CONTENT.HSG.GPE.B.5

Prove the slope criteria for parallel and perpendicular lines and use them to solve geometric problems

CCSS.MATH.CONTENT.HSG.C.A.2

Identify and describe relationships among inscribed angles, radii, and chords.

CCSS.MATH.CONTENT.HSG.SRT.B.5

Use congruence and similarity criteria for triangles to solve problems and to prove relationships in geometric figures.

Methodology

This lesson follows a constructivist philosophy as it focuses on students' use of prior knowledge to generate their own unique conclusions. During the introductory portion of the lesson, students share initial conjectures based primarily on personal beliefs regarding sunrise and sunset. Next, students explore the plausibility of their initial opinions as they craft final arguments, defending or revising their positions based on scientific research. As students begin to form more nuanced views about the direction of the sunrise and sunset, they are encouraged to use online resources to check their hypotheses. Research indicates that students who participate in online learning are more engaged with the material and work in a more self-directed manner (Delen, Liew & Wilson, 2014)¹. Online research also promotes active construction of knowledge. This lesson encourages students take control of the problem and construct a proof that satisfies their own curiosity. The added element of researching NASA

¹ Delen, E., Liew, J., & Willson, V. (2014). Effects of interactivity and instructional scaffolding on learning: Self-regulation in online video-based environments. *Computers & Education, 78*, 312-320.

materials encourages the class to complete the task in a manner that makes sense to them individually. Students will be posed with an initial question, time to research their hypotheses, and directions to form a geometric construction. Together with peers, students will work to form a sound argument to answer the overarching question for the lesson.

Materials Needed

- Paper
- Pencil
- Compass
- Ruler - straight edge
- Construction worksheet
- Large sheets of paper to hang on the wall
- Markers
- 1 mobile learning device per group

Lesson

Day 1: To introduce this cross content lesson to students, pose the following question: *In what direction does the sun set? In what direction does the sun rise?*

For many students this is foundational knowledge. Students who are not sure of the answer will be provided with time to research an answer using a mobile learning device. Once the class has come to a unified response, ask the following question: *In what direction does Earth rotate?*

This is likely a more difficult question for students. They are encouraged to use NASA websites that are listed on the board to further explore this question. As students begin to discover the correct answer, they are asked a final question.

Guiding Question: *Is it logical that the Earth rotates from west to east, but the sun, moon, stars and planets rise in the east and set in the west?*

Students are allowed time to ponder this question in small groups. As groups begin to form opinions on the question, they are asked to form a hypothesis in response to the guided question. Once a group has formed a hypothesis and written it down for later consideration, they are provided with a worksheet that guides them through a geometric construction. For the remainder of class, students work in groups to complete the construction. These constructions will test students' understanding of how to construct various geometric elements including a line, ray, circle, and parallel lines. These constructions will be used in subsequent classes to further explore possible solutions to the guided question.

Day 2: The second day of the lesson consists of mathematical proof and the collaborative journey towards a solution to the problem at hand. Prior to this lesson, students have learned theorems and have constructed two column proofs similar to one that could be used to solve the guiding question. Students are encouraged to return to their previous groups and compare their constructions. The class will then be asked how this construction could help them support their hypotheses. Students will be encouraged to use their construction to form a mathematical proof. A worksheet with guided questions is provided to students to assist them. The remainder of class will be spent completing the proof and turning it into a supporting argument for each group's hypothesis.

Day 3: On the final day of the lesson, students compile mathematical proof with research from NASA resources to produce a final answer to the guided question. Groups are given chart paper to outline their responses to the prompt with supporting evidence. Students are provided with additional time as needed for supplemental NASA research. Each group will present their findings to their classmates. Facilitating conversations challenges students to consider their arguments more deeply than possible with a written proof alone, affording students the chance to challenge and question their peers. Groups explain their hypotheses, how they completed the geometric proofs in words rather than table format, how research found through NASA supports their arguments, and finally if their hypotheses were correct or incorrect. This experience ensures that students are able to discuss the mathematics and research that they completed relating it to a real world application.

Conclusion

Throughout this proof based lesson, students were able to review their knowledge on geometric constructions and proofs. Often times students complete two column proofs in geometry but are unable to explain what they truly mean. This lesson resulted in students having a deeper understanding of the math that was taking place in each groups' geometry based proof. Additionally, students were exposed to research using NASA resources to obtain accurate results. This allowed students to gain valuable research skills while also exposing them to a new resource. This cross content lesson encouraged students to see math in a real world scenario while challenging them to apply their math knowledge and problem solving skills to a task they had never seen before.

References

1. Delen, E., Liew, J., & Willson, V. (2014). Effects of interactivity and instructional scaffolding on learning: Self-regulation in online video-based environments. *Computers & Education, 78*, 312-320.

Inundated Destinations: An Analysis on Sea Level Rise in Puerto Rico and the US Virgin Islands

Student Researcher: Lydia E. Tamburro

Advisors: Lisa Stanich, Mark Guizlo

Lakeland Community College
Geography and Geospatial Technology

Abstract

The Caribbean is susceptible to sea level rise, and it would affect much of the commercial resorts throughout Puerto Rico and the US Virgin Islands. By mapping resorts I will display a visual presentation of potential land loss due to sea level rise. The analysis will exhibit the severity of a 3 foot and 6 foot sea level rise impact in the study areas.

Project Objective

My project objective is to locate areas of commercial resorts in Puerto Rico and the US Virgin Islands using ArcGIS. By importing shapefiles into ArcGIS from NOAA, I will create a simulation map of a 3 foot and 6 foot sea level rise. After creating the simulation map, I will overlay the map of resorts displaying potential negative impact on these resorts' beaches, lodging, and transportation infrastructure.

Methodology

I gathered tourism data from The Caribbean Tourism Report to find the number of non-cruise travelers visiting Puerto Rico and the US Virgin Islands (Business Monitor International 2017). In the Caribbean Tourism Report, I found that Marriott resorts were prominent amongst the two islands. Using Google Earth, I was able to identify the latitudes and longitudes of each resort. I created an excel spreadsheet with the resorts x and y coordinates and transferred the data into ArcGIS. In ArcGIS, I input shapefiles of a 3 foot and 6 foot sea level rise found from NOAA (NOAA, Office for Coastal Management 2017). I overlaid the sea level inundation shapefiles onto the map of these resorts in ArcGIS to classify which resorts would be affected due to a 3 foot and 6 foot sea level rise. To range levels of inundation I used a numerical scale of one to three: one being no inundation, two being partial, and three being fully inundated. I created a stacked bar graph in PowerPoint to display inundation levels for each of the resorts and their beaches. I used a side by side graph to use as a visual comparison between a 3 foot and 6 foot sea level rise. With Google Earth I was able to find the resorts commercial airlines and the most direct routes to the resorts from the airports. I displayed the impact on transportation infrastructure in concentrated areas of resorts in San Juan and St. Croix using the map I created in ArcGIS. These images exhibit routes and access roads that are affected at a 3 foot and 6 foot sea level rise.

Results Obtained

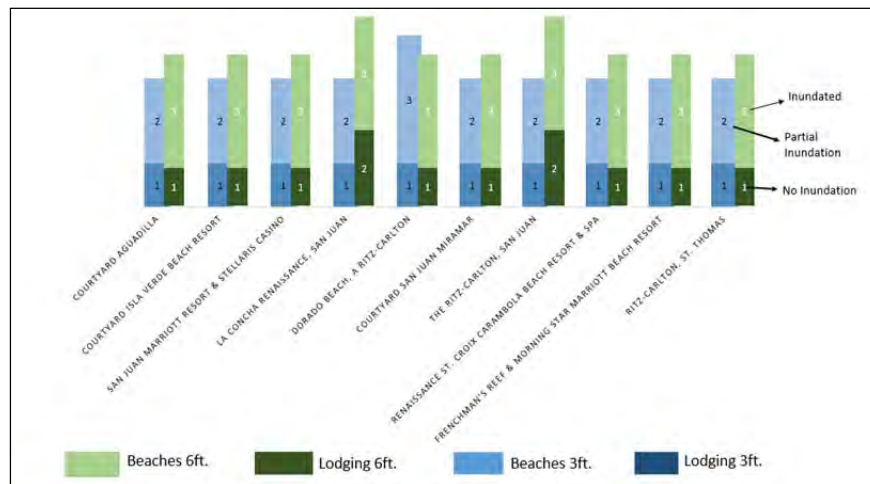
Projections show that infrastructure is significantly impacted by a 3 foot and 6 foot sea level rise. In San Juan, Puerto Rico routes: 17, 26, and 187 all see inundation at these levels. Route 26 is a direct route to the San Juan Marriott, La Concha Renaissance, and the Courtyard San Juan Miramar. Route 26 becomes partially inundated at a 3 foot rise and fully inundated at a 6 foot rise causing these three resorts to become estranged from the rest of the island. In St. Thomas, route 30 is the direct route from the Cyril E. King International airport to the Frenchman's Reef & Morning Star Marriott and the St. Thomas Ritz Carlton. Data shows route 30 becomes inundated at a 6 foot rise. In PowerPoint, I created a stacked chart displaying an inundation scale for beaches and lodging ranging one through three: 1- no inundation, 2-partial inundation, and 3- inundated. This graph is a comparison of impact to the resorts'

beaches and lodging at both a 3 foot and 6 foot sea level rise. Most of the resorts were not directly affected excluding the La Concha and Ritz-Carlton in San Juan seeing partial inundation. The beaches of these resorts all saw partial to full inundation at a 3 foot and 6 foot sea level rise. Some of the resorts sit close to the shore line and are severely at risk. I included a couple images of the La Concha in San Juan and the Ritz-Carlton in St. Thomas to give a visual of their proximity to the shoreline.

Significance and Interpretation of Results

Sea Level Rise is attributed to many things including greenhouse gasses, thermal warming, and melting glaciers. Predictions of sea level rise range from 0.2 meters to 2 meters. These figure assumptions are predicted for around the year 2100 (NOAA 2017). NOAA shapefiles of sea level rise projections overlaid on top of resort locations displayed significant negative impact to these resorts affecting their lodging, beaches, and transportation infrastructure. The analysis gives a clear projection of what might be if we do not assume action in reducing our carbon imprint.

Inundation Comparison Graph: Lodging & Beaches



References

1. Business Monitor International, *Caribbean Tourism Report*, 2017 Q1, pp. 1-47. EBSOhost. Web. 6 Dec. 2016.
2. NOAA, Office for Coastal Management. "Sea Level Rise Viewer." www.coast.noaa.gov. Web. 15 Jan. 2017.
3. NOAA, *Global and Regional Sea Level Rise Scenarios for the United States*, 2017, pp. 1-75. www.tidesandcurrents.noaa.gov. Web. 20 Mar. 2017.
4. Ritz-Carlton St. Thomas. *Ritz-Carlton, St. Thomas Resort*. 2014, www.nodestinations.com.
5. Julie, Karen. *La Concha Resort*. 2014, www.xtns.org.
6. La Concha Renaissance. *La Concha Resort*. 2016, www.laconcharesort.com.

A Comparison of the Efficiency of Two Types of Experimental Photovoltaic Cells

Student Researcher: Nicholas Z. Tolbert

Advisor: Joseph Arendt

Cuyahoga Community College
Engineering Technology

Abstract:

Using a Spectrolab X-25 solar simulator I created an environment in which I could test photovoltaic cells at an irradiance level equal to space. Using the data acquired from the tests along with the measurements of each cell I found the average maximum power of the TJC (Triple Junction Cell) to be 2.22 W and the SW (16 cell Silicon wafer) was 4.22 W. Using two equations to solve for their fill factors and efficiencies I found that the average TJC efficiency was 37.2% while the average for the SW was 17.3%. This means that my average efficiency of the TJC is above the stated value of 27.7% [4] by 34.3%. The efficiency of the SW is closer to a stated value of 18% [3].

Materials and Methods

First, I set up the Spectrolab X-25 and the program used to gather the data. The photovoltaic cells were then placed and secured inside the machine to be individually tested. Each cell was charted by voltage and current to plot the change in power. From these charts, it was then possible to find the maximum power (P_m) by taking the Graphs from the middle of the curve where the product of the current and voltage is greatest. The fill factors (FF) was then calculated through the equation [1, 3]

$$FF = \frac{P_m}{V_{OC} I_{SC}}$$

where the V_{OC} or the open circuit Voltage found where the current is equal to zero and the I_{SC} (Short Circuit Current) is found at the point where the voltage is zero. Using the fill factor, it was then possible to find each cells efficiency with the equation [1, 3]

$$\eta = \frac{FF * V_{OC} * I_{SC}}{A_C * G} * 100\%$$

as η is efficiency, G is 0.1 W/cm^2 the irradiation of the earth atmosphere, and A_C is the area of the cells. The area of the TJC were 59.65 cm and the SW were 243.36cm. The efficiencies for the TJC and SW were 37.2% and 17.3% respectively. Finally, I used the EduPack database to search the availability of each of the elements used in the photovoltaic cells to determine the rarity and thus level of cost in the cells.

Results

Graphs 1 and 2 show the current vs. voltage figure of the SWs used to find the fill factor and efficiency using the area of the cell and an irradiance of 0.1 W/cm^2 to simulate earth's atmosphere. The graphs of 3 – 6 were used to find the efficiency for the TJC. After calculating I found that while the TJC efficiencies were within a 40% error they exceeded the manufacturers efficiency level of 27.7% meaning that an error is likely to have been made. This is possibly due to the experimental irradiation settings used in the Spectrolab X-25 or an increase in one of the TJC's data values. However, the proximity of the SW's efficiency, 17.3%, to the known value of silicon wafers, 18%, disputes this conclusion. This means that

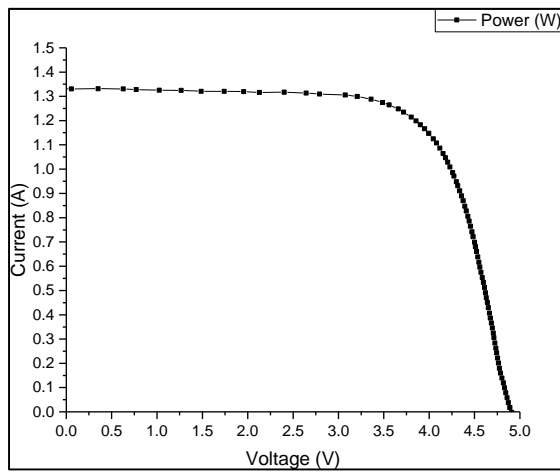
the discrepancy may be due to differences in testing environments between the production company and mine.

Conclusion

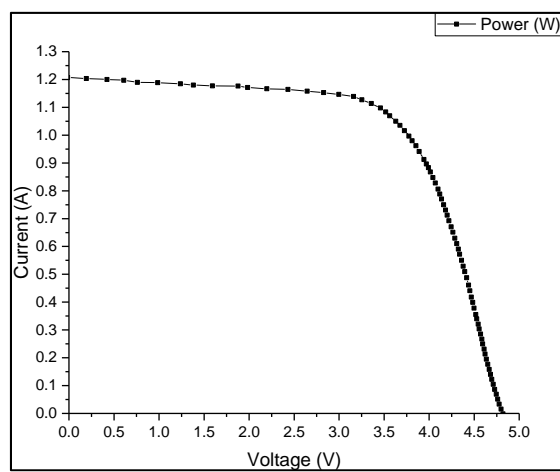
The experimentally measured efficiencies of TJC was 37.2% and SW was 17.3%, showing the TJC was 2.14 times more efficient. The reported specifications for TJC were 27.7% so this experiment had an error of 34.3% with the experimental measurement being more efficient. The reported specification of SW was 18% so this experiment had a small error of only 3.74% . Perhaps for TJC, the specifications are a minimum to be expected. While the TJC was 2.14 times more efficient experimentally than SW, it was 1.54 times by the specifications, so TJC is considerably more efficient than SW.

Figures and Charts:

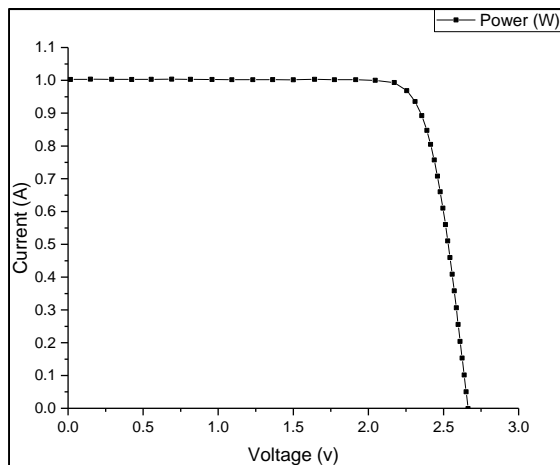
16 Cell Silicon Wafer Test 1



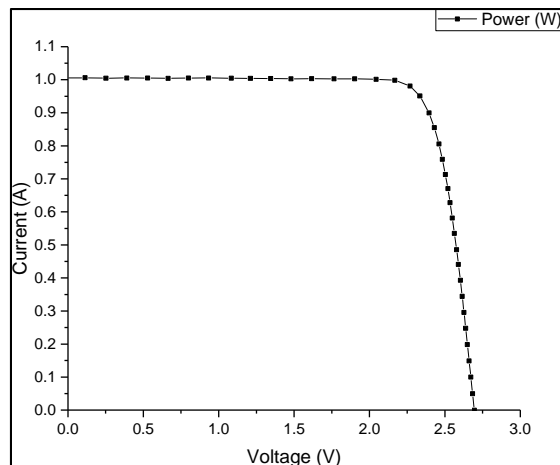
16 Cell Silicon Wafer Test 2



Triple Junction Cell Test 1

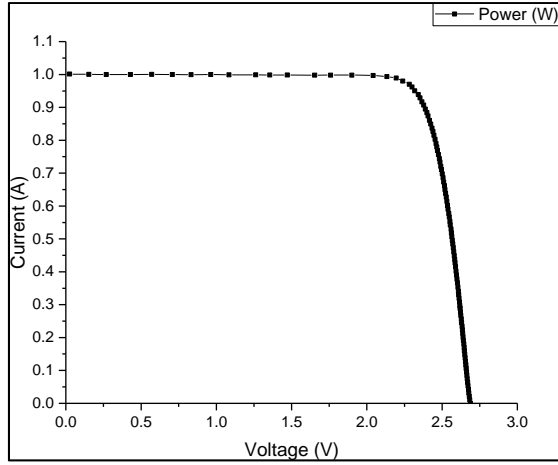
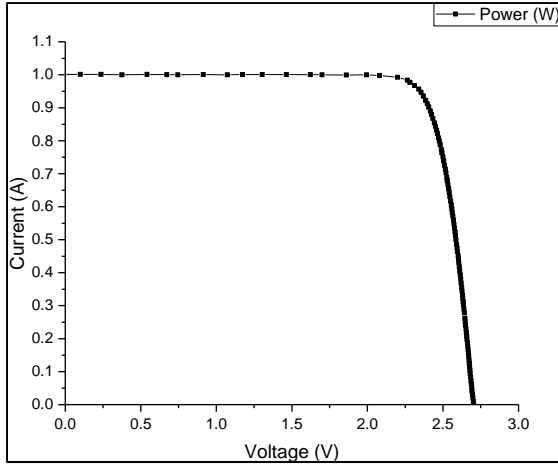


Triple Junction Cell Test 2

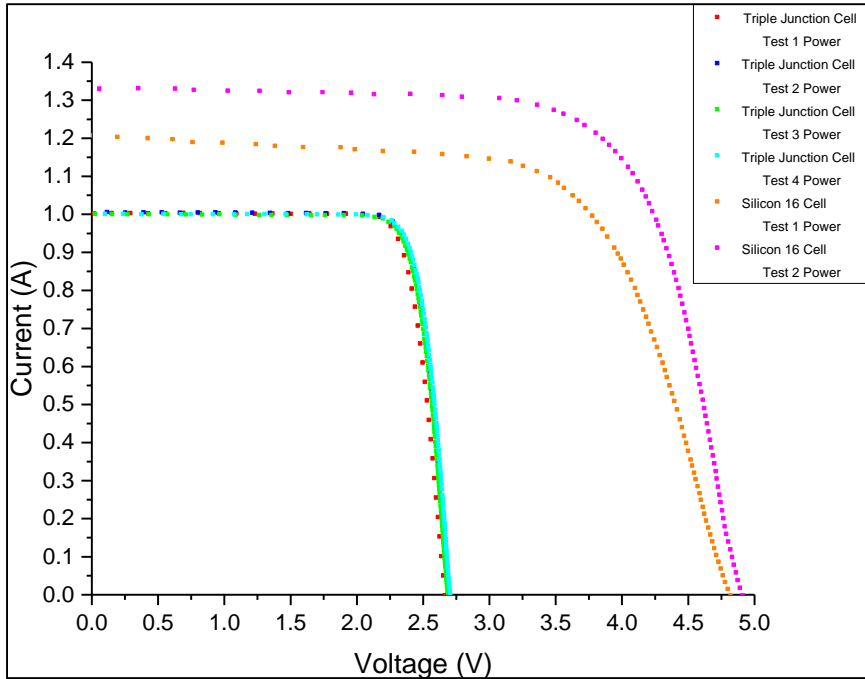


Triple Junction Cell Test 3

Triple Junction Cell Test 4



Voltage vs. Current Cell Test Comparison



Data

	Current (A)	Voltage (V)	Max Power (W)	Fill factor (W/AV)	Area (cm ²)	Efficiency (%)
TJC Test 1	1.00499	2.66401	2.18487	0.81607	59.65	36.62816
TJC Test 2	1.00594	2.69593	2.22622	0.82089	59.65	37.32137
TJC Test 3	1.00143	2.68422	2.21512	0.82406	59.65	37.13529
TJC Test 4	1.00143	2.70144	2.23834	0.82739	59.65	37.52456
--	--	--	--	--	--	--
SW Test 1	1.20757	4.79882	3.81163	0.65775	243.36	15.66252
SW Test 2	1.33296	4.88968	4.62185	0.70912	243.36	18.99182

Acknowledgments

I would like to thank Professor Arendt and Timothy Peshek for their support and guidance throughout this project.

References

1. Wikipedia contributors. "Solar cell efficiency." Wikipedia, The Free Encyclopedia. Wikipedia, The Free Encyclopedia, 17 Mar. 2017. Web. 22 Mar. 2017.
https://en.wikipedia.org/wiki/Solar_cell_efficiency
2. Wikipedia contributors. "Solar simulator." Wikipedia, The Free Encyclopedia. Wikipedia, The Free Encyclopedia, 28 Sep. 2016. Web. 22 Mar. 2017.
https://en.wikipedia.org/wiki/Solar_simulator
3. A. Khanna, T. Mueller, R. A. Stangl, B. Hoex, P. K. Basu, and A. G. Aberle, "A fill factor loss analysis method for silicon wafer solar cells," *IEEE J. Photovoltaics*, vol. 3, no. 4, pp. 1170–1177, Oct. 2013.
4. 28.3% Ultra Triple Junction (UTJ) Solar Cells. Spectrolab, Inc, 2010.
5. Green M. A., Emery K., Hishikawa Y., Warta W., and Dunlop E. D. (2014) Solar cell efficiency tables (Version 45), *Prog. Photovolt: Res. Appl.*, 23, 1–9, doi: 10.1002/pip.257

Self-Sustaining Ecosystems

Student Researcher: Emily D. Tornes

Advisor: Dr. Cathy Mowrer

Marietta College
Department of Education

Abstract

I will be using the idea of ecosystems as the basis for my project with 3rd grade students at Harmar Elementary School. The project will begin with several days of introduction and lessons on ecosystems and the vocabulary language that is associated with it. In addition to learning about ecosystems, the students will also be learning about food chains and self-sustaining ecosystems, as well as, brainstorming ideas to create an ecosystem on the moon. The lessons will consist of whole class instruction, small groups, and individual activities. As a class, we will read an article, “The Ecosystem of the Forest,” and then answer some comprehension questions together. We will also work as a whole class to define the new vocabulary and think of ways to help us remember the words. In small groups, we will use the “Ecosystem Investigation” from the NASA lesson plan “Field Trip to the Moon.” To conclude the lesson, we will build a model of a self-sustaining ecosystem.

Project Standards and Objectives

1. OH-2003.ELA.K-12.4: After reading “The Ecosystem of the Forest,” students will be able to answer comprehension questions and use the information to create/draw diagrams of an ecosystem on the lunar station.
2. US-CC-ELA-2010.L.K-5.ANCHOR.6: After repeated exposure to vocabulary, students will use the words in their expressive vocabulary to answer questions and explain their model ecosystems for the moon.
3. OH.SC.3-5.2: After sorting the organism cards from “Field Trip to the Moon,” the students will be able to explain how organisms rely and interact with one another. Students will also be able to describe how the organisms interact within their lunar station ecosystem and the self-sustaining ecosystem that they built.

Lesson

The basis for this activity came from the “Field Trip to the Moon” lesson contained in NASA’s Educator Guide. I chose not to do the entire lesson, rather focus specifically on one area, ecosystems. The lesson is designed for fourth or fifth grade students, but I am teaching third grade. I felt that the activity could still be completed with proper scaffolding and accommodations. Instead of teaching this lesson out of context, I decided to embed the science concepts into my reading lesson for the week.

Before we dug deep into the lesson, I had to begin explaining the difficult vocabulary. I added the following the words to our word wall: *organism, producer, consumer, decomposer, and ecosystem*. After establishing vocabulary, I read “Ecosystem of the Forest” to my students as a whole group. As we came to points in the text with vocabulary, we would stop and talk about the definition. I also asked comprehension questions throughout. The students then read the story in small groups, with a teacher there to help answer questions. The teacher acted as the facilitator and guided the students by asking questions that would help them understand the material. Homework was given to students, as well as,

a sheet of the words with the definitions. The sheet was kept in their take home folder and studied each night.

On day two, the vocabulary was reviewed. The students individually read the article and answered comprehension questions. Students were given vocabulary homework boxes in which they had to put the word, definition, sentence, and a picture within the boxes.

Day three, students returned to their groups and sorted the organism cards found in the “Field Trip to the Moon” lesson plan. Students were given a poster with three columns labeled, *producer*, *consumer*, and *decomposer*. Students were given various organism cards and had to explain why they wanted to place the organism in the certain category. We then reviewed the vocabulary words and the food chain that I created on an anchor chart for the students. Students thought of ways to remember the different words. We then brainstormed our ecosystems for the lunar station. I guided students to think about the ecosystem that we live in and what we need for survival. We started by talking about the types of organisms we would need. We discussed why we would need an ecosystem with all three organisms in it and how they related to one another. Students began to create a class list of the organisms that they wanted. After we had a list of the organisms, I explained that for homework we would write the vocabulary words in sentences. Students had to include context clues within the sentence to help define the word.

On the last day of the lesson, I had students create posters of their ecosystems on the lunar station. Students had to write a list of producers, consumers, and decomposers on the side and then draw their ecosystems. By having students in groups, they had to discuss the best organisms for their ecosystems. They had to think of the necessities for humans rather than just including organisms for no reason. After posters were created, we discussed how they decided what they would include in their ecosystems. This led to the discussion about food chains and the interaction amongst organisms. We moved onto the creation of our self-sustaining ecosystem. Students were unfamiliar with the words self-sustaining, so we had to clear this confusion up. Moving on to the experiment, we set the area up in a “fishbowl.” Some students sat in chairs, while others stood behind. As we discussed the steps to build the ecosystem, I called on various scientists to help complete each step. Students were very excited and loved the activity. As each layer was added, we discussed why we included the organisms and materials. I encouraged students to use vocabulary in a meaningful way. After we were finished, the student scientists went back to their seats and completed a vocabulary quiz.

Results/Interpretations

Students did extremely well with the vocabulary quiz. Only 3 out of the 21 students did not get a 100% on the quiz. By the end of the week, many of the students were able to define all five vocabulary words and did an excellent job incorporating it into their expressive vocabulary. Numerous times throughout the lesson, I did not have to prompt students to use the vocabulary; rather they used it on their own. Students also came up with unique ways to remember the various organisms. When students created posters of their lunar station ecosystems, they were able to work very well with their peers to decide on which organisms would be included. Meaningful discussions took place and students were able to explain to one another how the organisms interacted and why they were needed for their ecosystem. During the construction of the self-sustaining ecosystem, students were able to answer questions as to why we included certain organisms and even figured out why we wouldn’t have to feed the fish in our ecosystem. Students classified the various organisms and worked together as a class to create the model.

Acknowledgments

A large thank you to *We Love Pets* who donated materials to create the self-sustaining ecosystem for our classroom. The NASA lesson plan, "Field Trip to the Moon," was the basis for the entire lesson plan; essential for organism cards, and lunar station ecosystem challenge cards. "Ecosystem of the Forest" was an article from ReadWorks.org, which provided vocabulary words and comprehension questions. A blog post provided detail instructions for the construction of our self-sustaining ecosystem.

References

1. *Field Trip to the Moon. Educator's Guide. Eg-2007-09-120-Msfc.* (2007).
2. Kids' Summer Crafts: Build an Ecosystem. (2010, May 26). Retrieved March 20, 2017, from <http://scribbit.blogspot.com/2010/05/kids-summer-crafts-build-ecosystem.html>
3. The Ecosystem of the Forest. (n.d.). Retrieved March 20, 2017, from <http://www.readworks.org/passages/ecosystem-forest>

Hybrid Neuroprostheses for Individuals with Paraplegia

Student Researcher: Valerie A. Weaver

Advisor: Dr. Roger Quinn

Case Western Reserve University
Mechanical Engineering Department

Abstract

People with spinal cord injury (SCI) currently have few options beyond wheelchairs for day to day ambulation. By combining electrical stimulation and an engineered exoskeleton, another option can be offered and quality of life can be greatly improved. By tapping into the power of the muscles with electrical stimulation, device range can be extended and co-morbidities associated with SCI, such as muscle atrophy and osteopenia, can be reduced. The powered exoskeleton can provide support during walking with muscle use and can continue to be used after muscle fatigue through the use of small, low friction, integrated motors. In addition to providing support and, when needed, propulsion, the engineered exoskeleton frame provides hard stops to prevent abnormal range of motion to avoid injury. The device aims to allow for independent donning and doffing, which would enable independent use.

Project Objectives

One of the first exoskeletons was patented in 1890 as a way to augment human abilities [1]. Since then, the field of exoskeletons has expanded to include assistance for those who have abnormal gait patterns, notably people with SCI. SCI results in a complete lack of or decrease in sensory and motor function [2]. In the case of an injury causing paraplegia, two limbs are affected. Exoskeletons for people with SCI typically come in two forms, either a fully powered exoskeleton or a hybrid neuroprosthetic (HNP). HNPs combine an exoskeleton and functional electrical stimulation (FES) to tap into the power of the muscle while still providing additional power and support after the muscles fatigue.

The objective of this project is to design and fabricate a powered frame to be used with implanted FES in order to restore gait for individuals with paraplegia. Safety is the primary concern in the implementation of the frame, and convenience is a secondary objective. Donning and doffing, the acts of putting on and removing, are especially important to consider in terms of convenience. The end goal is to allow for independent donning and doffing to enable independent use. Powered knee joints and a reciprocal gait orthosis (RGO) make gait possible by providing the necessary support and constraints while allowing rotations in the sagittal plane. Backdrivable motors and transmissions allow the muscles to provide power for gait before fatigue occurs and the powered frame means gait can be maintained even after the muscles fatigue. Using FES as the first power source during device operation is intended to help decrease the detriments experienced from extended wheelchair use, like muscle atrophy, osteopenia, and increased risk of diabetes [3, 4].

Methodology

This version of the HNP is the third iteration, and is the first to use electric motors (the previous versions made use of hydraulic cylinders). Non-frame components, like the motor, transmission, and hydraulic cylinder, were selected prior to beginning design efforts. A design input document with technical specifications and non-frame component constraints were used to guide the design. SolidWorks 2016 version was used for 3D computer aided design, SolidWorks simulation package was used for finite element analysis (FEA), Mastercam X4 was used for computer aided manufacturing, and fabrication was completed in the Biorobotics manufacturing center with especially heavy usage of a Hurco 3-axis CNC

mill. 6061 aluminum was used for all manufactured parts due to its low weight and material properties that allowed required safety factors to be met, and verification was performed using FEA. In order to ensure a large safety factor, analysis was performed assuming the frame would be the only load bearing member, even though in reality there will be load sharing with the user's leg. The maximum user weight and maximum loads experienced in able-bodied individuals for standing and walking were used [5]. The only part that failed initial analysis, the pin, was able to be redesigned to pass requirements without a material change.

The torso and hip components are made up of an RGO. Although the intent is to eventually have a powered hip joint, testing and verification is to be performed on the knee joint first before designs are completed for the powered hip. An RGO was selected because the reciprocating bar across the low back prevents both hips from flexing at the same time, which prevents the wearer from falling forward at the hip. The orthosis also provides a mechanism for donning and doffing by allowing the leg piece to rotate out laterally at the hip. This mechanism allows for a wide enough area between the leg pieces for the user to transfer him or herself into the device independently. The uprights attached at the hip, the femoral uprights, have clearance holes to mate with a connector piece to allow for adjustability. Having the exoskeleton joints as close to concentric with the anatomical joints is essential, and the range covered by the femoral adjustability covers the 5th percentile female to the 95th percentile male hip center to knee center [6].

The powered knee joint attaches to the femoral upright via a connector piece. The knee joint proper consists of two housing plates that provide mounting for the transmission, motor, encoder, and hydraulic cylinder. The brushless DC motor is backdrivable, and the transmission was custom made for this exoskeleton. The motor and transmission each have a pulley and a belt couples the two. The encoder will be used for testing and for controller purposes, and the hydraulic cylinder acts as a lock for the knee joint. The most important safety features in the knee joint are the mechanical hard stops. With FES and potential user joint laxity, the joints may be forced out of their normal range of motion. In order to prevent this abnormal range of motion, protrusions were placed on the housing to prevent the piece that connects to the lower leg from exceeding 10° in extension and 120° in flexion.

The piece that connects to the lower leg, the tibial upright, has a one inch jog to follow the anatomical contour of the leg and a pin with a D profile to mate with the knee encoder. This piece also has a bolt hole pattern for knee joint center to ankle joint center length adjustability and a pickup point for the distal end of the knee hydraulic cylinder lock. The holes for adjustability mate with an ankle foot orthosis (AFO), which rigidly holds the user's ankle. The use of a rigid AFO is important to prevent foot drop which might cause a fall during walking.

Results Obtained

The end design was machined and assembled. Measurements confirm that the final design allows for an adjustable hip center to knee center of 15" to 19". Knee center to ankle center adjustability depends on the height of the AFO (which is user dependent), but is estimated to allow adjustment between 14" to 24". The knee joint is 3.825" thick at its thickest (outside of encoder to outside of transmission pulley). Measurements confirm that the hard stops prevent the knee from rotating beyond 10° in extension and 120° in flexion. The dimensions and constraints are important because the relatively small profile will result in reduced frame weight compared to previous iterations. Weight reduction is important to decrease power consumption for longer device life, and small profile is important for device use with other aids, like the ability to use in a normal width wheelchair. Final device weight is pending completion of controller component selection and design. Passive resistance testing and able-bodied energy expenditure testing are pending completion of controller programming.

Figures

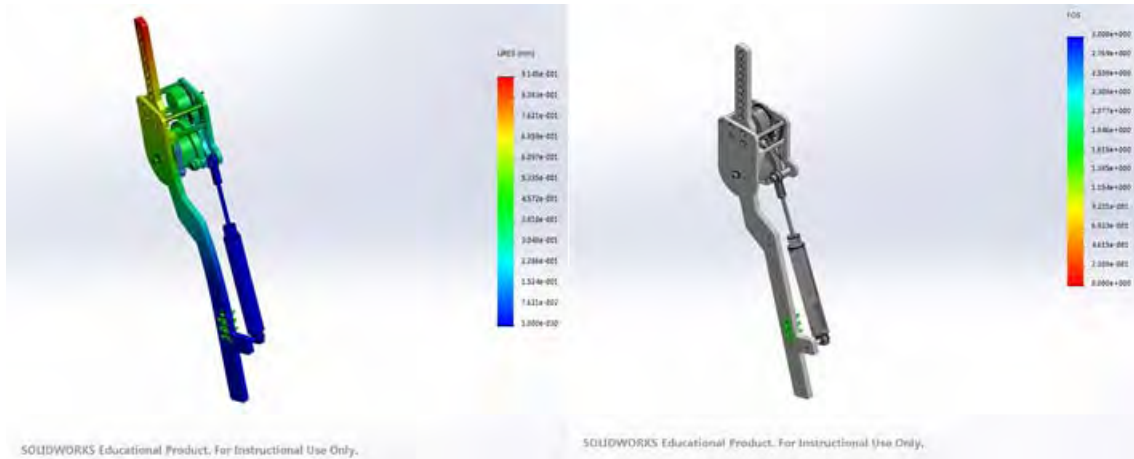


Figure 1. FEA for walking loads; displacement (left) and factor of safety (right) of the knee joint. Displacements are shown with a 71.97 scale, and the minimum factor of safety is 3.3.

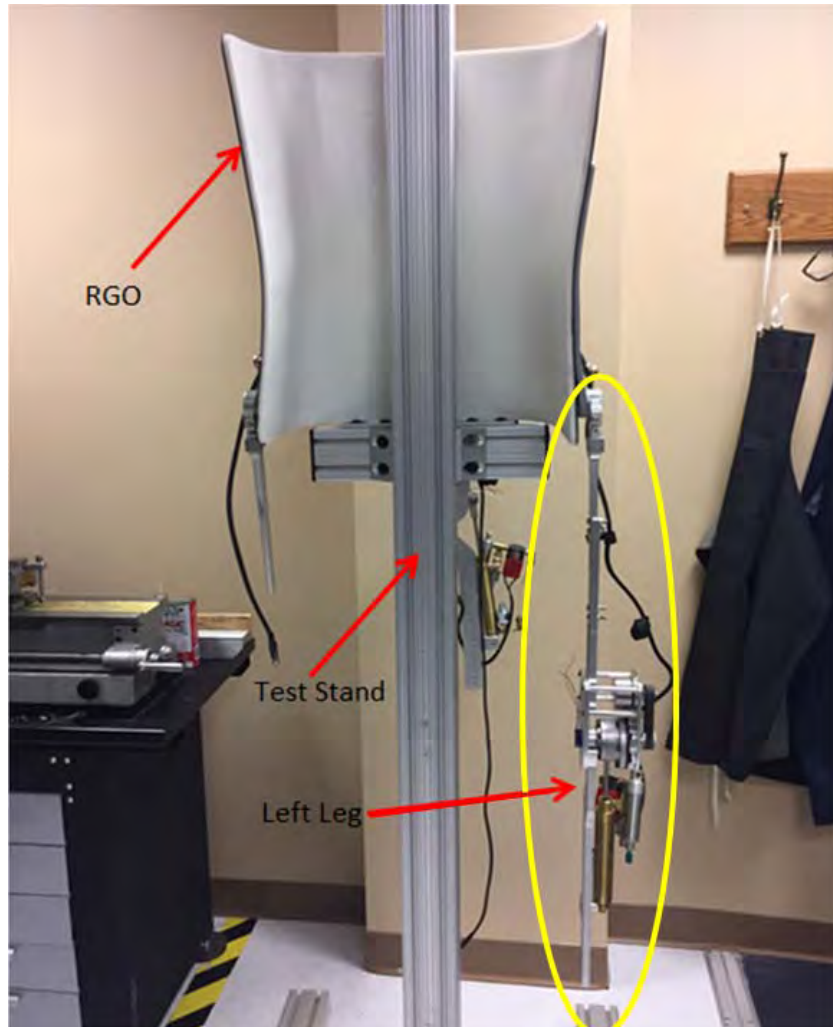


Figure 2. Exoskeleton on test stand, left leg only. See Figure 2 for left leg (yellow circle). AFO not shown.

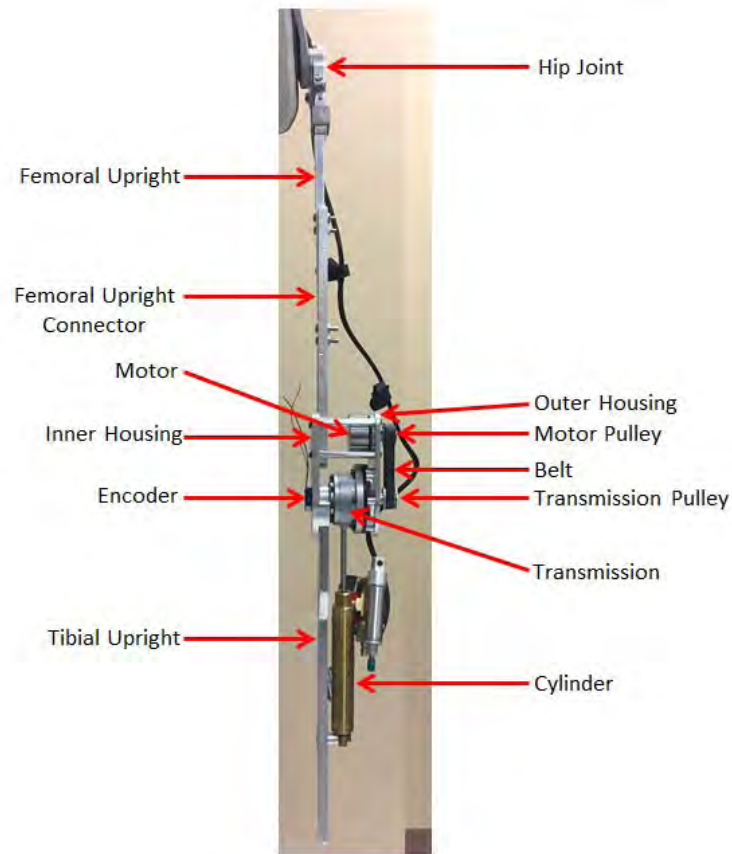


Figure 3. Left leg.

Acknowledgments

Special thanks to Mark Nandor for all his guidance and expertise and to Dr. Roger Quinn, Dr. Ronald Triolo, and Mr. Rudi Kobetic for their advising and project management. Additional thanks to the Biorobotics lab for assistance in manufacturing and use of manufacturing facilities.

References

1. N. Yagn, "Apparatus for facilitating walking". United States of America Patent 440684 A, 18 November 1890.
2. L. E. Buchanan and D. A. Nawoczenski, Spinal Cord Injury Concepts and Management Approaches, Baltimore: Williams & Wilkins, 1987.
3. E. T. Mahoney, C. S. Bickel, C. Elder, C. Blanck, J. M. Slade, D. Apple and G. A. Dudley, "Changes in skeletal muscle size and glucose tolerance with electrically stimulated resistance training in subjects with chronic spinal cord injury," Archives of Physical Medicine and Rehabilitation, vol. 86, no. 7, pp. 1502-1504, 2005.
4. R. D. Lew, "The effects of FNS on disuse osteoporosis," in Proceedings of the 10th Annual Conference of Rehabilitation Engineering Society of North America, San Jose, 1987.
5. V. C. Mow and W. C. Hayes, Basic Orthopaedic Biomechanics, New York: Raven Press, 1991.
6. Human Factors Branch, Federal Aviation Administration, "U.S. Department of Transportation Federal Aviation Administration," 30 December 2016. [Online]. Available: http://hf.tc.faa.gov/publications/2016-12-human-factors-design-standard/full_text.pdf. [Accessed 10 January 2017].

Parametric Reduced Order Model Applications in Gas Turbines

Student Researcher: Ryan S. Wilber

Advisor: Dr. Kiran D'Souza

The Ohio State University
Mechanical Engineering Department

Abstract

In the study of vibrations of bladed disks in gas turbines full finite element models analyzing dynamic responses are very computationally intensive. Reduced order models are often used to approximate the dynamic response of a system while being computationally efficient. Many reduced order models focus on applying slight changes to the stiffness of each blade which can lead to changes in the vibration of the system and ultimately damage the blades. However, another aspect that is relevant in this system is stress stiffening due to the rotational speeds experienced by the turbine. This stiffening changes the dynamic response of the blades when vibrating and changes based on speed. By utilizing Taylor Series approximations, the effects of rotational speeds can be applied in the reduced order model. Varying this parameter in the reduced space as opposed to a finite element analysis can increase the computational efficiency of the analysis. The purpose of this research project is to apply a new reduced order modeling method to vary rotational speed and couple it with an existing method of applying small stiffness changes in the blades to assist design stage vibration calculations of bladed disks.

Project Objectives

The use of reduced order models (ROMs) in previous research have focused on vary one parameter that affects the dynamic response of the bladed disk system in the reduced space. Many methods, such as the component mode mistuning (CMM) method developed by Lim et al. [1] have been constructed to be able to vary the mistuning, or differences in stiffness between blades in the reduced space. This is due to computational savings that are needed when using many mistuning patterns to test a bladed disk design in simulation. Only one rotational speed, however, can be used when constructing these ROMs, therefore new ROMs must be created at every rotational speed that is being tested. Alternatively, Sternchüss [2] has shown that a ROM can be created that can vary rotational speed in the reduced space, but it unable to vary the mistuning of the system.

The goal of this research project is to create a new methodology for creating a reduced order model that can vary both the rotational speed and vary mistuning in the reduced space. This new ROM will allow for more comprehensive testing of bladed disk designs while increasing computational efficiency in varying both of these parameters.

Methodology Used

The parametric reduced order modeling (PROM) method was developed by Hong et al. [3] to vary geometric changes in automotive components. This variation leads to changes in the mass and stiffness of the components, and likewise changes in the mass and stiffness matrices, \mathbf{M} and \mathbf{K} , of the system. The methodology used in PROM was used to vary the rotational speed of a bladed disk in the reduced space. Increases in speeds of bladed disks lead to stress stiffening effects, as shown in Sternchüss [2]. These stress stiffening effects cause the blades to become stiffer, meaning only the stiffness matrix needed to be varied using the PROM.

The PROM formulation presented in Hong et al. uses a Taylor series approximation to vary the stiffness matrices based on rotational speed, p , as seen in Equation (1) [3]. Due to the quadratic stress stiffening increasing [2], only the first three terms of the Taylor Series were needed. The derivatives are approximated using finite difference formulas, as shown in Equations (2) and (3).

$$\mathbf{K}_i(p) \approx \mathbf{K}_i(p_0) + \frac{\partial \mathbf{K}_i}{\partial p}(p - p_0) + \frac{1}{2} \frac{\partial^2 \mathbf{K}_i}{\partial p^2}(p - p_0)^2 \quad (1)$$

$$\mathbf{K}_{FD}^1 = \frac{-\mathbf{K}_i(p_0 + 2\Delta p) + 4 * \mathbf{K}_i(p_0 + \Delta p) - 3 * \mathbf{K}_i(p_0)}{2 * \Delta p} \quad (2)$$

$$\mathbf{K}_{FD}^2 = \frac{1}{2} \frac{\mathbf{K}_i(p_0 + \Delta p) - 2\mathbf{K}_i(p_0) + \mathbf{K}_i(p_0 - \Delta p)}{\Delta p^2} \quad (3)$$

The mode shapes of the system at each speed, arranged in Φ matrices, were compiled into $\Phi_{aug} = [\Phi_1 \Phi_2 \Phi_3]$ [3]. This matrix, however, is not orthogonal and a new transformation matrix, \mathbf{U} was created. This matrix represented the left singular vectors from a singular value decomposition of Φ_{aug} whose singular values were greater than 0.01% of the maximum singular value [3]. Using this, the PROM was constructed using Equations (4) and (5) below, where $\Lambda_0(p)$ is the eigenvalues of the system at rotational speed, p , and \mathbf{I} is the identity matrix.

$$\Lambda_0(p) \approx \mathbf{U}^t \mathbf{K}_i(p_0) \mathbf{U} + \mathbf{U}^t \mathbf{K}_{FD}^1 \mathbf{U}(p - p_0) + \frac{1}{2} \mathbf{U}^t \mathbf{K}_{FD}^2 \mathbf{U}(p - p_0)^2 \quad (4)$$

$$\mathbf{I} = \mathbf{U}^t \mathbf{M} \mathbf{U} \quad (5)$$

The CMM method proposed by Lim et al. [1] was used as the basis for applying mistuning to the system. This method, however, was meant to apply only to one rotational speed. Equations (6) and (7) were the original CMM formulations for calculating mistuned eigenvalues of the systems [1]. This method requires the use of cantilever blade eigenvalues, $\Lambda_{\delta,n}^B$ for mistuned and Λ_o^B for tuned, to approximate the mistuning in the bladed disk using the participation factors, \mathbf{q} . These vary due to stress stiffening effects, and therefore must be interpolated using the same formulation as before, shown in Equations (8) and (9).

$$\Lambda_\delta = \sum_{n=1}^N \mathbf{q}_n^{k^t} \mathbf{k}_{\delta,n} \mathbf{q}_n^k \quad (6)$$

$$\mathbf{k}_{\delta,n} = \Lambda_{\delta,n}^B - \Lambda_o^B \quad (7)$$

$$\Lambda_o^B(p) \approx \Lambda_o^B(p_0) + \Lambda_{FD,o}^1(p - p_0) + \frac{1}{2} \Lambda_{FD,o}^2(p - p_0)^2 \quad (8)$$

$$\Lambda_\delta^B(p) \approx \Lambda_\delta^B(p_0) + \Lambda_{FD,\delta}^1(p - p_0) + \frac{1}{2} \Lambda_{FD,\delta}^2(p - p_0)^2 \quad (9)$$

The participation factors in a standard CMM are calculated using the stiffness of a cantilever blade, \mathbf{K}^B , the tuned cantilever blade eigenvalues, Λ_o^B , the cantilever blade mode shapes, and the full system mode shapes in cyclic coordinates. Each of these terms, however, varies with rotational speed and must be approximated with an interpolation. The eigenvalues were computed in Equation (8) and the full system mode shapes were computed in the \mathbf{U} matrix. Following the same procedure for constructing the \mathbf{U}

matrix, an orthogonal basis for the cantilever blade modes were constructed in the \mathbf{U}^B matrix. These parameters were then used in a Taylor series approximation following the same procedure as Equations (1) - (4) to give Equation (10). Lastly, these cyclic coordinate participation factors $\tilde{\mathbf{q}}_h^k$ are expanded to the physical coordinate system using Equation (11), where \mathbf{F} is the Fourier matrix, \mathbf{I} is the identity matrix, and the participation factors are arranged in a block diagonal matrix [1]. These parameters are then used in Equation (6) to calculate the mistuned eigenvalues.

$$\tilde{\mathbf{q}}_h^k = \mathbf{A}^B(p)^{-1} \left(\begin{bmatrix} \mathbf{U}^B \\ \mathbf{0} \end{bmatrix}^t \mathbf{K}^B(p) \tilde{\mathbf{U}}_{b,h} + \begin{bmatrix} \mathbf{U}^B \\ \mathbf{0} \end{bmatrix}^t \mathbf{K}_{FD1}^B \tilde{\mathbf{U}}_{b,h} (p - p_0) + \frac{1}{2} \begin{bmatrix} \mathbf{U}^B \\ \mathbf{0} \end{bmatrix}^t \mathbf{K}_{FD2}^B \tilde{\mathbf{U}}_{b,h} (p - p_0)^2 \right) \quad (10)$$

$$\begin{bmatrix} \vdots \\ \mathbf{q}_n^k \\ \vdots \end{bmatrix} = (\mathbf{F} \otimes \mathbf{I}) \mathbf{B} \mathbf{diag}_h(\tilde{\mathbf{q}}_h^k) \quad (11)$$

After the calculation of the mistuned eigenvalues, the forced response equation modified from Lim et al. [1] can be written in the frequency domain as Equation (12), where \mathbf{p}_c is the modal coordinate of the response. The response of the blade in physical coordinates by multiplying \mathbf{U} by \mathbf{p}_c .

$$\mathbf{p}_c = (\mathbf{U}^t \mathbf{F})^{-1} \left(-\omega^2 \mathbf{I} + (1 + j\gamma)(\mathbf{A}_\delta(p) + \mathbf{A}_0(p)) \right) \quad (29)$$

Results Obtained

Using the methodology developed above a tuned system PROM was constructed to evaluate performance. The speeds used were 0 rpm, 10,000 rpm, and 20,000 rpm and the target speed was 17,500 rpm. The development of the transformation matrix \mathbf{U} left 149 modes in the system. A ROM was also constructed explicitly at 17,500 rpm to compare to the PROMs forced response. This ROM used 95 modes in the transformation matrix. Results from the simulation are shown in Figure 1. The PROM visually was nearly identical to the ROM that was created, with a 7.9×10^{-4} % difference in amplitude at the resonant frequency. The resonant frequency of this forced response was expected to be near a natural frequency for the harmonic that was excited, but not exactly matching due to the damping, γ , of 0.001 N-s/m. In this forced response the 1st harmonic was excited, which contained a natural frequency of 2206.86 Hz. The resonant frequency for the PROM was 2261.72 Hz, which showed the PROM was accurately predicting the forced response of the system.

Figure 2 shows the breakdown of the computation time needed to create a PROM from the information extracted from a FEA program. The full time to create a PROM and conduct the forced response analysis was 58.615 seconds, but the reduction of the stiffness terms are one-time calculations. There was a computational cost of 124.51 seconds to construct the \mathbf{U} matrix, but this is a one-time calculation. This shows savings over using FEA software for forced response, which can take multiple hours.

The ROM method present in this paper shows potential in combining multiple parameters that affect the forced response of a bladed disk and varying them in the reduced space. Due to time constraints, verification of the mistuning methodology presented in this report was not able to be performed. Future work would verify this part of the developed methodology and expand the method to other parameters, such as geometric changes in the bladed disk. Overall, this method shows that reduced order models can be used to assist design stage calculations in order to build safer, more reliable bladed disks.

Figures and Charts

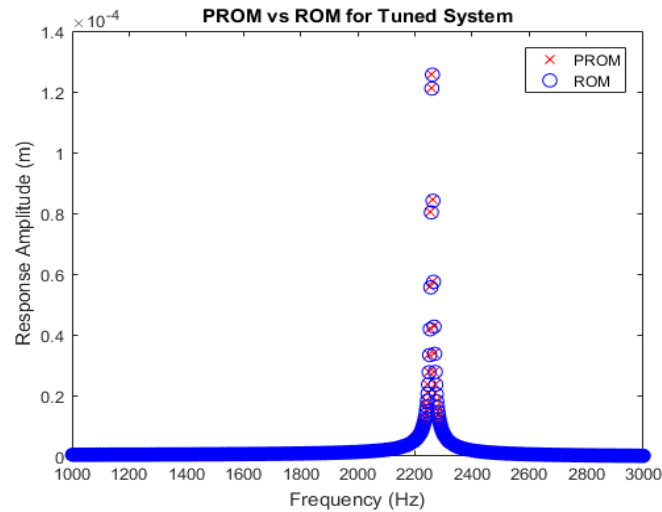


Figure 1. Forced response for PROM and ROM at 17,500 rpm.

PROM Time Breakdown	
Task	Time (seconds)
PROM Creation and Forced Response	
Matrix Loading/Reformatting	3.632
Finite Derivative 1	0.017
Finite Derivative 2	0.014
ROM Creation	50.446
Forcing Application	0.054
Forced Reponse	4.452
Total PROM/Forcing Time	58.615
Transformation Matrix Calculation	
U-Matrix Construction	124.51
Tranformation/PROM/Forced Response	
Total Time	183.125

Figure 2. Breakdown of computational time for PROM construction and forced response

Acknowledgments

I would like to thank Dr. Kiran D'Souza for his guidance and help on this project. I would also like to thank Eric Kurstak for his assistance on this project.

References

1. Lim, S.H., Bladh, R. Castanier, M. P., Pierre, C., "Compact, Generalized Component Mode Mistuning Representation for Modeling Bladed Disk Vibration," AIAA Journal, Vol. 45, No. 9, 2007, pp. 2285-2298.
2. Sternchüss, A., "Multi-level parametric reduced models rotating bladed disk assemblies" Ph.D. Thesis. Ecole Centrale des Arts et Manufactures, Paris, France, 2009.
3. Hong, S.K., Epureanu, B. I., Castanier, M. P., Gorisch, D. J. "Parametric reduced-order models for predicting the vibration response of complex structures with component damage and uncertainties," Journal of Sound and Vibration, Vol. 330, 2011, pp 1091-1110.

Capsule Endoscopy Lens Design

Student Researcher: Kweisi F. Wilson

Advisor: Nkorni Katte

Wilberforce University
Electrical Engineering

Introduction

Endoscopic imaging is very critical in the early diagnostic of several diseases. The Endoscope is often made up a probe that host the primary optical elements connected to a computer for viewing by a fiber optics. Endoscopic imaging is often coupled with other optical techniques such as optical coherence tomography and Raman spectroscopy to address specific details. In our research we seek to address a seemingly neglected problem, which is the lens that captures the primary images. This is a critical problem because poor lens design will altogether ruin the process. One important Lens design which can achieve great quality is the Capsule endoscopy lens.

Method

The goal of our initial lens design is to understand the typical sources of aberration for a Capsule endoscopic lens, and how to correct these aberrations. We will do so while at the same time ensuring good image quality. Another goal is to make sure that the design is manufacturable with available material. We also want smaller designs with low total track lengths and large fields of view (FOV). To do so we began with a design in literature [1] these has a focal length of 1.5mm, and proceed to set up a similar system. Then we defined an appropriate merit function and performed optimization with ZEMAX (Optics Studio software) for minimum spot radius. We avoided the use of aspheric surfaces which are typically more expensive to manufacture.

In our Optimization we allowed our system to increase in size, not to be limited to 4.5mm of total track length as the initial literature design. We maintained a focal length of 1.5mm and an f-number of 2.8. We will allow the software to select appropriate glasses for our 3 lens elements that will guarantee good imaging. A good imaging system is said to be diffraction limited which means it has a spot radius less than airy spot radius of $1.22\lambda f / \#$ which is about 2.1 microns for our design. An acceptable system could have an airy radius slightly higher than this value but not very large. The fields for incident beams are 0, 30 and 45 degrees. So the maximum full FOV is 90 degrees.

Results.

We obtained the following results, in the design process.

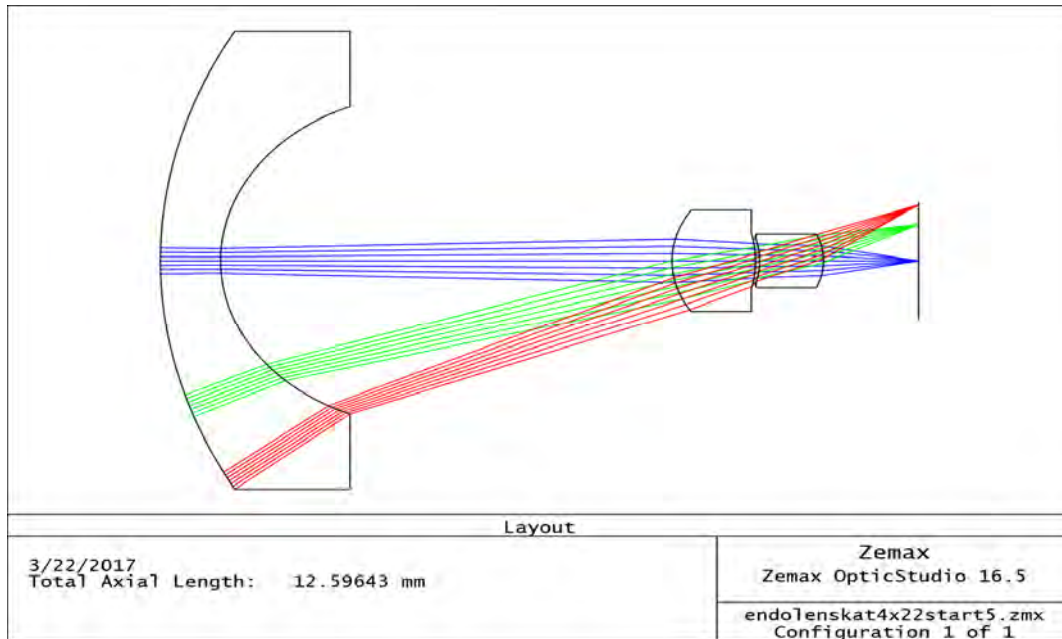


Figure 1. Shows an initial design, inspired by [1] with plastic materials used for the lenses.

After Optimization we get a design with a smaller spot radius for the on axis beam.

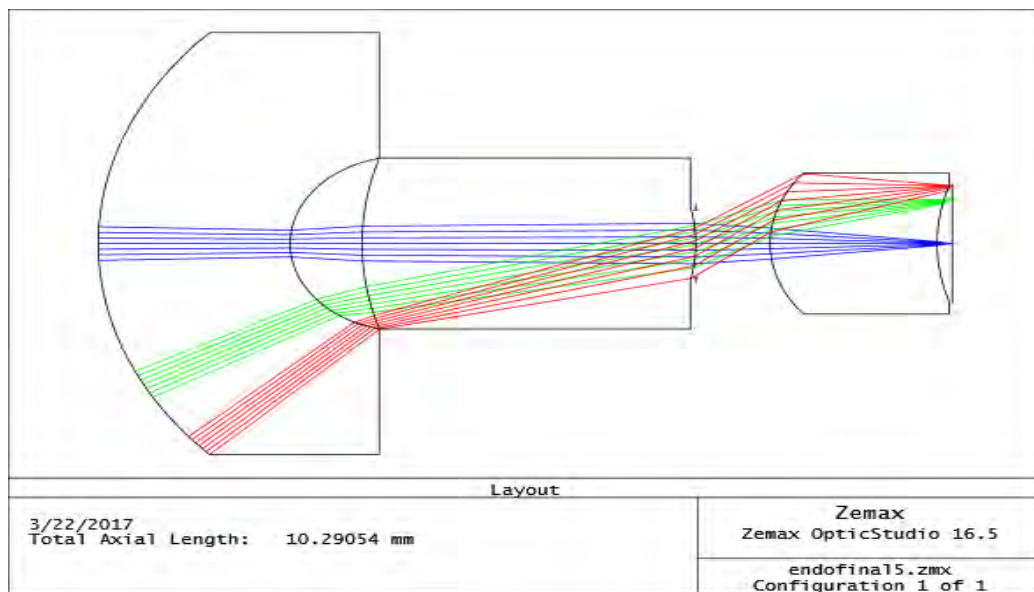


Figure 2. A final design which yields a spot size of 2.4 microns.

Conclusion

The Critical aberration is the distortion because of the large field of view. Optimizing with glass substitution has not reduced distortion. Distortion should be reduced by choosing aspheric surfaces. The spot sizes reduce from about 6.2 microns to 2.4 microns. But the distortion grows from 15% to 37%.The system has an acceptable Modulation transfer function (MTF) value .We will be consider a Multiphysics analysis of the Micro-mirror in our future work.

Acknowledgments

We acknowledge the financial support of the Ohio Space Grant Consortium for this research. We also acknowledge the moral support of the office of the provost and College of professional studies at Wilberforce University.

References

1. Chao Hu, Kang Xie, and Zhiyong Liu "Optimized design of Capsule endoscopy lens based on Zemax". Proceeding of the IEEE International conference on information and automation, Shenzhen China 2011.

Investigation of Thermodynamic Cooperativity Pseudourylation Enzyme RsuA and rProteins During Bacterial 30S Ribosomal Assembly

Student Researcher: Courtney N. Wolfe

Advisor: Sanjaya Abeysirigunawardena

Kent State University

Department of Chemistry and Biochemistry

Abstract

Ribosomes are important for all living organisms. Nucleotide modification found in various regions of the ribosomal RNA can influence ribosomal assembly, local structural, and thermodynamic stability changes in rRNA. At the same time modification enzymes can influence the binding thermodynamics and kinetics of various ribosomal proteins, hence influencing ribosome assembly. In particular, pseudouridine synthase, RsuA, is responsible for modifying uridine at position 516 in the 16S rRNA to a pseudouridine that can influence the structure and thermodynamic stability of 16S helix 18. Previous studies have shown that protein RsuA is unable to bind to 16S rRNA alone and can only weakly bind to 30S ribosomes. It is proposed that protein RsuA is binding to a ribosome assembly intermediate. However, this assembly intermediate is yet to be discovered. We have successfully overexpressed, purified and fluorescently labeled the RsuA protein. We are currently investigating the binding thermodynamics of RsuA enzyme in the presence of various ribosomal RNA substrates to determine the high affinity substrate for protein RsuA.

Project Objectives

Ribosomal assembly is a complex process with coupled processing and modifications. The ribosome is an excellent model for how modification affect RNA-protein interactions. The 30S ribosomal subunit is made in vitro from 16S rRNA and 21 rProteins. This assembly occurs in a hierarchical fashion, with only six proteins able to initially bind to the 16S rRNA as shown in Figure 1. These six proteins act as the primary assembly proteins and aid in the binding of additional proteins through cooperativity.

Many modifications occur in close proximity in the decoding center of the 30S ribosome. Of interest is pseudouridine synthase which acts at position 516. Pseudouridine is the most common modified nucleotide to date.¹ In fact it comprises up to 8% of all uridines found in large subunit RNAs.² In particular, pseudouridine synthase, converts uridine to pseudouridine as shown in Figure 2. In this reaction RsuA acts as the only catalysis enzyme, however other cofactors are present. The mechanism of this reaction is not currently known, however proposed mechanisms by Miracco involve Michael or Acyl Addition.

The conversion of uridine to pseudouridine strengthens the complex as an extra hydrogen bond donor is present and is proposed to stabilize base stacking in single stranded RNA and affect the helical orientations when located near bulge residues. The pseudouridine modification is common in rRNA and tRNA, and has even been shown to increase translational capacity. Bacterial ribosome with unmodified 23S rRNA showed a five-fold reduction in peptidyl-transferase activity.³ Pseudourylation is also linked to human disease. Lower levels or a malfunctioning enzyme are linked to dyskeratosis congenita and hypomodification of mitochondrial tRNAs. Interference with pseudourylation leads to temperature sensitive growth defects.⁴

Mass spectrometric detection with matrix assisted desorption ionization (MALDI) is one possible method of determining if pseudourylation has taken place. Uridine and pseudouridine are mass silent, however when complexed with CMC a 250.2Da mass shift occurs. N-cyclo-N-β-(4-methylmorpholinium)ethylcarbodiimide (CMC) reacts with guanosine, thymidine, and uridine-like components in DNA and RNA along with the N1 and N3 positions of pseudouridine.⁵ Guanosine, thymidine, uridine, and the N1 position of pseudouridine all release CMC under mild alkaline conditions, however removal of CMC from the N3 position of pseudouridine requires more basic conditions. However, CMC-derivatized 4-thiouridine is also stable under mild alkaline conditions and that 5-methyluridine releases CMC slower than unmodified uridine.⁶ The modified nucleoside 2-methylthio-N⁶-isopentenyladenosine (ms²i⁶A) can also undergo derivatization with CMC.⁷

Proteins, S4 and S12, potentially prevent binding of RsuA. It is possible that the modification enzyme binds, then leaves to allow binding of S4 and S12. RsuA contains an N terminal domain that is similar to the C terminal domain of S4 resulting in close binding proximity. For this reason, RsuA acts as a gatekeeper for S4 and it is questionable whether the pseudoknot forms before or after S4 is bound.

The stability of pseudoknot formation will also be tested with nucleotide modifications. The nucleotides at positions 505, 506, and 507 in helix 18 have been mutated to disrupt binding. The thermodynamics of different combinations of these mutations will be determined along with which of these nucleotides are necessary for pseudoknot formation.

The thermodynamics and kinetics of this process will be determined via fluorescence FRET experiments. RsuA acts as a fluorescence donor to the RNA complex. The dissociation constant, K_d will be determined from experiments with just RsuA present and then another trial will be done with the addition of S4. A higher dissociation constant is indicative of less stability as the complex will dissociate more quickly. Comparison of these two trials will indicate if cooperativity exists between RsuA and S4.

Methodology Used

A stock solution of 20μg CMC prepared in 1mL of 50mM Tris-HCl, 4mM EDTA, and 7M urea. The RNA sample, 0.5μg H18M was added to the CMC solution and incubated in a water bath for 2-24 hours. The solution was purified with ziptips to remove excess salt and unreacted materials and then reacted with 50mM NH₄OH (pH 10.4) for 1-2 hours at 65-80°C. The solution was then dried down and resuspended in 2μL of pure water.

Two matrixes were used, 3-HPA and a THAP/DAHC mixture. The 3-HPA matrix consisted of 0.7M 3-hydroxypicolinic acid and 0.07M ammonium citrate diluted in 1mL of 50:50 acetonitrile and water. The other matrix was composed of 300mM THAP in acetonitrile and 250mM DAHC in water. THAP and DAHC were combined equally in 2μL. In the first trial, CMC derived RsuA was combined with each of the two matrixes, vortexed and spotted onto a MALDI plate. In the second trial, a two-layer spotting method was used. 0.5μL of matrix was spotted on the plate, allowed to dry, and then the sample/matrix solution was spotted on top of this layer. The samples were run in negative mode with various modifications on the other parameters. A primer mix composed of RsmG seq 1, RsmG seq 2, Xho, Ndi, and RsuA Rev was used to standardize the mass spectrometry parameters.

Primers were designed to change the nucleotides involved in pseudoknot formation. The guanine at position 505 was changed to a cytosine (G505C), the guanine at position 506 to a cytosine (G506C), the cytosine at position 507 to a guanine (C507G), and both the guanines at positions 505 and 506 to cytosines (G505C:G506C). The samples underwent a Quikchange protocol to synthesize a new strand with the desired modification. The sample then underwent DPN I digestion. The samples were transformed on ampicillin plates and made into overnight cultures. The overnight cultures underwent a mini prep and were sent off for sequencing.

Results Obtained

It was determined that alkylation at 65°C for one hour best optimized the reaction. However, the mass spectrometry readouts had a significant amount of noise. Early experiments displayed the anticipated peaks, however later experiments were unable to replicate the results. In addition, the noise was not able to be removed from the read out.

The point mutations at G506C and C507G were unsuccessful. The nucleotide modifications G505C and G505C:G506C were successfully transformed into bacterial cultures. G505C:G506C and G505C also displayed turbidity in the overnight cultures. The samples are currently being sequenced to confirm the modification.

Significance and Interpretation of Results

The original mass spectrometry primer experiments displayed the anticipated peaks with some additional noise. The CMC derivatized RsuA sample was expected to have a peak around 14,000 Da, however there was no noticeable peak at this weight. It was theorized that the RNA was being broken down and after analyzing the location of peaks compared to those in the untreated sample via Oligo Mongo, no difference was found. Alterations were made to the CMC stock solution such as increased concentration of urea and addition of KCl and MgCl₂. No change were observed with these observations. The primers were tested again, however the peaks were no longer visible amongst the noise. It was determined halfway through these experiments that the detector on the mass spectrometer was broken.

During this time, samples were sent the mass spectrometry lab at the University of Akron for analysis. The samples sent to the University of Akron did not display any peaks and it was theorized that the concentration was too low. Samples underwent electrospray ionization which require a much lower concentration at the mass spectrometry lab and still no peaks were observed. It is possible that excess dust in the air from the construction and the lack of windows contaminated and degraded the samples prior to analysis. The samples may have displayed a peak at a higher concentration, however the samples were too expensive to concentrate further. It was ultimately determined that mass spectrometry would not be a practical method for detecting the presence of pseudouridine for our experiments.

Initial modifications of the nucleotides involved in pseudoknot formation were unsuccessful due to a problem with the template. A fresh stock of template fixed this problem and allowed the modifications G_505_C and G_505_C:C_506_G. The samples are currently being sequenced. In the future, these samples will be used to conduct fluorescence resonance energy transfer experiments to study the thermodynamics of pseudoknot formation.

Figures

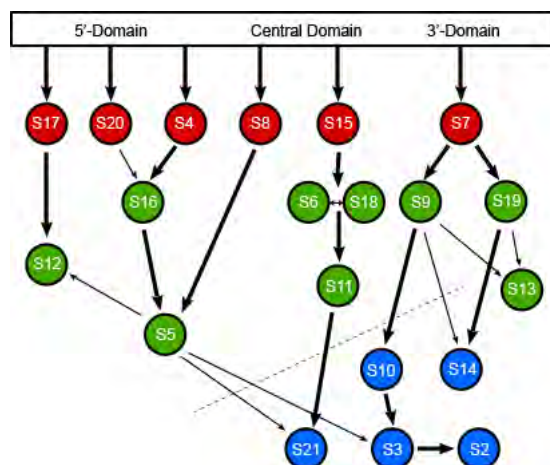


Figure 1. Proteins assemble in a hierarchical fashion.

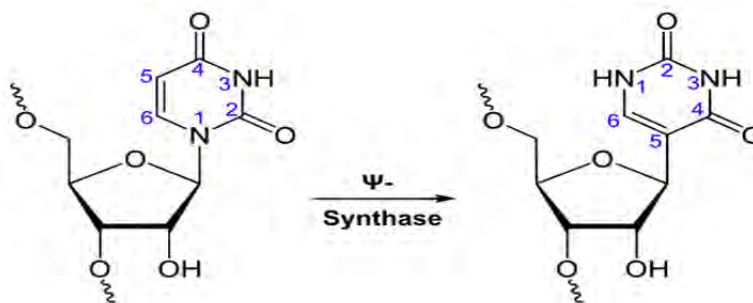


Figure 2. Pseudouridine synthase converts uridine to pseudouridine rotating the base 180 degrees.

References

1. Maden, B.E.H. (1990) *Prog. Nucleic Acids Res. Mol. Biol.*, **39**, 241-303.
2. Ofengand, J and Bakin, A. (1997) *J. Mol. Bio.*, **266**, 246-268.
3. Green, R., Noller, H.F. (1996) *RNA* **2**: 1011-1021.
4. Tollervey et al. (1993) *Cell* **72**: 443-457.
5. Ho NWY, Gilham PT. *Biochemistry* (1971) PUB MED: **10**: 3651.
6. Ofengand J, Campo DM, Kaya Y. *Methods* (2001) PUB MED: **25**: 365.
7. Durairaj Anita, Limbach Patrick. (2008) "Improving CMC-derivatization in RNA for mass spectrometric detection." *Analytica Chimica Acta*, 612(2), 173-181.

Prophylactic Braces and Athletic Performance

Student Researcher: Marlo Rose Wolfe

Student Advisor: Lisa Stanich

Lakeland Community College

Biology

Abstract

Knee and ankle injuries are two major problems that athletes face in sports today. Prophylactic athletic braces are used to prevent common injuries in high-risk sports. According to MedlinePlus.gov, the most common athletic related injuries are sprains and strains, knee injuries, Achilles tendon injuries, along with others. After the National Football League successfully tested prophylactic braces, many athletes were eager to test them in contact sports. The popularity of these braces has decreased due to the variance of results in different studies. There are many braces designed to be worn in order to prevent these common injuries, and to provide extra support for the athlete. With that being said, many athletes may be reluctant to wear these braces if they hindered their performance in any way. For this reason, many studies are still being conducted to test the effectiveness of knee and ankle braces.

Project Objective

My objective is to research the effectiveness of prophylactic braces on athletic performance, and also observe the results I obtain from running a drill called the “shuttle run” to test speed and lateral movement of the athlete in the presence and absence of a knee and ankle brace.

Methodology Used

I first found information from research and tests conducted on various groups of athletes, using different ankle and knee braces. In a study done by Zachariah Henderson, Paolo Sanzo, and Carlos Zerpa at the School of Kinesiology of Lakehead University, they tested for the effects of prophylactic ankle bracing on physical performance measured in jumping athletes. Fourteen athletes were gathered for the research with the mean age of 20.92+/-1.94, while their agility time and vertical jump height was recorded on three separate days and under three conditions: no brace, ASO EVO© Brace, or Active Ankle T1© Brace on both legs.

Another research article was written by Soheil Najibi, MD, PHD and John P. Albright, MD regarding the use of knee braces. They took information from two epidemiological studies. The first is from West Point, where a randomized control study of 71 injuries in 1396 cadets indicated knee braces effectiveness. The next study was conducted by The Big Ten Conference with 100 medial collateral ligament sprains among 987 football players in different positions and strings.

Using this information, I conducted a series of tests to better understand the ways these braces affect athletic performance. I had Trevor Morrison, a defensive lineman at John Carroll University’s football team do the shuttle run drill three times with each different prophylactic brace on each leg, then three times without the brace. We used a Tru-Fit Ankle Stabilizer brace and Futuro Knee Stabilizer brace. The findings show possible speed and lateral movement differences depending on the braces being applied.

Results Obtained

Results gathered from these different experiments can help people better understand the effectiveness of preventative braces and how different abilities may be hindered or improved with the use of these braces. The results from the trial done at the School of Kinesiology of Lakehead University displayed that ankle bracing may have a negative impact on vertical jump height, not depending on the type of brace being worn. Overall agility time was not affected by the ankle brace. As for the study conducted by Soheil Najibi and John P. Albright, results showed the insignificance but consistent reduction in injury rate for braced players in every position and string, during practice. During games, there was a reduced rate for lineman and linebacker/tight end group. Therefore, this study concludes that with the issue still open, prophylactic knee braces seem to provide some protection to the medial collateral ligament from applied valgus forces, but consequently braces may negatively affect performance level, leg cramping, and fatigue symptoms. As for the small trial I conducted, the best time we gathered was from the run being completed with a right knee brace on, compared to our slowest run with a right ankle brace being worn. Although the sample size was too small and the data was too inconsistent to draw a conclusion on the issue, it was interesting to find that my results disagreed with Najibi and Albright's study showing that knee braces may hinder performance level.

Significance and Interpretation of Results

From my research, the type of prophylactic brace that would be most effective for you can vary greatly based upon the type of activity you are participating in, and also what area of the body you may need extra support with. It is important to talk to a health care professional to better understand the areas of your body that are at high risk, depending on the activity you are doing, and to then choose a correct brace. Some researchers conclude that prophylactic braces greatly reduce MCL injuries, while others say the effects of prophylactic braces are minimal. With continuous research on this topic, consistency in results can assist those involved in athletics to better understand the most effective ways to avoid injuries commonly affecting the knee and ankle areas. In general, functional and rehabilitative braces seem to be the most effective brace, and the effects of prophylactic braces are still inconclusive.

References

1. McKeag, Scott A. Paluska | Douglas B. "Knee Braces: Current Evidence and Clinical Recommendations for Their Use." *Knee Braces: Current Evidence and Clinical Recommendations for Their Use - American Family Physician*. American Academy of Family Physician, 15 Jan. 2000. Web. 20 Mar. 2017. <<http://www.aafp.org/afp/2000/0115/p411.html>>.
2. Staff, Familydoctor.org Editorial. "Knee Bracing: What Works?" *Familydoctor.org*. American Academy of Family Physician, 21 Oct. 2016. Web. 19 Mar. 2017. <<https://familydoctor.org/knee-bracing-what-works/?adfree=true>>.
3. Henderson, Zachariah, Paolo Sanzo, and Carlos Zerpa. "The Effect of Prophylactic Ankle Bracing on Physical Performance Measures in Jumping Athletes." *International Journal of Sports Science*. Scientific & Academic Publishing, 2016. Web. 25 Mar. 2017. <<http://article.sapub.org/10.5923.j.sports.20160604.02.html#Sec1>>.
4. Najibi, Soheil, and John P. Albright. "The Use of Knee Braces, Part 1: Prophylactic Knee Braces in Contact Sports." *American Journal of Sports Medicine* 33.4 (2005): 602-11. Web. 02 Mar. 2017. <<http://journals.sagepub.com/doi/abs/10.1177/0363546505275128>>.

GC-MS Analysis of Chinese Baijiu Spirit Flavored as American Whiskey

Student Researcher: Christopher B. Wright

Advisor: Dr. Regan Silvestri

Lorain County Community College
Science and Mathematics Division

Abstract

Gas Chromatography-Mass Spectroscopy (GC-MS) is routinely used to profile the flavor compounds in alcoholic beverages. This method has been applied to unique experimental samples of Chinese Baijiu spirit flavored to taste more similar to American bourbon whiskey. Chinese Baijiu is a clear spirit, usually considered strong in flavor by the western palate. In an effort to modify these spirits into something more akin to the routine western palate, experimental samples have been produced of Chinese Baijiu liquors flavored to taste similar to American bourbon. This has been accomplished by subjecting Chinese Baijiu liquor to a novel accelerated aging process that employs pressure, as opposed to conventional time, to mature the spirit quickly and impart wooden barrel flavors. By processing Chinese Baijiu spirit via this innovative technology of accelerated pressure aging, the clear spirit becomes colored and flavored with wood in the short time of a few days. The distinct flavor compounds in these experimental liquors have been identified and profiled using routine straight injection GC-MS. As such, it has been discerned that Chinese Baijiu flavor is defined predominately by unbranched aliphatic esters. Foremost, the wood aged Chinese Baijiu flavor is characterized by an increase in ethyl hexanoate, which imparts a sweet and fruity nuance.

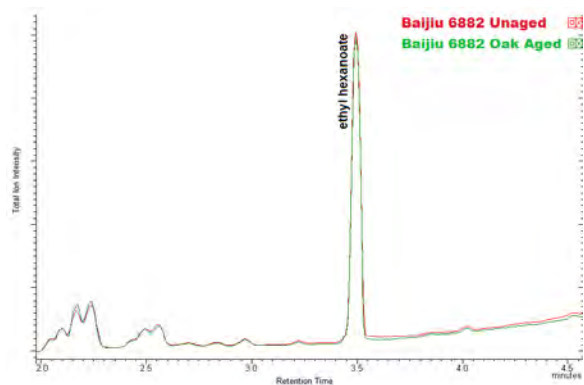
Project Objectives

Use Gas Chromatography-Mass Spectroscopy to profile the flavor compounds in rapid pressure aged whiskey provided by our industry partner Cleveland Whiskey and compare with the flavor compounds in conventionally aged whiskey.

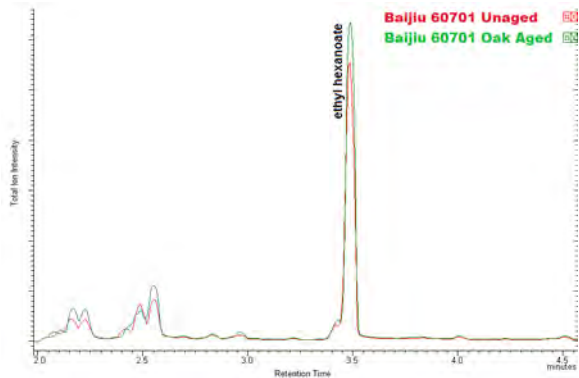
Use Gas Chromatography-Mass Spectroscopy to profile the flavor compounds in Chinese Baijiu spirit and compare with the flavor compounds in experimental samples of rapid pressure aged wood flavored Baijiu provided by our industry partner Cleveland Whiskey.

Results

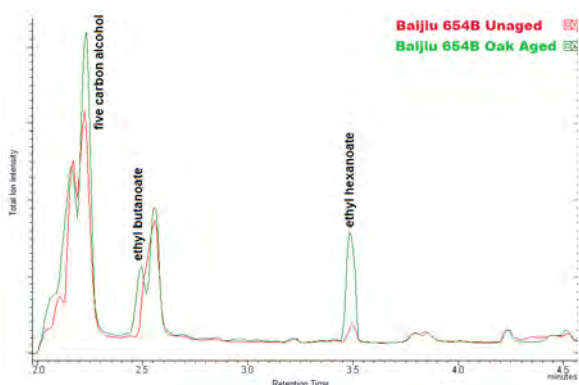
Chromatogram Traces for Three Different Starting Materials:



No significant differences were measured upon aging.



A slight increase in ethyl hexanoate was observed upon aging.



Substantial increases in ethyl hexanoate, ethyl butanoate, and a five carbon alcohol were observed upon aging.

References

1. "Imparting Whiskey Wisdom", Chemical and Engineering News, Volume 94, Number 18, page 40, May 2, 2016 <http://pubs.acs.org/doi/pdf/10.1021/cen-09418-newsprints>
2. "Distilling Lessons from a Whiskey Research Program", in Chemistry, Volume 25, Number 2, pages 12-13, November/December 2016 http://www.inchemistrydigital.org/inchemistry/november_december_2016?pg=14#pg14
3. "Chemistry of Whiskey Flavor", Reactions, April 6, 2016 <https://acsundergrad.wordpress.com/2016/04/06/chemistry-of-whiskey-flavor/>
4. "GC-MS Analysis of Unprecedented Whiskey Flavors Created by a Novel Aging Process", Proceeding from SAS 60th Annual May Conference, May 18, 2016 http://www.msneo.org/uploads/3/1/7/7/31779867/60th_annual_program-full.pdf

Plasma-Assisted Combustion in a Rotating Detonation Combustor

Student Researcher: Yonry Zhu

Adviser: Dr. David Burnette

Ohio University

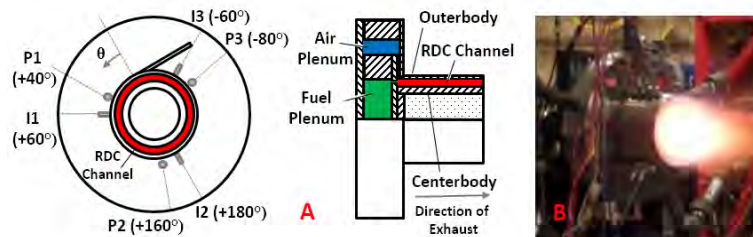
Department of Physics and Astronomy
Department of Mechanical Engineering

Abstract

A non-thermal plasma was generated in a rotating detonation combustor using nanosecond high voltage pulses and a novel ceramic and metal electrode. The plasma initiated and stabilized detonation under near stoichiometric fuel-air mixtures, but had a reduced effect for fuel-lean and fuel-rich conditions.

Project Objectives

When integrated into gas turbine engines, detonative combustion could yield thermal efficiency improvements up to 15% due to pressure gain across the combustor and reduced entropy rise over the cycle¹. The rotating detonation combustor (RDC), shown below, is a promising implementation of detonative combustion. In an RDC, reactants are continuously fed into an annular combustion chamber where they are consumed by a circumferentially propagating detonation.



The financial incentives of detonative combustion have placed immense demand on developing an RDC capable of using methane and air (power generation) and kerosene and air (aviation). To date, no RDC has been developed capable of using either fuel-air mixture due to poor mixing, flow instabilities, and the low reactivity of both mixtures².

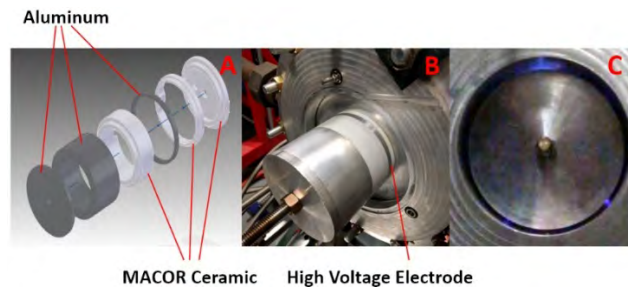
This research focuses on expanding the operating range of the RDC using non-thermal plasma. These plasmas have been widely studied for combustion enhancement and should improve the RDC in two ways. First, sub-acoustic timescale heating generated by the plasma forms compression waves which enhance mixing by inducing turbulence³. Second, high energy electron impact processes efficiently produce electronically excited species and free radicals which greatly increases the reactivity of fuel-oxidizer mixtures⁴.

This scope of this project is to provide proof-of-concept for the plasma-assisted RDC and to generate preliminary data characterizing the behavior of the RDC with and without the plasma over a wide range of conditions. The ultimate research goal is to enable RDC operation with methane-air and kerosene-air mixtures using plasma.

Methodology Used

The detonability of fuel-oxidizer mixtures is inversely related to a parameter known as the detonation cell size. If the characteristic dimension of an enclosure (in the case of an RDC, the channel width) is smaller than the cell size, detonation will not occur. For hydrogen-air mixtures, this cell size is approximately 8 mm^5 . To test the efficacy of the plasma, hot-fire testing of an RDC with a channel width of approximately 5 mm was conducted using hydrogen and air at the facility described in [2].

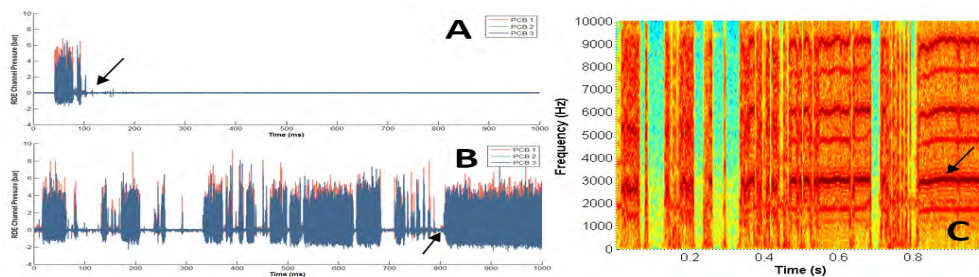
To generate the plasma, a custom 5.75 inch centerbody electrode was fabricated out of MACOR ceramic and aluminum. The electrode was positioned in the path of the detonation wave to maximize the effect of the discharge and was powered by 10 ns long, 20 - 40 kV pulses at a frequency of 3 kHz.



The air mass flow rate was set to 0.2 kg/s and the fuel-air mixture composition, or equivalence ratio, was varied from 0.8 to 1.4. At each equivalence ratio, the RDC was fired without plasma, allowed to cool, and then fired with plasma. Detonation wave behavior was captured using three PCB piezoelectric pressure sensors, each separated by 120° , and sampled at 1 MHz by a data acquisition system.

Results Obtained

An example pressure trace ($\dot{m} = 0.2 \text{ kg/s}$, $\phi = 0.98$) is shown below. Panel A shows the RDC without plasma, with the arrow indicating the extinction of the detonation. Panel B shows the RDC with plasma, with the arrow indicating sustained detonation. Panel C shows a spectrogram of the pressure signal, indicating a detonation rotation frequency of approximately 3 kHz.



As the mixture composition was moved away from stoichiometric conditions, the effects of the plasma were less pronounced, with no noticeable effects for $\phi < 0.9$ and $\phi > 1.3$. However, even in conditions with no plasma-induced detonation onset, the plasma shrank the exhaust plume length, indicating increased mixture reactivity.

Significance and Interpretation of Results

The direction of rotation of the detonation, indicated by pressure trace data, during each period of detonation onset appears to be random until the detonation stabilizes. It seems that during these periods, the plasma is re-initiating the detonation as opposed to sustaining a previous detonation. This experiment provides sufficient proof-of-concept for continued exploration of the plasma-assisted RDC.

Acknowledgments

Many thanks to Dr. Ephraim Gutmark and his research group at the University of Cincinnati for allowing me to run experiments using their RDC. Additional thanks go to Ohio University and the Ohio Space Grant Consortium for funding this project.

References

1. Heiser, W. H., Pratt, D. T., *AIAA J. Propulsion Power*, Vol. 18, No.1, 2002, pp. 68-76.
2. St. George, A., Driscoll, R., Anand, V., Randall, S., Munday, D., Gutmark, J., 53rd AIAA Aerospace Sci. Meeting, AIAA 2015-0635, 2015
3. Firsov, A., Savelkin, K. V., Yarantsev, D., Leonov, S., *Phil. Trans. R. Soc. A*, Vol. 373, 2015
4. Popov, N. A., *Plasma Sources Sci. Technol.*, Vol. 25, 2016.
5. Ciccarelli, G., Ginsberg, T., Boccio, J., Eonomos, K. S., and Kinoshita, M., *Combust. Flame*, Vol. 99, No.2, 1994, pp. 212-220.

Adjustable 3D Printed Prosthetics

Student Researcher: Bryce J. Zwagerman

Advisor: Mike Prochaska

Lakeland Community College

Associate of Science: Engineering Pathway

Abstract

Additive Manufacturing, such as 3D printing, could be an option for producing prosthetics. The 3D printing process could prove to be a simpler method of producing prosthetics for young consumers, while being more cost effective. The 3D printed prosthetic could be an economical option for younger people who are still in the growing process. It would allow them to perform everyday activities that they may not otherwise be able to do without the specific body part.

The adjustability of a 3D printed prosthetic leg, would provide a cheaper alternative for a child that is still growing. Rather than replacing the prosthetic every time the child grows, the prosthetic could be adjusted to accommodate the growth. This may also benefit those with a lower income. Rather than replacing a prosthetic every couple of years, the prosthetic would grow with them, saving them money over time. A typical prosthetic is between \$5,000 and \$50,000 (Jonathon Schwartz). The cost to produce the 3D printed prosthetic leg would be under \$200 (Jonathon Schwartz).

Projective Objective

My objective is to find a consumer friendly way of creating prosthetics for the youth in the growing stage by using the 3D printing process.

Methodology Used

The first step was to research the subject. Research is very important because there are many things that need to be considered when producing prosthetics. Some of the major issues include materials that will be used, the design of the prosthetic, any legal issues that may come up during the production or use of the product, the age that the product would be in the highest demand and the current market.

The second process would be the design. A design would need to be found that would function on an adjustable level. The design would have to be durable enough when printed in plastic from a 3D printer. The design would also have to allow for adjustability. Using the research, the key would be to create an end product that would be both durable and adjustable. Durability and adjustability would be key.

The final process would be to make a product that is both durable and adjustable. I will do this once I obtain the educational background needed to create a solid product.

Results Obtained

While researching prosthetics, I was unable to find a company that produced 3D printed limbs. There were not many companies that have been able to perfect an adjustable prosthetic that is consumer friendly. There are also no 3D printed prosthetics on the market.

I believe that I am on the right track for designing and producing an adjustable limb that could be used all over the world. My goal would be to help children with missing limbs be able to walk again. I believe with additional research while continuing my education, I may be able to help those who need an affordable option.

Significance and Interpretation of Results

My research leads me to believe that a prosthetic leg can not only be 3D printed but could also be adjustable. With the proper knowledge and design process, a prosthetic could be adjustable and cost effective at the same time.

Bibliography

1. Schwartz, Jonathan. "The Future of 3D-printed prosthetics." TechCrunch. TechCrunch, 26 June 2016. Web. 30 Mar. 2017.